Some numerical tools based on IGA for optimization applications in structural mechanics

Robin Bouclier

Habilitation à Diriger des Recherches

Université Fédérale Toulouse Midi-Pyrénées

Some numerical tools based on IGA for optimization applications in structural mechanics

(Quelques outils numériques basés sur l'IGA pour des applications d'optimisation en mécanique des structures)

Robin BOUCLIER

Soutenue le 8 septembre 2020

Jury :

Président :	Alessandro REALI	-	PR, Université de Pavie, Italie
Rapporteurs :	Piotr BREITKOPF	-	IR CNRS, HDR, Université de Technologie de Compiègne
	Frédéric NATAF	-	DR CNRS, Université Pierre et Marie Curie, Paris VI
	Julien RÉTHORÉ	-	DR CNRS, École Centrale, Nantes
Examinateurs :	Annalisa BUFFA	-	PR, École Polytechnique Fédérale de Lausanne, Suisse
	Patrick HILD	-	PR, Université Paul Sabatier, Toulouse
	Jérôme MONNIER	-	PR, Institut National des Sciences Appliquées, Toulouse
	Jean-Charles PASSIEUX	-	PR, Institut National des Sciences Appliquées, Toulouse

Contents

Foreword

This manuscript traces the major part of my research activities since obtaining my PhD thesis in 2014. The reported works were thus prepared during my post-doc (2015) at the "Institut de Mathématiques de Toulouse" (IMT) and then, while I was working as a "Maître de Conférences" at IMT (team "Mathématiques pour l'Industrie et la Physique") and as a research fellow at the "Institut Clément Ader" (ICA) (team "Modélisation des Systèmes et Micro-systèmes Mécaniques"). From a general point of view, I am interested in developing and implementing advanced computational methods for structural mechanics. More precisely, in order to meet the current concerns both in scientific and industrial terms, the algorithms that I design make a serious effort to deal with **the following challenges**:

1. High-Performance Computing: The demand for accurate and reliable numerical simulations is increasing exponentially across a broad range of scientific and engineering applications, such as in the field of structural mechanics. To be able to use a complex predictive numerical model (thus allowing to represent local non-linearities) at the scale of the entire structure (*e.g.*, a whole car or aircraft), the numerical efficiency of the methods has to be improved, which is the aim of High-Performance Computing (HPC). In particular, this appears of major interest in the current context of Virtual Testing, where part of the experimental tests are removed and replaced by numerical simulations to reduce the cost and time development of new products.

2. Reuse of available computational tools: The attractiveness of a new numerical method is often limited by practical considerations like the available hardware, software and human resources. Given the today myriad of existing tools and programming environments, it does not seem always necessary to start from scratch when designing and implementing a new method. In this context, the numerical strategies that are able to make use of commercial packages as black boxes appear appealing, since they can benefit from the ergonomic environment and from all the modeling and computing capabilities of already developed tools.

3. Ability to treat optimization problems: The fast development of efficient "direct" solvers, which take as an input a given model and return as an output the structural response, brings new opportunities to address the higher-level problem of optimization, that enables to question and adapt the numerical model with regard to key features. The ability of a (direct) computational strategy to be integrated into and to improve an optimization process thus seems essential, such as to perform design optimization during the product development in industry (thereby reducing the usual long trial-and-error learning process), or to perform data assimilation in the field of experimental solid mechanics (*i.e.*, to optimally combine a numerical model with observations).

To answer the aforementioned issues, my research works mostly concern **(i) IsoGeometric Analysis (IGA)** and **(ii) domain coupling** methods. Regarding the second point, besides developing new coupling formulations, my contributions are related to the construction of advanced algorithms, based on **(ii.a) non-invasive global/local** and **(ii.b) domain decomposition** procedures, for the efficient resolution of the coupling. Furthermore, in order to meet requirement **3.** above, I have recently focused my interest on **(iii) numerical optimization**, specifically to carry out **(iii.a) structural shape optimization** and to perform **(iii.b) image registration** for experimental solid mechanics (also commonly referred to as **(iii.b) Digital Image Correlation (DIC)** in the field). The corresponding scientific key points are given below. The working environment that brings me to consider such approaches in my research activities is also specified. References are voluntarily omitted here and are postponed to the remaining of the manuscript, where the scientific background for each method is further discussed.

IsoGeometric Analysis (IGA) has been originally introduced to reunify the fields of Computer-Aided Design (CAD) and Finite Element Analysis (FEA). The core idea is to resort to the same higher-order and

smooth spline bases for the representation of the geometry in CAD as well as for the approximation of solutions fields in FEA. The use of such families of functions makes IGA highly attractive for two main reasons: first, a common geometrical model can be used by both the designers and analysts; then, an increased per-Degree-Of-Freedom (per-DOF) accuracy can be reached in comparison to standard Finite Element Methods (FEM). This technology is thus often seen as a **high-performance computational tool** in the current literature. Benefiting also from the attractive geometrical feature, IGA appears particularly powerful for, *e.g.*, the **shape optimization of structures** since it eliminates the tedious successive meshing and/or smoothing of the geometry to be optimized in FEM. Pushing forward the reasoning, IGA actually provides a natural regularization procedure for **general optimization problems** since it allows to look for the solution in a more regular approximation space. I have had the opportunity to work on IGA during my PhD thesis (in the context of shell analysis), before bringing this technology to the scientific landscape of Toulouse, first for non-invasive global/local analysis during my post-doc and then, for shape optimization and image registration which are two important fields of research at IMT and ICA.

Broadly speaking, **domain coupling** in structural mechanics consists of appropriately transferring the kinematic and static information between several (usually different) meshes to connect them in a given simulation. This seems to be of major importance in the current context of **high-performance computing** and **reuse of available computational tools** since it constitutes the starting point to (i) combine different models at different scales (possibly coming from different software), and (ii) separate the computational resources between several subdomains. In particular, we will focus in this document on **global/local non-invasive coupling** schemes that enable to locally enrich a global model without altering its corresponding numerical operators. It thus becomes easy to interface several software or codes with this approach. We will also consider the family of **domain decomposition solvers**, that have been developed for high-performance computing on parallel computer architectures. Originally based on overlapping partitions, the non-overlapping methods seem to have now gathered a considerable momentum in the field of structural mechanics. Instead of solving one large system defined over the whole computational domain, the idea is to solve, in parallel, local systems defined per sub-domain, while the interface conditions are recovered through an iterative process. Finally, let us note that all these algorithms appear compatible with **optimization processes** since they allow not to recompute the full coupled problem when some regions are not optimized. I have been able to address domain coupling to perform non-invasive global/local IGA during my post-doc in Toulouse, and then to perform the parallel computation of digital image correlation and of multipatch isogeometric shell structures.

A stated above, mainly **two optimization problems** will be investigated in this manuscript: **structural shape optimization** and **DIC**. Although very different in terms of application, these two problems are quite close form a mathematical point of view; in particular, they are both solved using gradient-based algorithms since the gradient can be well computed and a "good" initial guess is available. **Structural shape optimization** aims at finding the optimal geometry of a structure with respect to a certain objective, such as minimal mass, maximal rigidity, etc. More precisely, we will focus on the optimal design of stiffened structures, which are ubiquitous in aeronautics. Today designs of wings and fuselages contain a lot of straight and aligned stiffeners uniformly distributed. However, it seems that defining curvilinear stiffeners instead of straight ones can further improve the mechanical behavior of the overall stiffened structures. Fig. 1(a) highlights what could be, in the future, the aerostructures based on free-form stiffeners. A general framework is proposed in this manuscript to compute such new structures and optimize their shape. Given a set of images taken over time that follow the deformation of a structure, the goal of **DIC** is to find the kinematic transformation that enables to move from one image to another. With the current improvement of imaging techniques (explosion of sensor definition and of acquisition time frames), it now becomes possible to observe in great detail the behavior at the surface of a (possibly non-planar) structure, or even at the interior of a material (as an illustration, see Fig. 1(b) that shows a volume image obtained by tomography). From a numerical point of view, the field now requires to develop innovative efficient algorithms (breaking with

the common practice in experimental mechanics) to extract mechanically sound information from such massive amount of image data. This problematic will be addressed in the document, especially by drawing inspiration from the **HPC** techniques of computational structural mechanics.

(a) Innovative stiffened structures with curvilinear stiffeners [Renard, 2018].

(b) Tomographic image of a composite sample [Chelaghma, 2018].

Figure 1 – Interest of the two main optimization problems addressed in the document.

Following these opening remarks, the manuscript is divided into two parts to **present the different contributions**: first, from chapter 1 to 3, the numerical tools that I have developed for the (direct) resolution of structural mechanics problems are presented; then, in chapters 4, 5 and 6, the constructed algorithms are extended and complemented by dedicated numerical devices to facilitate and improve some optimization processes in solid mechanics. More precisely, the first part starts by focusing on IGA before the works achieved in this field regarding non-invasive global/local coupling and domain decomposition are introduced. The second part is organized with respect to the different optimization applications tackled, going from the easiest to the most complicated one in terms of optimization resolution. From here on, it should be stressed that the contributions regarding optimization rather concern the modeling and the involved direct resolutions than the optimization algorithm itself. The manuscript structure is specified in the following. For each part, the related contributions are outlined. The resulting papers and the supervised students (if any) are also indicated.

In **Chapter 1**, **IGA** is outlined by providing an original point of view on its relation with standard FEM. Specifically, IGA is interpreted as the projection of classic FEM onto a specific, more regular, reduced basis. The increased per-DOF accuracy of IGA appears clear through this lighting: the discretization space for IGA is somehow included into the FE space, which allows to capture smooth mechanical solutions while saving a significant number of DOF. We also push forward the concept in this chapter in order to perform IGA in an available FE software in a truly non-invasive manner; that is, the total FE code can be used as a black box. This work, with in particular the construction of a non-invasive implementation scheme for IGA, has been achieved in the PhD thesis of Marie Tirvaudey [Tirvaudey, 2019], who I co-supervised with Prs. J.-C. Passieux (INSA Toulouse) and L. Chamoin (ENS Paris-Saclay), and has led to [Tirvaudey et al., 2019a].

Chapter 2 gives an overview of the numerous works I have been able to carry out regarding **non-invasive global/local coupling** [Bouclier et al., 2016, Bouclier et al., 2017, Guinard et al., 2018, Bouclier and Passieux, 2018, Tirvaudey, 2019, Tirvaudey et al., 2019b]. Originally introduced in the FEM framework to fulfill an industrial requirement, we show that this type of technology is of great interest for global/local IGA from a scientific point of view. The idea is to take the initial isogeometric model as the global model, so that the need for costly spline re-parametrization procedures when integrating a non-conforming local model is eliminated. Furthermore, the global (well-conditioned) stiffness operator is assembled and factorized only once regardless of the evolution of the local model. In particular, the progresses that we choose to report in this document concern the development of non-invasive numerical schemes to

(i) couple complex non-conforming FE models; (ii) perform hybrid global/local simulations combining IGA and FEM; and (iii) properly handle any non-conforming isogeometric configurations encountered through an arbitrary global/local process. Given its flexibility and robustness, the last algorithm will then be efficiently integrated into an optimization loop for performing structural design in chapter 6. Regarding the working environment, point (i) has been addressed in collaboration with AIRBUS, and more specifically with S. Guinard (Airbus Group Innovations), through the co-supervision of the master 2 internship of Mateus Toniolli in 2016, and has led to [Guinard et al., 2018]. Point (ii) has been investigated first during my post-doc in Toulouse with Prs J.-C. Passieux and M. Salaün (ISAE-SUPAERO) [Bouclier et al., 2016], and then through the PhD thesis of Marie Tirvaudey [Tirvaudey, 2019]. Finally, the progress related to point (iii) has been achieved more recently in collaboration with Pr. J.-C. Passieux [Bouclier and Passieux, 2018].

Chapter 3 is devoted to the analysis of non-conforming multipatch isogeometric shell structures. More precisely, we are interested, in terms of application, in the computation of complex curved stiffened panels (see Fig. 1(a) again). The work performed in this chapter will serve as a prerequisite to design innovative aerostructures with improved structural properties in chapter 6. A new Mortar coupling formulation for the proper connection of non-conforming Kirchhoff-Love shells that intersect with arbitrary angles is first proposed. In order to do so, two sets of Lagrange multipliers are considered to impose the continuity of both the displacement and rotation of the shell. Then, benefiting from this Mortar coupling, we build an iterative dual **domain decomposition solver** where, at each iteration, only local quantities defined at the patch level are involved which makes the overall algorithm naturally parallelizable. We also study the preconditioning step in order to tend to an algorithm which is numerically scalable. From a conceptual point of view, this work shares similarities with the one of chapter 2: the solver is adapted to perform multiresolution, such as during shape optimization since it allows to factorize once for all the stiffness matrices of patches located in non-design regions (as will be illsutrated in chapter 6). This work has been achieved in the PhD thesis of Thibaut Hirschler [Hirschler, 2019], who I co-supervised from Toulouse with Pr. T. Elguedj at INSA Lyon, and has been published in [Hirschler et al., 2019a, Hirschler et al., 2019b]. We shall also specifically mention at this stage the collaboration with Pr. D. Dureisseix (INSA Lyon) which was crucial for the construction of an efficient domain decomposition solver.

Chapter 4 concerns the first optimization application tackled, namely **Digital Image Correlation** (DIC). The chapter is composed of two main sections. First, a mathematical analysis of the most commonly used algorithm in DIC is performed. In particular, the choice of a constant operator over the iterations is clearly accounted for and appears sufficient for the measurement of almost all solid mechanics phenomena (including large deformations). Although this work may appear standard from the viewpoint of numerical optimization, it seems to us appropriate to clarify the mathematical background of DIC and correct some inaccurate terminologies in the literature, especially towards the experimental mechanics community. This work has been performed very recently in collaboration with Pr. J.-C. Passieux [Passieux and Bouclier, 2019]. Then, in the second section, an original domain coupling method is proposed to recover displacement continuity and mechanical equilibrium from two independent FE-based DIC analysis with mechanical regularization. As in chapter 3, two additional unknown fields are considered but, this time, the interface reaction force does not constitute a Lagrange multiplier from a numerical point of view. The method is also extended to parallel computing thanks to the use of a suitable Krylov solver and the construction of a dedicated preconditioner. The interest of integrating such an HPC tool in the optimization loop of DIC is highlighted. This work was actually the first one for me related to numerical optimization and was achieved with Pr. J.-C. Passieux at the beginning of my assistant professor position at INSA-Toulouse [Bouclier and Passieux, 2017]. It may eventually be noticed that I have been (or am currently) involved in some other works related to DIC that share the same philosophy as the ones reported here (see, especially, [Passieux et al., 2018] where model-order reduction is extended to DIC, [Rouwane et al., 2020] (from the PhD thesis of Ali Rouwane [Rouwane, 2021] who I co-supervise with J.-C. Passieux and J.-N. Périé (UPS Toulouse)) where the aim is to build an image-based mechanical model for the regularization of Digital

Volume Correlation, and [Fouque et al., 2020] (from the PhD thesis of Raphaël Fouque [Fouque, 2021] who I also co-supervise with J.-C. Passieux and J.-N. Périé) where the long-term goal is to perform mechanical identification from stereoscopic images).

In **chapter 5**, the optimization problem of **mesh-based 3D shape measurement** with stereocorrelation is addressed. By assimilating the data coming from at least two cameras, this problem consists of updating the initial theoretical geometry of the surface to fit with the actual 3D shape of the specimen. If the use of a FE mesh facilitates in the long-term the coupling of measurements with simulation tools, it also provides a unique, fine description of both the geometry and the displacement, which inevitably exacerbates the ill-posedness of the shape measurement problem. For the regularization, we propose to make use of the intrinsic attractive properties of splines and of the bridge between IGA and FEM established in chapter 1. The key idea is to extract, from the initial FE subspace, smoother multilevel spline parametrizations of the geometry and to relate them with the multi-scale images used for the initialization of shape measurement. From a practical point of view, the proposed approach simply consists of projecting the ill-posed FE shape measurement problem onto more regular spline subspaces adapted to the data provided by the multi-scale images. It results in a non-invasive and geometrically sound regularization which provides a spline parametrization of the optimal shape along with its FE twin. This work has been performed very recently in the PhD of thesis of Morgane Chapelier [Chapelier, 2021], who I co-supervise with Pr. J.C. Passieux, and has been published in [Colantonio et al., 2020].

Chapter 6 addresses the **isogeometric shape optimization of structures**. In this context, our main contribution concerns the optimal design of representative aerostructures. Following the work performed in chapter 3 regarding scientific computing, and resorting to the existing progresses in the area of isogeometric shape optimization, the main challenge to face is the geometrical handling of non-conforming multi-patch discretizations. Drawing inspiration from the Free-Form Deformation (FFD) concept, a novel, full geometrical framework is developed to perform the isogeometric shape optimization of any complex stiffened structure. More precisely, we introduce an embedded geometrical modeling that enables to properly impose shape changes to the stiffeners as well as to the panel. The final geometric model, which is obtained by spline composition, is also directly used in the analysis step by formulating an embedded Kirchhoff-Love shell element. An exact link between the shape parameters and the resulting analysis model thus exists, which makes our strategy very robust and generic in contrast with the current FE-based framework, where several intermediary approximation steps separate the design and analysis models. This brings the possibility to explore new types of design. The works on shape optimization of shells [Hirschler et al., 2019c, Hirschler et al., 2019b, Hirschler et al., 2020] have been performed in the PhD thesis of Thibaut Hirschler [Hirschler, 2019]. We shall also mention at this stage the collaboration with Pr. J. Morlier (ISAE-SUPAERO) which led to fruitful discussion regarding the optimization aspect. The results reported in this manuscript are mostly extracted from [Hirschler et al., 2019b]. Finally, the potential of the non-invasive procedures of chapter 2 for the efficient design of structural details within such complex macro-structures is highlighted through a numerical experiment at the end of the chapter. This last work shares the same philosophy as in [Hirschler et al., 2019b] and has been actually achieved before in [Bouclier and Passieux, 2018].

The document ends with a general conclusion and prospect.

Part I

Some numerical tools based on IGA . . .

CHAPTER 1

IGA: a projection of FEM onto a powerful reduced basis

Contents

IsoGeometric Analysis (IGA) was originally introduced by [Hughes et al., 2005] and formalized in [Cottrell et al., 2009] in order reunify geometric modeling and computational mechanics. The main idea is to resort to the same bases for analysis as the ones employed to describe the geometry in Computer-Aided-Design (CAD), so that delicate meshing procedures are avoided and a common geometrical model can be used by both the designers and analysts. In this framework, the method can be viewed as a generalization of the finite element method that considers smooth and higher-order functions, *e.g.* Non-Uniform-Rational-B-Spline (NURBS) functions [Cohen et al., 1980, Piegl and Tiller, 1997, Rogers, 2000, Farin, 2002], to replace typical Lagrange polynomials in the computations. Other geometry descriptions include T-Splines [Bazilevs et al., 2010] and subdivision surfaces [Cirak et al., 2002]. Within this work only NURBS (which constitute the most commonly used technology in CAD) and simpler B-Splines are used. In the whole manuscript, we employ the terminologies *spline* or *isogeometric* indifferently to denote a NURBS or a B-Spline object. Beyond the reinforced link between CAD and numerical simulation, IGA turned out to be a superior computational mechanics technology, which on a per-degree-of-freedom basis exhibits increased accuracy and robustness in comparison to standard Finite Element Methods (FEM) [Evans et al., 2009]. The reason for this is the higher-order regularity of spline-based functions, namely $C^{(p-1)}$ through the (knot-span) elements of the mesh for a polynomial degree p [Cottrell et al., 2007], whereas only C^0 continuity is available for Lagrange polynomials. In this respect, IGA has now been successfully applied to numerous disciplines of mechanics, such as shell analysis [Kiendl et al., 2009, Echter et al., 2013, Bouclier et al., 2015b], contact problems [Seitz et al., 2016, Antolin et al., 2018], fluid-structure interaction [Kamensky et al., 2017, Apostolatos et al., 2019], shape optimization [Wall et al., 2008, Nagy et al., 2013, Kiendl et al., 2014], Digital Image Correlation [Réthoré et al., 2010a, Dufour et al., 2015a], geometrical and material non-linear solid mechanics [Elguedj et al., 2008, Lipton et al., 2010, Bouclier et al., 2015a, Ambati et al., 2018], fluid dynamics [Bazilevs et al., 2007, Akkerman et al., 2011], structural vibration [Cottrell et al., 2006, Shojaee et al., 2012], to name a few. We shall also mention at this stage the work by [Morganti et al., 2015]

which may constitute one of the most significant illustration of the superiority of IGA over standard FEM; in particular, drastic reduction of the computational time was obtained for the simulation of a aortic valve closure.

From this brief overview, IGA and FEM seems to share an ambiguous relationship. On the one hand, IGA encompasses FEM since it offers the opportunity to involve (geometrically sound) basis functions with C^0 as well as higher-order regularities at the elements boundaries. In the same idea, a new refinement procedure, in which the polynomial degree and the regularity of the basis functions can be simultaneously increased, is available with spline technologies (while C^0-regularity is maintained through standard FE-mesh refinements). On the other hand, at least for polynomial spline bases, the (possibly more) regular discretization spaces offered by IGA are included into the C^0 spaces given by classic FEM (provided that both IGA and FEM come with the same number of elements and the same polynomial degree). When rational splines are considered such as NURBS, the inclusion does not strictly hold but we will see that a similar approximate link can still be formulated between NURBS-based IGA and FEM. As a result, from a pure analysis point of view, IGA can also be interpreted as a projection of FEM onto a specific reduced basis which is attractive for numerical simulation (especially when the polynomial degree increases). Although not explicitly stated, this is this second point of view that was followed in the original works aiming at implementing IGA using the elementary structure of standard FE codes [Borden et al., 2011]. By means of the Bézier extraction, smooth spline bases were expressed in terms of C^0 functions which enabled to compute the elementary contributions of the IGA operators inside conventional FE codes.

This first chapter undertakes to outline IGA from this second point of view. An alternative lighting on the relation between IGA and FEM is thus provided here compared to the more common one that consists of viewing IGA as simply encompassing FEM. To start with, the existing link between IGA and FEM is reviewed through the presentation of the initial Bézier and more recent Lagrange [Schillinger et al., 2016b] extractions. Then, we push forward the concept in order to perform IGA in an available FE software in the least possible invasive manner; that is, we seek to reduce the implementation effort to the minimal level. The ultimate goal is to make IGA more accessible for industrial engineers. More precisely, starting with the Lagrange extraction technology, we adopt a global view and formulate a complete algebraic bridge that directly goes from Lagrange nodal polynomials to B-Spline and NURBS functions. It leads to a novel, alternative implementation procedure where the total FE code can be used as a black-box. We close this chapter by showing some numerical results to illustrate our point of view on IGA. The developed non-invasive strategy is applied to simply incorporate isogeometric capabilities in the industrial FE code `Code_Aster`, which is a familiar open source software package for numerical simulation in structural mechanics developed by the EDF R&D company [CodeAster, 2014]. This work, with in particular the construction of a non-invasive implementation scheme for IGA, has been achieved in the PhD thesis of Marie Tirvaudey [Tirvaudey, 2019], who I co-supervised with Prs. J.-C. Passieux and L. Chamoin, and has led to [Tirvaudey et al., 2019a]. The interested reader is advised to consult this reference, especially for further details regarding the non-invasive implementation of IGA.

1 The link between IGA and FEM

In this first section, the main ingredients to tie (B-Spline and NURBS based) IGA and FEM closer together are given. A particular care is taken to introduce the concepts from the FEM community viewpoint. In this respect, we make comparisons between spline and nodal finite elements as much as possible. This facilitates the introduction of our alternative lighting on the relation between IGA and FEM. More precisely, starting with some global information regarding the B-Spline and NURBS technologies, we then move to the presentation of the so-called Bézier extraction [Borden et al., 2011] and more recent Lagrange extraction [Schillinger et al., 2016b] operators. Although the Lagrange extractor encompasses the Bézier one, we prefer to start with the original Bézier version before introducing the Lagrange transformation given the

importance of the concept of Bézier extraction in the state-of-the-art of IGA.

1.1 NURBS-based IGA

The concept of IGA being now mature and relatively well-known in the academic scientific computing community, only the fundamentals are given in the following. For further details, besides the pioneering contributions [Hughes et al., 2005, Cottrell et al., 2009], the interested reader is referred to the works cited hereafter. We recall that the idea is to use the spline-based parametrizations of CAD environments to build the approximation spaces when applying the Galerkin's method. Roughly speaking, this is the main difference with the classical FEM from the computational point of view. We state again that we restrict ourselves to B-Spline and NURBS technologies in this work. Thus, we give here key elements regarding the B-Spline and NURBS geometric modeling techniques.

1.1.1 Basics

The NURBS family is the spline technology which has become the standard over the years for geometric modeling in CAD and computer graphics [Cohen et al., 1980, Piegl and Tiller, 1997, Rogers, 2000, Farin, 2002]. The NURBS functions lend themselves to an exact representation of many shapes used in engineering, such as conical sections (circles, cylinders, spheres, ellipsoids, etc). NURBS are a generalization of B-Splines: they can be viewed as rational projections of B-Splines. Therefore, they possess many of the properties of B-Splines, the most interesting one being their possible increased smoothness, thus implying few degrees of freedom.

A general expression for a NURBS geometry with parameter $\xi \in \mathbb{R}^d$ (d being the dimension of the spline entity) is written as:

$$G^h(\xi) = \sum_{i=1}^{n_{IG}} R_i(\xi) x_i = \mathbf{R}^T(\xi)\mathbf{x}, \tag{1.1}$$

where $\mathbf{R}$ and $\mathbf{x}$ denote the matrix of the n_{IG} NURBS basis functions and the vector collecting the locations of the associated control points, respectively. Considering, for instance, control points in 3D, $\mathbf{R}$ and $\mathbf{x}$ formally read:

$$\mathbf{R} = \begin{bmatrix} R_1 & 0 & 0 \\ \vdots & \vdots & \vdots \\ R_{n_{IG}} & 0 & 0 \\ 0 & R_1 & 0 \\ \vdots & \vdots & \vdots \\ 0 & R_{n_{IG}} & 0 \\ 0 & 0 & R_1 \\ \vdots & \vdots & \vdots \\ 0 & 0 & R_{n_{IG}} \end{bmatrix} \quad \text{and} \quad \mathbf{x} = \begin{bmatrix} x_1^1 \\ \vdots \\ x_{n_{IG}}^1 \\ x_1^2 \\ \vdots \\ x_{n_{IG}}^2 \\ x_1^3 \\ \vdots \\ x_{n_{IG}}^3 \end{bmatrix}. \tag{1.2}$$

x_i in (1.1) is the subset of $\mathbf{x}$ gathering the coordinates $\{x_i^1, x_i^2, x_i^3\}$ of the ith control point. The multivariate NURBS basis functions are obtained from the multivariate B-Spline functions N_i as follows:

$$R_i(\xi) = \frac{w_i N_i(\xi)}{W(\xi)} \quad \text{with} \quad W(\xi) = \sum_{k=1}^{n_{IG}} w_k N_k(\xi), \tag{1.3}$$

and where w_i denotes the weight of the ith control point. The positions of the control points and the values of the associated weights can be adjusted in order to build conical sections exactly (see,

e.g., [Cottrell et al., 2007, Cottrell et al., 2009]). Given Eq. (1.3) (and verifying that the B-Spline functions satisfy the partition of unity), it may be noticed that if all weights are equal, the NURBS entity turns out to be a B-Spline entity. Then, all one needs to do in order to define the multivariate B-Spline function N_i at control point i is to perform the tensor product of the univariate B-Spline functions associated with this point in the different spatial directions. Considering, *e.g.*, a 3D entity, if one denotes

$$\left(M^1_{i_1}\right)_{i_1\in\{1,2,..,n_{IG_1}\}}, \quad \left(M^2_{i_2}\right)_{i_2\in\{1,2,..,n_{IG_2}\}} \quad \text{and} \quad \left(M^3_{i_3}\right)_{i_3\in\{1,2,..,n_{IG_3}\}}$$

the n_{IG_1}, n_{IG_2} and n_{IG_3} univariate B-spline functions associated with each of the three spatial directions, this means that at control point i (which corresponds to control point i_1, i_2 and i_3 in the spatial directions), one has:

$$N_i(\xi) = M^1_{i_1}(\xi_1) \times M^2_{i_2}(\xi_2) \times M^3_{i_3}(\xi_3). \tag{1.4}$$

In the end, the n_{IG_1} univariate B-Spline basis functions are piecewise polynomials defined by their polynomial degree p and a set of non-decreasing parametric coordinates $\xi^i_1 \in \mathbb{R}$ collected into a knot-vector $\Xi_1 = \left\{\xi^1_1, \xi^2_1, .., \xi^{n_{IG_1}+p+1}_1\right\}$. From knot-vector Ξ_1, the B-Spline basis functions are constructed recursively using the Cox-de Boor formula (see [Cohen et al., 1980]). The coordinates ξ^i_1, referred to as knots, divide the parametric space into (knot-span) elements, and the interval $\left[\xi^1_1, \xi^{n_{IG_1}+p+1}_1\right]$ constitutes the isogeometric patch. Simple geometries can be modeled with a single patch. Given the tensor product structure (1.4), a patch is a rectangle in the parametric domain for two-dimensional topologies. In three dimensions it is a cuboid. Unlike standard FE where each element has its own parametrization, the parametric space of B-Spline functions is localized onto the patch, that may be thought of as a macro-element. As an example, we plot in Fig. 1.1 the basis functions resulting from a two-element quadratic mesh in case of smooth B-Spline (see Fig. 1.1(a)) and standard FE (see Fig. 1.1(b)) discretizations. In the B-Spline situation, four global basis functions are generated. On the contrary, three Lagrange polynomials are defined locally and then mapped out each of the two elements in case of a FE modeling.

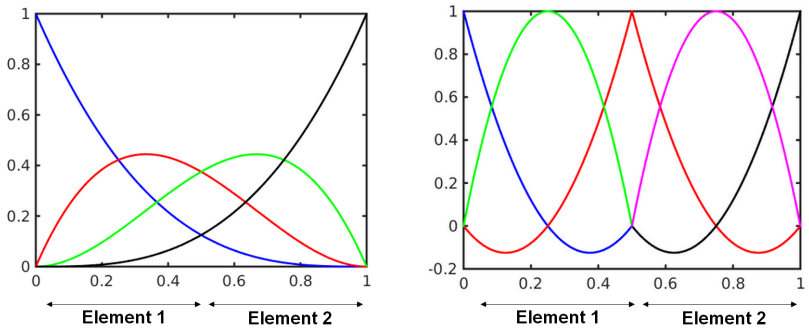

(a) B-Spline functions. (b) Lagrange functions.

Figure 1.1 – Quadratic univariate B-Spline and Lagrange functions for a mesh composed of two elements. The knot-vector for the B-Spline functions is $\Xi_1 = \{0, 0, 0, 0.5, 1, 1, 1\}$

The interesting feature of splines is their higher degree of regularity. Indeed, a B-Spline function of order p can reach a C^{p-1} regularity at knot ξ^i_1 if this one is single. There can be more than one knot at a given location of the parametric space. More precisely, if m is the multiplicity of a given knot, the functions are C^{p-m} continuous at that location which is in contrast with standard FE where only a C^0 regularity is encountered on the element boundaries. As an illustration, we refer again to the plots of Fig. 1.1: the four global B-Spline functions attain a C^1-regularity at knot $\xi^i_1 = 0.5$ while the FE space is built from five global shape functions that meet a C^0-regularity at that location. Consequently, for a given polynomial degree and a similar number of elements, a C^{p-1} B-Spline mesh comes with less degrees of freedom (DOF) than the

corresponding C^0 FE mesh, which is totally understandable since the space of C^{p-1} functions is included into the space of C^0 functions (in other words, a function that is C^{p-1} is also C^0 and not the other way around). The more elements and higher polynomial degree, the more DOF are saved using smooth spline over traditional FE discretizations. This is the main feature of IGA that provides increased per-degree-of-freedom accuracy with respect to FEM when smooth solutions are to be captured. This point will be further accounted for in this chapter. Obviously we will consider in this work splines of degree $p \geq 2$ to benefit from their increased smoothness.

For illustration purpose, Figs 1.2(a) and 1.2(b) show an example of B-Spline curve and NURBS surface, respectively. The B-Spline curve uses the univariate B-spline functions depicted in Fig. 1.1(a). In both cases, the linear combination (see Eq.(1.1)) of the spline functions using, as coefficients, the control points marked with circles on the figures is performed to generate the corresponding spline entities. A quarter of hemisphere is generated in Fig. 1.2(b) using, as an isogeometric patch, a single quadratic NURBS element. Four matching patches can then be assembled using a similar procedure as for FE assembly to get and compute the full hemisphere. We do not go further into the details here. Let us simply note that multipatch modeling seems to be necessary when the geometry differs topologically from a square or a cube (the tensor product structure (1.4) of the parametric space of a patch makes it poorly suited for representing complex, multiply connected domains). At this stage, we refer the interested reader to [Cottrell et al., 2009] and indicate that the multipatch modeling issue will be deeply addressed in the remaining of this manuscript.

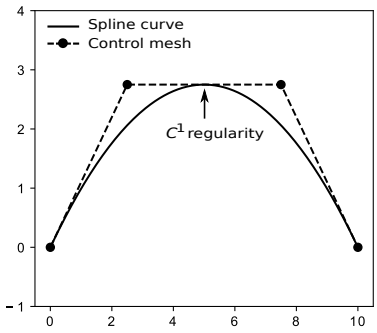

(a) Quadratic B-spline curve.

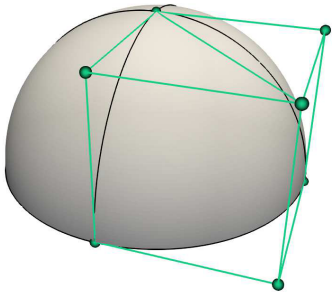

(b) Generating a hemisphere by means of NURBS.

Figure 1.2 – Examples of B-Spline and NURBS geometric entities (the control mesh is the linear interpolation of the control points).

1.1.2 k-refinement: increasing both the polynomial degree and the regularity

After building the initial (coarse) spline mesh allowing for an exact representation of the problem geometry, refinement is possible without changing the geometry. To this end, two mechanisms exist: *knot-insertion* and *order-elevation*. The knot-insertion technique enables to recover the h-refinement of FEM. It consists in adding new knots in the knot-vectors. To perfectly replicate h-refinement, one needs to insert each of the new knot values p times so that the functions will be C^0 across the new element boundary. The order-elevation technique is the analogous of the p-refinement in FEM: it consists in increasing the polynomial degree of the basis functions. Hence, it has to be noted that through the order-elevation all values in the knot-vector are repeated to preserve the initial discontinuities of the derivatives of the functions. If one starts with a spline mesh involving C^0 basis functions at the knots, order-elevation exactly coincides with p-refinement in FEM. These equivalences in terms of refinement procedures clearly indicate that IGA encompasses standard FEM. In other words, FEM can be recovered using the B-Spline technology.

Now, the flexibility of the knot-insertion and order-elevation processes allows to introduce a new refinement scheme in which the polynomial degree and the regularity of the basis functions can be simul-

taneously increased. The new refinement strategy is called k-refinement. It is achieved by first applying order-elevation and then inserting knots (with multiplicity one) so that elements are added while ensuring the maximum available regularity of the basis functions at the knots level, namely C^{p-1}. An example is given in Fig. 1.3. Starting with a quadratic C^1 two-element B-Spline curve (as in Fig. 1.2(a)), knot-insertion is performed with multiplicity one so that the spline curve is refined while maintaining its initial shape and offering a C^1 regularity at the new knots. In this work, unless otherwise stated, we will perform k-refinement to take advantage of the superior properties of splines. We eventually note that matrix representations of the spline refinement procedures are possible; that is, denoting by $\mathbf{R}^c$ and $\mathbf{R}^f$ the matrices collecting, respectively, the n^c_{IG} coarse and n^f_{IG} fine spline functions, we can build the refinement operator $\mathbf{D}^{c,f}$ such that:

$$\mathbf{R}^c = \mathbf{D}^{c,f}\mathbf{R}^f \quad (n^c_{IG} \leq n^f_{IG}). \tag{1.5}$$

Such a relation offers a simple way to build the refined spline mesh from the coarse one. Denoting by $\mathbf{x}^c$ and $\mathbf{x}^f$ the location of the control points associated to the coarse and fine description, respectively, and asserting that the geometry (see Eq. (1.1)) is not modified through the refinement, we can write the following equality:

$$\left(\mathbf{R}^c(\xi)\right)^T \mathbf{x}^c = \left(\mathbf{R}^f(\xi)\right)^T \left(\mathbf{D}^{c,f}\right)^T \mathbf{x}^c, \quad \forall \xi \ ; \tag{1.6}$$

which simply leads to:

$$\mathbf{x}^f = \left(\mathbf{D}^{c,f}\right)^T \mathbf{x}^c. \tag{1.7}$$

For more details on refinement strategies of splines and their matrix representations, reference is made to [Piegl and Tiller, 1997, Lee and Park, 2002, Cottrell et al., 2007].

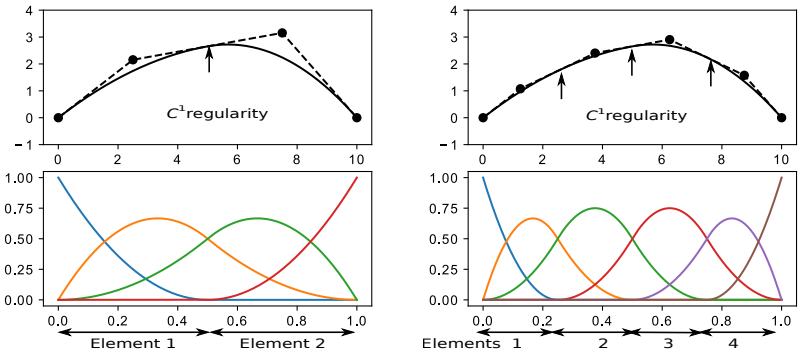

(a) Initial B-Spline model composed of two quadratic C^1 elements.

(b) Refined B-Spline model obtained by the insertion of knots $\xi_1 = 0.25$ and 0.75 to end up with four quadratic C^1 elements.

Figure 1.3 – An example of a spline refinement procedure that maintains a higher regularity at the new elements boundaries; (top) the curve with the control points and (bottom) the univariate shape functions plots realized in the parametric space ($\xi_1 \in [0,1]$).

Remark. *If the B-Spline and NURBS technologies can offer superior global accuracy for the analysis thanks to the k-refinement process, it has to be noticed that multivariate B-Spline or NURBS bases do not provide a natural possibility for local mesh refinement. The rigid tensor-product structure (1.4) of these functions actually precludes local mesh refinement within a patch. Indeed, refinement is a global process that propagates throughout the entire patch. Basically there exist two approaches to answer this issue: (i) the generation and coupling of (usually non-conforming) spline patches and (ii) the creation of alternative splines that enable local mesh refinement. In this work and particularly in chapter 2, we will contribute to approach (i) in order to perform not only local mesh refinement, but also to incorporate more*

general local phenomena within a B-Spline or a NURBS model. Regarding point (ii), one may cite, e.g., *the hierarchical B-Splines and NURBS [Vuong et al., 2011, Scott et al., 2014, Hennig et al., 2016], the locally refined B-Splines [Dokken et al., 2013], the T-Splines [Bazilevs et al., 2010, Scott et al., 2012, Veiga et al., 2012] and the hierarchical T-Splines [Evans et al., 2015, Chen and Borst, 2018]. Among these strategies, T-Splines gathered an important momentum from both the computational geometry and analysis communities since they also appeared suitable to address trimmed multipatch geometries (see discussion below). Nevertheless, if one seeks to perform local mesh refinement only, the hierarchical splines may be easier to implement [D'Angella et al., 2018] while the locally refined B-Splines seem to be compatible with the strucutre of conventional FE codes [Occelli et al., 2019]. Finally, note that the work on new splines is by no means complete, as demonstrated for example by the very recent introduction of U-Splines (unstructured splines) by Coreform for industrial applications [Thomas et al., 2018].*

1.1.3 The trimming concept and analysis-suitable model issue

Even if based on the same basis functions, the link between CAD and analysis originally advocated by IGA is not trivial in practice. Indeed, the prerequisites for the geometric modeling and for the numerical simulation are different. Standard IGA requires a boundary fitted discretization for the analysis while in CAD programs, where the only need is the rendering of the geometry, such a spline parametrization is not necessary. To clarify the problematic, we need to introduce here the concept of trimming. Trimming is one of the most fundamental tools in CAD environments, where complex geometries are built using boolean operations. The process enables to create an almost unlimited range of geometric shapes. The trimming concept is illustrated in 2D for the simple situation of a circular hole living in a rectangular structure, see Fig. 1.4. This surface can be classified as a trimmed surface. Its description is simply given by: a one-patch B-Spline surface parametrization for the plate (without the hole) and a NURBS curve parametrization for the trimming curve that forms the boundary of the hole (see Fig. 1.4(a)). In CAD, the trimming curve specifies visible and invisible regions on the surface patch (see Fig. 1.4(b)). As a consequence, the underlying spline patch remains unaffected by the trimming object and preserves its topology. Conversely, using standard IGA for the analysis of such a geometry would require a delicate re-parametrization of the whole spline model, including the splitting of the new geometry into several patches with C^0 regularity at the boundaries. An example of a boundary fitted NURBS parametrization of the plate including the hole (*i.e.*, without trimming) is shown in Fig. 1.4(c). This new spline model is commonly refereed as an analysis-suitable model in the field since it can be easily enhanced using classic spline refinement to compute the solution of a corresponding mechanical problem.

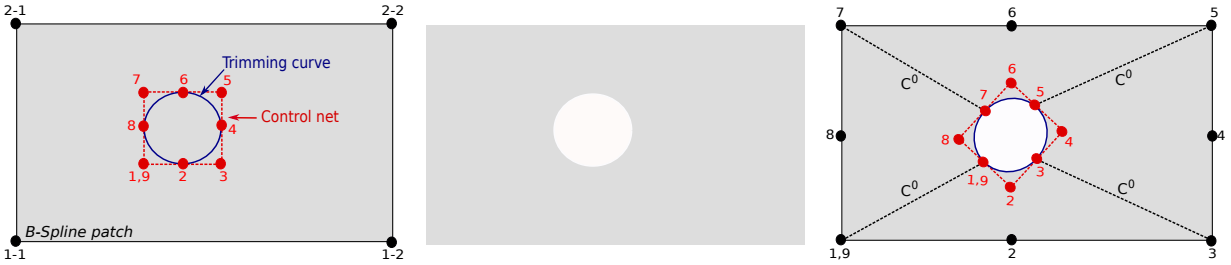

(a) Spline parametrization of the trimmed geometry.

(b) CAD rendering.

(c) Spline re-parametrization (without trimming).

Figure 1.4 – Illustration of the trimming concept.

The simple example of a plate with a hole underlines the difficulties of generating analysis-suitable models for IGA. In practice, a raw geometric model, as given by a CAD modeler, involves plenty of trimmed patches that arbitrary intersects with each other. Even more, a volume is built in CAD through its Boundary representation (B-rep); that is, by grouping together intersected trimmed surface patches and filling

the interior of the volume in the CAD rendering. Consequently, the generation of analysis-suitable models constitutes a very important problematic in IGA and is currently the object of intensive studies. There are mostly two ways to deal with this issue. Firstly, one can strive to remove all trimmed regions and non-conformity between patches by invoking re-parametrization strategies, which can appear cumbersome [Xu et al., 2013, Akhras et al., 2016, Massarwi et al., 2019]. The second option consists in using advanced numerical tools for analyzing models with the mentioned defects coming from the geometric modeling [Marussig and Hughes, 2018, Teschemacher et al., 2018]. The first part of this manuscript is heading in the second direction: it intends to design efficient algorithms for (i) modeling local phenomena within IGA models (see chapter 2) and (ii) analyzing multipatch shell models with non-conforming interfaces (see chapter 3). The discussion regarding the analysis-suitable model issue is thus not restricted to this paragraph: additional insights will be further given, especially in chapters 2 and 3.

1.2 The Bézier extraction

The concept of Bézier extraction has proved to be a milestone to tie IGA and FEM closer together. Originally introduced in [Borden et al., 2011] for B-Splines and NURBS, the concept has now been generalized to a large variety of advanced splines such as T-Splines [Scott et al., 2011], hierarchical B-Splines and NURBS [Hennig et al., 2016, D'Angella et al., 2018], and hierarchical T-Splines [Evans et al., 2015, Chen and Borst, 2018]. Focusing here on B-Splines and NURBS, the technology enables to formulate a smooth polynomial B-Spline (respectively NURBS) function in terms of C^0 polynomial Bernstein (resp. rational Bézier) functions. Once again, this is possible because the space generated by smooth spline functions is included in the one generated by C^0 functions. In other words, the idea here is to extract the smooth part of C^0 functions.

Although its name may suggest the opposite, it has to be stressed that the so-called Bézier extractor is related to the transformation for polynomials as B-Spline functions (and not for rational functions such as NURBS functions). As a result we start here by focusing on B-Splines (the treatment in case of NURBS being postponed to section 1.4). The Bézier extractor maps a Bernstein polynomial basis onto a smooth B-Spline polynomial basis. Given the previous discussion on spline mesh refinement procedures, the creation of a structured C^0 Bernstein mesh (with identical geometry) from a smooth B-spline mesh is obvious: one simply needs to repeat all the inside knots of the knot-vectors until they reach a p multiplicity. A specific knot-insertion process is thus performed which results in the computation of new control points to preserve the initial B-Spline geometry. An illustration is given in Fig. 1.5. Starting with (a) a quadratic C^1 two-element B-Spline curve (as in Fig. 1.3(a), associated knot-vector $\Xi_1 = \{0,0,0,0.5,1,1,1\}$), the knot $\xi_1^i = 0.5$ is added to get the discretization (b). The advantage of Bernstein functions is that they exhibit an elementary structure which is similar to FEM. This allows for a simple implementation method for IGA, where each element has its own parametrization.

The Bézier extractor $\mathbf{D}_{BEZ}$ is constructed by making use of the matrix representation of the corresponding refinement process. Similarly as in (1.5), it follows:

$$\mathbf{N} = \mathbf{D}_{BEZ}\mathbf{B}, \tag{1.8}$$

where $\mathbf{N}$ and $\mathbf{B}$ are the matrices gathering the B-Spline and Bernstein functions, respectively. We indicate that the only inputs required to construct this operator are the knot-vectors (see again [Cottrell et al., 2007] for more information regarding spline refinement). In order to determine the positions of the Bernstein control points the equality between the expression of the B-Spline entity and the Bernstein one is used (same treatment as in Eq. (1.6)). By expressing the B-Spline functions using (1.8), we obtain that $\mathbf{x}^{BER} = \mathbf{D}_{BEZ}^T\mathbf{x}^{BS}$, where $\mathbf{x}^{BER}$ and $\mathbf{x}^{BS}$ stand for the locations of the Bernstein and B-Spline control points, respectively. More details on the construction of this extractor can be found in [Borden et al., 2011].

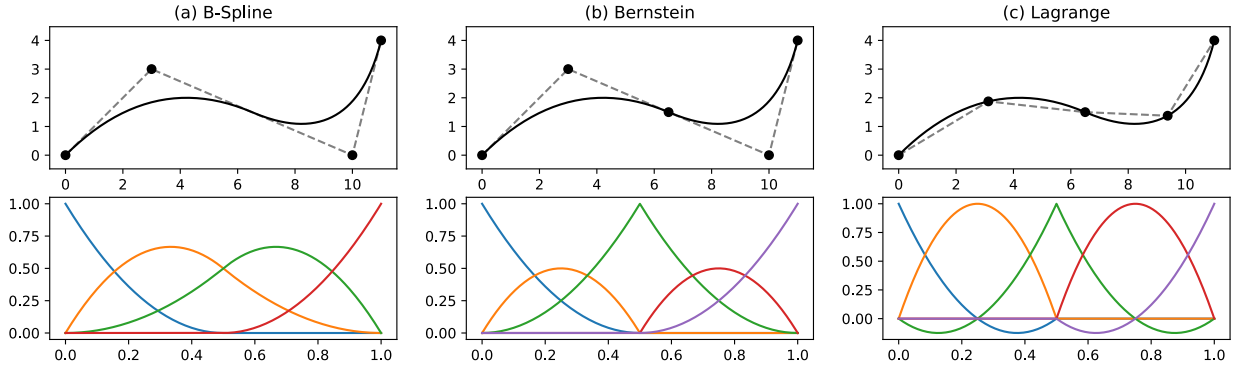

Figure 1.5 – From B-Spline to Lagrange: (left) the initial B-Spline based discretization (four control points associated with four global quadratic B-Spline functions, as in Fig. 1.3(a)) ; (middle) the Bernstein based discretization (one control point is added throughout the Bézier decomposition and each element has three local Bernstein shape functions) and (right) Lagrange (FE) discretization (same number of functions as Bernstein, the control points are now on the curve: these are the standard FE nodes).

Remark. *It may be noticed that there exist elementary Bézier extractors* $\mathbf{D}^e_{BEZ}$ *that relate local Bernstein functions* $\mathbf{B}^e$ *and B-Spline functions* $\mathbf{N}^e$ *defined over a given (knot-span) element e. In practice, these are the elementary operators that are computed first. Then, they can be assembled to explicitly define the global extractor if needed.*

1.3 The Lagrange extraction

An extension of the idea of Bézier extraction to standard nodal FE functions has been more recenlty proposed in [Schillinger et al., 2016b]. It gave birth to the Lagrange extraction operator that directly links Lagrange nodal basis with smooth B-Spline basis. This new operator encompasses the Bézier operator and offers an alternative implementation based on the interpolatory property of nodal basis functions. For a better understanding, we start by establishing the remaining link between Bernstein and Lagrange shape functions in the following and then we move to the direct construction of the Lagrange extractor.

From Lagrange to Bernstein polynomials. Denoting by $\mathbf{L}$ the classical FE Lagrange functions, we are interested here in building operator $\mathbf{D}_{LB}$ that satisfies:

$$\mathbf{B} = \mathbf{D}_{LB}\mathbf{L}. \tag{1.9}$$

Note that the above equality is consistent since Bernstein and Lagrange shape functions (of the same degree p and same number of elements) are two bases of the same polynomial space. Obviously, given the elementary structure of $\mathbf{B}$ and $\mathbf{L}$, operator $\mathbf{D}_{LB}$ is constructed from its elementary representation $\mathbf{D}^e_{LB}$ which is the same for each element. To construct operator $\mathbf{D}^e_{LB}$, one simply needs to express the Bernstein functions as a linear combination of the Lagrange functions at some interpolation points. Making use of the interpolatory property of the Lagrange functions, such an operator can be efficiently constructed by evaluating the Bernstein functions at the nodal points associated to the Lagrange basis. For instance, considering quadratic univariate functions and taking interval $[-1,1]$ as the parent element domain, we choose the points $\widetilde{\xi}_i$ equal to -1, 0 and 1, (*i.e*, such that $L_i(\widetilde{\xi}_j) = \delta_{ij}$ where δ_{ij} is the Kronecker delta) so that we directly obtain:

$$\mathbf{D}^{e^{1D}}_{LB} = \begin{bmatrix} B_1(-1) & B_1(0) & B_1(1) \\ B_2(-1) & B_2(0) & B_2(1) \\ B_3(-1) & B_3(0) & B_3(1) \end{bmatrix} = \begin{bmatrix} 1 & 1/4 & 0 \\ 0 & 1/2 & 0 \\ 0 & 1/4 & 1 \end{bmatrix}. \tag{1.10}$$

Once we have operator $\mathbf{D}_{LB}$, the same treatment as with the Bézier operator can be performed to construct the FE nodes from the Bernstein mesh: $\mathbf{x}^{FE} = \mathbf{D}^T_{LB}\mathbf{x}^{BER}$. Such nodes can be used to construct the input

mesh for classical FE codes. Obviously, these nodes interpolate the geometry. For illustration purpose, the process is applied to go from Fig. 1.5(b) to Fig. 1.5(c). Once again, let us observe that the generated geometry is the same while the basis functions change.

A direct link between Lagrange and B-Spline functions. With the previous operators $\mathbf{D}_{BEZ}$ and $\mathbf{D}_{LB}$ in hand, the formulation of the Lagrange extraction operator $\mathbf{D}$ that directly maps the nodal Lagrange basis onto the B-Spline basis becomes straightforward:

$$\mathbf{N} = \mathbf{DL} \quad \text{with} \quad \mathbf{D} = \mathbf{D}_{BEZ}\mathbf{D}_{LB}. \tag{1.11}$$

Nevertheless, for better numerical efficiency, the Lagrange extraction operator is not computed this way. Indeed, the same procedure as for the Lagrange-Bernstein operator $\mathbf{D}_{LB}$ can be directly applied to the full Lagrange extraction operator $\mathbf{D}$: it merely requires to evaluate the B-Spline basis functions at nodal points. An efficient algorithm for this has been proposed in [Schillinger et al., 2016b].

1.4 The extraction in case of NURBS

The Bézier and Lagrange extraction can be extended to the case of NURBS. In what follow, we directly focus on the Lagrange extractor. It consists of establishing a link between NURBS and rational Lagrange basis functions, as detailed in [Schillinger et al., 2016b].

Briefly, it can be extracted from Eqs. (1.3) and(1.11) that:

$$\mathbf{R} = \frac{\mathbf{W}\,\mathbf{DL}}{W}, \tag{1.12}$$

where $\mathbf{W}$ is the diagonal matrix of NURBS weights. Denoting by $\mathbf{w}$ the vector collecting the NURBS weights, the NURBS weight function W can be rewritten using the Lagrange basis as:

$$\begin{aligned} W &= \sum_{k=1}^{n_{IG}} w_k N_k = (\mathbf{w})^T \mathbf{N} = (\mathbf{w})^T \mathbf{DL} \\ &= (\mathbf{D}^T \mathbf{w})^T \mathbf{L} = (\mathbf{w}^{LAG})^T \mathbf{D} = W^{LAG}, \end{aligned} \tag{1.13}$$

where the weights associated to the rational Lagrange control points are:

$$\mathbf{w}^{LAG} = \mathbf{D}^T \mathbf{w}. \tag{1.14}$$

The rational Lagrange functions are then defined as follows:

$$\mathbf{R}^{LAG} = \frac{\mathbf{W}^{LAG}\mathbf{L}}{W^{LAG}}, \tag{1.15}$$

where $\mathbf{W}^{LAG}$ is the diagonal matrix of the Lagrange weights. The link between NURBS functions and rational Lagrange functions is finally made using Eqs. (1.15) and (1.13) in Eq. (1.12). Consequently, a new extraction operator $\mathbf{D}_W$ is created as described below:

$$\mathbf{R} = \mathbf{WD}(\mathbf{W}^{LAG})^{-1}\mathbf{R}^{LAG} = \mathbf{D}_W \mathbf{R}^{LAG}. \tag{1.16}$$

Eventually, the rational Lagrange control points depend on the NURBS control points: $\mathbf{x}^{LAG} = (\mathbf{D}_W)^T \mathbf{x}$.

We emphasize at this stage that this link from rational Lagrange functions to NURBS is exact since both bases are rational and NURBS are of higher-order smoothness. However, one must keep in mind that the definition of these rational Lagrange functions requires, from standard Lagrange polynomials, the incorporation of the Lagrange weights $\mathbf{W}^{LAG}$ and of the Lagrange weight function W^{LAG}. Those operations are not part of standard FE codes that are restricted to polynomial basis functions. However, As will be shown in next Section, an approximate global bridge can still be formulated to directly go from Lagrange polynomials to NURBS.

2 Non-invasive implementation using a global bridge between IGA and FEM

Despite its real enthusiasm in the computational mechanics community, the implementation of IGA in existing industrial codes still appears quite invasive, which limits its massive deployment in industry. Some isogeometric implementations in commercial FE packages exist such as in LS-Dyna [Hartmann et al., 2011, Hartmann et al., 2016], Abaqus [Duval et al., 2015, Lai et al., 2017] or Radioss [Occelli et al., 2019], but it is still quite a few. The potential of the Lagrange extraction technology to simplify the implementation of IGA in standard FE codes has been underlined in [Schillinger et al., 2016b]. Especially in case of geometries based on polynomial B-Splines, a strategy with minimal invasiveness has been derived. After exposing the current practice for setting up IGA using the previous extraction concepts, a novel, truly non-invasive implementation procedure is presented. We recall that the key aspect of our approach is to adopt a global point of view: we formulate a global, approximate link between NURBS and Lagrange polynomials. Our strategy thus applies not only to B-Spline but also to NURBS models. It enables the whole FE stiffness and right-hand side routines to be untouched during the implementation. From a conceptual point of view, the developed procedure highlights that (B-Spline as well as NURBS based) IGA can be viewed as the projection of FEM onto a specific regular reduced basis.

2.1 The current practice

In the current practice, as underlined in previous Section, the implementation effort to carry out IGA in a standard FE code has to be distinguished for the case of NURBS and the case of B-Splines. In the following, we begin with the general standard approach that enables to implement NURBS and then we show how minimal invasiveness can be met in the specific case of B-Splines.

General case of NURBS. The rational Lagrange geometry that has been created using $\mathbf{D}_W$ (see Eq. (1.16)) has an elementary structure which makes it more likely to be implemented in a FE software. Nevertheless, it must be stressed that implementing this strategy still requires modifications both at the elementary and at the assembly levels. More precisely, the following modifications to be done in the FE software can be listed:

1. Modify the standard FE shape functions subroutine to incorporate the Lagrange weights and the weight function and thus, construct the rational Lagrange shape functions from the existing Lagrange polynomials, as expressed in Eq. (1.15).

2. Apply the extraction for each element using operator $\mathbf{D}_W^e$ to compute the elementary isogeometric contributions.

3. Change the connectivity table in order to perform an isogeometric assembly.

Specific case of -Splines. When restricting ourselves to B-Splines, the standard FE subroutines do not need to be touched at the element level. In other words, point (i) above does not stand anymore. Indeed, after computing the standard FE elementary stiffness matrices $\mathbf{K}_{FE}^e$ and force vectors $\mathbf{f}_{FE}^e$, we can make use of transformation (1.11) to directly obtain the corresponding B-Spline elementary operators $\mathbf{K}_{BS}^e$ and $\mathbf{f}_{BS}^e$:

$$\mathbf{K}_{BS}^e = \mathbf{D}^e \mathbf{K}_{FE}^e \mathbf{D}^{eT} \quad ; \quad \mathbf{f}_{BS}^e = \mathbf{D}^e \mathbf{f}_{FE}^e. \tag{1.17}$$

Only additional matrix-matrix and matrix-vector products are thus required before the assembly step.

2.2 The proposed non-invasive implementation scheme

Principle. As stated above, no modification of the whole FE routines is envisaged in this work (*i.e.*, we seek to remove, both for B-Spline and NURBS bases, the modifications into the shape functions subroutine

(point (i) above) and concerning the assembly (point (ii) above)). In order to do so, we perform globally as depicted in Fig. 1.6. The path starting with a B-Spline mesh is exact and mainly consists of applying procedure (1.17), but in a global way. The path related to NURBS however requires the construction of an additional operator to go from polynomials to rational functions. Such a transformation cannot be exact since this is the space of the rational functions that includes the associated polynomials and not the other way around. A projection thus needs to be performed. For simplicity, we propose to act at the Lagrange level, *i.e.*, we choose to project the rational Lagrange discretization onto the polynomial Lagrange space. To this end, operator $\mathbf{D}_{LL}$ is introduced as:

$$\mathbf{R}^{LAG} = \mathbf{D}_{LL}\mathbf{L}. \tag{1.18}$$

Although we consider the equality in (1.18) by abuse of notation, it must be kept in mind that this transformation cannot be exact. However, $\mathbf{D}_{LL}$ can be constructed so that the error between $\mathbf{R}^{LAG}$ and $\mathbf{D}_{LL}\mathbf{L}$ is very low in practical applications. An explanation and some numerical proofs will be given in next paragraph. We also advise the interested reader to consult [Tirvaudey et al., 2019a] for additional insights regarding this point.

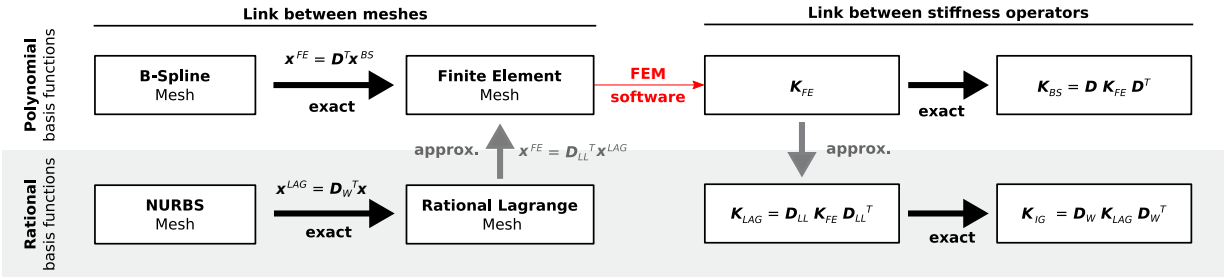

Figure 1.6 – Approach to link a B-Spline and a NURBS mesh to a FE mesh using different global operators. Those operators are then used to recover the B-Spline and NURBS stiffness matrix from the FE one computed using a classical FE software, taken as a black-box. Black arrows represent an exact link, gray arrows an approximation.

Once the FE mesh is created from the isogeometric mesh in a pre-processing step (see left part of Fig. 1.6), it is used as an input for the classical FE code in order to compute the FE stiffness matrix and load vector. With the different elaborated operators, successive transformations are then performed to obtain the final isogeometric stiffness matrix, as follows:

$$\mathbf{K}_{IG} = \mathbf{D}_W\mathbf{D}_{LL}\mathbf{K}_{FE}\mathbf{D}_{LL}^T\mathbf{D}_W^T. \tag{1.19}$$

This transformation is also applied on the right-hand side:

$$\mathbf{f}_{IG} = \mathbf{D}_W\mathbf{D}_{LL}\mathbf{f}_{FE}. \tag{1.20}$$

Consequently, the isogeometric system $\mathbf{K}_{IG}\mathbf{u}_{IG} = \mathbf{f}_{IG}$ can be solved to obtain displacement $\mathbf{u}_{IG}$. Finally, note that the resulting isogeometric displacement can be back-converted in terms of nodal displacements:

$$\mathbf{u}_{FE} = \mathbf{D}_{LL}^T\mathbf{D}_W^T\mathbf{u}_{IG}, \tag{1.21}$$

so that existing subroutines of the FE code can be used for post-processing.

In the remaining of the manuscript, for the sake of conciseness, we will denote the full algebraic IGA-FEM bridge $\mathbf{D}_{FE}$ indifferently for the case of B-Splines (*i.e.*, $\mathbf{D}_{FE} = \mathbf{D}$) or NURBS (*i.e.*, $\mathbf{D}_{FE} = \mathbf{D}_W\mathbf{D}_{LL}$). Our point of view on the relation between IGA and FEM becomes clear with Eqs. (1.19) and (1.20). This is typically the algebraic structure obtained when performing model order reduction (POD, Reduced Basis, see, *e.g.*, [Chinesta et al., 2011, Kerfriden et al., 2012, Quarteroni et al., 2015]). The spline basis is the reduced basis that allows to save DOF from the standard C^0 FE basis when sufficiently smooth solutions

are to be captured. Note finally that in contrast to more standard reduced basis methods, operator D_{FE} can still appear quite large but it is highly sparse here which enables good computational time saving.

Remark. *Regarding the numerical tests, we will restrict ourselves to quadratic functions since almost all industrial FE codes do not go beyond second-order Lagrange finite elements (the famous 9-node quadrilateral element in 2D, or the 27-node cubic element in 3D). Nevertheless, we emphasize that the global bridge holds for higher-order B-Splines and NURBS. As a result, the developed implementation could be directly applied to higher-order IGA, provided that the corresponding higher-order finite elements are available. From this reasoning, it seems also important to underline that our interpretation on IGA should not be viewed as limiting the attractiveness of this technology. The discussion actually leads us to make a distinction between the technology and the approximation capabilities of IGA. Indeed, the IGA technology definitely possesses many advantages over the FEM technology, among which is its ability to go to higher order (using the robust and optimized spline refinement routines).*

Going from polynomials to rational functions. We have developed two alternatives in [Tirvaudey et al., 2019a] for transformation (1.18). The first one is very simple and specific to the NURBS context. The second one is more rigorous and more standard from a mathematical point of view: it is based on a local least-squares procedure. For practical engineering applications, the first method appears to already produce very accurate results that are equivalent to the more rigorous approach. Therefore, we propose to only consider the first strategy in the following. Once again, we refer the interested reader to [Tirvaudey et al., 2019a].

Acting at the Lagrange level for performing the projection between the rational and associated polynomial spaces offers the opportunity to follow a pragmatic yet accurate strategy. Indeed, it has to be emphasized that the control points of the rational Lagrange discretization interpolate the geometry. As a result, it is possible to simply consider that the position of the FE nodes $\mathbf{x}^{FE}$ is exactly the same as the position of the rational Lagrange control points $\mathbf{x}^{LAG}$. In this case, $\mathbf{D}_{LL}$ formally reads as the identity operator $\mathbf{I}$, so that the procedure for NURBS does not add any extra-computational effort from the case of B-Splines. An illustration is provided in Figs. 1.7(a) and 1.7(b) for a quarter circular beam composed of one and two quadratic elements, respectively. On this typical and widely encountered NURBS geometry, it can be observed that the approximation is already very accurate for a single element and, obviously, it is improved through the refinement of the mesh since more interpolated control points are added.

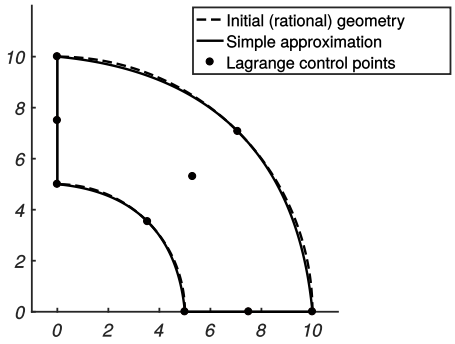

(a) Pragmatic approximation for one element.

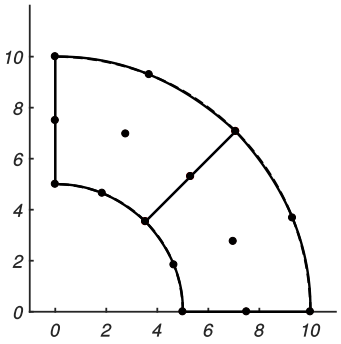

(b) Pragmatic approximation for two elements (in the arc direction).

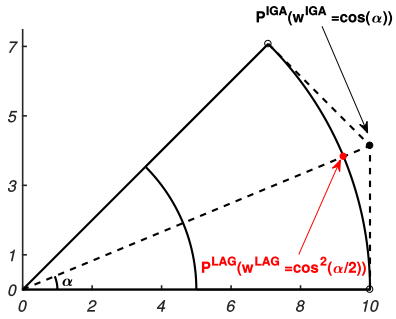

(c) Weight evolution with refinement. The weight of the rational Lagrange control point x^{LAG} is equal to $\cos^2(\alpha/2)$, which quickly converges to 1 as the mesh is refined.

Figure 1.7 – The pragmatic approximation in case of a quarter circular beam. The difference in terms of geometry quickly vanishes with the refinement of the mesh.

Recalling that a NURBS entity turns out to be a B-Spline entity if all the weights are equal to one, an alternative interpretation on our approximation can be given: the strategy simply consists of considering all the weights of the rational Lagrange discretization equal to one. Taking back the example of a quarter circular beam, the approximation can be illustrated as follows (see Fig. 1.7(c)). As explained in the NURBS technology, the weight of the middle point of a quadratic circular one-element arc is equal to the cosine of half of the angle subtended by the arc (the weights of the two boundary control points being one). From here on, we denote by α the angle of interest (see Fig. 1.7(c) again). Making use of previous equality (1.14), then expressing operator $\mathbf{D}$ using (1.11), and finally noting that $\mathbf{D}_{BEZ} = \mathbf{I}$ in case of a mesh composed of a single NURBS element, we can compute the weights associated to the rational Lagrange discretization of this circular arc as follows:

$$\mathbf{w}^{LAG} = \left(\mathbf{D}_{LB}^{e^{1D}}\right)^T \mathbf{w}. \tag{1.22}$$

With $\mathbf{w} = (1, \cos(\alpha), 1)$ and $\mathbf{D}_{LB}^{e^{1D}}$ expressed as in (1.10), we end up with the weight:

$$w^{LAG} = \frac{1}{2}(1 + \cos(\alpha)) = \cos^2\left(\frac{\alpha}{2}\right) \tag{1.23}$$

for the middle point of the rational Lagrange parametrization. Therefore, the good accuracy of the simple approximation is accounted for: with a single element, we have $\alpha = \pi/4$ so we get $w^{LAG} = 0.8536$, which is already quite close to one. $w^{LAG} = \cos^2(\alpha/2)$ enables also to appreciate the convergence of the strategy with the refinement of the mesh; for sure, when α decreases, $\cos^2(\alpha/2)$ tends towards one. Finally, it may be noticed from this study that the proposed procedure is of better quality when it is performed at the Lagrange level. Indeed, going from Bernstein polynomials to rational Bézier functions with the same treatment would lead to a convergence speed of $\cos(\alpha)$ instead, and going from B-Spline polynomials to NURBS functions similarly would converge even less quickly.

Implementation procedure for non-linear analysis. The most complex and optimized part of a robust FE code is undoubtedly the integration of the non-linear mechanical behavior. As a result, making IGA more accessible for industrial applications requires not to touch such routines. From a theoretical point of view, the extension of the approach of Fig. 1.6 to the non-linear framework is straightforward. The only difference lies in the fact that the resolution of the global tangent problem is embedded in a non-linear Newton-based solver which we want to be still realized by the FE code (thus not outsourced) to preserve the existing code optimizations. Not that this choice also allows the user to take advantage of all the options of the non-linear solver offered by the FE software. Technically, this requires additional functionalities of the FE code, which consists in being able to pause the non-linear resolution in order to externalize only the resolution of the global tangent system; then, to re-inject the displacement field solution; and finally, to restart the non-linear resolution without any other external treatments. We managed to implement the method using the familiar industrial `Code_Aster` software [CodeAster, 2014] which offers this possibility thanks to `python` subroutines (pseudo-dependent on the software) and the so-called `STAT_NON_LINE in splitted commands` solver. In what follows, we explain how the method works in a general context (*i.e.*, with any FE code including the functionalities specified above). We urge the reader interested in our specific implementation in `Code_Aster` to consult [Tirvaudey et al., 2019a].

More precisely, the global strategy is depicted in Fig. 1.8. After the pre-processing that does not change with respect to the linear case, we enter into the Newton loop. The non-linear behavior is integrated with the optimized routines of the FE code. The tangent FE operators are also built as when performing standard FE computations. However, the resolution of the tangent linear system is by passed and is replaced by a new (in principle `python`) subroutine. The latter consists in solving the isogeometric tangent problem that is recovered by making use of the developed IGA-FEM bridge $\mathbf{D}_{FE}$ (see (1.19) and (1.20)). Once this resolution is made, the isogeometric displacement solution vector is transferred on the FE space (see (1.21)) so that it can be re-introduced in the FE code in order to update the behavior. Finally, let us note that a second very

short subroutine is needed for the calculation of the isogeometric residual from the FE one.

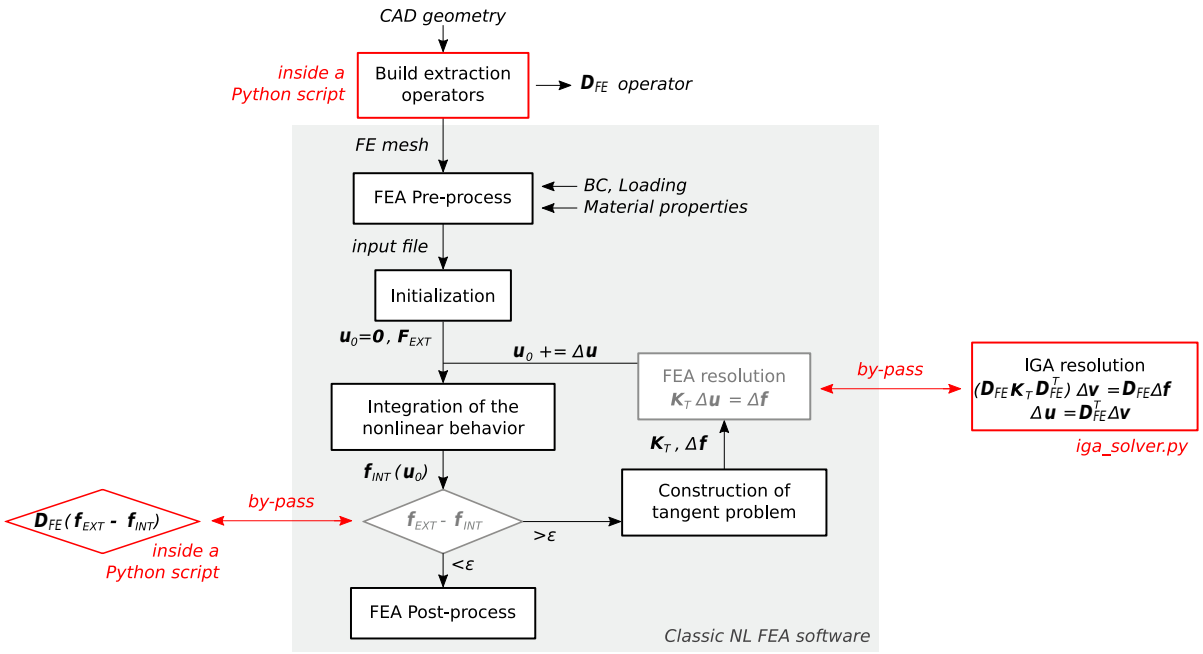

Figure 1.8 – Flowchart of the non-invasive and non-linear implementation in an existing FE software, taken as a black-box. Note that the CAD input has to be understood here as an analysis-suitable spline model.

Remark. *If pure numerical efficiency is the only criterion for qualifying an implementation of IGA, the best approach would certainly be to rewrite everything into a dedicated piece of code using a low-level language (see,* e.g., *PetIGA [Dalcin et al., 2016] for high-performance IGA based on PETSc and [Nguyen et al., 2015] for global implementation aspects). Furthermore, it has to be noticed that numerous works aiming at reducing the computational cost of IGA have emerged since the advent of the concept. It actually appeared that using as many integration points as in standard FEM (*i.e. $p+1$ *Gauss points for a degree p) is not necessary given the higher regularity of the spline functions. New quadrature rules more or less related to the entire isogeometric patch can thus be considered [Hughes et al., 2010, Auricchio et al., 2012a, Schillinger et al., 2014]. In the same idea, it may be preferred to focus on collocated-IGA [Auricchio et al., 2010, Auricchio et al., 2012b] when we increase the polynomial degree of splines. Finally, it appeared recently in the standard Galerkin framework that a revisit of the standard looping over elements in the assembly process could allow IGA to meet its full efficiency [Calabro et al., 2017]. However, most of these approaches may require significant development efforts, especially whenever a new non-linear constitutive law needs to be added, and appear incompatible with the use of standard FE codes. This is why, in this section, it is chosen to reduce the human time required for the program development (even if, obviously, this one may come with a little increase of the computational cost). Finally, let us emphasize once again that the interest of this study from a conceptual point of view is the alternative lighting on the relation between IGA and FEM that it provides.*

3 Numerical results

We now carry out some numerical experiments to assess the performance of our non-invasive implementation scheme and to illustrate our point of view on IGA. The framework of two-dimensional linear elasticity is first considered before the more complex simulation of a non-linear elastoplastic structure is performed. As stated previously, the open source package `Code_Aster` is used as an industrial FE software for the numerical tests.

3.1 A simple but illustrative example

The first example consists of an elastic 2D circular beam under plane stress subjected to end shear, as depicted in Fig. 1.9(a). A constant horizontal displacement of $u_0 = 0.01$ units is prescribed over the lower beam boundary. An analytical solution is available for the problem in [Zienkiewicz et al., 2005]. The geometry is perfectly generated using a single quadratic NURBS mesh. For the isogeometric computations, we will consider quadratic NURBS basis functions with the maximum available regularity at the interior knot-lines (*i.e.*, C^1). For comparison purpose, we will also perform classic FE simulations using the FE meshes built thanks to our IGA-FEM operator D_{FE} (*i.e.*, such that $\mathbf{x}^{FE} = \mathbf{D}_{FE}^T \mathbf{x}$, see Fig. 1.6 again). The resulting FE meshes will be thus composed of standard 9-node elements. To start with, the solution obtained using a NURBS mesh composed of 16 (along the radial direction) × 24 (along the circumferential direction) elements is shown in terms of displacement in Fig. 1.9(b) and in terms of Von Mises stress in Fig. 1.9(c). The computed solution is smooth and corresponds to the one of [Zienkiewicz et al., 2005].

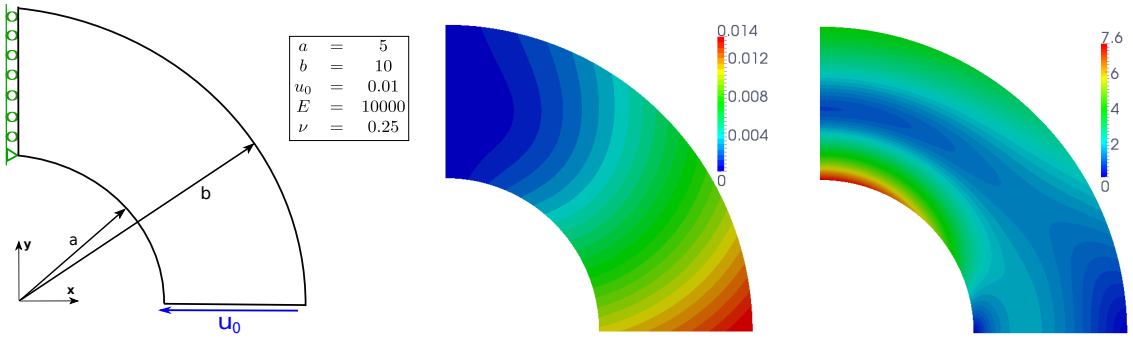

(a) Problem description. (b) Displacement (magnitude). (c) Von Mises stress.

Figure 1.9 – Isogeometric simulation of the curved beam problem (NURBS mesh composed of quadratic C^1 16 × 24 elements).

To better appreciate the accuracy of the simulation, we study the convergence of the computed solution with the refinement of the mesh (see Fig. 1.10(a)). We proceed in the same way as in [Zienkiewicz et al., 2005]: the convergence behavior of the strain energy is considered. The relative energy error is computed as:

$$\mathrm{Err}^h = \frac{|E_{\mathrm{ref}} - E^h|}{E_{\mathrm{ref}}}, \tag{1.24}$$

where E_{ref} denotes the reference exact strain energy and E^h the strain energy of the discrete model. In Fig. 1.10(a), the "IGA reference" is the solution obtained using a standard isogeometric code. To compute the "non-invasive IGA", we make use of the standard FE code and apply our non-invasive procedure (see Fig 1.6 again). Finally, as mentioned above, the "FE reference" is computed with the standard FE code using the FE mesh constructed from the associated NURBS one by means of $\mathbf{D}_{FE}$.

First, it can be observed that the two isogeometric solutions seem to be indistinguishable which accounts for the accuracy of the developed IGA-FEM bridge in case of NURBS. As stated previously, the only approximation is in operator $\mathbf{D}_{LL}$. From a geometrical viewpoint, the pragmatic approximation was already good for one element in the arc direction (see Fig. 1.7 as a reminder). Here, with the first refinement used, there are already 6 elements in this direction; therefore, the error related to approximation $\mathbf{D}_{LL} = \mathbf{I}$ is largely insignificant compared to the associated FE error. Then, and this is probably the most important point here, one can notice that for a given mesh refinement, the errors are about the same for FEM and IGA. The main difference is the number of DOF which significantly decreases when IGA is performed (the two curves are simply horizontally translated). This gap between the two curves illustrates the increased per-degree-of-freedom accuracy of IGA, making this technology often seen as a high-performance computational tool in the current literature. To better understand the behavior, we dare to draw the symbolic

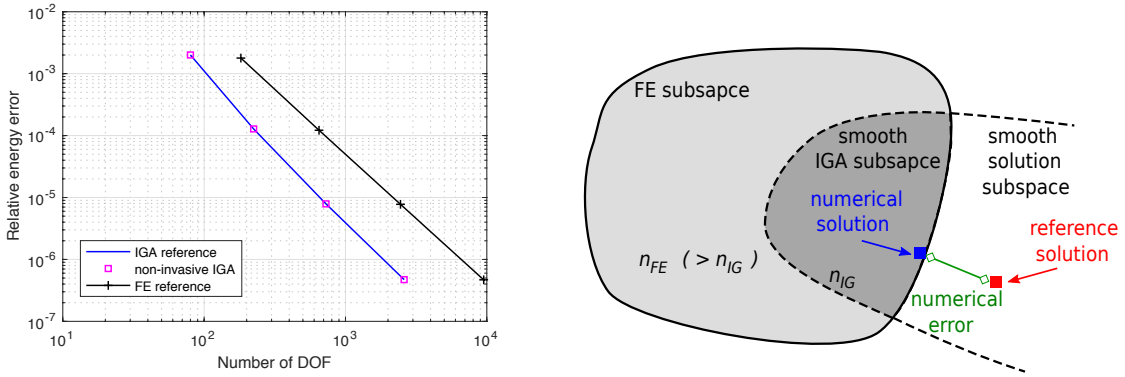

(a) Convergence of the relative energy error for the circular beam.

(b) Symbolic illustration of the increased accuracy of IGA.

Figure 1.10 – Comparison between IGA and FEM on the curved beam problem.

graphic of Fig. 1.10(b). This graphic illustrates again our point of view on the relation between IGA and FEM. The reference solution of the problem being smooth, it is as well captured with standard C^0 FE elements as with more regular spline-based elements (considering the same number of elements and the same polynomial degree). However, the more regular space being included into the C^0 space, it comes with less DOF.

3.2 An example of non-invasive non-linear isogeometric anaysis

We finally consider a 3D dog-bone sample in tension to demonstrate the performance and potential of our non-invasive implementation scheme for non-linear analysis. Such an experimental test is often used to characterize the hardening of metallic materials [Mathieu et al., 2015]. The specimen (see Fig. 1.11) is 100mm long, the ligament is 5mm wide and the sample is 2.5mm thick. An elastoplastic constitutive behavior is considered with a VonMises mixed non-linear hardening. The linear parameters are the Young modulus E=22.13GPa and Poisson ratio ν=0.3. The Prager constant is set to 2200MPa. More information regarding the non-linear constitutive law can be found in [Tirvaudey et al., 2019a]. The sample is subjected to a remote tension: the load goes from p = 0MPa to p = 80MPa within 10 (non-uniform) increments. We make use of one layer of quadratic 3D (standard solid) elements to discretize the structure. Although only one element is considered across the thickness, the number of DOF is significantly reduced between the initial isogeometric mesh and the associated FE mesh built using $\mathbf{D}_{FE}$. More precisely, with the refinement employed, the isogeometric mesh involves 6561 DOF while the FE mesh includes 23409 DOF.

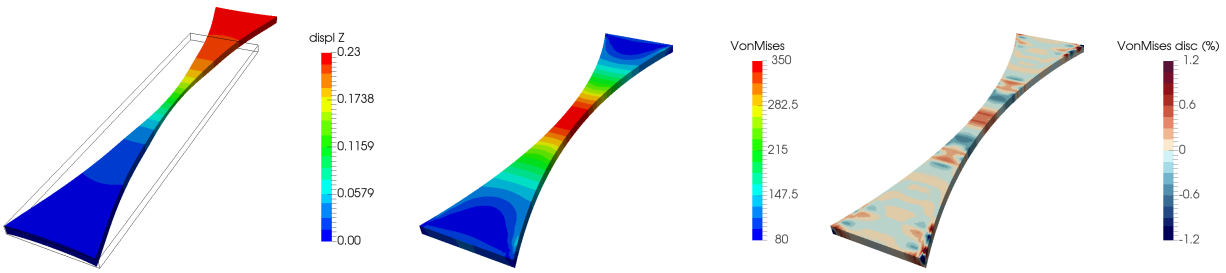

Figure 1.11 – Accuracy of the proposed non-invasive isogeometric implementation: Longitudinal displacement field (left, amplification 100) ; Von Mises stress field (middle); and the relative discrepancy with respect to the FE reference solution computed using the industrial FE code (right). The seventh increment, which corresponds to p = 70MPa, is considered for the plots.

The longitudinal component of the displacement field solution is plotted in Fig. 1.11 (left). The Von Mises stress field obtained with the non-invasive IGA method is also presented in Fig. 1.11 (middle). It may be observed that, in the region of the ligament, this field has values above the yield stress ($\approx$ 200MPa) which illustrates that in its central part, the specimen undergoes plastic deformations. This IGA stress field is compared to the Von Mises stress field obtained using the input FE mesh and the standard non-linear FE solver (see Fig. 1.11 (right)). Since the solutions are very close, the relative discrepancy between the isogeometric and FE solutions is plotted. Despite a reduction of more than 70% in the number of degrees of freedom, the solutions are very close (less than 2% of local mismatch while the two solutions come from different approximation subspaces). This result is in line with our interpretation of IGA as the projection of FEM onto a specific regular reduced basis (see Fig. 1.10(b)). We eventually show the tensile force-displacement curve obtained with the non-invasive isogeometric and reference FE methods. It can be seen that the isogeometric subspace is able to provide a solution almost identical to the one generated by FEM all over the loading.

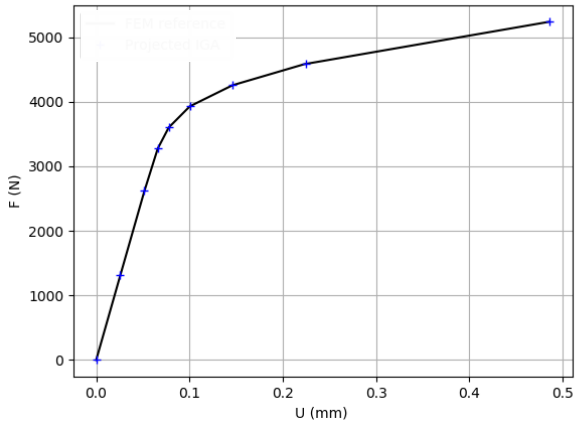

Figure 1.12 – Force versus displacement curve. Comparison between standard FEM (solid black line) and non-invasive IGA (blue crosses).

Summary and discussion. This chapter undertakes to outline IGA by providing an alternative lighting on its relation with standard FEM. If the common practice may be to view IGA as encompassing FEM since it offers the possibility to make use of (geometrically sound and) smoother basis functions, it is shown here that IGA can also be interpreted as the projection of FEM onto a specific, more regular, reduced basis. In this respect, the straightforward but key feature to keep in mind is that the (possibly more) regular discretization spaces offered by IGA are somehow included into the C^0 spaces given by classic FEM (in other words, a function that is C^{p-1} with $p \geq 2$ is also C^0). In case of B-spline bases, it suffices to make use of the original Bézier extraction [Borden et al., 2011] and more recent Lagrange extraction [Schillinger et al., 2016b] to account for this statement. Indeed, the Lagrange extractor enables to formulate a smooth polynomial B-Spline function in terms of standard C^0 nodal FE functions. After reviewing the existing link between IGA and FEM, we propose to push forward the concept by formulating an approximate, global and algebraic bridge between NURBS and Lagrange polynomials. In order to do so, an additional operator that enables to take into account the weights of the rational functions by creating equivalent Lagrange FE nodes needs to be constructed. Performing a very simple projection between rational Lagrange functions and Lagrange polynomials, we have been able to accurately map standard nodal polynomial bases onto smooth NURBS bases; thus, highlighting that our point of view applies for B-Spline as well as NURBS based IGA. The increased per-degree-of-freedom accuracy of IGA, which makes this technology often seen as a high-performance

computational tool in the current literature, appears clear through our lighting: the spline space, which is included into the standard FE space, allows to save a significant number of DOF when smooth solutions are to be captured. As a conclusion, this brings us to characterize IGA, from a pure analysis point of view, as a powerful reduced-order method of standard FEM. Of course, this interpretation on IGA should not be viewed as limiting the attractiveness of this technology. The discussion actually leads us to make a distinction between the technology and the approximation capabilities behind IGA. The IGA technology definitely possesses many advantages over FEM from a practical point of view, such as its ability to harmonize CAD and analysis, to perform mesh refinement, to go to higher-order, to be conducted at a very low computational cost [Calabro et al., 2017], etc.

Making use of the developed full IGA-FEM bridge, we also develop a novel implementation procedure that further simplifies the integration of IGA in well-established FE environments. The ultimate goal is to make IGA more accessible for industrial applications. The problematic is of great interest since the advent of IGA [Borden et al., 2011, Scott et al., 2011] and seems to still undergo large efforts (see, *e.g.*, the contemporary work [Kamensky and Bazilevs, 2019] that uses a global approach for implementing IGA in the open source FE-code `FEniCS`). The attractive property of our approach is that it reduces to the minimal possible level the implementation effort for industrial engineers. More precisely, the whole FE routines remain completely untouched. As a result, the total FE code that may integrate complex, non-linear numerical models and optimized routines can be used as a black box. The only requirement is that the commercial code is able to output the stiffness and right-hand side operators in a readable file format, so that it becomes possible to recover and solve, in an external script, the isogeometric system from the FE one. The performance of the implementation has been illustrated through different numerical experiments involving linear elastic and non-linear elastoplastic structures and the use of the industrial FE software `Code_Aster` developed by the EDF R&D company [CodeAster, 2014]. According to the authors knowledge, this is the first time that IGA has been implemented in `Code_Aster`. None of the FE routines (including those concerning the non-linearity) has been touched: only some sparse matrix-matrix and matrix-vector products are performed to relate, at each iteration of the nonlinear solver, the isogeometric tangent system and the isogeometric non-linear residual with their FE counterparts. This last computation constitutes a demonstrator of the method: it provides a concrete additional pathway to the opportunities of higher-order smoothness in industrial applications. Discussions are in progress with EDF to integrate some isogeometric capabilities in their new `Code_Aster` environment (`asterXX`).

CHAPTER 2

Non-invasive coupling algorithms for global/local IGA

Contents

This second chapter gives an overview of the various works I have been involved in, since my arrival in Toulouse as a post-doctoral researcher in 2015, in the area of multiscale global/local analysis of structures. Our approach to address the issue is based on the development of algorithms classified as "non-invasive". Originally introduced in the FEM framework to fulfill an industrial requirement, this type of technology appears to us of great interest for the field of IGA from a scientific point of view. The chapter is organized as follows: section 1 reviews the standard non-invasive methodology and presents the progress that we have performed in FEM; then, in section 2, we motivate the extension of the method to the field of IGA and outline the scientific difficulties to be addressed; finally, section 3 describes the dedicated algorithms that we have built in response to theses challenges.

1 Origin of non-invasiveness: a need for industry

The core idea of non-invasive global/local coupling has emerged in recent years to answer a present-day industrial issue. The development of this class of methods was the object of a french research project supported by the French National Research Agency (ICARE ANR-12-MONU-0002, 01/2013 - 12/2016). This first section establishes the non-invasive strategy as it comes in its initial FE form. Starting by highlighting the motivations using a real industrial example, the non-invasive coupling strategy is then properly derived with references to the state of the art in the field. To illustrate the performance of the method, we close this section by focusing on one contribution that we have performed in the field of FEM, for the multiscale analysis of real aeronautical structures [Guinard et al., 2018].

1.1 Motivation

1.1.1 Several scales of interest

During the design, justification and certification process of industrial structures (such as an aircraft), the design teams have to deal with different FE computer models ranging from global to local representations. Global models assume simplifications of the geometry, kinematics and constitutive properties: their characteristic size varies between 1 and 10 m, and their main purpose is to estimate loads in large sub-assemblies (*e.g.*, fuselage sections, wings, etc.). Local models address greater complexity: their characteristic size varies between 0.1 and 1 m, and their main purpose is to capture the behavior of structural details up to rupture. The ever-increasing power of high-performance computing (HPC [Bhardwaj et al., 2002]) may allow in the near future the advent of the mythic "complete predictive model", in which local model granularity would be propagated up to large scales, resulting in one bulk model driven by smallest scale constraints. However, this would be irrelevant with today's industrial processes and engineering mindsets. In particular, aircraft programmes (and, more broadly, any large-scale industrial programme) require permanent access to levels of representation graded in complexity, from the aerodynamic concept to the design of structural details. Consequently, according to the industrial engineers, the need to consider models at several scales within a given simulation is, and will continue to be, an essential feature in the development of large sized products of growing complexity.

1.1.2 Typical coupling techniques in industry

To ensure interaction between the different scales, it is necessary to construct suitable coupling methods. The most popular method in mechanical engineering is a top-down approach (often known as *submodelling* [Kelley, 1982, Jara-Almonte and Knight, 1988, Srinivasan et al., 1996, Cormier et al., 1999]), which is very present in commercial software. It consists of first carrying out a complete computation of the structure as a whole and then using the solution to prescribe the boundary conditions, as displacement [Kelley, 1982] or load [Jara-Almonte and Knight, 1988], on a more refined local model. This method presents the advantage of concentrating the computational effort on the zones that need it most. However, it is mainly reserved for cases in which the local detail has little or no influence on the rest of the structure at global level. The weak point of such a strategy is thus that it is only applied in one direction (from global to local), without considering the repercussions of local, non-linear effects on the global model: this may lead to severe disturbances of the overall balance of the structure [Cresta et al., 2007, Gendre et al., 2009].

As a result, it is necessary for most application to use strong coupling to take the influence of the local model into account beyond its domain of definition. The conventional strategy is then to use monolithic coupling [Hirai et al., 1984, Wyart et al., 2008, Touzeau et al., 2011]. In other words, the coupled solution is obtained through a direct computation (using a single direct solver). This requires a modification of the global model to remove certain elements and replace them by those of the local model. This reorganization of the global mesh (which certainly took many hours, days or even months to be constructed) is extremely invasive and has proved to be incompatible with industrial time cycles.

As a representative example, let us consider a real portion of an aircraft (about 7m large) subjected to a large cut (length: 170mm, radius at crack tips: 1mm), see Fig. 2.1 for illustration. The test case is extracted from real engineering practices. During aircraft design and certification process, one of the most demanding demonstrations towards airworthiness authorities originates from structural survivability to engine burst. When accidental in-flight engine burst occurs, fuselage panels may be subjected to large cuts, thus severely affecting the skin and the stiffeners. As a result, evidence must be made that under such circumstances, remaining load-carrying capabilities are still enough to make the aircraft fly and land. In order to do so, we are interested here in performing a multiscale simulation that combine, in particular, an homogenized non-planar shell model (without the large cut) at the global scale and, localized full 3D models at the meso-scale (located around the crack tips) where each ply is meshed (see Fig 2.1 again). The considered

global FE mesh for the simulation was extracted from actual sizing exercises practiced within AIRBUS stress offices. This modeling includes skin, floor, stiffeners and frames: its size ($> 10^6$ degrees of freedom) and complexity are thus fully representative of a situation where industrial time and cost constraints prohibit mesh refurbishments. Therefore, the aforementioned conventional engineering practices were not able to solve such a problem and we needed to resort to a dedicated *non-invasive* strategy (see section 1.3).

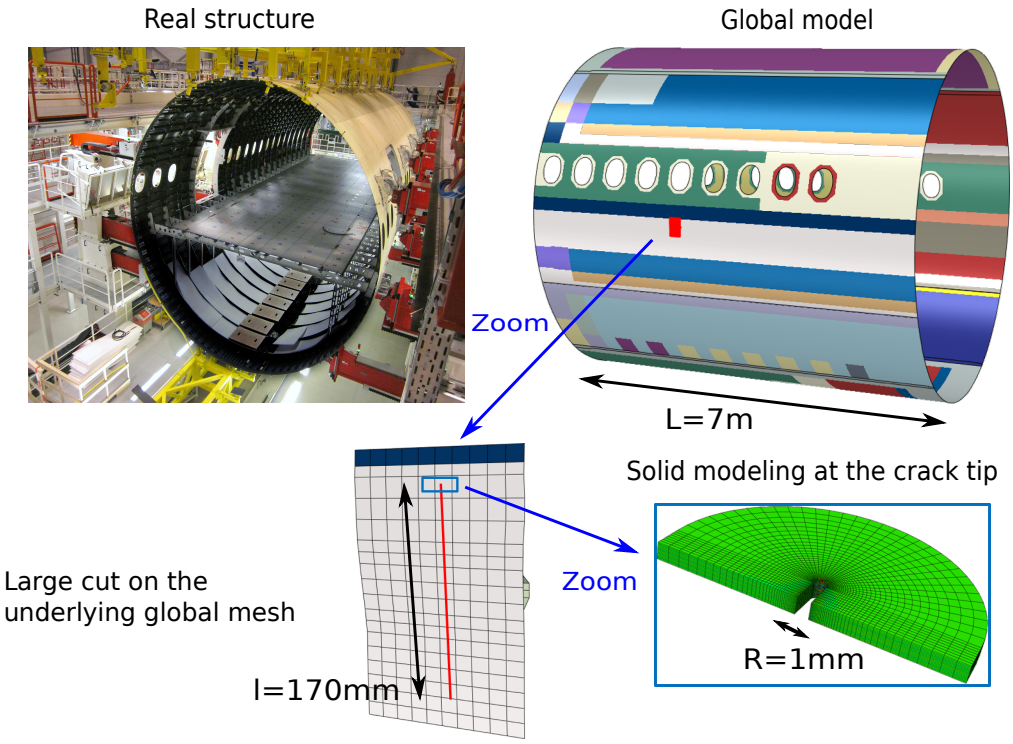

Figure 2.1 – Real fuselage section subjected to a large cut: description of the test case *(floor, stiffeners and frames not represented on the global model for confidentiality reasons)*.

1.1.3 A non-invasive approach as a remedy

In response to this issue, a new class of global/local coupling methods, called *non-invasive* methods, has recently emerged in the computational structural mechanics community. Based on an idea put forward by Whitcomb [Whitcomb, 1991] and later formulated by Allix's group [Gendre et al., 2009] for modelling local plasticity, the strategy enables a FE model to be modified locally without having an impact on the corresponding numerical operators. It then becomes easy to interface several software or codes. More precisely, the method relies on an iterative process between global and local computations. The replacement of part of a global model by a more detailed local model can be carried out exactly and non-invasively: the global model is never modified; only interface displacements and reaction forces are exchanged. This strategy has been successfully applied in many domains (see, *e.g.*, [Gupta et al., 2012, Passieux et al., 2013] for crack propagation, [Chevreuil et al., 2013, Nouy and Pled, 2018] for taking localized uncertainties into account, [Guguin et al., 2014, Guguin et al., 2016] for non-invasive plate/3D coupling, [Duval et al., 2016, Gosselet et al., 2018] for domain decomposition solvers, [Chantrait et al., 2014, Bettinotti et al., 2014] for transient dynamics analysis, [Oumaziz et al., 2018] for contact problems, [Guinard et al., 2018] for real aeronautical structures, and [Blanchard et al., 2019] for viscoplastic structures). The emergence of this type of coupling is thus clearly of major importance as it will enable more accurate sizing and more open exploration of the design envelopes without drastically changing the analysis procedures that are currently established in the industrial community and recognized by the certification authorities.

1.2 Formulation and iterative resolution

We now specify the construction of the (FE-based) non-invasive coupling strategy. After formulating the reference global/local problem, the non-invasive algorithm is presented as an alternative to the standard monolithic resolution. Finally, a discussion regarding the implementation issues faced by the current non-invasive methods is provided.

1.2.1 Governing equations

Let us start by considering a global (coarse) model of a structure. The model is characterized by a physical domain $\Omega_1 \subset \mathbb{R}^d$ ($d = 2$ or 3 being the dimension of the physical space), which is divided into two disjoint, open and bounded subsets Ω_{11} and Ω_{12}. Those two non-overlapping subdomains share a common interface denoted by Γ such that $\Omega_1 = \Omega_{11} \cup \Omega_{12} \cup \Gamma$ and $\Omega_{11} \cap \Omega_{12} = \varnothing$ (see Fig. 2.2(a)(left) for illustration). A simple linear elastic law is adopted for the global model. We assume that such a constitutive behavior and the coarse mesh is sufficient for the modeling except in the small region Ω_{12} where a local phenomena is to be introduced. As a consequence, a local (more detailed) "sub-model" characterized by domain Ω_2 is constructed to replace the global model in Ω_{12} (see Fig. 2.2(a)(right)). The substitution of the local model within the global one is achieved through interface Γ. The resulting global/local problem to be solved is a classical multi-domain problem in $\Omega_{11} \cup \Omega_2 \cup \Gamma$, the global solution in Ω_{12} being discarded (see Fig. 2.2(b)).

Remark. *In this work, the adopted global/local modeling is chosen* a priori, *but it could be determined, for example, by a criterion based on* a posteriori *error estimations [Oden and Zohdi, 1997, Duval et al., 2018]. In this context, we very recently proposed, through the PhD thesis of Marie Tirvaudey who I co-supervised with Prs. J.-C. Passieux and L. Chamoin, verification tools that enable to optimally adjust the coupling parameters of the non-invasive strategy* (i.e., *location of the coupling interface, local mesh size, number of iterations), see [Tirvaudey, 2019, Tirvaudey et al., 2019b]. Further investigations in this direction are in progress.*

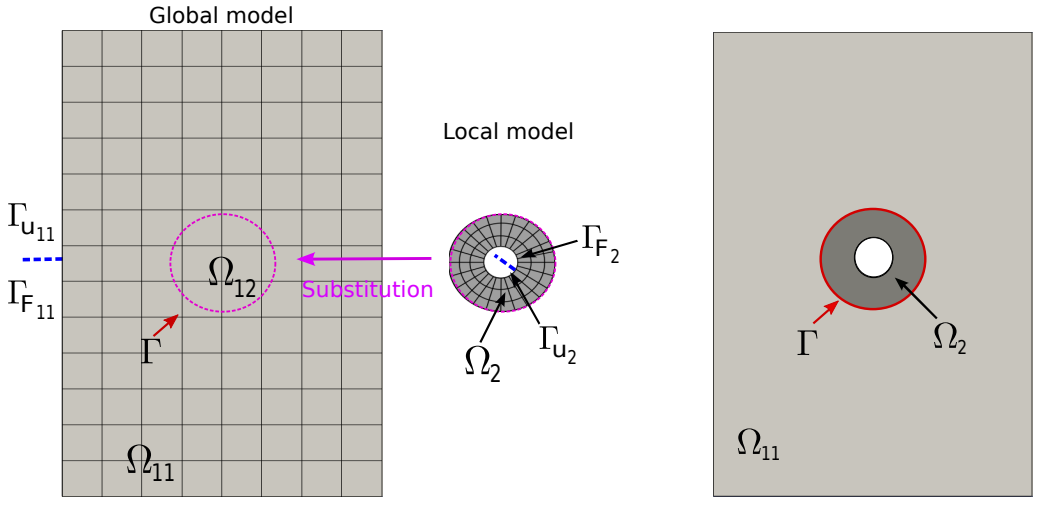

(a) Initial global and local model domains.

(b) Resulting coupling problem.

Figure 2.2 – Example of a global/local problem. The global model over subdomain Ω_{12} is replaced by the finer local model of domain Ω_2 through interface Γ, which enables to integrate a geometrical detail (a hole) within the initial coarse model.

Even if the method applies for any (possibly non-linear) local behavior, we consider here for simplicity in the presentation that the local model is also linear elastic. We assume that the two non-overlapping subdomains Ω_{11} and Ω_2 are subjected to body forces f_{11}^g and f_2^g, respectively. Furthermore, surface forces F_{11}^g and F_2^g are associated to boundaries $\Gamma_{F_{11}}$ and Γ_{F_2} and, displacements u_{11}^g and u_2^g are prescribed over

boundaries $\Gamma_{u_{11}}$ and Γ_{u_2} (see Fig. 4.2 again). In each subdomain, the kinematic constraints, the equilibrium equations and the constitutive relations have to be verified. Using subscript m to denote a quantity that is valid over region Ω_m, with m = 11 and 2, the corresponding governing equations read:

$$u_\mathrm{m} = u_\mathrm{m}^g \quad \text{over} \quad \Gamma_{u_\mathrm{m}} \,; \tag{2.1a}$$
$$\mathrm{div}(\sigma_\mathrm{m}) + f_\mathrm{m}^g = 0 \quad \text{in} \quad \Omega_\mathrm{m} \,; \tag{2.1b}$$
$$\sigma_\mathrm{m}\, n_\mathrm{m} = F_\mathrm{m}^g \quad \text{over} \quad \Gamma_{F_\mathrm{m}} \,; \tag{2.1c}$$
$$\sigma_\mathrm{m} = C_\mathrm{m}\, \varepsilon\left(u_\mathrm{m}\right) \quad \text{in} \quad \Omega_\mathrm{m}. \tag{2.1d}$$

In the above equations, $\varepsilon\left(u_\mathrm{m}\right)$ denote the infinitesimal strain tensors, σ_m the Cauchy stress tensors and C_m the Hooke tensors. n_{11} and n_2 represent the outward unit normals to Ω_{11} and Ω_2, respectively. We specify here that we perform as follows for the notations: continuous quantities are in normal type while discrete quantities (*i.e.*, vectors and matrices) will be in boldface type (see below). To complete the formulation of the boundary value problem, the interface condition has to be added:

$$u_{11} - u_2 = 0 \quad \text{over} \ \Gamma \,; \tag{2.2a}$$
$$\sigma_{11} n_{11} + \sigma_2 n_2 = 0 \quad \text{over} \ \Gamma. \tag{2.2b}$$

It ensures kinematic compatibility and equilibrium of the tractions, respectively, along the coupling interface Γ between the two subdomains.

1.2.2 Weak form and monolithic resolution

The starting point in the derivation of a non-invasive strategy in the sense of, *e.g.*, [Passieux et al., 2013, Guguin et al., 2014, Duval et al., 2016] is to weakly formulate the coupling problem (2.1)-(2.2) with a Lagrange multiplier approach. Without care of non-invasiveness at the moment, we write below the classical Lagrange multiplier weak form of the global/local problem. We note that the Lagrange multiplier approach is also sometimes referred to as the Mortar approach in the literature [Wohlmuth, 2000, Brivadis et al., 2015, Dornisch et al., 2015, Zou et al., 2018b, Wunderlich et al., 2019]. We will use the two terminologies indifferently in the whole manuscript.

Continuum version. Let us start by defining the functional spaces $\mathscr{U}_\mathrm{m}$ and $\mathscr{V}_\mathrm{m}$ over domain Ω_m that will contain the displacement solution and test functions respectively:

$$\mathscr{U}_\mathrm{m} = \left\{ u_\mathrm{m} \in \left[H^1\left(\Omega_\mathrm{m}\right)\right]^d,\ u_\mathrm{m}|_{\Gamma_{u_\mathrm{m}}} = u_\mathrm{m}^g \right\} \ ; \ \mathscr{V}_\mathrm{m} = \left\{ v_\mathrm{m} \in \left[H^1\left(\Omega_\mathrm{m}\right)\right]^d,\ v_\mathrm{m}|_{\Gamma_{u_\mathrm{m}}} = 0 \right\}. \tag{2.3}$$

In the context of Lagrange multiplier methods, a mixed formulation is set up to impose the coupling constraints (2.2). Classically, a single Lagrange multiplier $\lambda \in \mathscr{M}$ (where $\mathscr{M}$ is an appropriate space) is introduced, as the dual unknown, to represent both of the interface traction forces, *i.e.*, $-\sigma_{11} n_{11} = \sigma_2 n_2 = -\lambda$ in Eq. (2.2b). Then, the interface Dirichlet condition (2.2a) is imposed in a weak sense over Γ using the Lagrange multiplier. This leads to the formulation of the following Lagrangian of the coupled problem:

$$L_\mathrm{basic}\Big((u_{11}, u_2), \lambda\Big) = \frac{1}{2} a_{11}\left(u_{11}, u_{11}\right) + \frac{1}{2} a_2\left(u_2, u_2\right) - l_{11}\left(u_{11}\right) - l_2\left(u_2\right) + b\left(\lambda, u_{11} - u_2\right). \tag{2.4}$$

Bilinear form a_m and linear form l_m associated to domain Ω_m ($\mathrm{m} \in \{11, 2\}$) read:

$$\begin{cases} a_\mathrm{m}\left(u_\mathrm{m}, v_\mathrm{m}\right) = \displaystyle\int_{\Omega_\mathrm{m}} \varepsilon\left(v_\mathrm{m}\right) : C_\mathrm{m}\, \varepsilon\left(u_\mathrm{m}\right) \mathrm{d}\Omega_\mathrm{m} \,; \\ l_\mathrm{m}\left(v_\mathrm{m}\right) = \displaystyle\int_{\Omega_\mathrm{m}} v_\mathrm{m} \cdot f_\mathrm{m}^g \mathrm{d}\Omega_\mathrm{m} + \int_{\Gamma_{F_\mathrm{m}}} v_\mathrm{m} \cdot F_\mathrm{m}^g \mathrm{d}\Gamma_{F_\mathrm{m}} \,; \end{cases} \tag{2.5}$$

and bilinear form b is defined such that:

$$b(\mu,u)=\int_\Gamma \mu\cdot u\,\mathrm{d}\Gamma. \tag{2.6}$$

In the above equations, one may not that we use notations $\cdot$ and : to refer to the scalar product of vector fields and of second-order tensor fields, respectively. With above developments, we can finally obtain the classical Mortar coupling formulation of the reference problem as follows: find $u_{11}\in\mathcal{U}_{11}$, $u_2\in\mathcal{U}_2$, and $\lambda\in\mathcal{M}$ such that:

$$\begin{cases} a_{11}(u_{11},v_{11})+b(\lambda,v_{11})=l_{11}(v_{11}), & \forall v_{11}\in\mathcal{V}_{11}\,;\\ a_2(u_2,v_2)-b(\lambda,v_2)=l_2(v_2), & \forall v_2\in\mathcal{V}_2\,;\\ b(\mu,u_{11}-u_2)=0, & \forall\mu\in\mathcal{M}. \end{cases} \tag{2.7}$$

Discrete version. We now formulate the problem in the discrete setting. Regarding notations, we use capital letters for matrices and lowercase for vectors. To this end, let us introduce the finite element basis functions $\left(L^1_A\right)_{A\in\{1,2,..,n_1\}}$ and $\left(L^2_B\right)_{B\in\{1,2,..,n_2\}}$ that discretize the global and local model, respectively. In addition, we denote by $\left(L^{11}_C\right)_{C\in\{1,2,..,n_{11}\}}$ the restricted part to subdomain Ω_{11} of the shape functions of the global model. Following the principle of isoparametric elements, the basis $\left(L^{11}_C\right)_{C\in\{1,2,..,n_{11}\}}$ and $\left(L^2_B\right)_{B\in\{1,2,..,n_2\}}$ are used to build the above-mentioned finite element spaces $\mathcal{U}^h_{11}$ and $\mathcal{U}^h_2$ associated to $\mathcal{U}_{11}$ and $\mathcal{U}_2$ (see Eq. (2.3)), respectively. Finally, the finite element space for the Lagrange multiplier is denoted by $\mathcal{M}^h$ and the corresponding basis functions read $\left(L^\lambda_D\right)_{D\in\{1,2,..,n_\lambda\}}$. The construction of space $\mathcal{M}^h$ may require special attention [Wohlmuth, 2000] to avoid numerical problems (due to the non-satisfaction of the *inf-sup* condition). At this stage, we do not give more information regarding this point. This will be discussed further in the chapter. By substituting the finite element approximations of u_{11}, u_2 and λ in the weak form (2.7), and denoting by $\mathbf{u}_{11}$, $\mathbf{u}_2$ and $\boldsymbol{\lambda}$ the associated degrees of freedom (DOF) vectors, the following linear system is obtained:

$$\begin{bmatrix} \mathbf{K}_{11} & \mathbf{0} & \mathbf{C}_{11}^T \\ \mathbf{0} & \mathbf{K}_2 & -\mathbf{C}_2^T \\ \mathbf{C}_{11} & -\mathbf{C}_2 & \mathbf{0} \end{bmatrix} \begin{Bmatrix} \mathbf{u}_{11} \\ \mathbf{u}_2 \\ \boldsymbol{\lambda} \end{Bmatrix} = \begin{Bmatrix} \mathbf{f}_{11} \\ \mathbf{f}_2 \\ \mathbf{0} \end{Bmatrix}. \tag{2.8}$$

Operators $\mathbf{K}_{11}$ (respectively $\mathbf{f}_{11}$) and $\mathbf{K}_2$ (resp. $\mathbf{f}_2$) are the classical stiffness matrices (resp. vector forces) associated to subdomains Ω_{11} and Ω_2. $\mathbf{C}_{11}$ and $\mathbf{C}_2$ are the Mortar coupling operators that formally read as follows:

$$\mathbf{C}_{11}=\int_\Gamma \mathbf{L}_\lambda\mathbf{L}_{11}^T\mathrm{d}\Gamma\ ;\ \mathbf{C}_2=\int_\Gamma \mathbf{L}_\lambda\mathbf{L}_2^T\mathrm{d}\Gamma, \tag{2.9}$$

where $\mathbf{L}_{11}$ (resp. $\mathbf{L}_2$ and $\mathbf{L}_\lambda$) represents the standard shape function matrix (same notation as in chapter 1) related to subspace $\mathcal{U}^h_{11}$ (resp. $\mathcal{U}^h_2$ and $\mathcal{M}^h$).

Resolution (2.8) of the global/local problem constitutes the classical monolithic approach: the resulting multiscale model of Fig. 2.2(b) is computed directly using a single direct solver. This strategy can be characterized as invasive. Indeed, in addition of merging contributions from the global and local problems, it is important to note that the global operator $\mathbf{K}_{11}$ depends at this stage on the interface Γ or, in other words, on the shape of the local domain Ω_2. It is thus requested to modify the initial global model to remove some of its elements, and possibly pieces of elements (see Fig. 4.2 again). In case the local detail grows up (during optimization process, crack propagation, or expansion of damage or plasticity for instance), the situation is getting even worse since not only the local operator $\mathbf{K}_2$ but also the global operator $\mathbf{K}_{11}$ have to be fully re-built and re-factorized at each time step of the simulation.

1.2.3 Non-invasive iterative resolution

Rather than directly solving system (2.8), the non-invasive strategy is based on an iterative exchange procedure. For the construction, we proceed in two steps: we first split the initial system in order to identify

(in terms of boundary conditions applied on Γ) a Neumann and a Dirichlet problem over Ω_{11} and Ω_2, respectively; then, we apply the additivity of the integral with respect to domain $\Omega_1 = \Omega_{11} \cup \Omega_{12} \cup \Gamma$ in order to recover the initial whole global model.

Splitting of the coupled problem. For the alternative resolution of (2.7), on may apply the following asymmetric algorithm: for the nth iteration, starting with initial guess $\lambda^{(0)} \in \mathscr{M}$, we look for $u_{11}^{(n)} \in \mathscr{U}_{11}$, $u_2^{(n)} \in \mathscr{U}_2$, and $\lambda^{(n)} \in \mathscr{M}$ such that:

1. Resolution of a problem over Ω_{11}:

$$a_{11}\left(u_{11}^{(n)}, v_{11}\right) = l_{11}(v_{11}) - b(\lambda^{(n-1)}, v_{11}), \quad \forall v_{11} \in \mathscr{V}_{11}. \tag{2.10}$$

2. Resolution of a problem over Ω_2:

$$\begin{cases} a_2\left(u_2^{(n)}, v_2\right) - b(\lambda^{(n)}, v_2) = l_2(v_2), \quad \forall v_2 \in \mathscr{V}_2\,; \\ -b(\mu, u_2^{(n)}) = -b(\mu, u_{11}^{(n)}), \quad \forall \mu \in \mathscr{M}. \end{cases} \tag{2.11}$$

A mechanical interpretation of the above iterative strategy can be easily given by investigating the consistency of the two formulations (2.10) and (2.11). Starting with (2.11), integrating by parts, applying $\sigma_2 = C_2 \varepsilon(u_2)$, and bringing all terms in the left-hand side, we can write:

$$\begin{cases} -\displaystyle\int_{\Omega_2} v_2 \cdot \left(\operatorname{div}(\sigma_2^{(n)}) + f_2^g\right) \mathrm{d}\Omega_2 + \int_{\Gamma_{F_2}} v_2 \cdot \left(\sigma_2^{(n)}\, n_2 - F_2^g\right) \mathrm{d}\Gamma_{F_2} + \int_{\Gamma} v_2 \cdot \left(\sigma_2^{(n)}\, n_2 - \lambda^{(n)}\right) \mathrm{d}\Gamma = 0, \ \forall v_2 \in \mathscr{V}_2\,; \\ -\displaystyle\int_{\Gamma} \mu \cdot \left(u_2^{(n)} - u_{11}^{(n)}\right) \mathrm{d}\Gamma = 0, \quad \forall \mu \in \mathscr{M}. \end{cases} \tag{2.12}$$

As a result, looking for $u_2^{(n)}$ from $u_{11}^{(n)}$ with formulation (2.11) simply corresponds to solve:

$$u_2^{(n)} = u_2^g \quad \text{over} \quad \Gamma_{u_2}\,; \tag{2.13a}$$
$$\operatorname{div}(\sigma_2^{(n)}) + f_2^g = 0 \quad \text{in} \quad \Omega_2\,; \tag{2.13b}$$
$$\sigma_2^{(n)}\, n_2 = F_2^g \quad \text{over} \quad \Gamma_{F_2}\,; \tag{2.13c}$$
$$\sigma_2^{(n)} = C_2\, \varepsilon\left(u_2^{(n)}\right) \quad \text{in} \quad \Omega_2\,; \tag{2.13d}$$
$$u_2^{(n)} = u_{11}^{(n)} \quad \text{over} \quad \Gamma\,; \tag{2.13e}$$

and to get, as a reaction force:

$$\lambda^{(n)} = \sigma_2^{(n)}\, n_2 \quad \text{over} \quad \Gamma. \tag{2.14}$$

Problem (2.13) constitutes a Dirichlet problem (in terms of boundary conditions applied over Γ): the second step of the iterative strategy (2.10)-(2.11) thus corresponds to the exchange of the interface displacement from the global to the local problems. Using a similar procedure, we can write for formulation (2.10):

$$-\int_{\Omega_{11}} v_{11} \cdot \left(\operatorname{div}(\sigma_{11}^{(n)}) + f_{11}^g\right) \mathrm{d}\Omega_{11} + \int_{\Gamma_{F_{11}}} v_{11} \cdot \left(\sigma_{11}^{(n)}\, n_{11} - F_{11}^g\right) \mathrm{d}\Gamma_{F_{11}} + \int_{\Gamma} v_{11} \cdot \left(\sigma_{11}^{(n)}\, n_{11} + \lambda^{(n-1)}\right) \mathrm{d}\Gamma = 0, \ \forall v_{11} \in \mathscr{V}_{11}\,; \tag{2.15}$$

which corresponds to look for $u_{11}^{(n)}$ from $\lambda^{(n-1)}$ such that:

$$u_{11}^{(n)} = u_{11}^g \quad \text{over} \quad \Gamma_{u_{11}}\,; \tag{2.16a}$$
$$\operatorname{div}(\sigma_{11}^{(n)}) + f_{11}^g = 0 \quad \text{in} \quad \Omega_{11}\,; \tag{2.16b}$$
$$\sigma_{11}^{(n)}\, n_{11} = F_{11}^g \quad \text{over} \quad \Gamma_{F_{11}}\,; \tag{2.16c}$$
$$\sigma_{11}^{(n)} = C_{11}\, \varepsilon\left(u_{11}^{(n)}\right) \quad \text{in} \quad \Omega_{11}\,; \tag{2.16d}$$
$$\sigma_{11}^{(n)}\, n_{11} = -\lambda^{(n-1)} = -\sigma_2^{(n-1)}\, n_2 \quad \text{over} \quad \Gamma\,; \tag{2.16e}$$

where equality (2.14) has been used in Eq. (2.16e). Problem (2.16) constitutes a Neumann problem (still in terms of boundary conditions applied over Γ) which means that the first step of the iterative strategy (2.10)-(2.11) concerns the exchange of the interface traction force from the local to the global problem. Finally, one may notice that the fixed point between problems (2.16) and (2.13) enables to recover all the equations of problem (2.1)-(2.2); that is, if the iterative procedure converges, it converges towards the reference global/local solution.

We now switch to the matrix form as in (2.8). The fixed point (2.10)-(2.11) reads: for the nth iteration, starting with initial guess $\boldsymbol{\lambda}^{(0)}$, we look for $\mathbf{u}_{11}^{(n)}$, $\mathbf{u}_{2}^{(n)}$ and $\boldsymbol{\lambda}^{(n)}$ such that:

1. Resolution of a Neumann problem over Ω_{11}:

$$\mathbf{K}_{11}\mathbf{u}_{11}^{(n)} = \mathbf{f}_{11} - \mathbf{C}_{11}^{T}\boldsymbol{\lambda}^{(n-1)}. \tag{2.17}$$

2. Resolution of a Dirichlet problem over Ω_2:

$$\begin{bmatrix} \mathbf{K}_2 & -\mathbf{C}_2^T \\ -\mathbf{C}_2 & \mathbf{0} \end{bmatrix} \begin{Bmatrix} \mathbf{u}_2^{(n)} \\ \boldsymbol{\lambda}^{(n)} \end{Bmatrix} = \begin{Bmatrix} \mathbf{f}_2 \\ -\mathbf{C}_{11}\mathbf{u}_{11}^{(n)} \end{Bmatrix}. \tag{2.18}$$

Global model recovery. Even if two problems are now solved separately, procedure (2.17)-(2.18) is still invasive because only the contributions over Ω_{11} of the global model are involved. To go further, we make use of the continuous prolongation of the global solution from Ω_{11} to Ω_{12}. Denoting by $\mathbf{u}_1$ the DOF vector associated to domain Ω_1, we can write:

$$\mathbf{K}_1\mathbf{u}_1 = \overline{\mathbf{K}}_{11}\mathbf{u}_1 + \overline{\mathbf{K}}_{12}\mathbf{u}_1. \tag{2.19}$$

In the above equation, $\overline{\mathbf{K}}_{11}$ and $\overline{\mathbf{K}}_{12}$ are the extensions to Ω_1 of the classical stiffness matrices $\mathbf{K}_{11}$ and $\mathbf{K}_{12}$ related to subdomains Ω_{11} and Ω_{12}, respectively. They literally contain the classical stiffness operators and are padded with zeros to make them the same dimension of $\mathbf{u}_1$. As well, we define $\mathbf{f}_1 = \bar{\mathbf{f}}_{11} + \bar{\mathbf{f}}_{12}$ the load vector associated to domain Ω_1. Equality (2.19) is used to expand problem (2.17) from Ω_{11} to Ω_1. We finally end up with the following algorithm: for the nth iteration, starting with initial guesses $\boldsymbol{\lambda}^{(0)}$ and $\mathbf{u}_1^{(0)}$, we look for $\mathbf{u}_1^{(n)}$, $\mathbf{u}_2^{(n)}$ and $\boldsymbol{\lambda}^{(n)}$ such that:

1. Resolution of a Neumann problem over Ω_1:

$$\mathbf{K}_1\mathbf{u}_1^{(n)} = \mathbf{f}_1 - \mathbf{C}_1^{T}\boldsymbol{\lambda}^{(n-1)} + \mathbf{r}_{12}^{(n-1)}. \tag{2.20}$$

2. Resolution of a Dirichlet problem over Ω_2:

$$\begin{bmatrix} \mathbf{K}_2 & -\mathbf{C}_2^T \\ -\mathbf{C}_2 & \mathbf{0} \end{bmatrix} \begin{Bmatrix} \mathbf{u}_2^{(n)} \\ \boldsymbol{\lambda}^{(n)} \end{Bmatrix} = \begin{Bmatrix} \mathbf{f}_2 \\ -\mathbf{C}_1\mathbf{u}_1^{(n)} \end{Bmatrix}. \tag{2.21}$$

We note that the Mortar operator $\mathbf{C}_1$ simply consists of the prolongation of former operator $\mathbf{C}_{11}$ from Ω_{11} to Ω_1. $\mathbf{r}_{12}$ is introduced to denote the discrete reaction forces at Γ of the global model in the covered part Ω_{12}. It reads at iteration $n-1$:

$$\mathbf{r}_{12}^{(n-1)} = \overline{\mathbf{K}}_{12}\mathbf{u}_1^{(n-1)} - \bar{\mathbf{f}}_{12}. \tag{2.22}$$

On may observe that in expression (2.22), only the degrees of freedom concerned with interface Γ are not zero. It may also be stressed that the fictitious prolongation of the global solution over Ω_{12} has no physical meaning. In Ω_2, only the local solution should be considered. An overview of the iterative procedure is given in Fig. 2.3. The convergence test usually considered to stop this algorithm relies on the equilibrium of the reaction forces at the interface of the two models. More precisely, the following residual is used:

$$\eta^{(n)} = \frac{||\mathbf{C}_1^T\boldsymbol{\lambda}^{(n)} + \mathbf{r}_{11}^{(n)}||_2}{\sqrt{||\mathbf{f}_1||^2 + ||\mathbf{f}_2||_2^2}}, \tag{2.23}$$

where $\mathbf{r}_{11}^{(n)}$ characterizes the discrete reaction forces at Γ produced by the global model in subdomain Ω_{11}:

$$\mathbf{r}_{11}^{(n)} = \overline{\mathbf{K}}_{11}\mathbf{u}_1^{(n)} - \bar{\mathbf{f}}_{11}. \tag{2.24}$$

The calculation (2.24) is performed from the already computed stiffness and vector force $\overline{\mathbf{K}}_{12}$ and $\bar{\mathbf{f}}_{12}$ (see Eq. (2.22)). In the rest of this chapter, we employ the terminology "non-invasive residual" to denote residual (2.23).

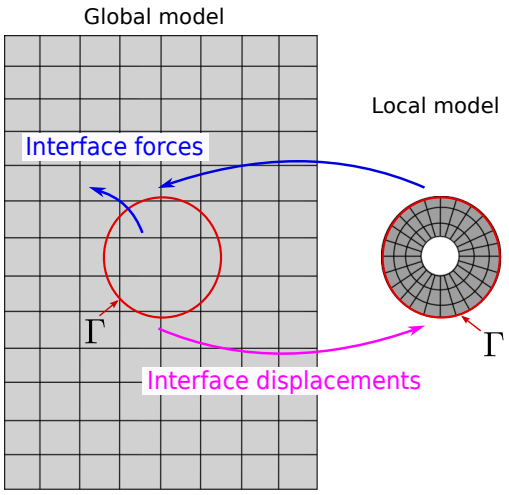

Figure 2.3 – The iterative non-invasive exchange procedure.

Algorithm (2.20)-(2.21) constitutes what is now referenced as the non-invasive coupling strategy in the literature. The whole stiffness matrix of the initial global model is now considered without any modification. Since the global model is unmodified, the global stiffness operator can be assembled and factorized only once during the pre-processing step. Furthermore, the global and local problems being solved alternatively and the interaction between the two models being restricted to interface Γ, the formalism offers the possibility to couple different numerical codes with few implementation effort. In particular, an industrial code can be used for the large-scale computation while a dedicated research code can be set up to solve a specific local behavior. The price to pay is the number of iterations of the fixed point solver. However, this one can be deeply reduced by means of accelerations techniques, such as based on an Aitken's Delta Squared method or a Quasi-Newton method (see, *e.g.*, [Gendre et al., 2009, Liu et al., 2014, Duval et al., 2016]), as will be demonstrated later in this chapter (see section 3).

Remark. *It may be noticed that the first iteration of the non-invasive algorithm exactly corresponds to the so-called submodeling approach typically used in industry (see section 1.1).*

Remark. *The convergence of the standard iterative procedure* (2.20)-(2.21) *depends on the stiffness gap between the global (fictitious) model in* Ω_{12} *and the local model in* Ω_2*. Theoretically, this can be shown by rewriting the fixed point as a modified Newton algorithm where the approximation of the tangent matrix depends on the gap in the primal Schur complements between the models in* Ω_{12} *and in* Ω_2 *(see,* e.g., *[Chevreuil et al., 2013, Duval et al., 2016, Nouy and Pled, 2018]). In particular, it can be shown that the standard strategy does not converge in case the local model is stiffer than the global model. In this challenging situation, it is necessary to resort to the Quasi-Newton acceleration technique to make the algorithm converge in a relatively low number of iterations (see,* e.g., *[Duval et al., 2016, Bouclier et al., 2016].*

Remark. *As stated above, the method is by no means limited to a linear elastic local model. Indeed, as long as we are able to apply Dirichlet boundary conditions to the local problem and to compute*

(directly or in a post-processing step) the corresponding reactions forces, any local behavior can be considered.

Remark. *Let us finally observe that this non-invasive methodology has similarities with some hierarchical global/local methods: for example, the Chimera method [Steger et al., 1983, Steger, 1991], the method of finite elements patches [Glowinski et al., 2005], numerical zoom [Kamga and Pironneau, 2007] or the hp-d method [Rank, 1992, Düster et al., 2007]. However, the difference here is that the contribution of the global solution in the local area is totally replaced by the local solution while in the hierarchical strategy, the approximate solution is sought as the sum of the global coarse contribution and a local fine one. As a result, the advantage of the used algorithm is that it reduces the interactions between global and local discretizations: the two models talk to each other with interface integrals only while the evaluation of mixed terms over the whole local domain is necessary in the hierarchical approach.*

1.2.4 Implementation issues

Depending on the discretization of the two subdomains Ω_{11} and Ω_2 along interface Γ, four distinct coupling situations may be listed (see Fig. 2.4 for illustration). Here, and in the remainder of the manuscript, we follow the nomenclature introduced in [Bouclier et al., 2017, Guinard et al., 2018]. Although this section is restricted to the context of standard FEM, we already emphasize that this classification holds in the case of IGA: in order to adapt it to IGA, the reader may consider the elements as the spline knot-span elements (*i.e.*, the different "pieces" that join along knot lines). From the most restrictive to the most general case, we may encounter the coupling situations of:

1. Matching meshes: the interface Γ is aligned with the edges of the elements and the meshes of the two subdomains along the interface are perfectly aligned (see Fig. 2.4(top-left)).

2. Non-matching meshes: the interface Γ is aligned with the edges of the elements but the meshes of the two subdomains along the interface may be shifted (see Fig. 2.4(top-right)).

3. Geometrically non-conforming meshes: the interface Γ is not aligned with the edges of the coarse elements which means that some elements of the global model are overlapped (see Fig. 2.4(bottom-left)).

4. Geometrically and topologically non-conforming meshes: the interface Γ is not aligned with the edges of the coarse elements, and the global and local models do not have the same topology along Γ (*e.g.*, shell on the global side versus solid on the local side, see Fig. 2.4(bottom-right)).

In the first contributions on non-invasive coupling [Gendre et al., 2009], the symplifying assumption of meshes and nodes compatibility was present. Then, interface projections were performed, which enabled to successfully handle non-matching meshes [Passieux et al., 2013, Duval et al., 2016, Liu et al., 2014]. For simplicity, it was recommended to consider the trace along the coupling interface Γ of the basis functions of the local model for the construction of $\mathscr{M}^h$. With this practical choice, no instability problems were reported in the field of non-invasive coupling, even in challenging situation [Duval et al., 2016]. Until very recently, it may be observed that the implementation is mostly made in these two coupling situations, which evidently limits the practicability of the method as it is desired to achieve a satisfactory level of flexibility in defining the region of interest for a more detailed analysis. The difficulty when facing geometrically non-conforming meshes relies on (i) the evaluation of integrals over pieces of coarse elements (to get the interface reaction force $\mathbf{r}_{12}$ (2.22)), and (ii) the formulation of a non-overlapping coupling method adapted to an immersed interface. As will be seen later in section 3.2, specific quadrature rules and a Nitsche-based coupling formulation have been set up to answer this issue in the field of IGA. However, returning to the original idea of non-invasive coupling in the context of FEM, such an approach appears inconsistent with

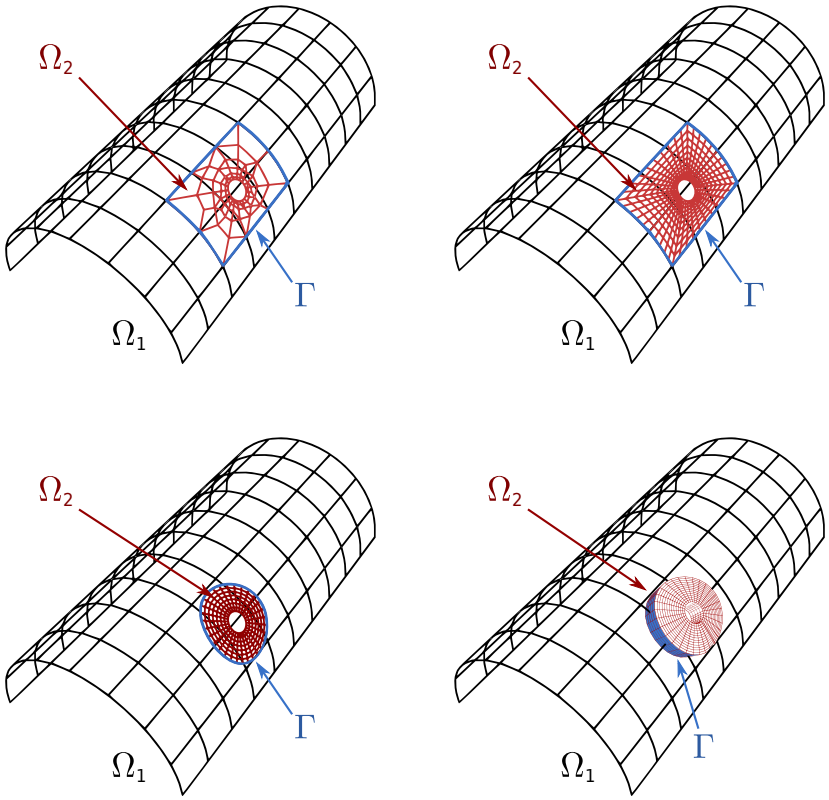

Figure 2.4 – Four distinct coupling situations: (top-left) Matching meshes; (top-right) Non-matching meshes ; (bottom-left) Geometrically non-conforming meshes; (bottom-right) Geometrically and topologically non-conforming meshes.

the use of standard industrial codes. Finally, the case of a global/local topologically non-conforming interface raises additional implementation issues related to the proper transmission of topologically inconsistent quantities (*e.g.*, surface displacement and rotation fields for a shell versus a 3D solid displacement field). A framework for the proper non-invasive coupling of a global plate model with local solid elements has been proposed in [Guguin et al., 2014, Guguin et al., 2016], but this one relies on a complex procedure involving the definition of a cumbersome buffer zone (see also [Gosselet et al., 2018]).

1.3 Multiscale FE analysis of complex aeronautical structures

As a solution to the aforementioned issues, we have developed a pragmatic yet robust strategy that enables to handle FE meshes of complex shapes, which are not only non-matching but also geometrically and topologically non-conforming. In particular, this allowed to solve the previously introduced industrial test case depicted in Fig. 2.1; *i.e.*, including the coupling of a fully non-planar shell with 3D solid models. This work has been performed in collaboration with AIRBUS through the co-supervision of the master 2 internship of Mateus Toniolli in 2016. For more information and additional numerical experiments, the interested reader is referred to [Guinard et al., 2018].

1.3.1 The proposed methodology

In order to ensure minimal invasiveness, the strategy makes extensively use of existing tools in industrial FE codes. The procedure is depicted in Fig. 5.6. The idea is very simple: starting with a free independent local solid model (see Fig. 5.6(a)), it is proposed to modify its geometry in order to recover the robust situation of a geometrically and topologically conforming global/local interface. This goal is achieved

by generating a surface transition mesh (*i.e.*, made of shell elements). First, a grid intersection problem [Gander and Japhet, 2013] is solved as classically in such methods in order to determine which are the elements from the global model that intersect the local model (see Fig. 5.6(b)). The region obtained by collecting these coarse elements forms the subdomain Ω_{12}. A new interface that corresponds to a set of element edges from the global model can then be defined (see red line in Fig. 5.6(b)). The second step of the approach is dedicated to the expansion of the local model to the new interface by means of a surface transition mesh. In other words, domain Ω_2 is modified so that its boundary fits with the new interface. As a consequence, it becomes possible to perform the global/local exchanges as classically across the new geometrically and topologically conforming interface (see Fig. 5.6(c).

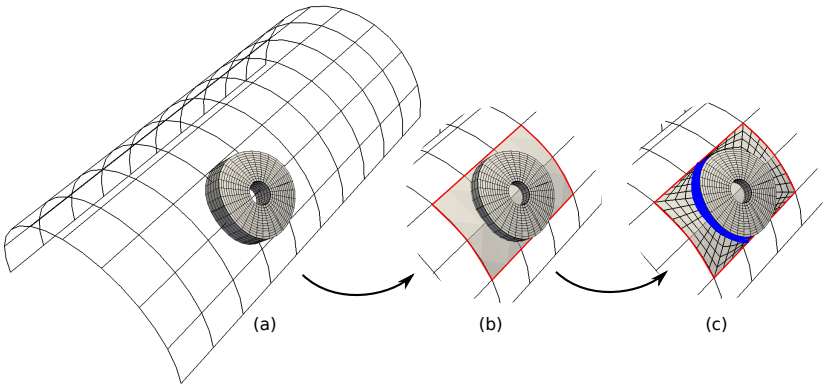

Figure 2.5 – Illustration of the proposed pragmatic strategy based on a transition mesh generation. Starting from (a) the initial meshes, step (b): determination of domain Ω_{12} (grey area) and a new interface (red line) and, step (c): transition mesh generation making appear two distinct interfaces (red line: global/local, blue zone: shell/solid).

To sum up, the proposed strategy makes appear two distinct interfaces which enables to separate the difficulties due to the combination of the global/local and shell/solid characters of the coupling. The shell/solid coupling is managed within the local model (see blue zone in Fig. 5.6(c)) while the global/local exchange is performed by means of a shell/shell coupling at the local model boundary (see red line in Fig. 5.6(c)). This offers the possibility to use standard methods employed in industry to connect shell and solid elements, thus avoiding to introduce cumbersome buffer zones.

1.3.2 Results : large cuts in a real fuselage section

By means of the strategy illustrated in Fig. 5.6, we have been able to perform the multiscale FE analysis of the real fuselage section depicted in Fig. 2.1. For the implementation, the Abaqus software suite has been chosen both for the resolution of the global and local problems. This FE software is one of the most employed in the aerospace industry, being used in the operational environment of AIRBUS Group. More precisely, Abaqus v6.14 co-simulation native capabilities [Abaqus, 614] have been extended through additional specific developments (user subroutine and Abaqus `python` script for time synchronization of global/local jobs). The proposed meshing strategy is applied through a main `python` script for Abaqus GUI pre-processor (CAE), that handles global and local model preparation (such as illustrated in Fig. 5.6). The main script also contains in its beginning the instantiation operation of the implemented classes, namely the coupling classes, the global model class and the local model class. The Abaqus based shell-to-solid coupling (see Abaqus documentation [Abaqus, 614]: section "Shell-to-solid coupling") is considered within the local model to handle the shell/solid character of the coupling (see again blue zone in Fig. 5.6).

We recall that the explored use-case is highly challenging for multiscale analysis: characteristic lengths at global and local scales are 7m (fuselage section length) and 10μm (ply thickness) respectively. The fuselage is clamped on its left side and subjected to traction on the other side. An internal pressure is also

prescribed so as to model the typical pressure gap encountered in flight. The composite material made of carbon fibers consists of a $[45°, 90°, -45°, 0°]_{sym}$ stacking sequence. The structure is studied in its elastic regime, the objective being to make sure that the crack will not propagate due to too high stress states around the crack tips. In the solid model, only the plies (without interfaces) are modeled with a linear orthotropic elastic behavior. The large cut is included in the local model by means fo a suitable transitional shell mesh. We stress here that other tests were performed in [Guinard et al., 2018] considering a non-linear local model that was able to take into account the damage of the composite structure.

Fig. 2.6 shows the results obtained with the proposed non-invasive method, which happens to be physically relevant. No acceleration techniques were used since we reached convergence with the standard fixed point (2.20)-(2.21) in about 15 iterations (leading to an overall time for the simulation of about two hours). We clearly observe the strong coupling between the two scales in the situation of large cuts: the material state in crack tip areas influences the kinematics of the crack lips and thus the global structural behavior. As an additional justification, we compare the results obtained for the global model to the one we get using the industrially-used top-down submodeling approach (see Fig. 2.7). We clearly see a discrepancy between the two solutions around the local area which highlights the necessity of an iterative strategy for a proper force redistribution at the global scale. As mentioned previously in section 1.1, a direct monolithic approach was not affordable given the complexity and size of the problem (global mesh refurbishments was prohibited by industrial engineers).

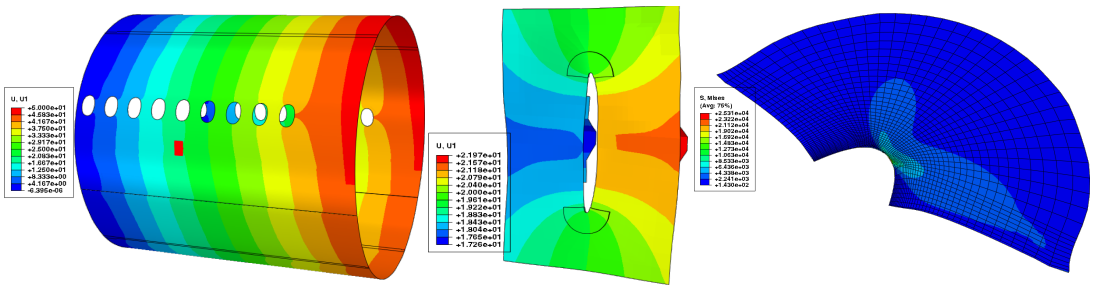

Figure 2.6 – Results for the real fuselage section: from left to right; global horizontal displacement (mm), local horizontal displacement (mm), and local von Mises stress (MPa) in the upper ply (3D area, top crack tip) *(floor, stiffeners and frames not represented on the global model for confidentiality reasons).*

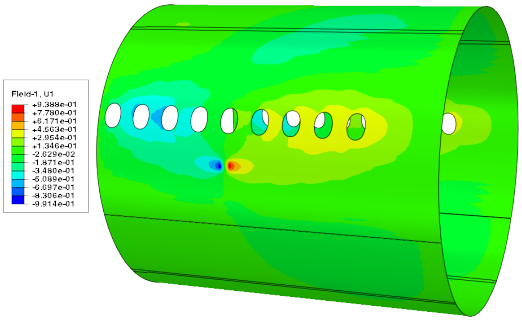

Figure 2.7 – Comparison between the submodeling and the iterative non-invasive approaches: distribution of the difference between the two global horizontal displacements (mm): $\mathbf{u}_{\text{non-invasive}} - \mathbf{u}_{\text{submodeling}}$ *(floor, stiffeners and frames not represented for confidentiality reasons).*

Summary and discussion. The non-invasive coupling approach has recently emerged in the field of standard FEM as a response to a present-day industrial issue: how to locally enrich a complex, costly global model without modifying it (and its associated numerical operators)? More than being an efficient alterna-

tive to couple different models, the method offers the possibility to combine different numerical codes with few implementation effort. From a mathematical point of view, the strategy starts with a Lagrange multiplier type formulation of the resulting global/local coupling problem. Then, by making use of the additional interface unknowns, we split the obtained system to make the global and local models communicate, in an iterative manner, through interface exchanges while keeping the initial structure of their stiffness operator. Most of the current implementations are restricted to the coupling of conforming global and local models (*i.e.*, the interface is aligned with the edges of the global and local elements), which evidently limits the practicability of the method in a general multiscale context. To go a step further in the field of FEM, we developed a pragmatic yet robust strategy based on a transitional shell meshing that enabled to handle FE meshes of complex shapes, which were geometrically and topologically non-conforming. In particular, in collaboration with AIRBUS, we were able to perform a realistic multiscale aeronautical simulation involving, at the global scale, an homogenized non-planar shell model fully representative of a portion of aircraft (about 7m large) and, at the local scale, several full 3D models where each ply was meshed (ply thickness: $10\mu m$).

2 Interest for the field of IGA

We believe that non-invasive coupling techniques are good candidates for isogeometric global/local analysis. More than being attractive from an industrial engineering point of view as in FEM, the non-invasive coupling idea appears to us completely relevant, from a scientific point of view, to improve the field of global/local structural IGA. This section highlights the interest of building non-invasive (NURBS or B-Spline based) isogeometric coupling methods. The challenge regarding the extension of those methods to the field of IGA is also discussed. This section serves as a prerequisite to present the contributions that we have performed in this field (see section 3 and [Bouclier et al., 2016, Bouclier et al., 2017, Bouclier and Passieux, 2018, Tirvaudey, 2019]). The context for each contribution with the corresponding state of the art is given.

2.1 Global/local modeling in IGA

As outlined in chapter 1, (standard) multivariate spline bases comprise a rigid tensor product structure, which evidently constitutes a drawback to perform global/local simulation. Indeed, we necessarily end up with a structured mesh in a B-Spline or NURBS patch which precludes the simple modeling of local phenomena. More precisely, this unavoidably leads to the overlap of some global knot-span elements to allow for a truly global-mesh independent local region to be incorporated for the modeling of any specific local behaviors (*e.g.*, introduction of a hole [Guo, 2017], of an inclusion [Nguyen et al., 2014], of a crack [Bouclier et al., 2016], etc). From that point of view, the academic case depicted in Fig. 2.2(a) seems to be well appropriate to illustrate a situation frequently happening in IGA. In this context, one should consider in Fig. 2.2(a) the global model as a B-Spline patch and the local model as a NURBS patch. Due to the presence of a non-conforming interface, the analysis of trimmed isogeometric patches actually needs to be addressed, which is known not to be a trivial task in the IGA community (see chapter 1 again). From the literature, it seems that three main strategies could be applied to numerically solve the resulting isogeometric global/local problem (see Fig. 2.8).

Spline re-parametrization. The first strategy, already mentioned in chapter 1 (see Fig. 1.4), consists in recovering the usual situation of boundary fitted discretizations. In order to do so, a re-parametrization of the whole global/local isogeometric model is required, leading to the splitting of the new geometry into several patches with C^0 continuity at the boundaries (see, *e.g.*, [Xu et al., 2013, Akhras et al., 2016,

Massarwi et al., 2019]). An illustration for the simple example of Fig. 2.2(a) is given in Fig. 2.8(a). For more complex models, this may entail a considerable modeling and computational effort which is often as complex and time consuming as standard mesh generation and then, is opposed to the core idea of IGA.

Coupling of immersed domains. Concurrently, a second approach initiated in [Ruess et al., 2014] and based on the combination of a fictitious domain method with a weak coupling, may constitute an interesting option to carry out global/local isogeometric simulations. This technique can be viewed as the extension in IGA of the monolithic coupling described above in case of FEM (see section 1.2 and, in particular, Eq. (2.8)). To this purpose, the authors made use of the so-called Finite Cell Method (FCM) (see, *e.g.*, [Schillinger and Ruess, 2015] for a detailed review). Unlike the first approach, the idea here is to simply use the resulting unfitted structured mesh for the interpolation of the global fields (see Fig. 2.8(b)), while the trimmed geometry is accurately captured by means of suitable quadrature rules for cut knot-span elements [Legrain, 2013, Nagy and Benson, 2015, Kudela et al., 2015, Fries and Omerovic, 2016, Stavrev et al., 2016, Fries et al., 2017]. This strategy appears suitable and has proved to be highly efficient in the context of immersed finite elements. However, let us notice that in the general case of a local region that may evolve during the simulation; *e.g.*, to carry out the shape optimization of local entities (see chapter 6), or to model crack propagation, or the expansion of a plastic zone, etc, we expect several re-assemblies and re-factorizations of the resulting global/local stiffness operator during the multiresolution process. The left-hand side operator may also appear ill-conditioned depending on the encountered trimmed configuration [Burman et al., 2015, Dauge et al., 2015, Verhoosel et al., 2015, de Prenter et al., 2017].

Non-invasive coupling. Relatively connected to the previous approach, the last strategy revolves around the concept of non-invasiveness that has been introduced in section 1 in its initial FE form. The idea is to take the initial large-scale isogeometric (possibly multi-) patch to be enriched as the global model. Consequently, the global patch is never modified during the simulation (see Fig. 2.8(c)), which eliminates the need for costly spline re-parametrization procedures. In addition, the global stiffness operator is assembled and factorized only once and the system to be solved remains well-conditioned. Especially in case the local region evolves, thus leading to the resolution of a sequence of similar problems (in a multiresolution fashion [Gosselet et al., 2013, Néron et al., 2015]), the method meets its full potential since the global stiffness operator remains the same, which ensures both robustness and computational time saving [Bouclier and Passieux, 2018]. Moreover, it should be mentioned that the flexibility of the strategy allows simple modeling of a variety of local behaviors. Indeed, since two different numerical codes can be used to compute the global and local models, a linear isogeometric code can be used for the global simulation of the isogeometric patch while any other existing robust code integrating any other numerical method (such as coming from the FE-based community) can be used to incorporate an accurate local model. In this context, one may end up with a combined global-IGA/local-FEM method that draws up the best of each technology [Bouclier et al., 2016, Tirvaudey, 2019]. All of these advantages will be further accounted for (through numerical experiments) in section 3 and later on in chapter 6.

2.2 Challenge: non-conforming coupling

As stated above and illustrated in Figs. 2.2(a) and 2.4(bottom-left), the situation of (geometrically) non-conforming interfaces is to be expected to tackle general applications in IGA. More importantly, a technique similar to the one proposed in case of FEM (*i.e.*, based on the building of a transition mesh to recover a conforming interface, see section 1.3) appears unthinkable in case of both the global and local models are discretized by means of spline shape functions. Indeed, given the tensor product structure of spline basis, building a tentative isogeometric transition mesh would lead to carry out complex spline

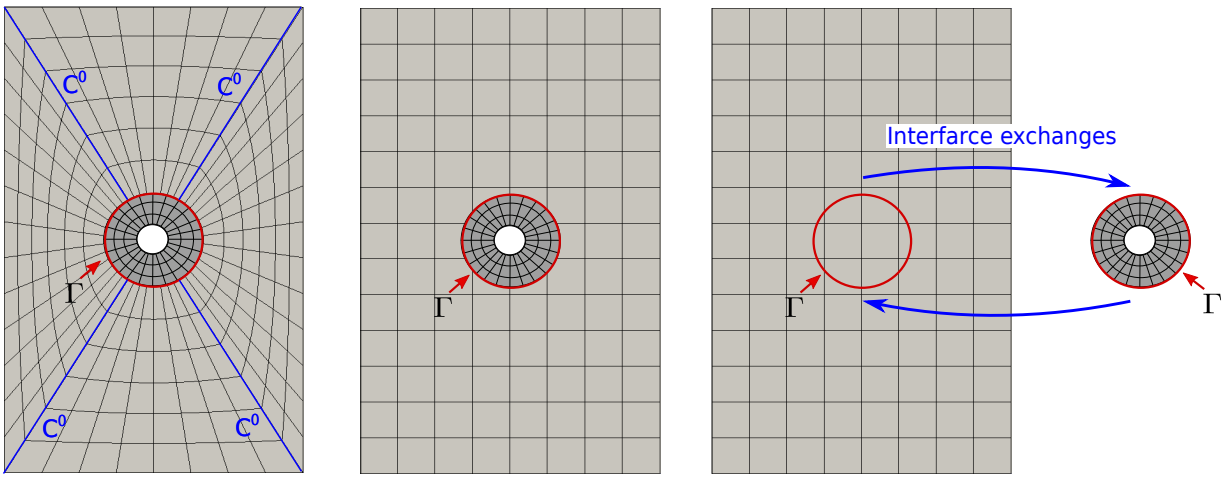

(a) Approach 1: Spline re-parametrization.

(b) Approach 2: coupling of immersed domains.

(c) Approach 3: non-invasive coupling.

Figure 2.8 – Three different strategies may be applied in IGA to numerically solve a global/local problem.

re-parametrization procedures (as in approach 1, see Fig. 2.8(a)). In case we perform an hybrid global-IGA/local-FEM modeling [Bouclier et al., 2016, Tirvaudey, 2019], we will see in section 3.1 that a strategy based on a standard meshing procedure can be applied using the IGA-FEM bridge developed in chapter 1. However, in case of a general global-IGA/local-IGA modeling, we need to truly address the situation of non-conforming interfaces, which requires (i) to implement specific quadrature rules (to integrate over Ω_{12}, see Eq. (2.22)) and (ii) to formulate a coupling procedure adapted to any cut scenarios encountered through the non-invasive multi-resolution process. Regarding domain coupling in (NURBS or B-Spline based) IGA, many attempts have been devoted to the connection of isogeometric patches to foster the study of multi-patch geometries. In order to do so, weak coupling approaches have been developed. The resulting strategies can be divided into three classes: penalty coupling [Apostolatos et al., 2014a, Apostolatos et al., 2014b], Mortar coupling [Hesch and Betsch, 2012, Brivadis et al., 2015, Dornisch et al., 2015, Zou et al., 2018b, Wunderlich et al., 2019], and Nitsche coupling [Nguyen et al., 2014, Apostolatos et al., 2014b]. In their primary versions, such methods were limited to the coupling along a patch boundary. More recently, several strategies have been proposed to answer the issue in the field of immersed (or also referred to as embedded domain) methods [Burman et al., 2015, Schillinger and Ruess, 2015]. In particular, Nitsche coupling schemes have been formulated for properly connecting embedded domains along arbitrary, immersed interfaces (see [Annavarapu et al., 2012] for the origin and then, *e.g.*, [Ruess et al., 2014, Jiang et al., 2015, Schillinger et al., 2016a, Elfverson et al., 2019, Buffa et al., 2019]). In section 3.2, we extend such advanced techniques to build a new non-invasive algorithm that is able to handle all the non-conforming coupling scenarios encountered when performing global-IGA/local-IGA (see also [Bouclier and Passieux, 2018]).

Remark. *When addressing domain coupling in IGA, one may also be interested in designing a coupling method that preserves the higher regularity offered by the spline functions. This is of particular interest in the context of higher-order partial differential equations, such as for shell analysis in strucutral mechanics. In other words, the challenge would consist of formulating a more regular coupling method that allows for a smoother transition of the solution across the coupling interface. In [Bouclier et al., 2017], we have developed a coupling scheme based on two sets of Lagrange multipliers that enables to enforce a C^1 regularity at the interface. Drawing inspiration from this work, we have then built a new Mortar formulation adapted to the coupling of isogeometric Kirchhoff-Love shells (see [Hirschler et al., 2019b, Hirschler et al., 2019a]). The work achieved regarding more regular coupling will thus be presented later on in the context of shell anal-*

ysis (see chapter 3). Let us finally notice that subsequent studies from other authors with a similar objective have been very recenlty performed in the field of monolithic coupling (see, e.g.*, [Dittmann et al., 2019, Schuß et al., 2019]).*

Summary and discussion. Given the rigid tensor product structure of the multivariate spline basis, the non-invasive global/local coupling approach appears relevant, from a scientific point of view, for the field of IGA. It offers an original alternative to compute the resulting global/local trimmed isogeometric configuration. The idea is to take the initial isogeometric (possibly multi-) patch model as the global model, so that the need for costly spline re-parametrization procedures when integrating a non-conforming local model is eliminated. In addition, unlike standard immersed coupling methods, the global stiffness operator is assembled and factorized only once and the system to be solved remains well-conditioned, regardless of the evolution of the local model. However, more critically than in FEM, the challenge of handling a non-conforming coupling interface is crucial when extending the technology to IGA, since no simple meshing procedure can be achieved this time.

3 Some advanced numerical schemes for IGA

Recapitulating, our contributions in the field of global/local isogeometric structural analysis concern the development of non-invasive numerical schemes for (i) performing global-IGA/local-FEM and (ii) handling arbitrary non-conforming interfaces for global-IGA/local-IGA. Since the context of these contributions has been underlined in the previous section, we now focus on the developed algorithms and obtained results. We restrict ourselves to the case of a local model that is linear elastic in this section. However, the extension to non-linear local behaviors is discussed for each developed strategy.

3.1 Non-invasive global-IGA/local-FEM coupling

When moving to the field of IGA with the existing non-invasive FE strategy in hand, our first idea was to adopt an hybrid global-IGA/local-FEM modeling, so as to end up with a combined strategy which draws up the best of each analysis technology. Indeed, as seen in chapter 1, IGA appears efficient with respect to the geometrical representation and the computation of a global, regular response of the structure. Conversely, FEM seems to be more adapted to describe local, singular behaviors (*e.g.*, when displacement and/or strain discontinuities are encountered (crack, contact, heterogeneities)). Furthermore, beyond being an efficient strategy to couple different element types, the non-invasive formalism offers the possibility to couple different numerical codes with very few implementation efforts. As a consequence, the idea here is to use an advanced isogeometric code to compute the global model in combination with a robust conventional FEM code to integrate a specific local behavior (such as local fracture, local contact, local plasticity, etc). In order to perform the global/local coupling in a robust and automatic manner, we propose here to extend the FEM strategy of section 1.3 by resorting to the previously developed IGA-FEM bridge (see chapter 1 and [Tirvaudey et al., 2019a]). In addition to obtaining the simple situation of geometrically conforming coupling interfaces, it becomes possible with our strategy to easily build the coupling operators from standard FE ones. The idea of merging IGA and FEM for global/local simulations originates from my postdoc in Toulouse in 2015 and the automatic hybrid IGA/FEM procedure has been further developed in the PhD thesis of Marie Tirvaudey. The interested reader is referred to [Bouclier et al., 2016] for additional numerical experiments and to [Tirvaudey, 2019] for more information regarding the methodology.

3.1.1 Towards an automatic non-invasive global-IGA/local-FEM coupling

The proposed strategy for the automatic building of the global-IGA/local-FEM modeling is illustrated in Fig. 2.9. Consistent notations with the ones of chapter 1 are considered for the different operators (*i.e.*,

$\mathbf{R}$ and $\mathbf{L}$ represent isogeometric and Lagrange shape functions, and $\mathbf{D}^{c,f}$ and $\mathbf{D}_{FE}$ are associated to spline refinement and IGA-FEM transformations, respectively). Starting with a global (linear elastic) isogeometric model of the whole structure (a), a specific local FE model (e), meant to replace (in a non-invasive manner) the global model in an area of interest, is built. The area of interest is chosen as a set of initial global knot-span elements so that we reach the simple situation of a conforming coupling interface. More precisely, from the initial global isogeometric model (a), we apply standard spline refinement procedures to obtain the refined isogeometric model (b). Then, we make use of the previously developed IGA-FEM bridge to obtain the corresponding global fine FE model (c). It is therefore possible to extract the finite element description of the interface (d) by calling upon a restriction operator, *i.e.*:

$$\mathbf{L}_\Gamma = \mathbf{D}_\Gamma \mathbf{L}_1, \tag{2.25}$$

where $\mathbf{D}_\Gamma$ is the Boolean trace operator that selects only the nodes concerned by the interface, and $\mathbf{L}_\Gamma$ collects the resulting Lagrange shape functions generating the interface. Finally, applying standard FE meshing procedure, we can build a local FE mesh that is geometrically conforming with the interface. In order to do so, it may be noticed that the constructed FE mesh must have the same polynomial degree as the interface. As is standard practice in FEM, we choose to take the functions $\mathbf{L}_\Gamma$ to discretize the Lagrange multiplier field in the non-invasive coupling (2.20)-(2.21).

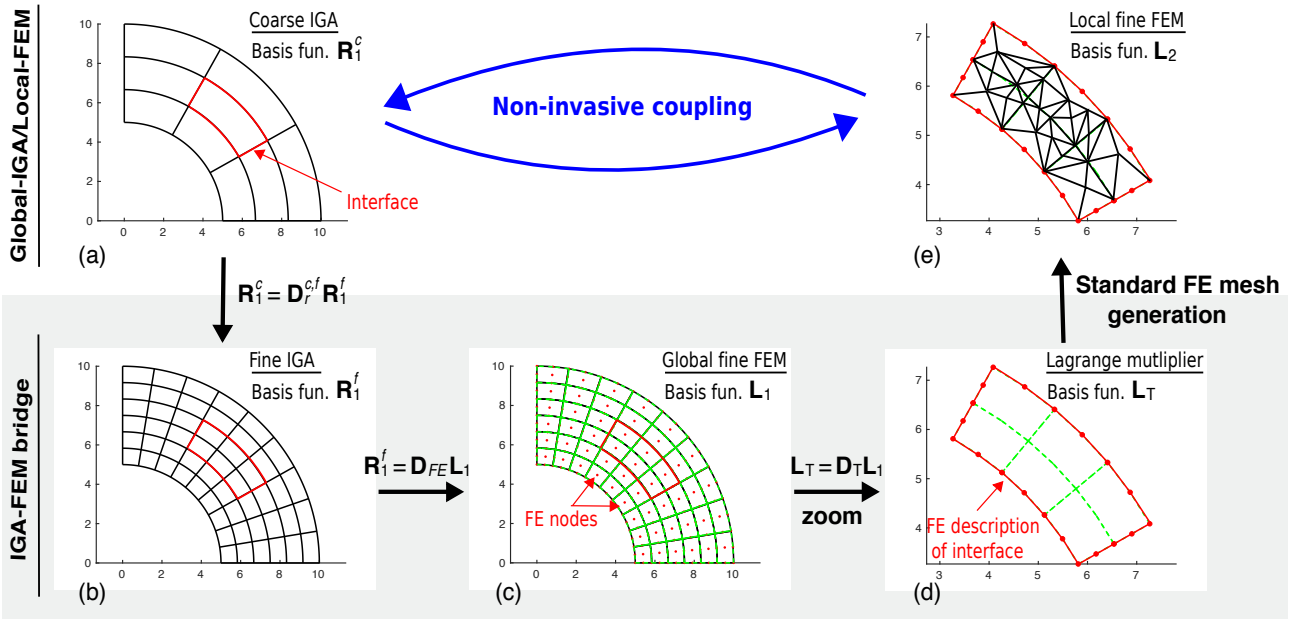

Figure 2.9 – Illustration of the proposed strategy to automatically perform global-IGA/local-FEM. The use of the previously developed IGA-FEM bridge (see chapter 1) enables to reach a geometrically conforming interface and offers the opportunity to simplify the implementation by calling upon standard FE operators.

With the strategy depicted in Fig. 2.9, we are also able to automatically compute the Mortar coupling operators $\mathbf{C}_1$ and $\mathbf{C}_2$ (see Eq. (2.9)) from their standard FE counterparts denoted by $\mathbf{C}_1^{FE}$ and $\mathbf{C}_2^{FE}$, respectively. Indeed, for subdomain Ω_2, since $\mathbf{L}_\Gamma$ is chosen for the Lagrange multiplier, we directly have:

$$\mathbf{C}_2 = \int_\Gamma \mathbf{L}_\Gamma \, \mathbf{L}_2^T \, \mathrm{d}\Gamma = \mathbf{C}_2^{FE}, \tag{2.26}$$

and for domain Ω_1, we can write:

$$\mathbf{C}_1 = \int_\Gamma \mathbf{L}_\Gamma \left(\mathbf{R}_1^c\right)^T \mathrm{d}\Gamma = \int_\Gamma \mathbf{L}_\Gamma \, \mathbf{L}_1^T \mathrm{d}\Gamma \; \mathbf{D}_{FE}^T \left(\mathbf{D}^{c,f}\right)^T = \mathbf{C}_1^{FE} \, \mathbf{D}_{FE}^T \left(\mathbf{D}^{c,f}\right)^T. \tag{2.27}$$

Realizing that the global isogeometric stiffness operator $\mathbf{K}_1$ in (2.20) could also be obtained without implementing IGA but simply from its FE counterpart using the IGA-FEM bridge, we end up with a fully

non-invasive global-IGA/local-FEM strategy, *i.e.* that the procedure is not only non-invasive in terms of coupling but also in terms of construction of the operators.

Remark. *The standard FE Mortar coupling operators* $\mathbf{C}_1^{FE}$ *and* $\mathbf{C}_2^{FE}$ *are defined formally and generally above. However, it has to be emphasized that we almost always meet in FEM the situation of matching or (at least) nested meshes to be coupled (see,* e.g., *[Duval et al., 2016]). In these cases,* $\mathbf{C}_1^{FE}$ *and* $\mathbf{C}_2^{FE}$ *are explicit (and basically consist of connectivity matrices relating the interface DOF with the domain DOF). The need for computing mass matrices is thus completely removed to obtain* $\mathbf{C}_1$ *and* $\mathbf{C}_2$ *with the proposed procedure.*

Remark. *The developed strategy is restricted to quadratic functions in practice since almost all standard FE codes do not go beyond second-order finite elements. Nevertheless, we emphasize that the proposed methodology could be directly applied to higher-order discretizations, provided that the corresponding higher-order finite elements are implemented.*

Remark. *One may eventually notice that equality* (2.27) *does not strictly hold in case of an initial NURBS geometry since we are not able to build a FE representation of a NURBS geometry. However, as stated in chapter 1, the error is so low that it does not affect the coupling.*

3.1.2 Numerical examples

Two examples are investigated in the following to demonstrate the performance and potential of the developed non-invasive hybrid IGA/FEM coupling method. In the first test case, the approach illustrated in Fig. 2.9 is strictly followed to introduce geometrical details such as holes and cracks in an initial global isogeometric patch. The potential of the proposed methodology to combine analysis models coming from different numerical codes is then further highlighted through the careful study of an edge-cracked plate. As of now, it has to be said that the automatic procedure of Fig. 2.9 was not applied for the second test case since this one was computed before we established the hybrid IGA/FEM methodology. However, the interested reader may notice that the same procedure as in Fig. 2.9 could have been applied, which would have obviously led to more simplicity (with respect to the implementation) and to equivalent accuracy. From here on, an isogeometric mesh composed of N elements along the first length and M elements along the second length will be denoted $N \times M$. In addition, the k-refinement strategy is applied so that the maximum regularity is met at the interior knot-lines (*i.e.*, $C^{(p-1)}$, p being the polynomial degree, see chapter 1).

Introduction of geometrical details into a 2D curved beam. As a first example, we consider the local enrichment of a 2D NURBS beam by means of a specific FE mesh incorporating a few holes and cracks. The structure is studied here in its elastic regime. The adopted global/local modeling and the problem parameters are specified in Fig. 2.10. The automatic procedure described above is used to perform the hybrid global-IGA/local-FEM simulation. More precisely, we start with a global model composed of a standard quadratic 16×24 NURBS mesh. Then, we select the area of interest as a set of global knot-span elements and apply the IGA-FEM and restriction operations depicted in Fig. 2.9 to obtain a quadratic FE description of the interface. Using this interface and the available GMSH mesh generator [Geuzaine and Remacle, 2009], we build the local FE mesh composed of quadratic triangles (*i.e.*, the typical `TRI6` element largely encountered in classic FEM). This FE mesh exactly matches the FE description of the interface: the boundary nodes of the FE mesh coincide with the nodes of the interface. We therefore end up with a matching coupling interface for which it is very easy to compute $\mathbf{C}_2^{FE}$ and $\mathbf{C}_1^{FE}$ (since they consist of Boolean operators). We finally make use of Eqs. (2.26) and (2.27) to directly obtain $\mathbf{C}_2$ and $\mathbf{C}_1$ and run the non-invasive analysis.

Less than 10 iterations are necessary to reach convergence with the combined IGA/FEM version of algorithm (2.20)-(2.21). Fig. 2.10 also shows the deformation of the meshes. The cracks open up which seems to be consistent with the applied load and Dirichlet boundary conditions. In addition, we plot in Fig. 2.11 the

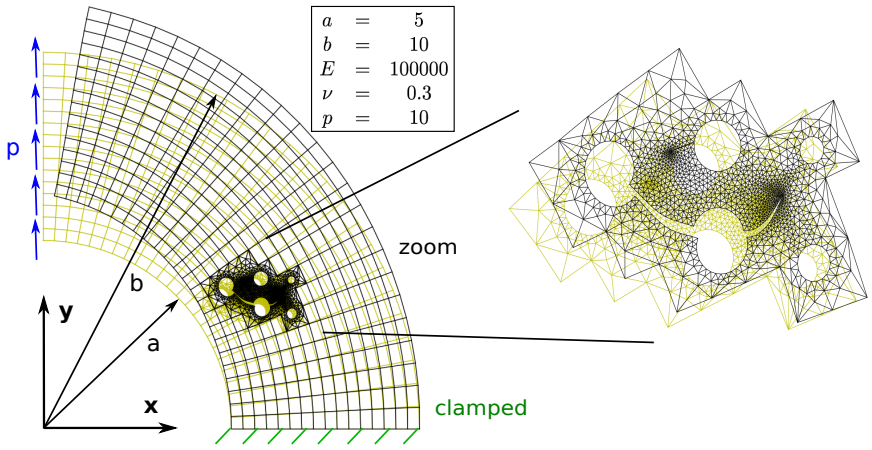

Figure 2.10 – Non-invasive introduction of holes and cracks in an initial 2D NURBS beam with the proposed hybrid global-IGA/local-FEM methodology. The yellow plot concerns the initial configuration while the black plot shows the deformed configuration (amplification factor 10).

attained coupled solution in terms of displacements and strains. The displacement is perfectly continuous at the coupling interface while a slight discontinuity appears on the strain plot, which is totally normal given the C^0 interface (note that the FE strain field plotted results from the use of a standard FE post-processing procedure for the derivative fields: a Gauss point based field is transformed into a nodal field, that is why no discontinuities are shown within the local FE model).

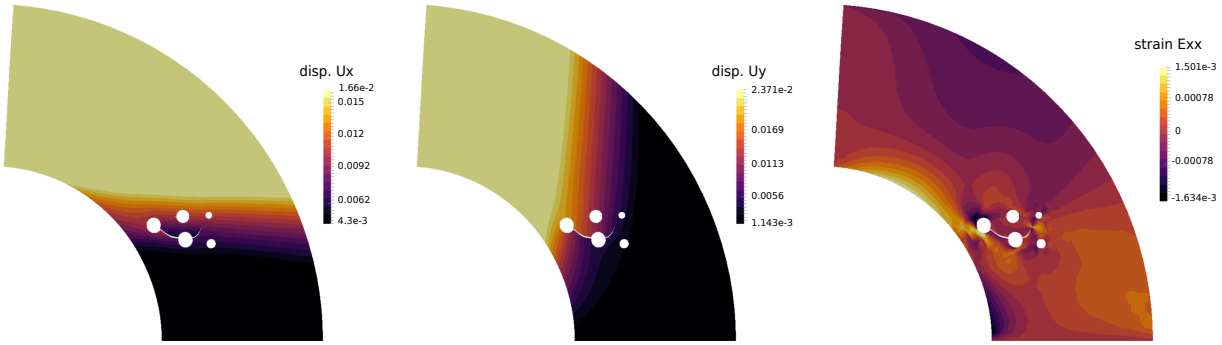

Figure 2.11 – Converged solution obtained with the hybrid IGA/FEM version of algorithm (2.20)-(2.21): (left) horizontal displacement; (middle) vertical displacement; (right) stain component ε_{xx}.

Stress Intensity Factor evaluation for an edge-cracked plate. As a second example, a 2D edge-cracked plate, as shown in Fig. 2.12(left), subjected to a uniform tensile stress is analysed. The crack size ($a = 1$) is very small in comparison with the lengths of the plate ($H = 17$ and $L = 7$), so the problem exhibits two different scales. Such a problem has already been studied in the context of non-invasive FE coupling (see, *e.g.*, [Passieux et al., 2013]). The reference value of the mode I Stress Intensity Factor (SIF) can be accurately approximated by the value that holds for an infinite plate, corrected by a factor depending on the ratio a/L:

$$K_I^{ref} = p\sqrt{a\pi}\left[1.12 - 0.231\frac{a}{L} + 10.55\left(\frac{a}{L}\right)^2 - 21.72\left(\frac{a}{L}\right)^3 + 30.39\left(\frac{a}{l}\right)^4\right]. \tag{2.28}$$

The non-invasive numerical model considered is illustrated in Fig. 2.12(middle). To model the behavior around the crack, we propose to make use of the well-established X-FEM method (in the context of usual FEM). More precisely, the local model is discretized by means of X-FEM triangles and an analytical domain, which contains the Williams' expansion [Réthoré et al., 2010b], is added at the crack tip. The interest of this

local modeling is that the stress intensity factors can be derived directly. For details regarding crack modelling, the interested reader is invited to consult [Passieux et al., 2013] and references cited therein. The local model is computed using the code of [Passieux et al., 2013]. Simultaneously, a quadratic 15×30 B-Spline mesh is used in our IGA code as the global model to compute the plate without the crack. This model is intended to be replaced around the crack by the local model described above (see, again, Fig. 2.12(middle)).

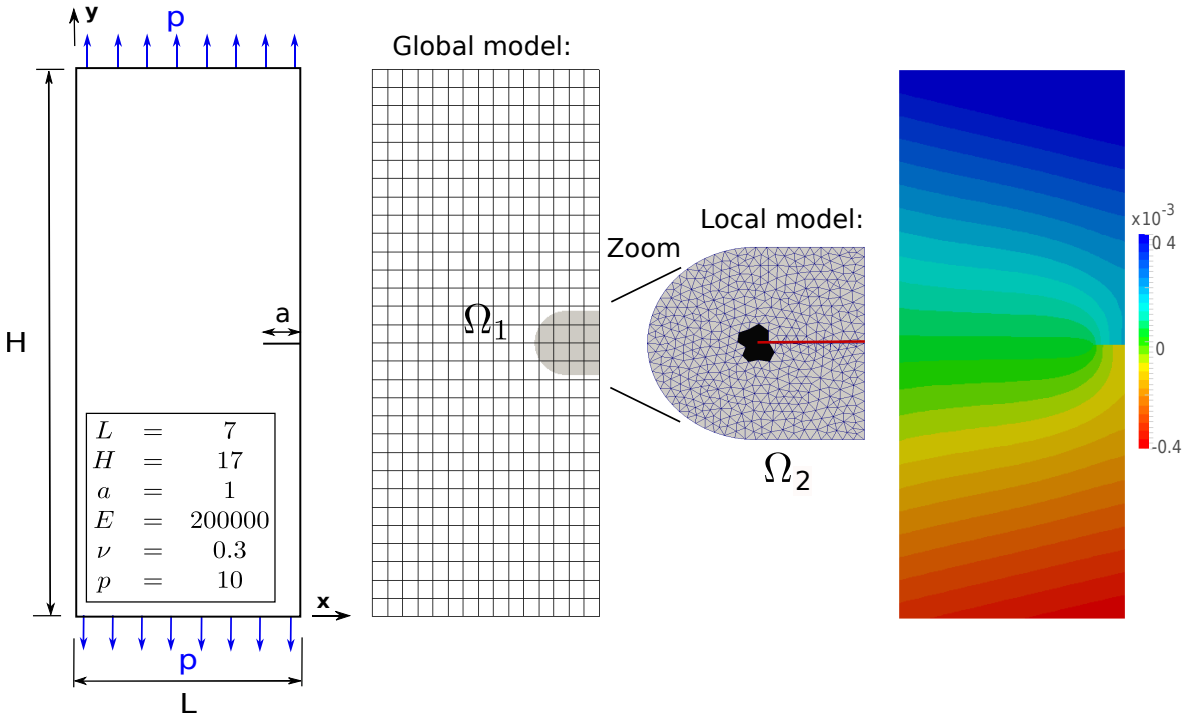

Figure 2.12 – Non-invasive analysis of an edge-cracked plate under uniaxial stress: (left) problem description; (middle) global quadratic B-Spline model (the local region in grey) and local model including X-FEM triangles (crack in red) and the analytical domain (black); (right) converged global/local solution (disp. u_y).

The vertical displacement obtained (once the non-invasive algorithm has converged) with the discretizations of Fig. 2.12(middle) is plotted in Fig. 2.12(right). A deformation similar to that in [Passieux et al., 2013] can be observed. In addition, the convergence behavior of the mode I SIF K_I with the non-invasive algorithm is shown in Fig. 2.13. We note that only five iterations are required to obtain the converged value with the Newton acceleration technique. For the discretization considered, a relative error of 0.08% on K_I with respect to K_I^{ref} (Eq. (2.28)) is reached.

Remark. *Once again, it has to be noticed that the approach of Fig. 2.9 was not followed here. Conversely, a non-conforming coupling strategy was used to connect the global and local models (see section 3.2 for handling properly non-conforming interfaces). However, we emphasize that the same procedure as in Fig. 2.9 could have been used for more simplicity and would have provide equivalent accuracy. The interest of this test case is to show the potential of using a global-IGA/local-FEM modeling for performing efficient multiscale simulations.*

Summary and discussion. These preliminary results account for the robustness and interest of the developed automatic procedure to connect IGA and FEM in a global/local manner. The strategy can be interpreted as an extension of the non-invasive coupling procedure proposed to handle non-conforming interfaces in the FEM framework (see section 1.3), which has been possible by making use of the previ-

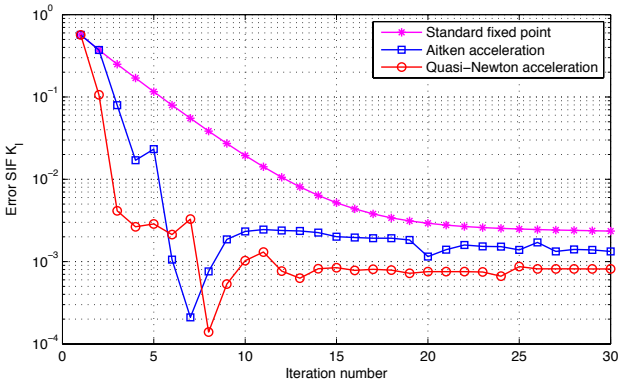

Figure 2.13 – Convergence of the SIF K_I during the non-invasive algorithm.

ously developed IGA-FEM bridge (see chapter 1 and [Tirvaudey et al., 2019a]). We end up with an hybrid IGA/FEM (non-matching coupling) strategy that draws up the best of each analysis technology: the global (regular) response of the structure is efficiently captured by the isogeometric basis while an existing robust FE code is used to compute local (possibly singular) phenomena. The method is fully non-invasive in the sense that it is non-invasive both in terms of coupling and of construction of the operators from standard FE ones. Although only elasticity results are shown, it may be emphasized that the extension to incorporate non-linear local FE models is straightforward. Further investigations demonstrating the attractiveness of performing non-invasive global-IGA/local-FEM simulations are in progress. Moreover, since the established strategy allows for easy merging of robust conventional FE codes with newly developed isogeometric codes, it may foster, in our opinion, the integration of IGA in the industrial engineering world.

3.2 A robust algorithm for non-conforming global/local IGA

We close this chapter by addressing the isogeometric non-invasive global/local coupling along a (geometrically) non-conforming interface (see once again Fig. 2.4(bottom-left) for the coupling situation). More precisely, the interaction of two non-conforming linear elastic spline meshes is considered: one domain is the foreground and defines the local model, the other is the background and constitutes the global spline model to be enriched. Special care is taken to handle the most general situations we may encounter. This results in a local mesh that is truly independent from the underlying global spline discretization. This work has been performed quite recently in collaboration with Pr. J.-C. Passieux. A deeper insight regarding the proposed methodology can be found in [Bouclier and Passieux, 2018], from which this part is extracted.

3.2.1 Idea

As introduced in sections 1.2 and 3.1, the standard FEM and first isogeometric versions of the non-invasive strategy come with a Lagrange multiplier based coupling method. As stated in section 1.2, the performance of these techniques is closely related to the compatibility between the approximation subspaces considered for the primal and the dual variables, especially in case of IGA [Brivadis et al., 2015, Dittmann et al., 2019]. In the more general case of arbitrary, non-conforming coupling configurations, this may rule out many convenient choices for the subspaces. As a result, Nitsche-based couplings seem to have been preferred in the field of immersed boundary methods. Nitsche formulations ensure variational consistency by introducing flux terms along the coupling interface expressed by primal unknowns of the coupling domains. Thus, the method is free of auxiliary fields, which simplifies the theory. Nevertheless, in its widespread symmetric version (see, *e.g.*, [Annavarapu et al., 2012, Nguyen et al., 2014, Ruess et al., 2014,

Elfverson et al., 2019, Buffa et al., 2019]), additional stabilization terms are required to ensure coercivity of the formulation. Appropriate estimates of the stabilization parameters involving to solve an additionnal eigenvalue problem (whose resolution can be performed locally per element [Jiang et al., 2015]) are generally involved, which may appear delicate from an algorithmic viewpoint. Therefore, there has been an increasing interest these last years in developing methods without such mesh-dependent stabilization parameters [Baiges et al., 2012, Kollmannsberger et al., 2015].

In this context, the non-symmetric version of the Nitsche method has recently reemerged in [Schillinger et al., 2016a] for isogeometric immersed methods. Originally introduced as a discontinuous Galerkin method [Oden et al., 1998, Rivière et al., 2001, Arnold et al., 2002], it is based on variationally consistent numerical flux conditions that are introduced in such a way that the criterion for stability is (weakly) satisfied. Therefore, it does not require the introduction of additional stabilization terms in contrast to its symmetric counterpart and thus, its performance does not rely on an appropriate estimation of additional sensitive parameters. We also note that similar ideas are present in the literature under the naming of skew-symmetric coupling (see, *e.g.*, the Variational Theory of Complex Rays [Ladeveze et al., 2001]). The object of this section is to further improve the initial non-invasive approach by extending it to incorporate the non-symmetric Nitsche coupling.

3.2.2 Theory

Initial weak form. Unlike Mortar-based approaches, the stiffness operators of the different subdomains are merged together in the Nitsche coupling technique, which eliminates the need of additional degrees of freedom. Both the interface Dirichlet and Neumann conditions (2.2) are enforced in a weak sense. More precisely, the non-symmetric Nitsche coupling formulation associated to the reference global/local problem (2.1)-(2.2) (as a reminder, see Fig. 2.2(b) for illustration) reads: find $u_{11} \in \mathscr{U}_{11}$ and $u_2 \in \mathscr{U}_2$ such that:

$$\sum_{\mathrm{m}\in\{11,2\}} a_{\mathrm{m}}(u_{\mathrm{m}}, v_{\mathrm{m}}) + \int_\Gamma \{C\varepsilon(v)\}\, n_{11}\cdot[\![u]\!]\mathrm{d}\Gamma - \int_\Gamma [\![v]\!]\cdot\{\sigma\}\, n_{11}\mathrm{d}\Gamma = \sum_{\mathrm{m}\in\{11,2\}} l_{\mathrm{m}}(v_{\mathrm{m}}),\ \forall (v_{11}, v_2) \in \mathscr{V}_{11}\times\mathscr{V}_2, \quad (2.29)$$

where the same notations as in section 1.2 are used. In addition, the jump and average operators are introduced, respectively, as follows:

$$[\![u]\!] = (u_{11} - u_2)\ ; \quad (2.30a)$$

$$\{\sigma\} = \frac{1}{2}(\sigma_{11}+\sigma_2) = \frac{1}{2}(C_{11}\,\varepsilon(u_{11}) + C_2\,\varepsilon(u_2)) \quad \text{and} \quad \{C\varepsilon(v)\} = \frac{1}{2}(C_{11}\,\varepsilon(v_{11}) + C_2\,\varepsilon(v_2)). \quad (2.30b)$$

In view of carrying out a consistency study of the coupling method, another formulation can be written. Indeed, integrating by parts and bringing all terms on the left-hand side, we can write:

$$-\sum_{\mathrm{m}\in\{11,2\}}\int_{\Omega_{\mathrm{m}}} v_{\mathrm{m}}\cdot\left(\mathrm{div}(\sigma_{\mathrm{m}}) + f^g_{\mathrm{m}}\right)\mathrm{d}\Omega + \sum_{\mathrm{m}\in\{11,2\}}\int_{\Gamma_{F_{\mathrm{m}}}} v_{\mathrm{m}}\cdot\left(\sigma_{\mathrm{m}}\, n_{\mathrm{m}} - F^g_{\mathrm{m}}\right)\mathrm{d}\Gamma \quad (2.31a)$$

$$+\int_\Gamma \frac{1}{2}C_{11}\varepsilon(v_{11})\, n_{11}\cdot(u_{11}-u_2)\,\mathrm{d}\Gamma + \int_\Gamma v_{11}\cdot\frac{1}{2}(\sigma_{11}-\sigma_2)\, n_{11}\mathrm{d}\Gamma \quad (2.31b)$$

$$+\int_\Gamma \frac{1}{2}C_2\varepsilon(v_2)\, n_{11}\cdot(u_{11}-u_2)\,\mathrm{d}\Gamma + \int_\Gamma v_2\cdot\frac{1}{2}(\sigma_{11}-\sigma_2)\, n_{11}\mathrm{d}\Gamma = 0. \quad (2.31c)$$

Expression (2.31) will be of interest to highlight the physical meaning of the developed algorithm (see below). We note at this stage that terms (2.31a) represent the mechanical equilibrium of each subdomain Ω_{m} while terms (2.31b) and (2.31c) correspond to the non-symmetric Nitsche enforcement of the coupling conditions (2.2). It can be proven that the formulation is variationally consistent with respect to the strong form of the initial problem (2.1)-(2.2), that the criterion for stability is (weakly) satisfied and that the method converges with optimal rates in the strain energy norm [Riviere, 2008, Burman, 2011].

Remark. *The average operator in Eq. (2.30b) is chosen to be the mean of the traction forces of the coupled domains. Any convex combination can actually be chosen without violating the consistency of the formulation [Hansbo, 2005, Bazilevs et al., 2012]. In particular, when there is an important contrast between the two materials to be coupled, one may adjust the convex combination to counterbalance the material gap and thus preclude the emergence of undesirable mesh locking phenomena [Sanders et al., 2012]. Such treatment has been performed in the non-invasive algorithm proposed hereafter to properly introduce a stiff inclusion within a soft B-Spline patch (see [Bouclier and Passieux, 2018]). In what follows, we keep the choice of (2.30b) for simplicity and we note that the two models to be coupled in the forthcoming numerical experiments will include similar material properties.*

Monolithic resolution. For ease of understanding of the next developments, let us first notice that Eq. (2.29) reads: find u_{11} and u_2 such that:

$$a_{11}(u_{11},v_{11}) - \int_\Gamma v_{11}\cdot\{\sigma\}\, n_{11}\mathrm{d}\Gamma + \int_\Gamma \frac{1}{2}C_{11}\varepsilon(v_{11})\, n_{11}\cdot[\![u]\!]\mathrm{d}\Gamma = l_{11}(v_{11}),\ \ \forall v_{11}\in\mathcal{V}_{11}\,; \tag{2.32a}$$

$$a_2(u_2,v_2) - \int_\Gamma v_2\cdot\{\sigma\}\, n_2\mathrm{d}\Gamma - \int_\Gamma \frac{1}{2}C_2\varepsilon(v_2)\, n_2\cdot[\![u]\!]\mathrm{d}\Gamma = l_2(v_2),\ \ \forall v_2\in\mathcal{V}_2. \tag{2.32b}$$

Resolution (2.32) of the coupling problem constitutes the classical monolithic approach: in other words, this is the counterpart of (2.7) using the non-symmetric Nitsche theory.

Construction of a non-invasive resolution algorithm. To start with, we propose for the resolution of (2.32) the following algorithm that enables to split the initial multi-domain problem into one problem over Ω_{11} and a second one over Ω_2. For the nth iteration, starting with initial guesses $u_{11}^{(0)}$ and $u_2^{(0)}$, we look for $u_{11}^{(n)}$ and $u_2^{(n)}$ such that:

1. Resolution of a problem over Ω_{11}:

$$a_{11}\left(u_{11}^{(n)},v_{11}\right) = l_{11}(v_{11}) + \int_\Gamma v_{11}\cdot\left\{\sigma^{(n-1)}\right\} n_{11}\mathrm{d}\Gamma - \int_\Gamma \frac{1}{2}C_{11}\varepsilon(v_{11})\, n_{11}\cdot[\![u^{(n-1)}]\!]\mathrm{d}\Gamma. \tag{2.33}$$

2. Resolution of a problem over Ω_2:

$$a_2\left(u_2^{(n)},v_2\right) - \int_\Gamma v_2\cdot\frac{1}{2}\sigma_2^{(n)}n_2\mathrm{d}\Gamma + \int_\Gamma \frac{1}{2}C_2\varepsilon(v_2)\, n_2\cdot u_2^{(n)}\mathrm{d}\Gamma = l_2(v_2) \tag{2.34a}$$

$$+\int_\Gamma v_2\cdot\frac{1}{2}\sigma_{11}^{(n)}n_2\mathrm{d}\Gamma + \int_\Gamma \frac{1}{2}C_2\varepsilon(v_2)\, n_2\cdot u_{11}^{(n)}\mathrm{d}\Gamma. \tag{2.34b}$$

A mechanical interpretation of the resulting iterative strategy will be given later in the section. Nevertheless, one may already notice that formulation (2.34) corresponds to the non-symmetric Nitsche weak imposition of the coupling conditions for subdomain Ω_2 only. Indeed, integrating by parts, and bringing all terms on the left-hand side, we find:

$$-\int_{\Omega_2} v_2\cdot\left(\mathrm{div}(\sigma_2^{(n)}) + f_2^g\right)\mathrm{d}\Omega + \int_{\Gamma_{F_2}} v_2\cdot\left(\sigma_2^{(n)}\, n_2 - F_2^g\right)\mathrm{d}\Gamma \tag{2.35a}$$

$$+\int_\Gamma \frac{1}{2}C_2\varepsilon(v_2)\, n_2\cdot\left(u_2^{(n)} - u_{11}^{(n)}\right)\mathrm{d}\Gamma + \int_\Gamma v_2\cdot\frac{1}{2}\left(\sigma_2^{(n)} - \sigma_{11}^{(n)}\right)n_2\mathrm{d}\Gamma = 0. \tag{2.35b}$$

The above equation clearly shows that, at each iteration of the proposed algorithm, the interface term (2.31c) is recovered from the initial coupling formulation.

We now switch to the matrix form for ease of reading with respect to the implementation of the method. From procedure (2.33)-(2.34), the only thing that remains to be done to truly reach a non-invasive algorithm

consists of recovering the initial global model over Ω_1 in Eq. (2.33). To this end, one may simply repeat the procedure of Eq. (2.19). This leads us to build the following non-invasive algorithm based on the non-symmetric Nitsche coupling. Reusing the notations introduced in section 1.2, the algorithm reads: for the nth iteration, starting with initial guesses $\mathbf{u}_1^{(0)}$ and $\mathbf{u}_2^{(0)}$, we look for $\mathbf{u}_1^{(n)}$ and $\mathbf{u}_2^{(n)}$ such that:

1. Resolution over Ω_1:

$$\mathbf{K}_1\mathbf{u}_1^{(n)} = \mathbf{f}_1 - \left(\overline{\mathbf{K}}_{11}^{N\,T} - \overline{\mathbf{K}}_{11}^{N}\right)\mathbf{u}_1^{(n-1)} - \left(\overline{\mathbf{K}}_{21}^{N\,T} - \overline{\mathbf{K}}_{12}^{N}\right)\mathbf{u}_2^{(n-1)} + \mathbf{r}_{12}^{(n-1)}. \tag{2.36}$$

2. Resolution over Ω_2:

$$\left[\mathbf{K}_2 + \left(\overline{\mathbf{K}}_{22}^{N\,T} - \overline{\mathbf{K}}_{22}^{N}\right)\right]\mathbf{u}_2^{(n)} = \mathbf{f}_2 - \left(\overline{\mathbf{K}}_{12}^{N\,T} - \overline{\mathbf{K}}_{21}^{N}\right)\mathbf{u}_1^{(n)}. \tag{2.37}$$

The different blocks of the Nitsche coupling operator are computed as follows:

$$\overline{\mathbf{K}}_{11}^{N} = \int_\Gamma -\frac{1}{2}\left(\mathbf{Z}_{11}\,\mathbf{H}_1\,\mathbf{B}_1\right)^T\mathbf{R}_1^T\,\mathrm{d}\Gamma\,; \tag{2.38a}$$

$$\overline{\mathbf{K}}_{12}^{N} = \int_\Gamma \frac{1}{2}\left(\mathbf{Z}_{11}\,\mathbf{H}_1\,\mathbf{B}_1\right)^T\mathbf{R}_2^T\,\mathrm{d}\Gamma\,; \tag{2.38b}$$

$$\overline{\mathbf{K}}_{21}^{N} = \int_\Gamma -\frac{1}{2}\left(\mathbf{Z}_{11}\,\mathbf{H}_2\,\mathbf{B}_2\right)^T\mathbf{R}_1^T\,\mathrm{d}\Gamma\,; \tag{2.38c}$$

$$\overline{\mathbf{K}}_{22}^{N} = \int_\Gamma \frac{1}{2}\left(\mathbf{Z}_{11}\,\mathbf{H}_2\,\mathbf{B}_2\right)^T\mathbf{R}_2^T\,\mathrm{d}\Gamma\,; \tag{2.38d}$$

where $\mathbf{R}_1$ and $\mathbf{R}_2$ represent the standard spline shape functions matrices, $\mathbf{B}_1$ and $\mathbf{B}_2$ are the standard spline strain-displacement operators, $\mathbf{H}_1$ and $\mathbf{H}_2$ model the Hooke constitutive law, and operator $\mathbf{Z}_{11}$ is introduced to perform the product between the stress tensor and the outward unit normal to Ω_{11} (see [Nguyen et al., 2014, Ruess et al., 2014] for more details regarding the construction of such operators).

As stated in section 2, specific quadrature rules need to be implemented in case of a global/local non-conforming interface to evaluate $\mathbf{r}_{12}$ (see again Eq. (2.22)). In order to do so, a large amount of techniques, mostly taken from immersed boundary methods, may be used: for instance, the standard sub-triangulation technique in the context of X-FEM [Moës et al., 1999], the technique used in the NURBS Enhanced FEM [Sevilla et al., 2008], the recursive quadrature approach applied in the FCM [Ruess et al., 2014, Schillinger and Ruess, 2015, Schillinger et al., 2016a], or more recent geometrically faithfull quadratures [Legrain, 2013, Nagy and Benson, 2015, Kudela et al., 2015, Fries and Omerovic, 2016, Stavrev et al., 2016, Fries et al., 2017], that can also be based on the moment fitting scheme [Müller et al., 2013, Joulaian et al., 2016, Hubrich et al., 2017, Hubrich and Düster, 2019]. In this work, for simplicity and robustness, we perform the recursive quadrature approach of FCM.

Remark. *It may be again emphasized here that the issue of ill-conditioning usually encountered in immersed methods [Dauge et al., 2015, Verhoosel et al., 2015, de Prenter et al., 2017] is circumvented with algorithm* (2.36)-(2.37). *Indeed, the initial global stiffness operator, which is symmetric and well-conditioned, is involved in* (2.36) *(instead of the cut global model over* Ω_{11}*). According to us, this feature is another attractiveness of our algorithm and such an idea may be of interest to solve the ill-conditioning issue in a more general cut finite element context [Burman et al., 2015, Schillinger and Ruess, 2015].*

Incremental formulation and mechanical interpretation. Another incremental formulation of the non-invasive algorithm (2.36)-(2.37) can be derived for a better understanding of the numerical procedure. This alternative formulation is directly given in the following. The interested reader is urged to consult [Bouclier and Passieux, 2018] for more details.

Denoting by $\mathbf{r}^N$ the Nitsche-based discrete reaction forces at Γ applied to the global model in Eq. (2.36):

$$\mathbf{r}^N = \left(\overline{\mathbf{K}}_{11}^{N\,T} - \overline{\mathbf{K}}_{11}^{N}\right)\mathbf{u}_1 - \left(\overline{\mathbf{K}}_{21}^{N\,T} - \overline{\mathbf{K}}_{12}^{N}\right)\mathbf{u}_2, \tag{2.39}$$

and reusing the discrete reaction forces $\mathbf{r}_{11}$ of Eq. (2.24), procedure (2.36)-(2.37) can actually be rewritten as follows: for the nth iteration, starting with initial guess $\mathbf{u}_1^{(0)}$, we look for $\mathbf{u}_1^{(n)}$ such that:

$$\mathbf{u}_1^{(n)} = \mathbf{u}_1^{(n-1)} - \mathbf{K}_1^{-1}\mathbf{g}\left(\mathbf{u}_1^{(n-1)}\right), \tag{2.40}$$

where the application $\mathbf{g}$ is defined as:

$$\mathbf{g}\left(\mathbf{u}_1^{(n-1)}\right) = \mathbf{r}^{N(n-1)} + \mathbf{r}_{11}^{(n-1)}, \tag{2.41}$$

provided the local solution $\mathbf{u}_2^{(n-1)}$ in $\mathbf{r}^{N(n-1)}$ is computed from $\mathbf{u}_1^{(n-1)}$ through system (2.37) (expressed at iteration $n-1$). Formulation (2.40) exhibits that the iterative procedure simply consists in a fixed point aiming at solving $\mathbf{g} = \mathbf{0}$. The non-invasive residual (2.23) thus becomes here:

$$\eta^{(n)} = \frac{||\mathbf{r}^{N(n)} + \mathbf{r}_{11}^{(n)}||_2}{\sqrt{||\mathbf{f}_1||_2^2 + ||\mathbf{f}_2||_2^2}}. \tag{2.42}$$

Moreover, writing the continuous version of Eq. (2.41), we literally find:

$$g\left(u_1^{(n-1)}\right) = \int_\Gamma \frac{1}{2} C_{11}\varepsilon(v_{11})\, n_{11} \cdot \left(u_1^{(n-1)} - u_2^{(n-1)}\right) \mathrm{d}\Gamma - \int_\Gamma v_1 \cdot \frac{1}{2}\left(\sigma_1^{(n-1)} + \sigma_2^{(n-1)}\right) n_{11}\,\mathrm{d}\Gamma + \int_\Gamma v_1 \cdot \sigma_1^{(n-1)} n_{11}\,\mathrm{d}\Gamma, \tag{2.43}$$

which corresponds to the consistency term (2.31b) of the initial Nitsche coupling formulation. Therefore, the proposed iterative strategy aims at ensuring the coupling conditions for subdomain Ω_{11} in a non-symmetric Nitsche weak sense. In addition, reminding that the other interface consistency term (2.31c) is enforced at each iteration of the non-invasive procedure through the local problem (2.37) (see term (2.35b) that corresponds to the coupling conditions related to domain Ω_2), we ensure that if the proposed algorithm is convergent, all the interface terms of the initial Nitsche coupling formulation (2.31) are recovered. This numerical procedure is original and its mechanical interpretation is quite different from the standard non-invasive strategies that aim at recovering the interface forces equilibrium provided that the Dirichlet conditions (over Γ) are transmitted, at each iteration, form the global to the local problem through the use of a Lagrange multiplier field (see again section 1.2).

Although it is different from the existing non-invasive strategies in its mechanical interpretation, the algorithm can still be interpreted as a modified Newton method prescribed on $\mathbf{g} = \mathbf{0}$ (it can be shown that $\nabla\mathbf{g}^{-1} \approx \mathbf{K}_1^{-1}$ in Eq. (2.40)). As a consequence, the application of the same acceleration techniques as the ones usually performed in the context of non-invasive Lagrange multiplier coupling appears straightforward. In particular, a Quasi-Newton method can be used (see, *e.g.*, [Gendre et al., 2009, Duval et al., 2016]) to deeply accelerate the speed of the algorithm and to make it convergent even in challenging situations (see forthcoming numerical experiment).

3.2.3 Example: Infinite plate with a circular hole

To assess the performance of the developed algorithm (2.36)-(2.37), a series of two-dimensional elastic benchmarks involving conforming and non-conforming couplings, along straight, curved, and bi-material interfaces have been investigated in [Bouclier and Passieux, 2018]. In this manuscript, only the numerical experiments related to the introduction of a geometrical detail within a B-Spline patch are presented. Once again, the interested reader is referred to [Bouclier and Passieux, 2018] for further numerical proofs regarding the performances of the algorithm.

Description of the test case and non-invasive analysis. More precisely, we consider here the popular test case of an infinite plate with a circular hole under in-plane tension. The geometry, material, boundary conditions and the analytical stress solution [Saad, 2009] are given in Fig. 2.14. The hole constitutes the geometrical detail to be incorporated. The discretization of the problem following the developed non-invasive strategy is illustrated in Fig. 2.15(a). A regular B-Spline mesh is used for the plate without the hole (domain Ω_1) and a circular refined ring-shaped NURBS domain is constructed, as the local model, for an accurate representation of the stress concentration around the hole. The case of a geometrical non-conforming interface is met, as desired. 6 levels of recursive quadrature sub-cells [Schillinger and Ruess, 2015] are employed to ensure accuracy with regard to the evaluation of $\mathbf{r}_{12}$ (see Figs. 2.15(b) and 2.15(c)). Finally, To integrate over the non-conforming interface, we refine the NURBS interface Γ irrespective of the underlying global and local meshes.

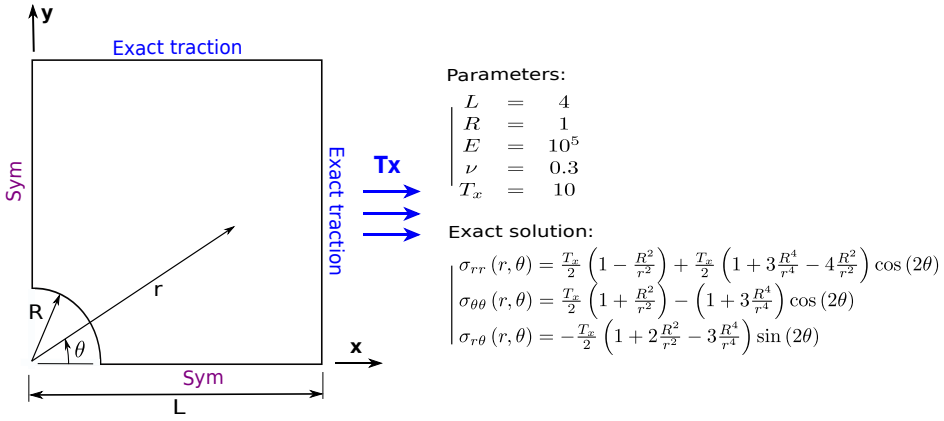

Figure 2.14 – Infinite plate with a hole: description and data of the problem.

The results obtained with algorithm (2.36)-(2.37) and the discretization of Fig 2.15(a) are shown in Figs. 2.15(d) and 2.15(e) in terms of stress and non-invasive convergence, respectively. Removing the smooth non-physical fictitious prolongation in Ω_{12}, and replacing part of it by the local solution in Ω_2, the resulting global/local solution appears smooth and to be in good agreement with results obtained using NURBS fitted discretizations [Hughes et al., 2005, Cottrell et al., 2009]. Regarding the convergence of the proposed algorithm, the Quasi-Newton acceleration technique seems to be necessary on this test case. This may be expected here since the stiffness gap between domains Ω_{12} and Ω_2 is significant. Taking the advantage of the Quasi-Newton update, we are able to make the number of iterations relatively low: a residual of 10^{-4} is obtained in about 20 iterations.

Finite element convergence of the method. The finite element convergence of the method when applied to this non-conforming scenario is then investigated (see Figs. 2.16 and 2.17). 2^{nd}, 3^{rd} and 4^{th}-order spline shape functions are considered for both of the global and local models. The different meshes of Fig. 2.16 are built for the numerical study. They correspond to several uniform refinements starting from a mesh of 3×3 B-Spline elements for the global model and 2×2 NURBS elements for the local model. We insist here that our interest is to assess the finite element convergence of the method and not the global/local modeling. The corresponding convergence curves obtained with the error in the energy norm are plotted in Figs. 2.17(a) and 2.17(b) for the proposed Nitsche-based strategy and for the standard Lagrange multiplier based strategy (see Eqs. (2.20)-(2.21)). A pragmatic strategy is adopted to build the space for the Lagrange multiplier field: it is the trace along the interface of the local shape functions.

The Lagrange multiplier approach appears to fail to reproduce the optimal convergence rates, especially when increasing the polynomial order of the spline shape functions. The reason for this poor accuracy may be due to the non-conforming situation encountered which rules out the practical choice adopted for the dual subspace. Conversely, without any additional specific treatment, the proposed

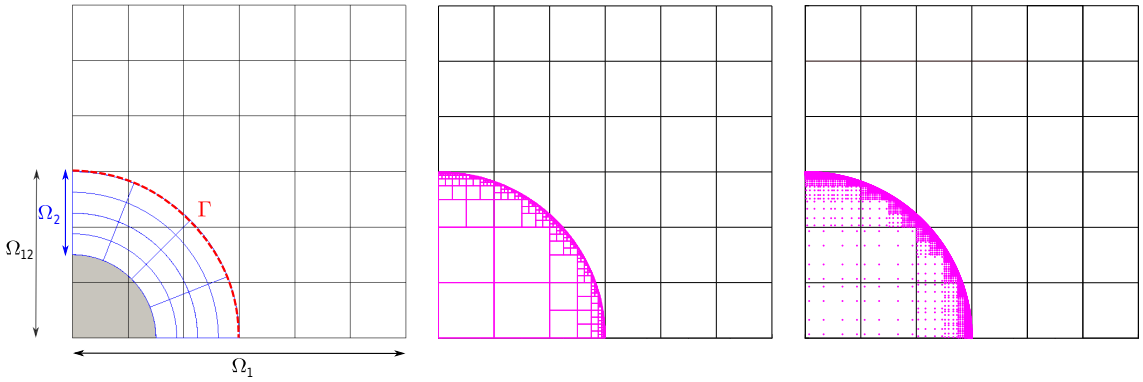

(a) Discretization of the coupled problem.

(b) Adaptive sub-cells for integration over Ω_{12}.

(c) Corresponding quadrature points.

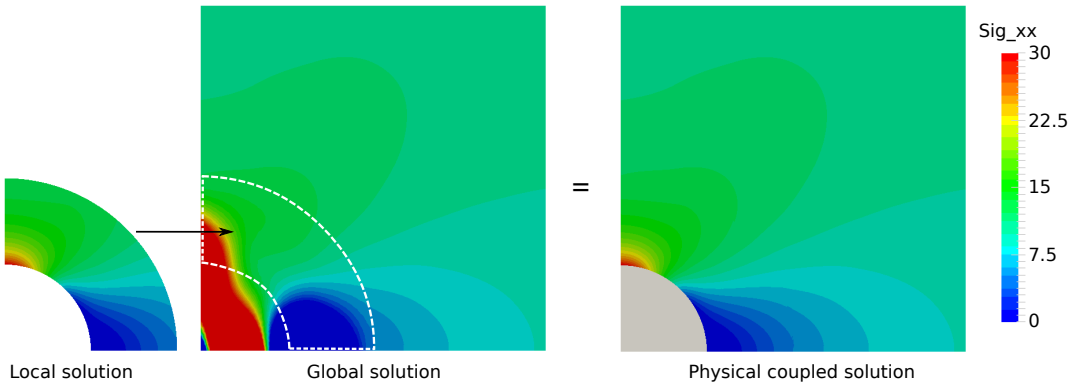

(d) Normal stress σ_{xx}.

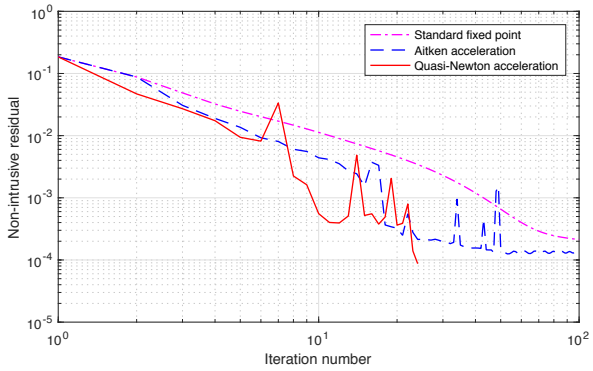

(e) Convergence of the iterative strategy: non-invasive residual.

Figure 2.15 – Global/local non-invasive Nitsche analysis of the infinite plate with a hole (rectangular B-spline mesh of cubic 6×6 elements for Ω_1, recursive Gaussian [Schillinger and Ruess, 2015] quadrature with 6 levels of sub-cells for Ω_{12}, and circular NURBS mesh of cubic 4×4 elements for Ω_2).

non-symmetric Nitsche version seems to achieve the optimal rates of convergence, which demonstrates that the methodology does not interfere with the accuracy of the spline functions regardless of the coupling scenario encountered. Note that for the finest quartic coupling discretization, the error level is so low that it may be deteriorated by rounding errors.

Remark. *Let us eventually underline that the extension of Nitsche-based methods to material non-linearities (*e.g.*, plasticity or damage) does not have an obvious way forward. Indeed, the definition of*

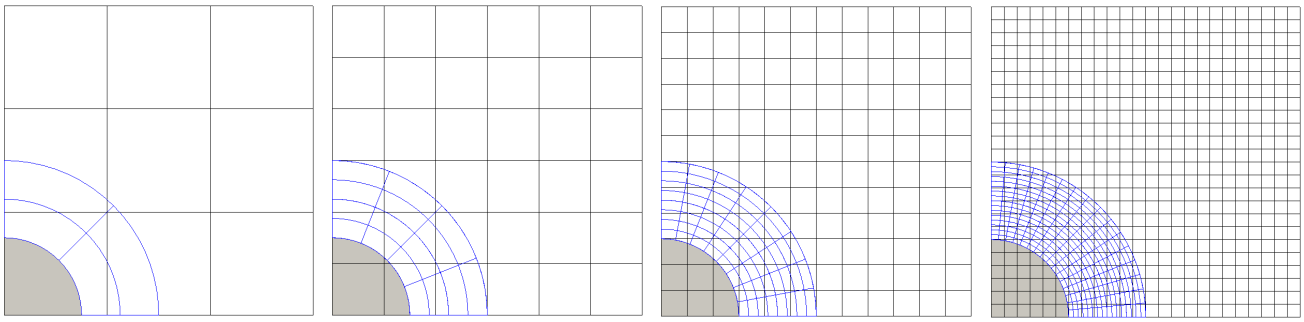

Figure 2.16 – Sequence of meshes considered for the convergence study.

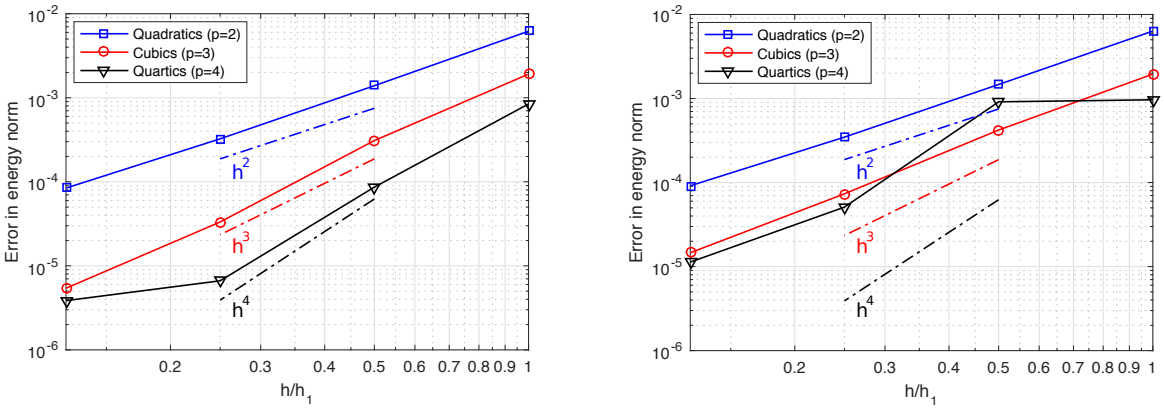

(a) Non-invasive Nitsche strategy.

(b) Standard non-invasive Lagrange strategy.

Figure 2.17 – Convergence curves in energy norm for the infinite plate with a hole.

the virtual mean interface resultant force appears delicate in this context (see right term of Eq. (2.30b)*). Nevertheless, what can be done in our case of global/local modeling is to take a local region that is large enough so that the local non-linearity does not play a major role at interface* Γ*. As a result, we end up with a coupling in a region where both models can be assumed to be linear elastic, thus making able to use the present approach without any additional ingredients.*

Summary and discussion. These results clearly indicate the superiority of the proposed non-symmetric Nitsche non-invasive approach when addressing any arbitrary non-conforming situation: we always achieve optimal accuracy while the standard Lagrange version appears to fail to reproduce optimal behavior in some situations. In addition, mesh locking was reported in [Bouclier and Passieux, 2018] when coupling at a severe bi-material interface with the standard Lagrange multiplier method whereas the Nitsche counterpart handled successfully such interfaces thanks to the use of a suitable averaging operator. The developed method thus appears particularly suitable to compute any evolution of a local model within a fixed global isogeometric one. The reason for this is the robustness and simplicity of the coupling: it is (1) free of auxiliary fields which enables to circumvent the difficulty of choosing a suitable dual space, and (2) intrinsically stable, thus eliminating the need for additional stabilization terms with appropriate parameters. From an engineering point of view, this may be of great interest since in many applications it is necessary to solve a sequence of similar problems, in a multiresolution process, where only the behavior at a local scale needs to be updated (*e.g.*, to carry out the shape optimization of local entities [Mulani et al., 2013, Fußeder et al., 2015, Hirschler et al., 2019b], or to perform the identi-

fication of local mechanical parameters [Passieux et al., 2015a, Réthoré, 2015], or to model crack propagation [Passieux et al., 2013], or the expansion of a plastic zone [Gendre et al., 2009, Duval et al., 2016], a damage zone [Guinard et al., 2018], etc). In particular, we will see in chapter 6 that the algorithm can be efficiently integrated into an optimization loop for performing structural design, which simplifies the optimization process and ensures computational time saving.

Finally, let us highlight that such a non-invasive procedure provides an iterative resolution of an immersed problem while circumventing the conditioning issue. As a result, combining it with some recent FE non-invasive techniques that enable parallel computations while considereing non-linear constitutive laws [Duval et al., 2016, Oumaziz et al., 2018] may open the door for efficient iterative solution strategies in the field of immersed methods, which represents today a real challenge [de Prenter et al., 2017, Badia and Verdugo, 2018, Jomo et al., 2019]. Corresponding investigations are in progress to accurately and efficiently compute, in the non-linear regime, heterogeneous microstructures coming from image data.

CHAPTER 3

A domain decomposition solver for multipatch isogeometric shells

Contents

We are interested in this third chapter in the efficient and accurate computation of global aeronautic-type structures: *i.e.*, broadly speaking, made of complex curved stiffened panels [Totaro and Nicola, 2012, Shroff et al., 2017, Guinard et al., 2018]. These structures are obtained by the assembly of a main part (usually denoted by the skin or the panel) with subparts as stringers and ribs (the stiffeners). The fastening of the stiffeners with the panel gives a final structure with a high stiffness to weight ratio. Based on the work performed in this chapter, innovative stiffened panels with improved structural properties will be designed in chapter 6 using a proper optimization framework.

In order to do so, we seek to employ IGA which has proved to be highly relevant for the fields of shell analysis and shape optimization (see [Kiendl et al., 2009, Echter et al., 2013, Kiendl et al., 2015, Maurin et al., 2018] for Kirchhoff-Love, [Benson et al., 2010, Echter et al., 2013, Dornisch et al., 2013, Kikis et al., 2019] for Reissner-Mindlin, [Hosseini et al., 2013, Bouclier et al., 2013b, Cardoso and Cesar de Sa, 2014, Bouclier et al., 2015b, Caseiro et al., 2015, Bouclier et al., 2015a] for solid-shell theories and [Wall et al., 2008, Nagy et al., 2013, Kiendl et al., 2014, Fußeder et al., 2015, Bandara and Cirak, 2017, Hirschler et al., 2019c] for solid and shell shape optimization, to name a few). More precisely, since stiffened structures are built with thin shells, we focus on isogeometric Kirchhoff–Love shell elements [Kiendl et al., 2009, Echter et al., 2013], for which IGA is even more attractive since it naturally satisfies the C^1 requirement of such formulations. This enables to derive a rotation-less

shell formulation, thereby minimizing the number of DOF. In this context, the challenge faced concerns the analysis of non-conforming multipatch isogeometric shell models since a single B-Spline or NURBS patch cannot represent stiffened structures. More importantly, we are interested in having an independent discretization between the panel and the stiffeners to simplify the definition of the design space for the optimization.

After reminding some main aspects about multipatch discretizations, we first introduce (i) a new Mortar coupling formulation for Kirchhoff-Love shells to answer the issue. Then, step-by-step we build (ii) a dual domain decomposition solver for the iterative resolution of the coupling. In the same idea of what was performed in previous chapter, the solver appears to us more appropriate in a multiresolution context, such as during shape optimization since it allows to factorize once for all the stiffness matrices of patches located in non-design regions. From a conceptual point of view, a parallel can actually be drawn between this chapter and the previous one, as will be demonstrated in the following with several references to chapter 2. This work has been achieved in the PhD thesis of Thibaut Hirschler [Hirschler, 2019], who I co-supervised from Toulouse with Pr. T. Elguedj at INSA Lyon, and has been published in [Hirschler et al., 2019a, Hirschler et al., 2019b]. The interested reader is advised to consult these references for further details on this topic.

1 Isogeometric non-conforming multipatch analysis

As stated in chapter 1, the analysis of multipatch isogeometric models is currently the object of intensive studies since it represents one of the challenges to truly bridge the gap between CAD and Analysis. Focusing on shell structures, it is actually one of the two key issues (with trimming) to be addressed since the Boundary representation (B-rep) of surfaces is directly available in CAD.

1.1 Multipatch geometric models

As outlined in chapter 1, the prerequisites for the geometric modeling and for the numerical simulation are different. As a result, an automatic transfer from a spline-based CAD model to an analysis-suitable model is still not straightforward, even with the concept of IGA. More specifically, because again of the rigid tensor product structure of (standard) multivariate spline basis, a single B-Spline or NURBS patch cannot represent complex industrial structures, even in case of shells whose geometry is simply derived from a surface. Instead, multiple (possibly trimmed) spline patches are required where each of them describes a specific part of the overall structure. Multipatch modeling appears thus inevitable when dealing with structures with non-trivial geometries using IGA. The main issue from an analysis point of view concerns the treatment of the junctions between those patches. Figure 3.1 illustrates the problematic. In particular, an example of stiffened structure's geometry is given in Fig. 3.1(right). The difficulty lies in the fact that geometric modeling does not pay a special attention to the presence of multiple patches: each patch is defined independently. The parametrization of one patch is not defined under a particular constraint due to any other patches. It leads to patch interfaces with non-matching or even non-conforming properties.

Regarding the coupling terminology, we recycle the nomenclature introduced in previous chapter (see section 1.2 and Fig. 2.4) and adapt it to the case of isogeometric patch coupling:

- it is *matching* when the discretizations are exactly the same on both sides of the interface ;
- it is conforming but *non-matching* when the interface is aligned with the edges of the patches but the control points on both sides do not match ;
- it is *non-conforming* when some elements are overlapped by the interface.

Spline-based CAD models seldom, if ever, have matching interfaces. Depending on the geometry, isogeometric modeling can lead to non-matching interfaces as depicted in Fig. 3.1(left). But in the more general case, non-conforming interfaces between the patches are to be expected (see Fig. 3.1, right).

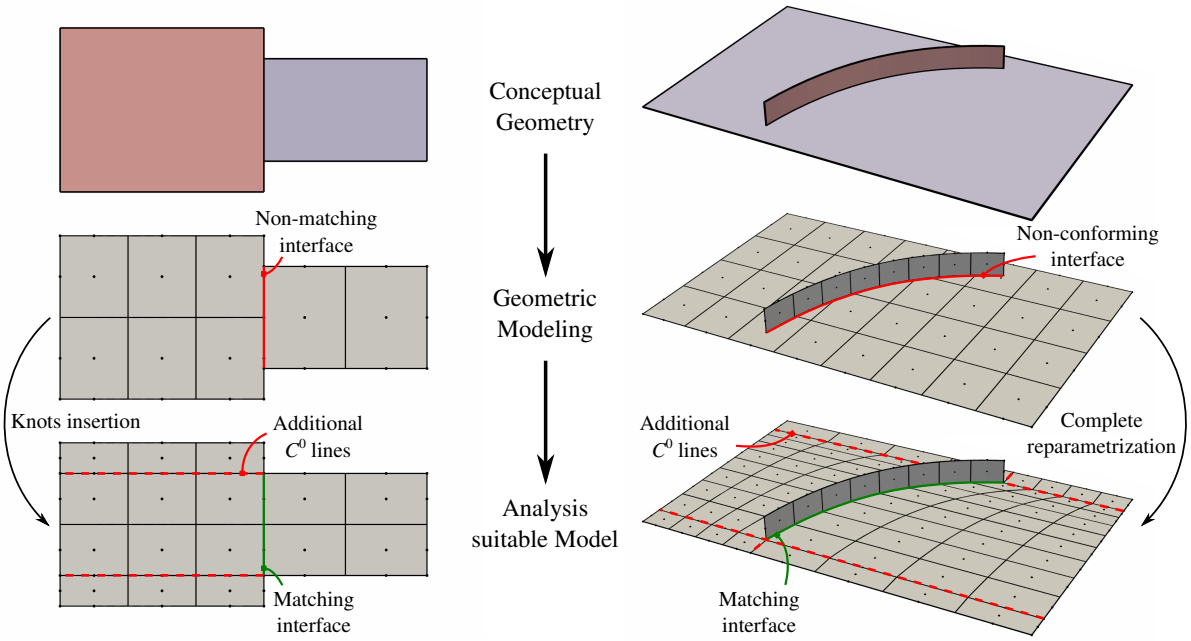

Figure 3.1 – B-Spline and NURBS modeling generate multipatch geometries where each patch represents a specific part of the complete structure. Naturally, these patches undergo non-matching or even non-conforming parametrizations at their interfaces. Additional cumbersome procedures are required to get a final (standard) analysis-suitable model with conforming and matching interfaces.

1.2 Analysis-suitable models

For the analysis of multipatch models, two approaches can be classified. Similarly as for solving an isogeometric global/local problem (see section 2.1 and Fig. 2.8(a)), the first approach consists in calling upon **spline re-parametrization procedures** to transform the patch junctions into fully matching interfaces [Maquart, 2019]. As stated previously, this task is far from trivial in practice. In the simplest case of a non-matching but conforming interface (see Fig. 3.1, left), knot-insertion (or removal) and degree elevation (or reduction) allow to comply the requirement for obtaining a matching interface. However, transforming non-conforming interfaces into fully matching interfaces is much trickier (see Fig. 3.1, right). It cannot be done by invoking the fundamental geometric algorithms (knot-insertion, degree-elevation, etc.) as for the non-matching case. Instead, a complete re-parametrization has to be performed since the local changes introduced to reach a matching interface have a global influence on the whole discretization. As an illustration, despite its simple in-plane rectangular shape, the panel of Fig. 3.1(right) needs to be decomposed into six patches to get an overall parametrization with a matching interface. The problem stems from the fact that this re-parametrization can hardly be automated.

In contrast, the second option for analyzing multipatch models consists in developing **advanced numerical tools** for coupling the non-conforming patches. In this work, we follow this path because it appears more appropriate in a multiresolution context, as will be seen later in chapter 6. In particular, we want to avoid modifying the parametrization of the whole model at every iteration of an optimization process (for instance, we seek to leave the discretization of the panel unchanged if only the position and shape of the stiffener are to be optimized). Otherwise, this would lead to a too cumbersome method to be able to perform shape optimization properly and in a reasonable time.

Remark. *Since our focus is on stiffened structures, the notion of non-conforming interface as depicted in Fig. 3.1(right) is less general than in previous chapter (see,* e.g.*, Fig. 2.4(bottom-left) for illustration). Indeed, here, we do not need to consider trimmed patches at the coupling interface in the sense that some parts of the two patches to be coupled are removed. As will be shown in section 4 and later in chapter 6, the "non-conforming" modeling of Fig. 3.1(right) appears sufficient to design advanced aeronautical stiffened structures, that is why we did not investigate trimmed IGA in this work. However, we quote that extending the proposed approach to real trimmed IGA may be of great interest for a wider range of applications. In what follows, we refer to the situation of Fig. 3.1(right) when we employ the terminology "non-conforming" to characterize the shell interface.*

2 Mortar coupling for Kirchhoff-Love shells

We now truly address the analysis of isogeometric multipatch Kirchhoff-love shells in view of simulating stiffened structures. We develop a new Mortar approach which involves two sets of Lagrange multipliers in order to impose the continuity of the mid-surface displacement and of the rotation of the shell. After explaining why we choose a Mortar approach to formulate the coupling, the basics of the standard isogeometric Kirchhoff-Love shell formulation are given before the Mortar method is built and assessed through preliminary numerical examples.

2.1 Motivation

As seen in previous chapter, various schemes based on weak couplings have been proposed these last years to connect arbitrary isogeometric domains. Focusing now on shell analysis, both of the three main methods have been recenlty investigated (see, *e.g.*, [Apostolatos et al., 2014a, Breitenberger et al., 2015, Herrema et al., 2019] for penalty coupling, [Dornisch et al., 2017, Sommerwerk et al., 2017, Duong et al., 2017, Hirschler et al., 2019b, Schuß et al., 2019, Hirschler et al., 2019a] for Mortar coupling and [Guo and Ruess, 2015, Guo et al., 2017, Nguyen-Thanh et al., 2017, Guo et al., 2018] for Nitsche coupling). Given its ability to model thin structures and its low computational cost, we remind that we consider more precisely the isogeometric Kirchhoff–Love shell formulation [Kiendl et al., 2009, Echter et al., 2013]. Penalty [Herrema et al., 2019], Mortar [Schuß et al., 2019] and Nitsche [Guo et al., 2018] methods have been successfully applied for large and complex industrial Kirchhoff-Love structures, even for non-linear analysis. Among all methods, various arguments are put forward regarding different criteria as for example the simplicity, the accuracy, the robustness, or even the range of applications. Nevertheless, a great potential of the Mortar technique seems not to have been yet fully exploited in IGA: there exists a close link between this class of coupling technologies and the family of Domain Decomposition (DD) algorithms.

In fact, the additional DOF associated to the Lagrange multiplier field of the Mortar approach enable to formulate an interface problem which is naturally suitable for parallel computing [Stefanica, 2001, Stefanica, 2005]. The point of interest thus lies in the potential of Domain Decomposition Methods (DDM) for solving large-scale systems. Those non-overlapping DDM have been actively studied over the past decades in FEM as efficient parallel solvers for systems with possible millions of DOF [Gosselet and Rey, 2006]. The idea is to subdivide the computational domain into non-overlapping sub-domains: instead of solving one large system, multiple independent local systems are solved per subdomain (in parallel) and interface conditions are recovered through an iterative process (see figure 3.2). More specifically, the Finite Element Tearing and Interconnecting (FETI) [Farhat and Roux, 1991] and the Balancing Domain Decomposition (BDD) [Le Tallec et al., 1991, Mandel, 1993] are often seen as originators of the two main branches of those non-overlapping DDM. BDD is usually referred to as a primal approach since it chooses the interface displacement field as main unknown, whereas FETI is usually referred to as a dual approach because it privileges the interface loads. Since then, a large number of papers and vari-

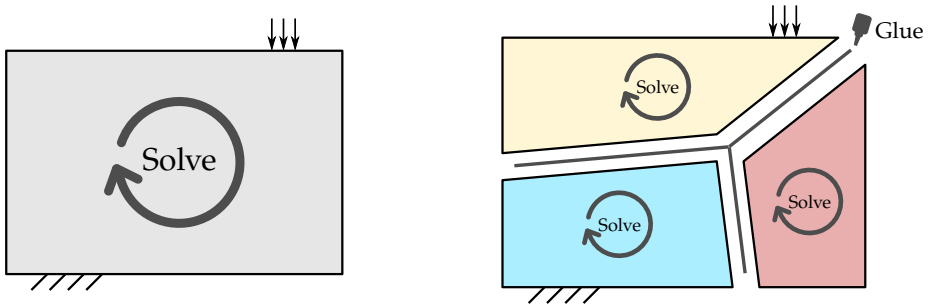

(a) Reference problem (b) Domain Decomposition

Figure 3.2 – Non-overlapping Domain Decomposition Methods (DDM): (a) instead of solving one large system defined over the whole computational domain Ω, (b) the domain is subdivided into multiple subdomains Ω_s. The resolution is performed by solving, in parallel, local systems defined per sub-domain, and interface conditions are recovered through an iterative process. IGA offers a natural splitting of the initial domain into several subdomains: each isogeometric patch may be associated to a subdomain.

ants have been developed and successfully applied in many context: *e.g.*, in the field of solid mechanics, see [Farhat et al., 1998, Farhat et al., 2001, Amini et al., 2009] for plates and shells, [Jolivet et al., 2014, Gosselet et al., 2015, Bovet et al., 2017] for heterogeneous problems, [Dureisseix and Farhat, 2001] for contact problems, etc.

In the context of IGA, although marginally investigated, this class of solvers appears all the more relevant as multipatch spline discretizations can be seen as a natural domain decomposition (each subdomain being an isogeometric patch). [Kleiss et al., 2012] noticed this logical link between IGA and DDM, which led to the Isogeometric (I) ETI solver [Kleiss et al., 2012, Hofer and Langer, 2017, Stavroulakis et al., 2018], *i.e.* the isogeometric variant of the FETI Dual-Primal (FETI-DP) solver [Farhat et al., 2001] for the coupling of matching patches in standard elasticity. Based on all these discussions, we propose in the following to build a dual DD algorithm that is efficient from the computational point of view (suitable for parallel computing) and also accurate (quality of the resolution, especially at the interface junctions) for analyzing complex, non-conforming Kirchhoff-Love sells. In particular, when used in the context of shape optimization, such a strategy will allow not to recompute the parts of the structure in non-design areas at each optimization iteration.

2.2 Kirchhoff-Love shell formulation: basics

Since we are about to couple Kirchhoff-Love shell patches, a brief overview of the standard isogeometric Kirchhoff-Love shell formulation [Kiendl et al., 2009] is necessary. This the object of this subsection. At this stage, we underline that we refer to as standard to characterize the following isogeometric Kirchhoff-Love shell formulation to make a distinction with the new, embedded domain based, isogeometric Kirchhoff-Love shell formulation developed in chapter 6.

In a shell formulation, the thin structure is defined by its mid-surface A and its thickness h. Using IGA, the mid-surface is described as a spline surface $A^h(\theta_1,\theta_2)$, where the curvilinear coordinates θ_1 and θ_2 are simply the parameters of the corresponding bivariate spline functions (see chapter 1). A^h provides at each material point of the volume $x^h \in \Omega$ a straightforward parametrization in terms of a system of curvilinear coordinates:

$$x^h(\theta_1,\theta_2,\zeta) = A^h(\theta_1,\theta_2) + \zeta a_3^h(\theta_1,\theta_2), \quad \text{where} \quad -\frac{h}{2} \leq \zeta \leq \frac{h}{2}. \tag{3.1}$$

In the above equation, a_3^h denotes the unit normal vector to the mid-surface and is computed with the

standard covariant vectors a_1^h and a_2^h of A^h as follows:

$$a_1^h = \frac{\partial A^h}{\partial \theta_1} = A^h_{,\theta_1} \quad ; \quad a_2^h = \frac{\partial A^h}{\partial \theta_2} = A^h_{,\theta_2} \quad ; \quad a_3^h = \frac{1}{J^h} a_1^h \times a_2^h \quad \text{with} \quad J^h = |a_1^h \times a_2^h|. \tag{3.2}$$

The subscript $(\cdot)_{,\theta_i} = \partial(\cdot)/\partial\theta_i$ indicates the partial derivative with respect to variable θ_i and $\times$ stands for the cross product between two vectors. For Kirchhoff-Love shells, the kinematic is then based on the Kirchhoff kinematic assumptions which postulate that straights lines normal to the mid-surface are characterized by rigid-body motions and remain normal to the mid-surface after deformation. This makes the transverse shear strains vanish and enables to describe the deformation of the shell body only by the displacement u of the mid-surface. The overall (resulting solid) displacement field U of the shell body takes the form:

$$U(\theta_1, \theta_2, \zeta) = u(\theta_1, \theta_2) + \zeta \, [\Phi \times a_3] \, (\theta_1, \theta_2), \tag{3.3}$$

where the linearized rotation vector Φ is defined as [Echter et al., 2013]:

$$\Phi = \phi_1 a_1 + \phi_2 a_2, \tag{3.4}$$

with the rotation angles ϕ_1 and ϕ_2 given by:

$$\phi_1 = \frac{1}{J} u_{,\theta_2} \cdot a_3 \quad \text{and} \quad \phi_2 = -\frac{1}{J} u_{,\theta_1} \cdot a_3. \tag{3.5}$$

Regarding notations, similarly as in previous chapters, we use normal type characters for continuous quantities while we will use boldface type letters for the resulting finite element operators and DOF vectors. In addition, we use exponent h to indicate that a quantity is discretized in terms of some shape functions.

With the introduced kinematic modeling, the linearized strain tensor of the shell body is found to be of the form:

$$\varepsilon_{\alpha\beta} = e_{\alpha\beta} + \zeta \kappa_{\alpha\beta}, \tag{3.6}$$

where membrane strains e and bending strains κ are given by:

$$e_{\alpha\beta} = \frac{1}{2}\Big(u_{,\theta_\alpha} \cdot a_\beta + u_{,\theta_\beta} \cdot a_\alpha \Big), \tag{3.7}$$

$$\begin{aligned} \kappa_{\alpha\beta} = & - u_{,\theta_\alpha\theta_\beta} \cdot a_3 \\ & + \frac{1}{J}\Big[u_{,\theta_1} \cdot \big(a_{\alpha,\theta_\beta} \times a_2 \big) + u_{,\theta_2} \cdot \big(a_1 \times a_{\alpha,\theta_\beta} \big) \Big] \\ & + \frac{a_3 \cdot a_{\alpha,\theta_\beta}}{J} \Big[u_{,\theta_1} \cdot \big(a_2 \times a_3 \big) + u_{,\theta_2} \cdot \big(a_3 \times a_1 \big) \Big]. \end{aligned} \tag{3.8}$$

Greek subscripts take the values 1 and 2 (as stated above, the transverse shear strains vanish, *i.e.*: $\varepsilon_{\alpha 3} = 0$, $\forall \alpha$). Finally, in the standard isogeometric version of the Kirchhoff-Love shell, the displacement u is discretized using the same basis as for A^h which, provided that higher-order spline functions are used, naturally satisfies the C^1 requirement brought by the bending term (3.8) (note that second derivatives of the displacement field are involved). In the end, the equilibrium configuration of the shell followed from the principle of minimum potential energy leads to the typical linear system:

$$\mathbf{K}\mathbf{u} = \mathbf{f}, \tag{3.9}$$

where vector $\mathbf{u}$ concatenates the DOF of the mid-surface displacement field and, $\mathbf{K}$ and $\mathbf{f}$ denote the isogeometric Kirchhoff-Love stiffness and external force operators, respectively. More precisely, the stiffness matrix involves a membrane and a bending contribution and reads:

$$\mathbf{K} = \int_S h \mathbf{B}_m^T \, \mathbf{H} \, \mathbf{B}_m + \frac{h^3}{12} \mathbf{B}_f^T \, \mathbf{H} \, \mathbf{B}_f \mathrm{d}S, \tag{3.10}$$

where $\mathbf{B}_m$ and $\mathbf{B}_f$ are the operators that relate the membrane and bending strains, respectively, to the mid-surface displacement. $\mathbf{H}$ sands for the material tensor describing the linear elastic behavior of the shell. Further details on the expression of $\mathbf{K}$ and $\mathbf{f}$ can be found in [Kiendl, 2011], and, for example, in the following papers; [Cirak et al., 2000, Kiendl et al., 2015, Hirschler et al., 2019c].

2.3 Formulation of the coupled problem

We recall that we are interested in the computation of stiffened structures as illustrated in Fig. 3.1(middle-right). As a consequence, the junctions between the panel and the stiffeners have only C^0 regularity along the non-conforming interface. Mortar coupling of Kirchhoff–Love shells has been studied for G^1 surfaces [Apostolatos et al., 2014a, Schuß et al., 2019] and for non-linear analysis. However, the formulation in the context of linear elasticity analysis of multipatch Kirchhoff–Love shells which connect with arbitrary angles does not seem to have been performed yet. Some aspects can be found in [Duong et al., 2017] but the applicability in the context of linear analysis may not appear obvious: the kinematic constraints are built by dot and cross products between quantities of neighboring patches which results in non-linear terms (with respect to the displacement). Differences with our approach mainly lie in the kinematic constraints imposed by the Lagrange multiplier. Similarities with already published papers in the standard FEM community can be found with our method, especially with [Bernadou et al., 1989, Bernadou and Cubier, 1998] where theoretical studies are carried out.

2.3.1 Kinematic coupling conditions

For the sake of simplicity, the method is presented in the case of two non-overlapping subdomains Ω_1 and Ω_2, without loss of generality. Subscripts 1 and 2 are now used to denote quantities related to subdomains Ω_1 and Ω_2, respectively. At the common interface denoted by Γ, the continuity of the displacement has to be ensured, obviously. Furthermore, in case of a shell junction with rigid hinge, an additional constraint is required which enforces the continuity of the rotation in the tangential direction associated to the interface curve (see Fig. 3.3 for illustration). Thus, we formulate the kinematic constraints as:

$$u_1 = u_2 \quad \text{on } \Gamma \qquad \text{[3 displacements]}, \tag{3.11}$$

$$\Phi_1 \cdot t = \Phi_2 \cdot t \quad \text{on } \Gamma \qquad \text{[1 rotation]}, \tag{3.12}$$

where t is a unit tangent vector associated to the interface curve.

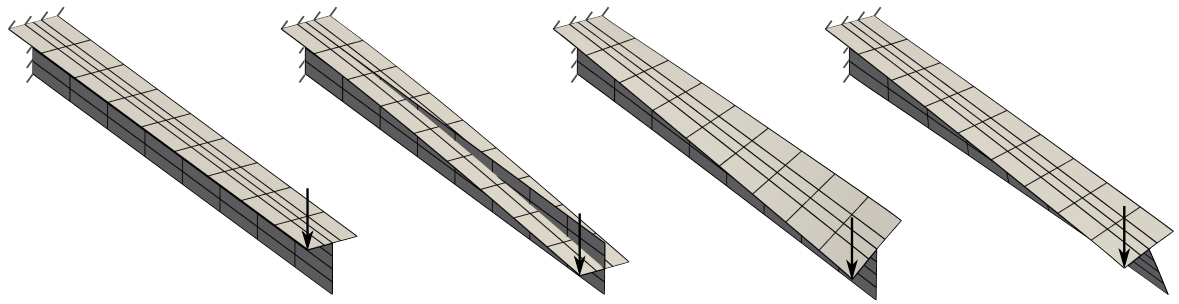

(a) Initial Configuration (b) No coupling (c) Displacement only (d) Full coupling

Figure 3.3 – Kinematic constraints for Kirchhoff-Love shells: at the patch junction, obviously, the three components of the displacement fields need to be coupled (c). Additionally, the continuity of the rotation in the tangent direction of this interface curve has to be imposed (d).

2.3.2 Weak coupling with Mortar approach

The two sets of constraints are ensured in a weak sense by introducing two Lagrange multipliers $\lambda_d \in \mathscr{M}_d$ and $\lambda_r \in \mathscr{M}_r$ ($\mathscr{M}_d$ and $\mathscr{M}_r$ being *ad-hoc* spaces). It results in the formulation of the following Lagrangian for

the coupled problem:

$$\begin{aligned} L_{\mathrm{KL}}(u_1,u_2,\lambda_d,\lambda_r) = &\tfrac{1}{2}a_1(u_1,u_1) - l_1(u_1) \\ &+ \tfrac{1}{2}a_2(u_2,u_2) - l_2(u_2) \\ &+ b(\lambda_d, u_1-u_2) \\ &+ b(\lambda_r, \Phi_1\cdot t - \Phi_2\cdot t), \end{aligned} \tag{3.13}$$

where bilinear forms a_s and linear forms l_s constitute the standard variational forms of the Kirchhoff-Love shell problem on each subdomain ($s\in\{1,2\}$), and b is defined as in Eq. (2.6).

Then, repeating the procedure of previous chapter, the variational principle written in the discrete form gives the following coupled linear system to be solved:

$$\begin{bmatrix} \mathbf{K}_1 & \mathbf{0} & \mathbf{C}_1^T & \mathbf{F}_1^T \\ \mathbf{0} & \mathbf{K}_2 & -\mathbf{C}_2^T & -\mathbf{F}_2^T \\ \mathbf{C}_1 & -\mathbf{C}_2 & \mathbf{0} & \mathbf{0} \\ \mathbf{F}_1 & -\mathbf{F}_2 & \mathbf{0} & \mathbf{0} \end{bmatrix} \begin{pmatrix} \mathbf{u}_1 \\ \mathbf{u}_2 \\ \boldsymbol{\lambda}_d \\ \boldsymbol{\lambda}_r \end{pmatrix} = \begin{pmatrix} \mathbf{f}_1 \\ \mathbf{f}_2 \\ \mathbf{0} \\ \mathbf{0} \end{pmatrix}, \tag{3.14}$$

where vectors $\mathbf{u}_1$, $\mathbf{u}_2$, $\boldsymbol{\lambda}_d$ and $\boldsymbol{\lambda}_r$ collect the DOF corresponding to the discretizations of u_1, u_2, λ_d and λ_r, respectively. As in previous chapter, the Mortar operators $\mathbf{C}_s$ and $\mathbf{F}_s$ consist in sparse rectangular matrices (see [Hirschler et al., 2019a] for more information regarding their construction).

As for any mortar method, a special care may be required for the construction of the approximation subspaces of the Lagrange multipliers to avoid undesirable energy-free oscillations. Let p denote the smaller polynomial degree of both subdomain displacement fields. We adopt the following strategy:

- for the displacement constraint (3.11), a vector-valued spline function λ_d^h with degree $p-1$ is defined since it is mainly related to membranes forces (*i.e.*, involving the first derivative of the displacement according to (3.7));
- for the rotation constraint (3.12), a scalar-valued spline function λ_r^h with degree $p-2$ is defined because it is associated to a bending moment (*i.e.*, involving the second derivative of the displacement according to (3.8));
- same mesh refinement is chosen for both Lagrange multipliers λ_d^h and λ_r^h. We discretize these fields using as many elements as the coarsest of the domains Ω_1 and Ω_2 over the interface.

As in previous chapter, it is important to say that this strategy is only based on physical considerations and on numerical experiments . We assert that we never encountered spurious, undesirable phenomena in our computations. All numerical examples presented in this chapter and later in chapter 6 highlight the good behavior of this Mortar coupling to handle the non-conforming shell interfaces encountered in stiffened structures (see, again, Fig. 3.1(middle-right)). Moreover, one can also notice that the choice of the approximation spaces for the Lagrange multipliers is completely decoupled from the overall approach applied in this chapter to build the DD solver (see section 3). With other choices in hand, the remaining part of the method performs identically.

Remark. *Once again, we emphasize that the notion of non-conforming interface in this chapter is restricted to the coupling of a stiffener lying arbitrarily on a panel with a fixed discretization. As a consequence, it has to be noticed that the whole patch domain that constitutes the panel is involved, which is different from the case of the coupling of trimmed shell patches (*i.e.*, where some parts of the patches are removed). Perhaps, this partially explains the good behavior of our Mortar-based coupling (we did not need to resort to some*

Nitsche techniques as in previous chapter). However, let us notice that even in case of real trimmed IGA, the same basis functions (as those of the whole panel patch) would be involved to apply constraints (3.11)-(3.12)*, which makes us think that our coupling strategy might be interesting to tackle trimmed IGA as well.*

2.4 Preliminary results: monolithic resolution

Prior to the development of the dual DD algorithm, we present here preliminary numerical examples, where analytical results are known, in order to highlight the correctness of our Mortar coupling for Kirchhoff-Love shells. The resolution is done with a direct solver applied to the coupled linear system (3.14).

2.4.1 Bending and shear of a simple beam

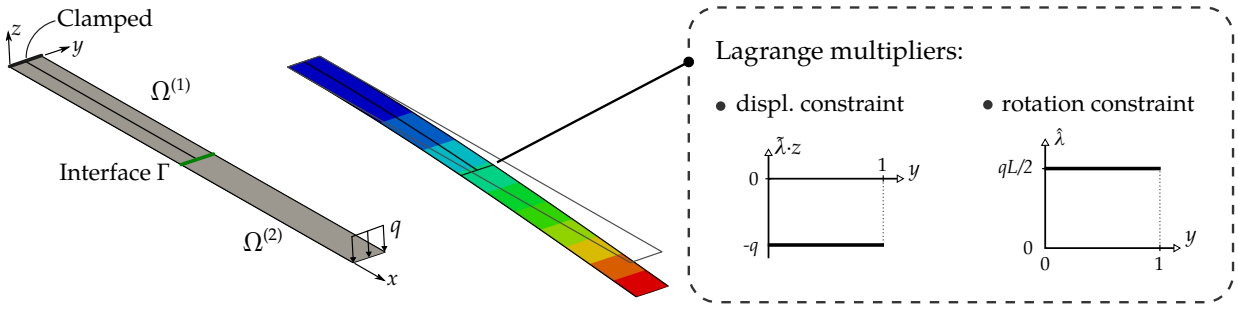

Figure 3.4 – Cantilever beam with end load: the beam is decomposed in two non-matching patches and coupled with the proposed Mortar approach. The shape of the Lagrange multipliers for the displacement and the rotation continuity constraints are shown one the right.

We start by investigating a cantilever beam subjected to bending and shear due to a load applied on its right-end (see Fig. 3.4(left)). Using the Euler-Bernoulli beam theory, it is possible to express analytically the vertical displacement, shear force and bending moment. The values of the problem parameters can be found in [Hirschler, 2019](chapter 4). Note that we took a Poisson ratio $\nu = 0$ so as to be consistent with the beam theory. The beam is decomposed in two non-matching cubic patches of same size (*i.e.*, the interface is located at half the length), as shown in Fig. 3.4(left). Two shell elements are considered for the left part while one shell element is used in the right part. Applying the strategy described above for the coupling, the Lagrange multipliers are discretized as follows: one quadratic (one-dimensional) B-Spline element for the displacement constraint, and one linear (one-dimensional) B-Spline element for the rotation constraint. We run the analysis and we verify that we exactly obtain the theoretical results since the analytical deflection is expressed as a polynomial of degree 3. More interestingly, the values obtained for the Lagrange multiplier fields λ_d^h and λ_r^h exactly correspond to the analytical values of the shear force and bending moment, respectively (see Fig. 3.4(right)). This test case demonstrates the mechanical meaning of the proposed Lagrange multiplier formulation.

2.4.2 T-shape beam

The T-beam problem is built using two planar patches that are connected in a non-conforming way as depicted in Fig. 3.5. The interface crosses the middle elements of the upper patch. The upper patch has one more element than the other in the beam direction, and both patches are discretized with cubic elements. We take the same numerical setting as in [Herrema et al., 2019], which is also given in Fig. 3.5. We obtain a similar deformation as in [Herrema et al., 2019] where penalty coupling was performed. In order to show that the rotation constraint is well prescribed, we plot in Fig. 3.5(c) the resulting angle between the patches along the interface. It can be seen that it remains equal to 90° after deformation. Without the rotation constraint, the angle between the patches was found to be equal to 86.6° at the end of the

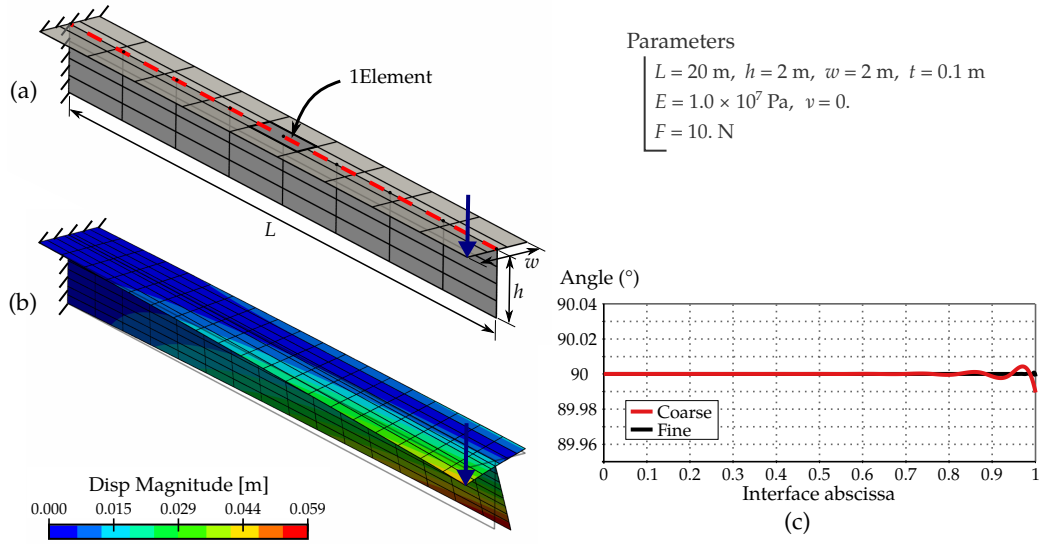

Figure 3.5 – T-Beam non-conforming coupling: (a) Description of the problem: the interface cuts the upper patch at the middle of some elements. (b) Deformed configuration with scale factor of 10 and the magnitude of the displacement field. (c) Angle between the patches along the interface after deformation. Coarse case corresponds to the mesh depicted in (b). Fine mesh is three times refined.

beam because the interface acted as a hinge [Herrema et al., 2019]. The presence of small oscillations for the coarser parametrization may be due to the non-optimality of the chosen spaces for the Lagrangian fields. Once again, it could be interesting to investigate the *inf–sup* condition to clarify the stability of the method [Wunderlich et al., 2019], but this is beyond the scope of the present work. However, these oscillations vanish with a finer parametrization which, in our opinion, is satisfying.

3 A dual domain decomposition algorithm

Henceforth, we address the general case of n_s sub-domains (*i.e.*, n_s patches) Ω_s, $s = 1 \dots n_s$. We define as $\mathbf{K} = \text{diag}(\mathbf{K}_1, \mathbf{K}_2, \dots, \mathbf{K}_{n_s})$ the block diagonal matrix that stores all the stiffness matrices of all the sub-domains. We define the resulting load vector $\mathbf{f} = (\mathbf{f}_1^T, \mathbf{f}_2^T, \dots, \mathbf{f}_{n_s}^T)^T$ as well. The total displacement and Lagrange multiplier DOF are stored in column vectors $\mathbf{u}$ and $\boldsymbol{\lambda}$, respectively. We concatenate the displacement and the rotation Mortar coupling matrices into single coupling matrices $\mathbf{C}_s^F$ such that:

$$\mathbf{C}_s^F = \left[\mathbf{C}_s^T, \, \mathbf{F}_s^T\right]^T. \tag{3.15}$$

The matrices $\mathbf{C}_s^F$ are of size $n_\lambda \times n_{u_s}$, where n_λ denotes the size of the whole $\boldsymbol{\lambda}$ while n_{u_s} denotes the size of the local $\mathbf{u}_s$. Finally, we introduce the global coupling operator $\mathbf{C}^F = [\mathbf{C}_1^F, -\mathbf{C}_2^F, \dots, \mathbf{C}_{n_s}^F]$ such that the generalization of the coupled system (3.14) reads:

$$\begin{bmatrix} \mathbf{K} & \mathbf{C}^{F\,T} \\ \mathbf{C}^F & \mathbf{0} \end{bmatrix} \begin{pmatrix} \mathbf{u} \\ \boldsymbol{\lambda} \end{pmatrix} = \begin{pmatrix} \mathbf{f} \\ \mathbf{0} \end{pmatrix}. \tag{3.16}$$

We are now looking for an efficient algorithm to solve the coupled linear system (3.16) based on the DDM, as motivated in section 2.1. In the classical FEM framework, the FETI-DP (and BDD by Constraints (BDDC)) has been especially developed for fourth-order problems [Farhat et al., 1998, Farhat et al., 2001, Amini et al., 2009]. However, in case of non-conforming interfaces, this approach seems to be difficult to apply: it is less trivial to identify the equivalent of the so-called corner nodes (subset of global DOF where

exact continuity is enforced) since non-conforming parametrizations do not share common DOF by definition. We thus resort to the initial one-level FETI problem [Farhat and Roux, 1991] to build our dual DD algorithm.

3.1 Formulation of the interface problem

The first step of the approach consists in splitting problem (3.16) into the following coupled set of equations:

$$\mathbf{K}_s\mathbf{u}_s = \mathbf{f}_s - \mathbf{C}_s^{F\,T}\boldsymbol{\lambda}, \quad \text{for } s = 1,\dots,n_s \tag{3.17}$$

$$\sum_{s=1}^{n_s} \mathbf{C}_s^F\mathbf{u}_s = \mathbf{0}. \tag{3.18}$$

The goal is then to formulate a dual interface problem with the Lagrange multiplier DOF vector as the only unknown. This interface problem is obtained by introducing the local equilibria (3.17) into the coupling condition (3.18).

Equilibrium of floating sub-domains. Generally, the local stiffness matrices $\mathbf{K}_s$ are not invertible. Indeed, if no Dirichlet boundary conditions are imposed on the floating subdomain Ω_s then corresponding matrix $\mathbf{K}_s$ is singular. Therefore, $\mathbf{K}_s$ being symmetric, Eq. (3.17) has a solution if and only if the right-hand side $\mathbf{f}_s - \mathbf{C}_s^{F\,T}\boldsymbol{\lambda}$ belongs to the image of operator $\mathbf{K}_s$. It leads to an additional equation, called the admissibility condition, which is:

$$\mathbf{R}_s^T\left(\mathbf{f}_s - \mathbf{C}_s^{F\,T}\boldsymbol{\lambda}\right) = \mathbf{0}, \quad \text{for } s = 1,\dots,n_s, \tag{3.19}$$

where $\mathbf{R}_s$ is a rectangular matrix. Its columns describe a basis of the null space $\ker(\mathbf{K}_s)$ of matrix $\mathbf{K}_s$. From a mechanical point of view, these vectors are the local rigid body modes. Then, for each sub-domain, the equilibrium is given by:

$$\mathbf{u}_s = \mathbf{K}_s^+\left(\mathbf{f}_s - \mathbf{C}_s^{F\,T}\boldsymbol{\lambda}\right) + \mathbf{R}_s\boldsymbol{\alpha}_s, \tag{3.20}$$

where $\boldsymbol{\alpha}_s$ is a vector that collects the different amplitudes of the rigid body modes (or null-energy modes) for sub-domain s and $\mathbf{K}_s^+$ is a pseudo-inverse of the stiffness matrix, *i.e.* that satisfies $\mathbf{K}_s\mathbf{K}_s^+\mathbf{K}_s = \mathbf{K}_s$. If the stiffness matrix is non-singular, then the pseudo-inverse is unique and is equal to the inverse of matrix $\mathbf{K}_s$, *i.e.* $\mathbf{K}_s^+ = \mathbf{K}_s^{-1}$.

Substitution Now, the local solutions (3.20) can be introduced into the compatibility condition (3.18). It yields the following equation:

$$\sum_{s=1}^{n_s} \mathbf{C}_s^F\mathbf{K}_s^+\mathbf{C}_s^{F\,T}\boldsymbol{\lambda} - \sum_{s=1}^{n_s} \mathbf{C}_s^F\mathbf{R}_s\boldsymbol{\alpha}_s = \sum_{s=1}^{n_s} \mathbf{C}_s^F\mathbf{K}_s^+\mathbf{f}_s. \tag{3.21}$$

Finally, combining this last equation with the admissibility condition given by (3.19), we end up with the interface problem. The resulting system is generally called the FETI system and is given by:

$$\begin{bmatrix} \mathbf{F} & \mathbf{G} \\ \mathbf{G}^T & \mathbf{0} \end{bmatrix} \begin{pmatrix} \boldsymbol{\lambda} \\ \boldsymbol{\alpha} \end{pmatrix} = \begin{pmatrix} \mathbf{d} \\ \mathbf{e} \end{pmatrix}, \tag{3.22}$$

where $\boldsymbol{\alpha}$ concatenates the rigid body unknowns of each sub-domain. The dual Schur complement $\mathbf{F}$, the constraint matrix $\mathbf{G}$, and the right-hand sides $\mathbf{d}$ and $\mathbf{e}$ are expressed as:

$$\begin{aligned}
\mathbf{F} &= \sum_{s=1}^{n_s} \mathbf{C}_s^F \mathbf{K}_s^+ \mathbf{C}_s^{F\,T}, \\
\mathbf{G} &= -\left[\mathbf{C}_1^F \mathbf{R}_1 \;\; \mathbf{C}_2^F \mathbf{R}_2 \;\; \cdots \;\; \mathbf{C}_{n_s}^F \mathbf{R}_{n_s}\right], \\
\mathbf{d} &= \sum_{s=1}^{n_s} \mathbf{C}_s^F \mathbf{K}_s^+ \mathbf{f}_s, \\
\mathbf{e} &= -\left(\mathbf{f}_1^T \mathbf{R}_1 \;\; \mathbf{f}_2^T \mathbf{R}_2 \;\; \cdots \;\; \mathbf{f}_{n_s}^T \mathbf{R}_{n_s}\right)^T.
\end{aligned}$$

3.2 Solving the interface problem

The resolution of system (3.22) relies on an iterative solver where only matrix-vector products are performed. This way, there is no need for assembling the dual Schur complement which would be computationally very demanding since pseudo-inverses $\mathbf{K}_s^+$ are involved. Moreover, it avoids inverting the dual Schur complement which has a dense structure. More precisely, we call upon a Conjugate Projected Gradient (CPG) -type algorithm. The idea is to iteratively solve a symmetric positive definite linear system (involving $\mathbf{F}$) under the constraint (3.19). In the following, we only recall the main aspects of the algorithm without clearly detailing it. Once again, we urge the interested reader to consult [Hirschler, 2019](chapter 4) and [Hirschler et al., 2019a] for further insight regarding the CPG algorithm. Note finally that we will improve the algorithm by building an adapted preconditioner (see section 3.4), thereby ending up with an efficient Preconditioned-CPG (PCPG) solver to analyze multipatch Kirchhoff-Love shells.

Projection. From a global point of view, starting with the well-known CG algorithm an additional projection step enables to eliminate the DOF vector associated to the rigid body motions of the floating subdomains. In order to do so, a projector $\mathbf{P}$ onto the null space of $\mathbf{G}^T$, *i.e.* onto $\ker(\mathbf{G}^T)$, is introduced to satisfy (3.19). This brings into play a symmetric matrix denoted by $\mathbf{Q}$ for which the product $\mathbf{G}^T\mathbf{Q}\mathbf{G}$ is invertible. Matrix $\mathbf{Q}$ can be taken as being the preconditioner, identity or a scaling matrix [Rixen et al., 1999]. We define:

$$\mathbf{P} = \mathbf{I} - \mathbf{Q}\,\mathbf{G}\left(\mathbf{G}^T\mathbf{Q}\,\mathbf{G}\right)^{-1}\mathbf{G}^T. \tag{3.23}$$

For most problems, the simplest choice $\mathbf{Q} = \mathbf{I}$ is the most computationally efficient, and many studies reported in the literature have been performed with this choice [Rixen et al., 1999, Stefanica, 2005]. We apply the same treatment herein. Furthermore, full re-orthogonalization of the gradient at every iteration is adopted [Gosselet and Rey, 2006].

Parallel computing. Let us now highlight the interest of such algorithms for parallel computing. To understand this point, one can observe what happens during the product between a given vector $\mathbf{y}$ and the dual Schur complement $\mathbf{F}$:

$$\mathbf{F}\,\mathbf{y} = \left[\sum_s \mathbf{C}_s^F \mathbf{K}_s^+ \mathbf{C}_s^{F\,T}\right]\mathbf{y} = \sum_s \left(\mathbf{C}_s^F \mathbf{K}_s^+ \mathbf{C}_s^{F\,T}\mathbf{y}\right). \tag{3.24}$$

It results in a sum of local contributions that can be computed independently and thus in parallel. Furthermore, each local contribution involves the local pseudo-inverse $\mathbf{K}_s^+$ and the coupling matrix $\mathbf{C}_s^F$ which remain unchanged during the iterative resolution, and thereby are built once and for all in a pre-processing step. More precisely, each local contribution is computed as follows:

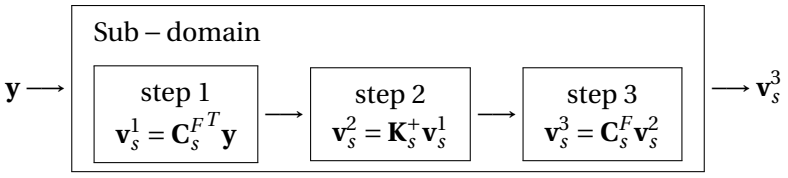

As a consequence, a sub-domain can be seen as a black box: taking as an input a vector $\mathbf{y}$, it returns the local contribution $\mathbf{v}_s^3$.The most time consuming step is the product by the pseudo-inverse (*i.e.*, step 2). As will be discussed in next section, the pseudo-inverse is generally given as a factorization (as a classical inverse). As a result, this step can be seen as the resolution of a linear system where the matrix is already factorized.

Unlike the dual Schur complement, the projection step can apparently not be done in parallel. Indeed, in the expression of the projector (3.23), there is the so-called *coarse problem* which is related to the term $\left(\mathbf{G}^T\mathbf{Q}\,\mathbf{G}\right)^{-1}$. This coarse problem takes the rigid body DOF as unknowns. It is therefore of low dimension and easy to be factorized before entering into the gradient loop. It can be seen as a coarse correction that plays a particular role in the scalability of the algorithm. For more details regarding parallel computing, interested readers can find a large amount of information in the literature since DDMs have been intensely developed during the past decades (see, for example, [Toselli and Widlund, 2006, Kozubek et al., 2013, Dolean et al., 2015]).

3.3 Null-space and pseudo-inverse

Up to now, we did not mention how are formulated the null space $\mathbf{R}_s$ and the pseudo-inverse $\mathbf{K}_s^+$ that come into play in the DD solver. There are different possibilities but here we resort to a purely algebraic method because of the new, embedded Kirchhoff-Love shell formulation which will be introduced in chapter 6 for shape optimization.

For clarity, we voluntarily skip here the sub-domain identification through subscript s, but the reader should view the following operators as local quantities. The purely algebraic method used in this work has been presented in [Farhat et al., 1998] and already used in [Farhat and Roux, 1991]. The pseudo-inverse and the null space are constructed during the factorization of the stiffness matrix. It is based on the partition of matrix $\mathbf{K} \in \mathbb{R}^{n\times n}$ as:

$$\mathbf{K} = \begin{bmatrix} \mathbf{K}_{11} & \mathbf{K}_{12} \\ \mathbf{K}_{12}^T & \mathbf{K}_{22} \end{bmatrix}, \tag{3.25}$$

where $\mathbf{K}_{11} \in \mathbb{R}^{r\times r}$ is a submatrix with full rank r equal to the rank of the initial matrix (*i.e.* $r = \mathrm{rk}(\mathbf{K}) = \mathrm{rk}(\mathbf{K}_{11})$). With such a partition in hand, the following relation holds:

$$\mathbf{K}_{22} - \mathbf{K}_{12}^T\mathbf{K}_{11}^{-1}\mathbf{K}_{12} = \mathbf{0}. \tag{3.26}$$

One can then define the pseudo-inverse and the null space as:

$$\mathbf{K}^+ = \begin{bmatrix} \mathbf{K}_{11}^{-1} & \mathbf{0} \\ \mathbf{0} & \mathbf{0} \end{bmatrix}, \qquad \mathbf{R} = \begin{bmatrix} -\mathbf{K}_{11}^{-1}\mathbf{K}_{12} \\ \mathbf{I} \end{bmatrix}, \tag{3.27}$$

where $\mathbf{I}$ is now the identity matrix of size $m = n - r$.

In practice, partition (3.25) is not known in advance but it is obtained in an unordered form during a Gaussian-based factorization (as for example a LU decomposition). At each step of the factorization, one can check if a null pivot is encountered. If true, the corresponding equation is redundant and is removed from the system. The reduced column can be recycled to later recover the null space.

3.4 Preconditioning

Last but not least ingredient involved in our algorithm is the preconditioner. A good preconditioner is crucial for the computational performance of the iterative resolution. Its goal is to reduce the conditioning number of operator $\mathbf{F}$ since the performance of an iterative Krylov solver is known to be highly dependent on the conditioning of the system to be solved. It can thus be seen as an approximation of the inverse of the system. The better the approximation, the more efficient is the preconditioning step during the iterative resolution. However, it has to be cheap to be built and evaluated within the algorithm.

Dirichlet preconditioner. Several preconditioners of the dual Schur complement have been studied in the literature. In the context of FEM matching grids, the Dirichlet preconditioner is said to be optimal regarding the asymptotic bound and thus offers an excellent numerical scalability [Rixen, 2002]. The Dirichlet preconditioner is obtained under the approximation that the inverse of the sum of the local contributions is the sum of the inverses of each of these local contributions. More precisely, it is obtained by exactly inverting the local dual Schur complements and summing each local contribution. In case of a Mortar interface, we can rewrite this Dirichlet preconditioner as:

$$\tilde{\mathbf{F}}_I^{-1} = \sum_{s=1}^{n_s} \left(\mathbf{C}_s^F \, \mathbf{C}_s^{F\,T}\right)^{-1} \mathbf{C}_s^F \begin{bmatrix} \mathbf{0} & \mathbf{0} \\ \mathbf{0} & \mathbf{S}_{s_{bb}} \end{bmatrix} \mathbf{C}_s^{F\,T} \left(\mathbf{C}_s^F \, \mathbf{C}_s^{F\,T}\right)^{-1}, \tag{3.28}$$

where matrix $\mathbf{S}_{s_{bb}}$ denotes the local primal Schur complement and is given by:

$$\mathbf{S}_{s_{bb}} = \mathbf{K}_{s_{bb}} - \mathbf{K}_{s_{bi}} \, \mathbf{K}_{s_{ii}}^{-1} \mathbf{K}_{s_{ib}}. \tag{3.29}$$

Subscript b corresponds to the boundary DOF on the interface and subscript i is associated to the internal DOF. The interested reader can find in [Hirschler, 2019](chapter 4) the proof of the equality between expression (3.28) and the sum of the inverses of the local Schur complements.

Generalized preconditioner. In the particular case of Mortar coupling, some improvements of the initial version of the Dirichlet preconditioner have been studied [Lacour, 1997, Stefanica, 2001, Rixen, 2002, Stefanica, 2005]. For instance, scaling factors can be added in order to take into account the possible gap between the stiffnesses on both sides of the interface [Rixen and Farhat, 1999, Klawonn and Widlund, 2001]. These heterogeneities are particularly numerous in the case of stiffened structures with the presence of T-junctions, different shell thicknesses and different material behaviors [Amini et al., 2009]. Thus, it is primordial to efficiently deal with those heterogeneities to analyze complex shell structures. Therefore, it is proposed here to follow the extended Dirichlet preconditioner suggested by [Rixen, 2002] and mentioned by [Stefanica, 2005] which can be written as:

$$\tilde{\mathbf{F}}_A^{-1} = \sum_{s=1}^{n_s} \left(\mathbf{C}^F \, \mathbf{A} \, \mathbf{C}^{F\,T}\right)^{-1} \mathbf{C}_s^F \, \mathbf{A}_s \begin{bmatrix} \mathbf{0} & \mathbf{0} \\ \mathbf{0} & \mathbf{S}_{s_{bb}} \end{bmatrix} \mathbf{A}_s \, \mathbf{C}_s^{F\,T} \left(\mathbf{C}^F \, \mathbf{A} \, \mathbf{C}^{F\,T}\right)^{-1}, \tag{3.30}$$

with $\mathbf{C}^F$ the global coupling operator of Eq. (3.16) and where matrix $\mathbf{A}_s$ is chosen here as the superlumped scaling: $\mathbf{A}_s = \text{diag}(\mathbf{K}_s)^{-1}$. The global matrix $\mathbf{A}$ is the diagonal block assembly of all these local scaling matrices, which leads to a diagonal matrix in the present case.

The extended Dirichlet preconditioner has shown better performance in comparison with the original Dirichlet preconditioner in the case of Mortar interfaces [Lacour, 1997, Stefanica, 2001, Stefanica, 2005]. [Rixen, 2002] shows that this preconditioner is mechanically consistent and mentions its mechanical meaning: once applied to the residual of the interface problem (3.18), it computes the correction for the Lagrange multipliers. [Stefanica, 2005] discusses the parallelization properties of this generalized preconditioner. The critical point concerns the two global multiplications by $\left(\mathbf{C}^F \, \mathbf{A} \, \mathbf{C}^{F\,T}\right)^{-1}$ which cannot be done in parallel. One may build local matrices $\tilde{\mathbf{C}}^F = \left(\mathbf{C}^F \, \mathbf{A} \, \mathbf{C}^{F\,T}\right)^{-1} \mathbf{C}_s^F$ once and for all at the beginning of the resolution. In order to preserve the sparsity, biorthogonal Mortars could be helpful in this case [Stefanica, 2005, Wunderlich et al., 2019].

4 Numerical investigation of the developed algorithm

We eventually run several examples to highlight the good behavior of the constructed DD algorithm. Let us quote at this stage that only a sequential implementation has been performed. The goal here is to make sure that the algorithm can be envisaged for HPC: the true parallel implementation being postponed to

future works. Firstly, the bending of an heterogeneous plate is investigated; then, the famous Scordelis-Lo roof benchmark is revisited in a DD context; finally, a quite complex stiffened panel is computed. At this stage, let us quote that a more complex test case representative of an aircraft wing substructure will be computed and optimized in chapter 6. For every example here, we depict the number of iterations versus the level of refinement of the mesh given a fixed decomposition. The results are given in tables where the headers n_{tot} and n_λ denote the number of total and interface DOF respectively (*i.e.*, by referring to (3.16), n_λ is the size of $\boldsymbol{\lambda}$, and n_{tot} is the total number of unknowns). Columns with headers $\mathbf{I}$, $\tilde{\mathbf{F}}_I^{-1}$ and $\tilde{\mathbf{F}}_A^{-1}$ give the iteration number without any preconditioner, with the Dirichlet preconditioner (3.28), and with the generalized preconditioner (3.30), respectively. The goal of these tables is to assess the numerical scalability of the DD algorithm with respect to the mesh refinement. Furthermore, to show the accuracy of the coupling, we study the convergence of the final iterative solution with respect to mesh refinement for the Scordelis-Lo roof. In order to do so, we compute the relative energy error as:

$$\text{Err}^h = \frac{|E_{\text{ref}} - E^h_{\text{coupling}}|}{E_{\text{ref}}}, \tag{3.31}$$

where the reference energy E_{ref} is computed on a very fine single patch discretization.

4.1 Heterogeneous plate bending

Fig. 3.6(top) describes the numerical setup for the heterogeneous plate bending. The plate is fully fixed at one side while an uniform pressure $P = 1$Pa is applied over the whole structure. We decompose the plate into two patches with different thicknesses such that the ratio is $h_1/h_2 = 0.1$. As a result, we address here an heterogeneous plate since its behavior (in particular its bending) continuously depends on its thickness. Cubic B-Spline basis functions are used and the discretization of the patch with the fixed edge is twice finer than the second one. The results in terms of bending moments are plotted in Fig. 3.6(bottom). Note that the Poisson ratio is not taken as 0 here. As a result, the x-component of the bending moment does not vanish and it is discontinuous across Γ given the thickness gap between the two patches. Conversely, the y-component of the bending moment is continuous over the whole structure.

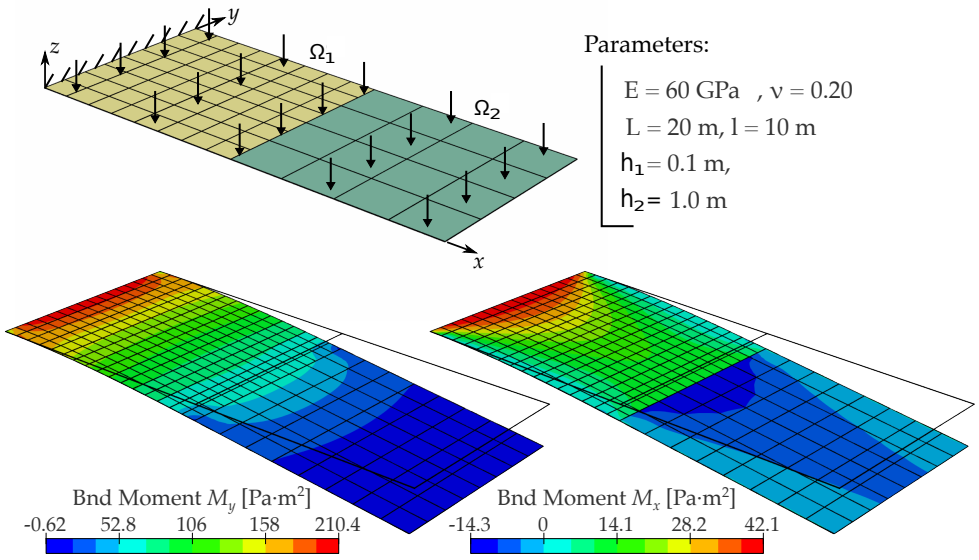

Figure 3.6 – Description and results of the bending plate problem. The plate is decomposed into two non-matching patches. We study an heterogeneous case: the two coupled shells have different thicknesses.

In addition, Tab. 3.1 presents the performance study of the algorithm for this problem. One can see that the algorithm requires few iterations to reach convergence with a preconditioner and, more specifically,

ref	n_{tot}	n_λ	**I**	$\tilde{\mathbf{F}}_A^{-1}$	$\tilde{\mathbf{F}}_I^{-1}$
0	222	28	7	4	7
1	510	44	14	4	11
2	1446	76	28	6	18
3	4758	140	59	11	28
4	17142	268	117	16	33

Table 3.1 – Performance study for the bending plate problem described in figure 3.6.

when the generalized preconditioner (3.30) is used. This accounts for the correct tackling of the heterogeneity between the subdomains with $\tilde{\mathbf{F}}_A^{-1}$. Furthermore, it can be observed that the increase of iterations between two mesh refinement steps is drastically reduced thanks to the help of a preconditioner. Consequently, for the finest refinement levels, the gain is significant in comparison with the un-preconditioned version. Ideally, the number of iterations should be constant versus the mesh refinement. Here, we do not have a perfect numerical scalability but it is not surprising. In fact, the one-level FETI equipped with the Dirichlet preconditioner is known to be numerically scalable for second-order problems. However, it does not hold true for fourth-order problems as shown for example by [Farhat et al., 1998]. That is why extensions of the classical FETI method, as for instance the two-level FETI and latter on the FETI-DP, have been introduced to optimally deal with plates and shells [Farhat et al., 1998, Farhat et al., 2001]. Based on these remarks, we understand the slight increase of the iteration counts versus the mesh refinement. Nevertheless, for this test case, the developed DD algorithm performs well and leads to entirely acceptable results.

4.2 Scordelis-Lo roof

The Scordelis-Lo roof is part of the shell obstacle course which is widely used to study the performance of shell formulations [Belytschko et al., 1985]. It consists in a portion of cylinder subjected to a vertical gravity load and fixed at its two end sections using rigid diaphragms. The problem parameters and some results for this test case can be found in the abundant shell literature: *e.g.*, in [Belytschko et al., 1985, Kiendl et al., 2009, Bouclier et al., 2013a]. For our DD study, we decompose the Scordelis-Lo roof into two non-matching configurations as depicted in Fig. 3.7(left):

- 2A – four quasi-identical patches which intersect at a cross point;
- 2B – nine patches with different levels of mesh refinement and of polynomial degree. The coarsest are quartic patches while the finest are cubic patches.

	2A					2B			
ref	n_{tot}	n_λ	**I**	$\tilde{\mathbf{F}}_A^{-1}$	Err^h	n_{tot}	n_λ	**I**	$\tilde{\mathbf{F}}_A^{-1}$
0	708	92	70	34	3.55e-3	1513	276	167	44
1	1652	156	117	38	6.44e-5	3017	468	317	52
2	4692	284	188	48	1.92e-6	7537	842	558	64
3	15380	540	276	64	8.54e-8	22625	1620	949	87
4	55188	1052	405	86	3.52e-9	76993	3156	1783	121

Table 3.2 – Performance study for the Scordelis-Lo roof shell problem described in figure 3.7. The reference energy was taken as $E_{\text{ref}} = 4826.577028$ to compute the relative energy error Err^h of the coupled solution.

Fig. 3.7 shows the vertical displacement field and the distribution of a bending moment for each configuration, which appear smooth as expected. The results investigating the numerical scalability are given in Tab. 3.2. It can be seen that the benefit of the preconditioning step is increasing from the first configuration 2A to the second one 2B. For the first configuration 2A, the iteration counts is reduced by a factor of 4 for

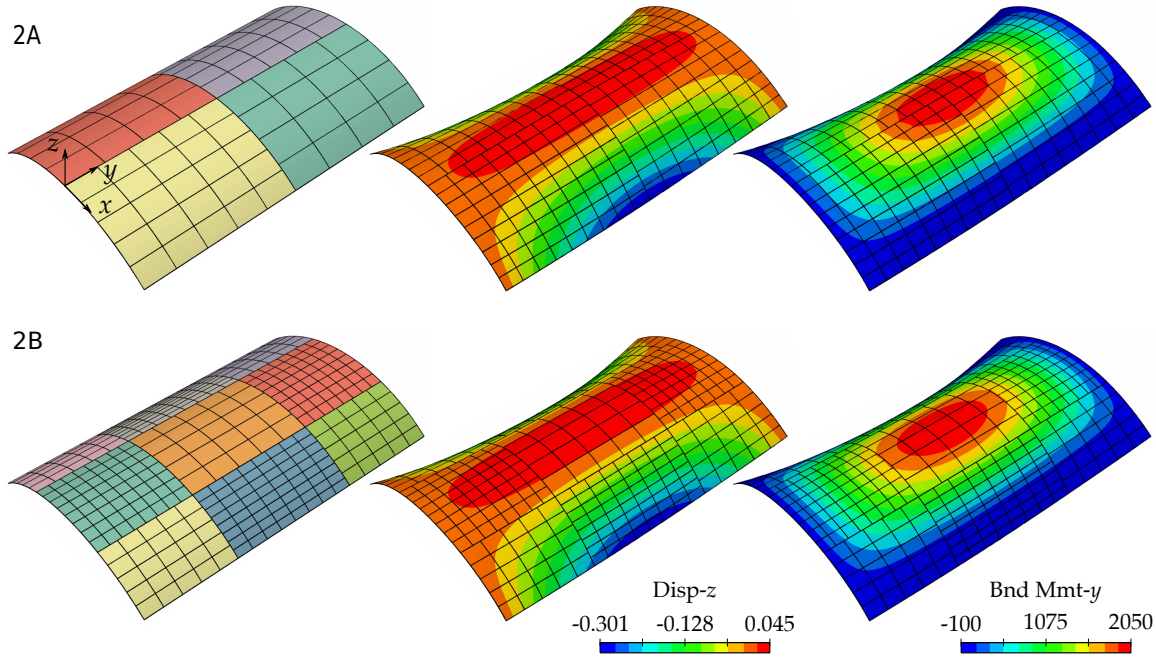

Figure 3.7 – Description and results for the Scordelis–Lo roof test case. Two different non-matching subdivisions are studied: 2A is made of four quasi-identical patches (two patches have one more element per direction) and 2B is made of nine patches with different levels of mesh refinement and of polynomial degree.

the refinement levels above 1. For the more complex decomposition 2B, the iteration counts is drastically reduced when using the generalized Dirichlet preconditioner. Looking at the refinement levels 3 and 4 in Tab. 3.2 (and columns referred to configuration 2B), we observe that the number of iterations is reduced by a factor of 10, and 15 respectively. Thus, the benefit provided by the preconditioner is all the more remarkable in case of complex DD. Even if numerical scalability is not fully reached, the growth of the iteration counts with the refinement level is very slow for each configuration and it leads to satisfactory results.

Additionally, the results in terms of energy errors (3.31) for decomposition 2A are provided in Tab. 3.2. It enables to show that the coupling strategy presented in section 2 is valid. The relative energy error is low and decreases with the mesh refinement. Particularly, this convergence rate is similar to the one we observe for the cubic monopatch discretization. Note finally that we do not perform the convergence study for configuration 2B since it contains patches of different degrees (cubic and quartic).

4.3 Stiffened panel

The problem of the stiffened panel is presented in Fig. 3.8(top). It consists in the assembly of a square plate with subparts called the stiffeners. We design three stiffeners: two with a parabolic shape and the third one with a straight shape. The straight patch intersects the two curved stiffeners. As a result, five non-conforming interfaces are defined: each interface cuts several isogeometric elements. Every patch is discretized using cubic Kirchhoff-Love shells. The material and geometric parameters of the study are given in Fig. 3.8 along with the results in terms of displacements and stress resultants. The edges of the panel are fixed (no displacement). The uniform pressure is equal to $P = 1000$Pa.

Once again, we run the analysis for several levels of mesh refinement with and without the preconditioning step. The results of the study are given in Tab. 3.3. We observe the same behavior as for the previous test cases. Indeed, the iteration counts is drastically reduced with the use of a preconditioner and it is all the more true when increasing the refinement level. We give the results for both the classical Dirichlet preconditioner $\tilde{\mathbf{F}}_I^{-1}$ and the generalized preconditioner $\tilde{\mathbf{F}}_A^{-1}$ in order to highlight the positive influence of the scaling step occurring in the second one. In fact, in case of stiffened structures, the T-shape interfaces are

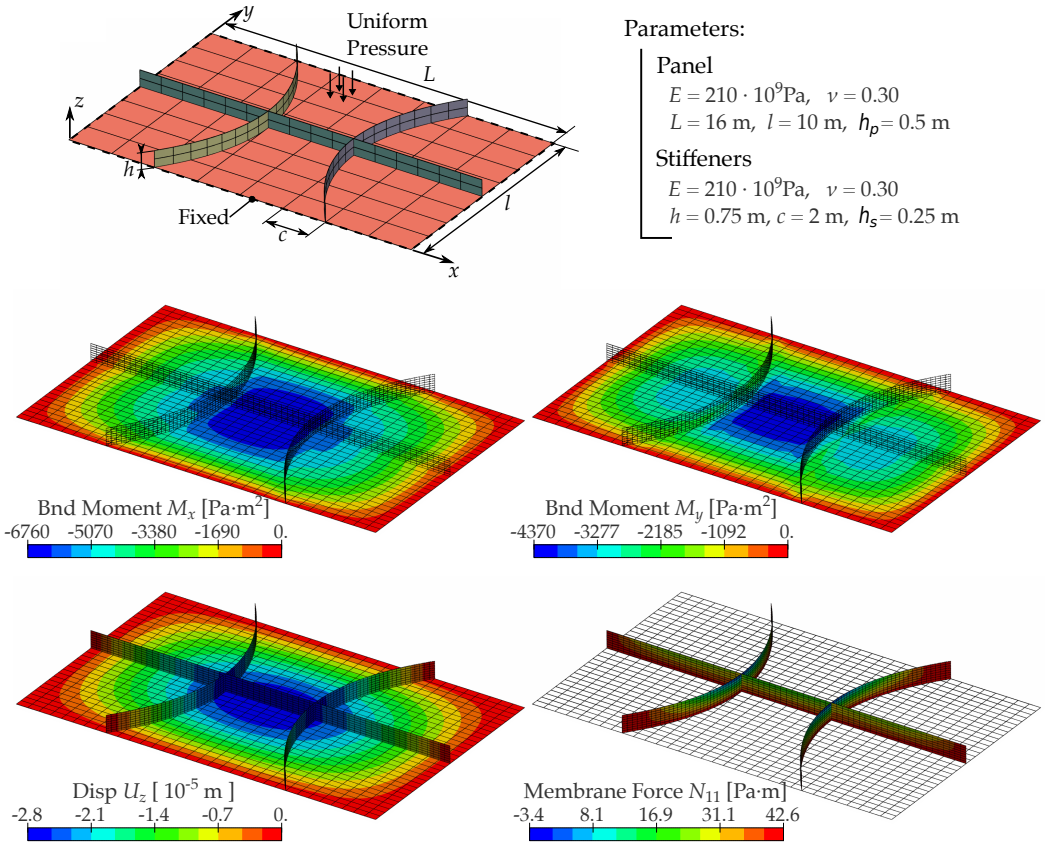

Figure 3.8 – Description and results for the stiffened panel problem. It consists in the assembly of a rectangular plate with three stiffeners; two with a parabolic shape crossed by a straight one. It leads to four non-conforming patches and five coupling interfaces (three stiffener/panel and two stiffener/stiffener interfaces). The main stress resultants for the panel are the bending moments whereas the stiffeners are mainly subjected to membrane forces, which highlights the heterogeneity of the test case.

sources of heterogeneities even if both subdomains are of the same material properties. For instance, the stiffener is mainly subjected to membrane forces whereas the panel mostly undergoes bending. This leads to high differences in terms of stiffness at the interface. A shell is much stiffer under membrane loading than under bending loading. Thus, as shown in Tab. 3.3, the generalized preconditioner performs better than classical the Dirichlet preconditioner.

As for the previous shell problems, the numerical scalability is not completely achieved but the growth of the number of iterations remains slow while introducing the preconditioning step. Especially, satisfactory results are obtained even for very fine meshes. For instance, with the refinement level of 4, the dual decomposition domain algorithm converges in 125 iterations even though the total number of DOF is over 100000. This is a crucial point. Because the algorithm solves an interface problem where the unknowns are the Lagrange Multiplier DOF, we are able to measure, during the resolution, the residual of the coupling condition (3.18). The convergence criteria is formulated on this residual which, in other words, ensure the good fulfillment of the coupling condition. For large problem, the monolithic solution obtained with a basic direct solver applied directly to the linear system (3.16) does not give suitable results. The numerical errors during the resolution significantly affect the correct imposition of the coupling conditions. Thus, we believe that the presented algorithm is viable and therefore attractive to tackle more complex models as encountered in industrial applications.

ref	n_{tot}	n_λ	$\mathbf{I}$	$\tilde{\mathbf{F}}_A^{-1}$	$\tilde{\mathbf{F}}_I^{-1}$
0	1227	147	109	50	81
1	3313	259	193	68	94
2	10365	483	341	85	110
3	35989	931	613	103	137
4	133317	1827	1106	125	189

Table 3.3 – Performance study for the stiffened panel problem described in figure 3.8.

Summary and discussion. In order to be able to design innovative aeronautic-type structures, *i.e.* complex curved stiffened panels, we require to face the difficulty of handling multipatch shell models with non-conforming parametrizations. This chapter tackles the problematic from an analysis point of view before the geometric modeling and optimization challenges are addressed in chapter 6. In order to do so, we build in this chapter a dual DD solver for the analysis of non-conforming multipatch isogeometric Kirchhoff-Love shell models. The starting point is the development of a new Mortar coupling which weakly imposes the interface conditions regarding the displacement and the rotation of the shell through two sets of Lagrange multipliers. In the literature, one argument against Mortar methods is commonly claimed; it concerns the additional unknowns introduced by the Lagrange multiplier field that increase the overall size of the system to be solved. We believe that this argument is not relevant and the present work fully takes advantage of those additional DOF. In fact, it allows us to formulate an interface problem, namely the one-level FETI problem, where the unknowns of the system are these interface DOF. We highlight for different examples with increasing levels of complexity that it enables to accurately analyze non-conforming multipatch structures, even for very fine levels of refinement, since we track the interface residual during the resolution. Moreover, the algorithm is naturally parallelizable. Instead of solving one large linear system, only local problems defined at the patch level are solved in parallel. As the non-invasive algorithm of previous chapter, this is particularly of interest in the context of shape optimization since it enables not to recompute the parts of the structure in non-design areas at each optimization iteration, as will be seen in chapter 6.

Focusing on the coupling approach, the extension to face real trimmed IGA (*i.e.* when some parts of the patches to be coupled are removed next to the inteface) may be of great interest to enlarge the scope of applications and truly bridge the gap between CAD and shell analysis. One issue to perform such an extension might be related to the construction of suitable dual approximation spaces for the Lagrange multipliers [Wunderlich et al., 2019], which is not a trivial task as underlined in previous chapter. However, let us notice that the case of real trimmed IGA differs from our case of stiffened panels in terms of domains for integration but not in terms of basis functions involved to formulate the coupling conditions. As a result, our coupling approach may appear relatively well adapted to truly handle trimmed IGA. Another solution would consist in developing an "equivalent" Nitsche method. A connection between standard Lagrange multiplier and (at least symmetric) Nitsche couplings can actually be made (see, e.g., [Fritz et al., 2004, Bazilevs et al., 2012]). Starting with the standard Lagrange multiplier method, the idea to obtain the Nitsche method is to replace the Lagrange multipliers by the mean interface stress resultants coming from the primal variables. If some Nitsche strategies have been proposed for the case of G^1 junctions [Guo and Ruess, 2015, Guo et al., 2018], the explicit formulation of the stress resultants transfer in case of rigid hinges seems complicated. In this context, it may be quoted that the very recent work of [Schöllhammer and Fries, 2019] regarding the development of a new Kirchhoff-Love shell formulation, which is not based on the curvilinear coordinates, may be appealing to more simply write the stress resultants transfer occurring in Nitsche-type coupling.

Finally, returning to the DD solver, it appears obvious that the true implementation in parallel would be of great interest to handle realist complex industrial structures, as demonstrated in the field of FEM [Gosselet and Rey, 2006]. Regarding the improvement of the solver, a remaining ques-

tion revolves around the choice of operator **Q** in the coarse problem (3.23) to handle the heterogeneities [Rixen et al., 1999]. Other interesting points to look at would concern the extension of the FETI-DP framework [Farhat et al., 1998, Farhat et al., 2001] and/or the construction of dedicated coarse spaces based on spectral techniques [Spillane and Rixen, 2013, Spillane et al., 2013, Jolivet et al., 2014], or even the extension of the adaptive multipreconditionned FETI scheme [Bovet et al., 2017] to our case of non-conforming IGA, so as to be efficient both with respect to fourth-order problems and heterogeneities. The present work aims at motivating future researches in that direction. In our opinion, the direct use of geometric models with non-conforming interfaces for the structural analysis could be pushed forward with those new Domain Decomposition solvers.

Part II

… for optimization applications in structural mechanics

CHAPTER 4

FE-based digital image correlation

Contents

Digital Image Correlation (DIC) denotes in the field of experimental mechanics (of structures and/or materials) what is also referred to as image registration in the computer vision and applied mathematics communities. This problem is frequently encountered in image processing: given a set of images taken over time that follow the deformation of an object, the goal is to match them; that is, to find a geometrical transformation which enables to move from one image to another. With the advent of electromagnetic (visible, IR, UV, RX, terahertz, etc) and electronic imaging technologies, as well as derived techniques (stereo, volume, confocal, hyperspectral imaging, etc), the experimental mechanics field is currently experiencing a genuine digital revolution. In this context, imaging offers the possibility to measure mechanical fields that could redefine standard mechanical characterization procedures used daily in the industry, and significantly reduce the design time of structures. However, given the explosion of the sensor definition (up to several tens of millions of pixels in 2D and several tens of billions of voxels in 3D) and of the acquisition time frames (up to several millions of images per second), it implies developing innovative efficient algorithms (breaking with the common practice in experimental mechanics) to extract mechanically sound information from this massive amount of image data. This work is heading in this direction: it intends to extend the HPC techniques of computational structural mechanics, in particular those based on Domain Decomposition (DD) (see chapter 3), to treat the today BigData of experimental mechanics.

In experimental mechanics, DIC has become one of the most commonly used full-field measurement methods, because of its simplicity (it is non-contact and makes use of multipurpose reusable hardware) and its modularity (no intrinsic physical scale). The first work is attributed to [Lucas and Kanade, 1981] from the computer vision community and the first application in experimental mechanics is due to [Sutton et al., 1983, Sutton et al., 2009]. These pioneering works propose to split the image into subsets and to look for the rigid displacement (and possible basic warping) for each sub-image. Since in experimental mechanics the measured kinematic fields are useful for the validation (or the identification of the parameters) of a (FE-based) numerical model [Molimard et al., 2005, Périé et al., 2009, Leclerc et al., 2009, Réthoré, 2010, Réthoré et al., 2013, Mathieu et al., 2015], the use of a finite element interpolation of the displacement in the DIC algorithm seems to have now gathered considerable momentum in the community (leading to FE-DIC, see [Kirchner and Niemann, 1992, Sun et al., 2005, Besnard et al., 2006, Fehrenbach and Masmoudi, 2008, Rannou et al., 2010, Fedele et al., 2013, Van Beeck et al., 2014, Passieux et al., 2015a, Wittevrongel et al., 2015], to name a few). Indeed, it appears more convenient

with FE-DIC to couple measurement with simulation software as they both use FE for the interpolation of the kinematic fields. In other words, FE-DIC allows for interpolation (or even, let us say "treatment") -free communications with finite element simulations. In the same idea, FE-DIC also offers the opportunity to mechanically control the DIC solution. As a result, we will focus on FE-DIC here to foster the extraction of useful (in the sense of the mechanics) information from image data.

This chapter is divided into two parts. In section 1, we review the DIC method (with a particular emphasis on FE-DIC) from a numerical optimization point of view [Nocedal and Wright, 2006]. We take advantage of this section to introduce some basics regarding gradient-based optimization, which may be useful for the whole second part of this manuscript dedicated to optimization applications. Regarding DIC, we justify through a rigorous mathematical analysis the use of a constant operator over the iterations, which is the common practice in the experimental mechanics community. This is of crucial interest to ensure minimal computational cost. Then, in section 2, we build a coupling method for FE-DIC with mechanical regularization that enables us to derive, in particular, an efficient DD solver to analyze large and high resolution images. The interest of integrating such an HPC tool in the optimization loop of FE-DIC is highlighted.

1 Introduction of FE-DIC from an optimization point of view

It first seems appropriate to clarify the mathematical background of DIC and correct some inaccurate terminologies in the literature, especially towards the experimental mechanics community. More importantly, a relevant idea of the standard DIC solver consists in replacing the gradient of the deformed state image with that of the reference image, so as to obtain a constant operator. Different arguments (small strains, small deformations, equality of the two gradients close to the solution, etc) have been given in the literature to justify this approximation, but none of them are fully accurate. Indeed, the convergence of the optimization algorithm has to be investigated from its ability to produce descent directions. Herein, a mathematical understanding of the standard DIC algorithm is proposed. The validity domain of the underlying approximation is studied, and a condition on DIC operators is derived and interpreted as a condition on the nature of the measured displacement field. Although an emphasis is performed on FE-DIC, our findings also hold in the context of subset-DIC since the same standard solver is often applied.

We proceed as follows for the presentation: first, the DIC problem is formulated in an algebraic setting to exhibit its non-linear least-squares nature in $\mathbb{R}^m$ (m being the number of data). Then, the standard descent algorithms that are usually considered to solve such an unconstrained, regular optimization problem are built. Once again, it should be emphasized at this stage that the developments carried out in the first part of this section are very basic in the field of gradient-based optimization, but we believe that they provide an interesting alternative lighting compared to the presentation of the method usually performed in the field of experimental mechanics. Finally, making use of the introduced mathematical framework, we propose an analysis of the classic DIC solver and mention some possible alternatives, in the field of FE-DIC, based on the Inverse Compositional Gauss-Newton (ICGN) scheme, which ensure both better convergence properties and minimal computed overhead in comparison with the common solver. This work has been performed very recently in collaboration with Pr. J.-C. Passieux and following fruitful discussions with F. de Gournay regarding optimization. The interested reader is advised to consult [Passieux and Bouclier, 2019] for further details on this topic.

1.1 Formulation of DIC: a non-linear least-squares problem

1.1.1 Continuous formulation

Let us consider two grayscale images $f(x)$ and after $g(x)$ corresponding to the reference and deformed states of the specimen, respectively. The principle of Digital Image Correlation is to experimentally measure at the surface of the specimen the kinematic transformation $\phi(x,u)$, related to any pixel position x of the region

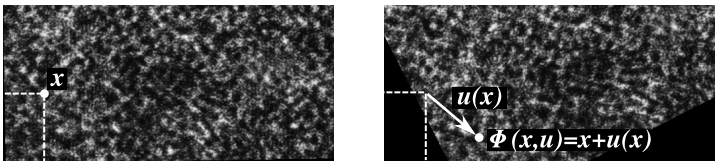

reference state image f deformed state image g

Figure 4.1 – Graylevel conservation problem: find transformation ϕ (or, in other words, displacement u) that enables to match the two graylevel digital images $f(x)$ and $g \circ \phi(x,u)$.

of interest Ω of the images, by the comparative analysis of those two graylevel digital images (see Fig. 4.1 for illustration). Mathematically, this reads: find the transformation $\phi(x,u)$ that ensures the graylevel conservation equation [Horn and Schunck, 1981]:

$$r(x,u) = f(x) - g \circ \phi(x,u) = 0, \qquad \forall x \in \Omega, \tag{4.1}$$

where a digital image f maps any sampling point $x \in \Omega$ to a quantized graylevel value $f(x)$, and $\circ$ refers to the composition operator between two applications. Note that in practice the images are obviously interpolated so as to be able to evaluate $g \circ \phi(x,u)$. This is performed in this work using a cubic spline scheme available in `python` (library: `scipy.interpolate` [Jones et al., 01]). This scheme will also enable us to directly obtain the gradient of the images at any desired point. The residual map $r(x,u)$, quantifying the non-compliance with the graylevel conservation, can be used to validate or improve the kinematic model [Réthoré et al., 2008, Neggers et al., 2017]. The unknown transformation $\phi(x,u)$ is of the form:

$$\phi(x,u) = x + u(x), \tag{4.2}$$

where $u(x)$ is the unknown displacement field. The latter is usually sought in an approximation subspace $\mathscr{U}^h$ spanned by a set of chosen basis functions $(N_i)_{i\in\{1,\dots,n\}}$:

$$u^h(x) = \sum_{i=1}^{n} N_i(x)\, u_i, \tag{4.3}$$

in which the $(u_i)_{i\in\{1,\dots,n\}}$ are the unknown coefficients of the linear combination, the so-called DOF.

Depending on the choice made for N_i, the DIC methods are divided into two main families: subset methods using mostly low-order piecewise polynomials that are discontinuous across the subsets, and global methods mainly based on finite elements, *i.e.* using piecewise polynomials continuous across elements. Using this formalism, the developments performed in this section 1 actually apply both to subset and FE-DIC, except those regarding the application of ICGN-type algorithms to the field of FE-DIC (see last paragraph of this section). Finally, pointwise problem (4.1) being ill-posed, it is classically solved in a non-linear least-squares sense over domain Ω:

$$u^{h\star} = \underset{u^h\in\mathscr{U}^h}{\arg\min}\ \frac{1}{2}\sum_{p=1}^{m} \omega_p \left(f(x_p) - g \circ \phi(x_p, u^h) \right)^2, \tag{4.4}$$

where the $(x_p)_{p\in\{1,\dots,m\}}$ are the m integration points and $(\omega_p)_{p\in\{1,\dots,m\}}$ the corresponding quadrature weights.

Remark. *One may notice that a more general FE-DIC formulation relies on camera models P:*

$$u^{h\star} = \underset{u^h\in\mathscr{U}^h}{\arg\min}\ \frac{1}{2}\sum_{p=1}^{m} \omega_p \left(f \circ P(X_p) - g \circ P \circ \phi(X_p, u^h) \right)^2. \tag{4.5}$$

A camera model $P(X)$ maps any point X in the 3D space Ω^{FE} to its corresponding point $x = P(X)$ in the image frame Ω. This formulation is required in stereo FE-DIC (FE-SDIC) (see Eq. (5.1) and Fig. 5.1 in

chapter 5, and [Pierré et al., 2017, Serra et al., 2017a] for completeness) but may improve also 2D FE-DIC [Pierré et al., 2016]. In this chapter, for the sake of clarity, the camera models are omitted. Their presence does not add any particular difficulty. Only the number, the location and the weight ω_p (including quadrature weight and determinant of the jacobian of the transformation) of the integration points would be different. In the following, we will also consider that the quadrature is performed in the image frame using pixels centers as integration points. Like this, the weights are all equal to $\omega_p = 1$ (rectangle-type rule) which further improves readability without altering generality.

Remark. *The interested reader could also notice that only standard FE will be used in this chapter for the discretization while an emphasis on spline functions is performed all over the present manuscript. It may be stressed here that the forthcoming developments could be simply applied in case of spline-based global DIC. In fact, the use of the same functions as in IGA for the discretization of global DIC has already been performed and has proved to be of high interest since it offers a natural regularization of the underlying optimization problem (see,* e.g., *[Cheng et al., 2002, Xie and Farin, 2004, Réthoré et al., 2010a, Elguedj et al., 2010, Kleinendorst et al., 2015]). In this manuscript, the attractiveness of using such functions in the context of image registration will be underlined in chapter 5 through the regularization of mesh-based 3D shape measurement.*

1.1.2 Algebraic reformulation

We now reformulate the DIC problem (4.4) algebraically so as to be closer to the standard writing encountered in an optimization framework. For the sake of clarity, we consider a one-dimensional problem for the presentation in the following. The displacement u (see Eq. (4.3)) thus constitutes an unidirectional field and x_p refers to a one-dimensional coordinate that locates pixel p. We emphasize that such a choice is adopted only to ease the reading, the implementation being, however, achieved in 2D (see section 2.3). To begin with, let us introduce vectors $\mathbf{u}$ and $\mathbf{x}$ that collects, respectively, the n parameters of our model (*i.e.*, the DOF of u^h) and the m positions of our data (*i.e.*, the pixels):

$$\mathbf{u} = \begin{pmatrix} u_1 \\ \vdots \\ u_n \end{pmatrix} \quad \text{and} \quad \mathbf{x} = \begin{pmatrix} x_1 \\ \vdots \\ x_m \end{pmatrix}. \tag{4.6}$$

Regarding notations, we perform as in previous chapters: we use capital letters in boldface type for matrices, lowercase in boldface type for vectors and letters in normal type for scalar. Let us also define the images as vectors which gather the graylevel values associated to the different pixels:

$$\mathbf{f} : \mathbf{x} \rightarrow \mathbf{f}(\mathbf{x}) = \begin{pmatrix} f(x_1) \\ \vdots \\ f(x_m) \end{pmatrix} \quad \text{and} \quad \mathbf{g} : \mathbf{x} \rightarrow \mathbf{g}(\mathbf{x}) = \begin{pmatrix} g(x_1) \\ \vdots \\ g(x_m) \end{pmatrix}. \tag{4.7}$$

The kinematic transformation $\boldsymbol{\phi}$ between reference image $\mathbf{f}$ and deformed image $\mathbf{g}$ then reads:

$$\boldsymbol{\phi} : (\mathbf{x}, \mathbf{u}) \rightarrow \boldsymbol{\phi}(\mathbf{x}, \mathbf{u}) = \mathbf{x} + \mathbf{L}_\mathbf{p}^T(\mathbf{x})\mathbf{u}, \tag{4.8}$$

where $\mathbf{L}_\mathbf{p}^T$ is a $m \times n$ matrix that collects the value of the basis functions at the pixels:

$$\mathbf{L}_\mathbf{p}^T = \begin{pmatrix} L_1(x_1) & \dots & L_n(x_1) \\ \vdots & \ddots & \vdots \\ L_1(x_m) & \dots & L_n(x_m) \end{pmatrix}. \tag{4.9}$$

With above notations, problem (4.4) consists of solving the following non-linear least-squares problem:

$$\mathbf{u}^\star = \underset{\mathbf{u}\in\mathbb{R}^n}{\arg\min}\, j(\mathbf{u}), \tag{4.10}$$

where functional j reads:

$$j(\mathbf{u}) = \frac{1}{2}\|\mathbf{r}(\mathbf{x},\mathbf{u})\|_2^2 = \frac{1}{2}\mathbf{r}(\mathbf{x},\mathbf{u})^T\mathbf{r}(\mathbf{x},\mathbf{u}), \tag{4.11}$$

the residual map $\mathbf{r}(\mathbf{x},\mathbf{u})$ being defined as:

$$\mathbf{r} : (\mathbf{x},\mathbf{u}) \rightarrow \mathbf{r}(\mathbf{x},\mathbf{u}) = \mathbf{f}(\mathbf{x}) - \mathbf{g}\circ\boldsymbol{\phi}(\mathbf{x},\mathbf{u}). \tag{4.12}$$

1.2 Resolution of DIC: descent algorithms

1.2.1 Basics

Problem (4.10) formally consists in an unconstrained optimization problem over $\mathbb{R}^n$. The functional is also differentiable since a regular interpolation scheme is used to evaluate the images. Such a problem is classically solved using descent-type algorithms [Nocedal and Wright, 2006], such as steepest (or gradient) Descent [Doumalin, 2000], Newton [Bruck et al., 1989], Gauss-Newton [Black and Jepson, 1998, Fehrenbach and Masmoudi, 2008], or Levenberg-Marquardt [Cheng et al., 2002]. The principle is as follows: starting from an initial guess $\mathbf{u}^{(0)}$, a descent algorithm iterates to generate a series $\left(\mathbf{u}^{(k)}\right)_{k\in\mathbb{N}}$ such that:

$$\mathbf{u}^{(k+1)} = \mathbf{u}^{(k)} + s^{(k)}\mathbf{d}^{(k)}. \tag{4.13}$$

$\mathbf{d}^{(k)}$ is called the descent direction. To ensure that it is a descent direction (*i.e.*, that we are able to minimize the functional along this direction), $\mathbf{d}^{(k)}$ must satisfy:

$$\nabla j\left(\mathbf{u}^{(k)}\right)^T\mathbf{d}^{(k)} < 0, \tag{4.14}$$

where ∇j denotes the gradient of j with respect to $\mathbf{u}$, namely:

$$\nabla j = \begin{pmatrix} \frac{\partial j}{\partial u_1} \\ \vdots \\ \frac{\partial j}{\partial u_n} \end{pmatrix}. \tag{4.15}$$

$s^{(k)} > 0$ is the step. The procedure consisting of determining it is called the line search procedure. Depending on the choice of the descent direction, several algorithms can be constructed. The most standard ones are written in the following for the DIC functional, *i.e.*, for j (see Eq. (4.11)). In particular, the developments hereafter will enable to better understand the foundations of the usual DIC solver which merely consists of a modified Gauss-Newton (see section 1.3).

Remark. *An important issue in gradient-based optimization concerns the initialization of the algorithms. Indeed, since the DIC problem is certainly not convex in general, the descent algorithms (if they converge) will converge to a critical point of j* (i.e., *such that $\nabla j(\mathbf{u}) = \mathbf{0}$), which thus may not be the global minimum [Nocedal and Wright, 2006]. As an improvement, some regularization schemes have been proposed in the DIC context, as will be further discussed in section 2. However, we still need to start close to a (if not gobal at least) "physical" minimum to reach it. This can be relatively well performed in DIC by resorting to coarse-graining techniques (see,* e.g., *our very recent work [Fouque et al., 2020] where a dedicated multiscale speckle pattern has been developed). The idea is to start with a coarse version of the DIC problem (thus assumed to be of better mathematical properties), find a solution, and then use it to initialize a finer DIC problem. The process is repeated until the images of highest resolution are used. More precisely, it consists in decreasingly filtering the images (usually by means of pixel aggregation [Hild and Roux, 2006, Gomes Perini et al., 2014]) and modifying the size of the apparent approximation subspace simultaneously (by acting on a Tikhonov regularization level for instance [Dufour et al., 2016, Pierré et al., 2017]).*

1.2.2 Gradient method.

As its name suggests, the gradient algorithm relies on the use of the gradient of the functional to define the descent direction. More precisely, $\mathbf{d}^{(k)} = -\nabla j\big(\mathbf{u}^{(k)}\big)$ is chosen, so that relation (4.14) is automatically satisfied. $\mathbf{x}$ being fixed, we drop it in the following. As a result, we notice that when a differential operator of the residual map $\mathbf{r}(\mathbf{x},\mathbf{u})$ is computed, this is the derivation with respect to $\mathbf{u}$ that is implicitly performed. Let us start by computing the gradient of functional j. Given its least-squares structure, we obtain:

$$\nabla j(\mathbf{u}) = \mathbf{J_r}(\mathbf{u})^T \mathbf{r}(\mathbf{u}), \tag{4.16}$$

where $\mathbf{J_r}$ is the Jacobian matrix of $\mathbf{r}$, that is, the $m \times n$ matrix such that:

$$\mathbf{J_r} = \begin{pmatrix} \frac{\partial r_1}{\partial u_1} & \cdots & \frac{\partial r_1}{\partial u_n} \\ \vdots & \ddots & \vdots \\ \frac{\partial r_m}{\partial u_1} & \cdots & \frac{\partial r_m}{\partial u_n} \end{pmatrix}. \tag{4.17}$$

Reminding that $\mathbf{r}$ is a composed application (see Eq. (4.12)), we can then write the following relation for $\mathbf{J_r}$:

$$\mathbf{J_r}(\mathbf{u}) = -\mathbf{J_g}\big(\boldsymbol{\phi}(\mathbf{u})\big)\mathbf{J}_{\boldsymbol{\phi}}(\mathbf{u}), \tag{4.18}$$

which yields:

$$\mathbf{J_r}(\mathbf{u}) = -\nabla\mathbf{G}(\mathbf{u})\ \mathbf{L}_\mathbf{p}^T, \tag{4.19}$$

where $\nabla\mathbf{G}(\mathbf{u})$ is a $m \times m$ diagonal matrix that collects the values of $\nabla g \circ \phi(x_p, u^h)$; that is, the value of ∇g evaluated at the deformed coordinate $\phi(x_p, u^h)$ of pixel p (see Eqs. (4.2) and (4.3)). We end up with:

$$\nabla j(\mathbf{u}) = -\mathbf{L_p}\ \nabla\mathbf{G}(\mathbf{u})\mathbf{r}(\mathbf{u}), \tag{4.20}$$

and therefore the gradient method series is built as follows:

$$\mathbf{u}^{(k+1)} = \mathbf{u}^{(k)} + s^{(k)}\mathbf{L_p}\ \nabla\mathbf{G}\big(\mathbf{u}^{(k)}\big)\mathbf{r}\big(\mathbf{u}^{(k)}\big). \tag{4.21}$$

Although this method may appear interesting since no linear system resolution at each iteration is required, this procedure is rarely used in DIC because it is known to converge very slowly (only the information regarding the first derivative of the functional is used), even with a suitable line search strategy. Regarding the latter, one may wish to perform the optimal line search strategy, that is, find s_k solution to:

$$s_k = \underset{s>0}{\arg\min}\ j\big(\mathbf{u}^{(k)} + s\,\mathbf{d}^{(k)}\big) \tag{4.22}$$

at each iteration. In practice, given the complexity and the cost of problem (4.22), this is seldom performed. The step is usually chosen more pragmatically so that it is not too small to limit the number of iterations of the algorithm and it is not too large to ensure its convergence. However, the gradient algorithm has the interest to be robust since it intrinsically verifies condition (4.14) and provided the step is adequately picked, it converges towards a critical point of j.

Remark. *The conjugate gradient algorithm that was the basis of our iterative solver in chapter 3 can be viewed as an improved version of the gradient algorithm to minimize a quadratic functional. Indeed, the idea behind the conjugate gradient algorithm to solve linear system* $\mathbf{Ax} = \mathbf{b}$*, with* $\mathbf{A}$ *symmetric positive-definite, is to make use of the gradient algorithm to minimize* $j(\mathbf{x}) = \frac{1}{2}\mathbf{x}^T\mathbf{Ax} - \mathbf{x}^T\mathbf{b}$*. In addition, the successive descent directions are orthogonalized in the sense of the scalar product built upon* $\mathbf{A}$*.*

1.2.3 Newton method.

To define the descent direction in the Newton method, it is required to additionally compute the Hessian matrix of j, that is, the symmetric matrix such that:

$$\mathbf{H}_j = \begin{pmatrix} \frac{\partial^2 j}{\partial u_1^2} & \cdots & \frac{\partial^2 j}{\partial u_1 \partial u_n} \\ \vdots & \ddots & \vdots \\ sym & \cdots & \frac{\partial^2 j}{\partial u_n^2} \end{pmatrix}. \tag{4.23}$$

From here on, it may be noticed that the second derivatives (*i.e.*, the curvature of the functional) are used for the minimization. As a result, the method will exhibit a higher rate of convergence as compared to that of the gradient method. Exploiting again the least-squares structure of functional j, one can write:

$$\mathbf{H}_j(\mathbf{u}) = \mathbf{J_r}(\mathbf{u})^T \mathbf{J_r}(\mathbf{u}) + \sum_{p=1}^{m} \mathbf{H}_{r_p}(\mathbf{u}) r_p(\mathbf{u}), \tag{4.24}$$

where $\mathbf{H}_{r_p}$ refers to the Hessian matrix of component p of $\mathbf{r}$, *i.e.*, of $r_p = r(x_p, u^h) = f(x_p) - g \circ \phi(x_p, u^h)$ (see Eq. (4.1)). Making use of Eq. (4.19), the first term above is easily estimable. However, the computation of $\mathbf{H}_{r_p}(\mathbf{u})$ may require further developments. In order to do so, one may first compute $\nabla r_p(\mathbf{u})$, and then, the Jacobian matrix associated to this gradient: $\mathbf{H}_{r_p}(\mathbf{u}) = \mathbf{J}_{\nabla r_p}(\mathbf{u})$. Once again, it has to be underlined that both of these operations require the derivation of a composed application. Making these precautions, we finally get:

$$\mathbf{H}_j(\mathbf{u}) = \mathbf{L_p}\, \nabla \mathbf{G}(\mathbf{u}) \nabla \mathbf{G}(\mathbf{u})\, \mathbf{L_p}^T - \mathbf{L_p}\, \mathbf{H_g}(\mathbf{u}) \mathbf{R}(\mathbf{u}) \mathbf{L_p}^T, \tag{4.25}$$

where $\mathbf{H_g}(\mathbf{u})$ and $\mathbf{R}(\mathbf{u})$ are $m \times m$ diagonal matrices that collect, respectively, $H_g \circ \phi(x_p, u^h)$ and $r(x_p, u^h)$. With the Hessian matrix at hand, the descent direction of the Newton method is obtained through the following linear system resolution:

$$\mathbf{H}_j^{(k)} \mathbf{d}^{(k)} = -\nabla j\big(\mathbf{u}^{(k)}\big). \tag{4.26}$$

$\mathbf{d}^{(k)}$ above does constitute a descent direction (see Eq. (4.14)) when $\mathbf{H}_j^{(k)}$ (*i.e.* $\mathbf{H}_j(\mathbf{u}^{(k)})$) is positive definite. Indeed, we can write in this case:

$$\nabla j\big(\mathbf{u}^{(k)}\big)^T \mathbf{d}^{(k)} = -\nabla j\big(\mathbf{u}^{(k)}\big)^T \left[\mathbf{H}_j^{(k)}\right]^{-1} \nabla j\big(\mathbf{u}^{(k)}\big) < 0. \tag{4.27}$$

With such a descent direction, it can also be shown that a good choice for the step is, for all iteration, $s^{(k)} = 1$. We thus end up with the following procedure to build the Newton method series:

$$\mathbf{u}^{(k+1)} = \mathbf{u}^{(k)} - \left[\mathbf{H}_j^{(k)}\right]^{-1} \nabla j\big(\mathbf{u}^{(k)}\big), \tag{4.28}$$

where the Hessian and the gradient operators read as in Eqs. (4.25) and (4.20), respectively.

The interest of the Newton method is that it converges quadratically. However, only a local convergence can be proven. In addition, the process requires the assembling and the resolution of a linear system at each iteration of the algorithm, which may not be desirable from a computational cost point of view. Finally, note that the presence of the second derivatives of the image may increase the sensitivity to noise.

1.2.4 Gauss-Newton method.

The Gauss-Newton method is especially built to address the minimization of a non-linear least-squares functional, which is the case in DIC. The process is particularly appealing in this case since it somehow combines the interests of the gradient method (robustness) and of the Newton strategy (convergence speed). The derivation of the algorithm can be performed in two different ways. The first one, which is almost never

carried out in the field of FE-DIC, consists of simplifying the Newton method. Indeed, it may be noticed that once the correlation residual $\mathbf{r}(\mathbf{u})$ (and so $\mathbf{R}(\mathbf{u})$) is small, that is, when we get close to the intended solution, the second term in the Hessian matrix (4.25) becomes insignificant. The Gauss-Newton method simply consists of neglecting this term. Using a step-size of 1 ($s^{(k)}$=1), the following iterative procedure is thus obtained:

$$\widetilde{\mathbf{H}}_j^{(k)}\,\mathbf{d}^{(k)} = \mathbf{b}_G^{(k)} \qquad \text{with} \qquad \mathbf{u}^{(k+1)} = \mathbf{u}^{(k)} + \mathbf{d}^{(k)}, \tag{4.29}$$

and

$$\left\{\begin{array}{rcccl} \widetilde{\mathbf{H}}_j^{(k)} & = & \mathbf{J_r}(\mathbf{u}^{(k)})^T\mathbf{J_r}(\mathbf{u}^{(k)}) & = & \mathbf{L_p}\,\nabla\mathbf{G}\big(\mathbf{u}^{(k)}\big)\nabla\mathbf{G}\big(\mathbf{u}^{(k)}\big)\,\mathbf{L_p}^T, \\ \mathbf{b}_G^{(k)} & = & -\nabla j\big(\mathbf{u}^{(k)}\big) & = & \mathbf{L_p}\,\nabla\mathbf{G}\big(\mathbf{u}^{(k)}\big)\,\mathbf{r}(\mathbf{u}^{(k)}), \end{array}\right. \tag{4.30}$$

where $\widetilde{\mathbf{H}}_j^{(k)}$ approximates the Hessian matrix $\mathbf{H}_j^{(k)}$ of j with only first derivatives. The right hand side remains the same as for Newton method (4.26). As $\widetilde{\mathbf{H}}_j^{(k)}$ still depends on $\mathbf{u}^{(k)}$, the computational cost of the standard Gauss-Newton algorithm may still appear potentially important since one assembling and one factorization need to be performed at each iteration.

Remark. *The Gauss-Newton algorithm can also be constructed by replacing, at each iteration, the non-linear least-squares problem to be solved by an approximate, linear least-squares problem. This second approach for obtaining the solver is the one that is almost always carried out in the DIC community. It is built as follows: given the current solution* $\mathbf{u}^{(k)}$*, problem* (4.10) *is replaced in the neighborhood of* $\mathbf{u}^{(k)}$ *by:*

$$\mathbf{d}^{(k)} = \underset{\mathbf{d}\in\mathbb{R}^n}{arg\,min}\left(\frac{1}{2}\left|\left|\mathbf{r}\big(\mathbf{u}^{(k)}\big) + \mathbf{J_r}\big(\mathbf{u}^{(k)}\big)\,\mathbf{d}\right|\right|_2^2\right), \tag{4.31}$$

i.e., *where* $\mathbf{r}$ *has been linearized around* $\mathbf{u}^{(k)}$*. Problem* (4.31) *being a linear least-squares problem: its solution* $\mathbf{d}^{(k)}$ *satisfies the associated normal equations, namely:*

$$\mathbf{J_r}\big(\mathbf{u}^{(k)}\big)^T\mathbf{J_r}\big(\mathbf{u}^{(k)}\big)\mathbf{d}^{(k)} = -\mathbf{J_r}\big(\mathbf{u}^{(k)}\big)^T\mathbf{r}\big(\mathbf{u}^{(k)}\big), \tag{4.32}$$

which is equivalent to (4.29)*.*

Applying the same reasoning as the one conducted for the Newton algorithm (see Eq. (4.27)), it can be shown that we do have a descent direction for the Gauss-Newton algorithm when $\widetilde{\mathbf{H}}_j^{(k)}$ is definite (it is positive by nature). In practice, provided the images possess a regular texture (*i.e.*, the gradient may vanish exclusively over a null measure subset), the condition is satisfied in FE-DIC [Fedele et al., 2013]. For higher performance, a line search strategy can also be performed to ensure the convergence of the algorithm. Therefore, this algorithm provides a good trade-off between robustness (we almost always have a descent direction), simplicity (no need to compute the second derivatives) and convergence speed (close to a quadratic convergence when $\mathbf{r}(\mathbf{u})$ becomes small). Nevertheless, as stated above, we still need to solve a linear system (that is different) at each iteration, that is why the usual DIC solver is not exactly a Gauss-Newton algorithm, as will be shown in the forthcoming section.

Remark. *The Levenberg-Marquardt algorithm can be viewed as a regularization of the Gauss-Newton algorithm. It enables to get closer to the situation of the gradient algorithm when the descent direction of the Gauss-Newton algorithm becomes less pronounced. Rather than performing such a (non-physical) regularization, we usually resort to some Tikhonov-like techniques in the field of FE-DIC which, in particular, enables to mechanically regularize the problem (see section 2).*

1.3 Classic DIC solver

We now present the algorithm conventionally used in DIC. Given the basic theoretical results recalled above, we try to understand how and why it works. We also briefly mention the alternative algorithms that we

have proposed for FE-DIC in [Passieux and Bouclier, 2019] in order to provide both better convergence and minimal computational cost.

1.3.1 Modified Gauss-Newton

In the context of DIC, starting from the Gauss-Newton algorithm (4.29), a common (and quite smart) practice is to replace term $\nabla\mathbf{G}(\mathbf{u}^{(k)})$ by $\nabla\mathbf{F}$ (*i.e.*, the diagonal matrix collecting $\nabla f(x_p)$) in the construction of the operators of the linear systems to be solved [Hild and Roux, 2012, Leclerc et al., 2011]. The resulting algorithm is no longer a Gauss-Newton. It will be referred to as modified Gauss-Newton herein:

$$\widetilde{\widetilde{\mathbf{H}}}_j\,\mathbf{d}^{(k)} = \mathbf{b}_F^{(k)} \qquad \text{with} \qquad \mathbf{u}^{(k+1)} = \mathbf{u}^{(k)} + \mathbf{d}^{(k)}, \tag{4.33}$$

and

$$\begin{cases} \widetilde{\widetilde{\mathbf{H}}}_j &= \mathbf{L_p}\,\nabla\mathbf{F}\,\nabla\mathbf{F}\,\mathbf{L_p}^T, \\ \mathbf{b}_F^{(k)} &= \mathbf{L_p}\,\nabla\mathbf{F}\,\mathbf{r}(\mathbf{u}^{(k)}). \end{cases} \tag{4.34}$$

The interest of making such a modification is obvious since the linear operator $\widetilde{\widetilde{\mathbf{H}}}_j$ can be assembled and factorized once before entering into the Gauss-Newton iterations. However, as we leave the strict framework of Gauss-Newton, there is no proof that the method is convergent.

This approximation is frequently justified in the literature by the fact that, by virtue of the graylevel conservation principle, these two quantities would be equal in the neighborhood of the final solution and when small deformations are expected (see [Réthoré, 2010, Leclerc et al., 2012, Passieux and Périé, 2012, Réthoré et al., 2013, Van Beeck et al., 2014, Passieux et al., 2015b, Wittevrongel et al., 2015, Neggers et al., 2016, Bouclier and Passieux, 2017, Buljac et al., 2018a, Neggers et al., 2018a], to name a few). From here on, it seems important to clarify the terminology employed for the standard continuum mechanics assumptions mentioned here. The case of small deformations means that displacements, rotations and strains are small while only the strains are assumed to be small in the small strain or large deformation context. In the same idea, we will use the naming large strains when large strains (and so, including large deformations) are expected. Returning to the justification of the replacement of $\nabla\mathbf{G}(\mathbf{u}^{(k)})$ by $\nabla\mathbf{F}$, perhaps the more advanced reasoning so far comes as follows [Neggers et al., 2016]: denoting the converged solution by $\mathbf{u}^{(\infty)}$, the derivative with respect to $\mathbf{x}$ of the graylevel conservation (4.1) gives:

$$\begin{aligned} \nabla\mathbf{F} &= \nabla\big(\mathbf{g}\circ\boldsymbol{\phi}(\mathbf{x},\mathbf{u}^{(\infty)})\big) && (4.35)\\ &= \nabla\boldsymbol{\phi}(\mathbf{x},\mathbf{u}^{(\infty)})\,\nabla\mathbf{g}\circ\boldsymbol{\phi}\big(\mathbf{x},\mathbf{u}^{(\infty)}\big) && (4.36)\\ &= \big(\mathbf{I}+\nabla\mathbf{U}^{(\infty)}\big)\,\nabla\mathbf{G}\big(\mathbf{u}^{(\infty)}\big) && (4.37)\\ &= {\boldsymbol{F}^{(\infty)}}^T\,\nabla\mathbf{G}\big(\mathbf{u}^{(\infty)}\big), && (4.38) \end{aligned}$$

where $\nabla\mathbf{U}$ and $\boldsymbol{F}^{(\infty)}$ are $m\times m$ diagonal matrices that collect the value of the gradient of the displacement and the gradient of the kinematic transformation at integration point x_p, respectively. $\mathbf{I}$ is the identity matrix of size m. Given equality (4.38) and assuming small defomations as well as a good initialization of the optimization algorithm, the replacement of $\nabla\mathbf{G}(\mathbf{u}^{(k)})$ by $\nabla\mathbf{F}$ can be partly explained [Gras et al., 2013, Neggers et al., 2016, Passieux et al., 2018]. However, as will be shown below, the framework of small deformations is a sufficient condition, but it is certainly not a necessary condition. Indeed, investigating the equality of the two image gradients is actually not the good path to follow to qualify the convergence properties of the usual DIC solver. The convergence of the optimization algorithm should rather be studied with respect to its ability to produce a descent direction. This is what we propose in the following.

The search direction provided by the standard DIC solver must satisfy condition (4.14), that is for the present situation:

$$-\left(\mathbf{b}_G^{(k)}\right)^T\,\widetilde{\widetilde{\mathbf{H}}}_j^{-1}\,\mathbf{b}_F^{(k)} < 0. \tag{4.39}$$

It may be noticed, by the way, that it would not be excessively expensive (scalar product only) to test this condition, for example, at the first iteration of the modified Gauss-Newton. This convergence condition on the search direction can be interpreted as the following condition on the unknown displacement field $\mathbf{u}^{(\infty)}$:

$$-\mathbf{r}^T \nabla\mathbf{G}\, \mathbf{L}_\mathbf{p}^T \tilde{\tilde{\mathbf{H}}}_j^{-1} \mathbf{L}_\mathbf{p} \left(\mathbf{I} + \nabla\mathbf{U}^{(\infty)}\right) \nabla\mathbf{G}\, \mathbf{r} < 0, \tag{4.40}$$

where the dependence on $\mathbf{u}^{(k)}$ of $\mathbf{r}$ and $\nabla\mathbf{G}$ has been omitted for clarity. The transformation gradient $\boldsymbol{F}^{(\infty)} = (\mathbf{I} + \nabla\mathbf{U}^{(\infty)})^T$ being diagonal, its positivity is a necessary and sufficient condition, in 1D at least, to fulfill condition (4.40). As a result, the non-compliance of relation (4.40) can be interpreted mechanically as the following condition on u:

$$\varepsilon_x = \frac{\partial u}{\partial x} < -1, \tag{4.41}$$

which is an unlikely event in continuum mechanics (overlap of matter). In any case, it is much less restrictive than the simple framework of small deformations. We conjecture that in the general case (2D), the positivity of the transformation gradient $\boldsymbol{F}^{(\infty)}$ is closely related to the convergence of the modified GN algorithm. In [Passieux and Bouclier, 2019], we investigated the behavior of the algorithm when measuring large rigid rotations as in [Neggers et al., 2016]. Through this test case, we have been able to numerically confirm the link between the positivity of $\boldsymbol{F}^{(\infty)}$ and the ability of the modified Gauss-Newton to converge. In particular, unlike in [Neggers et al., 2016], we obtained good results for rotation angles up to 90° using an appropriate choice of the step-size. For larger rotations, the algorithm failed since $\boldsymbol{F}^{(\infty)}$ was negative. However, it has to be said that there is no reason to proscribe general large deformations (or even large strains) with regard to condition (4.40). Another test has been performed in [Passieux and Bouclier, 2019]: large stretch and shear strains (up to 180%) have been prescribed and the modified Gauss-Newton perfectly worked (as long as a good initialization was performed).

1.3.2 Some alternatives for FE-DIC

To further improve the classic solver when applied to FE-DIC, we developed several variants in [Passieux and Bouclier, 2019] that involve a constant Hessian operator through the optimization iterations, and that converge regardless of the measured kinematic field. The goal is to provide both robustness and efficiency when dealing with a massive amount of data. Only the fundamentals are given here. Once again, the interested reader is urge to consult [Passieux and Bouclier, 2019] for further details.

A very simple strategy. Based on consideration (4.40), a very simple way to build up an algorithm that ensure a descent direction consists in replacing $\nabla\mathbf{G}(\mathbf{u}^{(k)})$ by $\nabla\mathbf{F}$ for the construction of the approximate Hessian only and to keep the exact expression of the right hand side:

$$\tilde{\tilde{\mathbf{H}}}_j\, \mathbf{d}^{(k)} = \mathbf{b}_G^{(k)}. \tag{4.42}$$

As the true Gauss-Newton (4.29), this method should almost always provide a descent direction (4.14). From the numerical experiments we have done, this method worked well and in any case. However, it may be noticed that this involves computing $\nabla\mathbf{G}(\mathbf{u}^{(k)})$ for $\mathbf{b}_G^{(k)}$ which (with our implementation) did not provide sufficiently reduced computing overhead as compared to that of the true Gauss-Newton method. Still, it may be an interesting alternative since it is safe and very easy to implement.

Inverse and forward compositional Gauss-Newton. The second approach is based on the family of Compositional Gauss-Newton (CGN) algorithms which was first introduced in image processing in [Baker and Matthews, 2001]. Many variants (inverse, forward, compositionnal, etc) were then developed [Baker and Matthews, 2004, Tong, 2013] and applied to subset-DIC [Tong, 2013, Pan et al., 2013, Sánchez, 2016, Stanier et al., 2016] and subset-Digital Volume Correlation (DVC) [Pan et al., 2014]. The elegant idea behind these algorithms is to perform a specific linearization of the minimization problem in

such a way that the use of a Gauss-Newton naturally leads to a constant operator. More precisely, displacement $\mathbf{u}^{(k)}$ being known, it consists in computing a correction $-\tilde{\mathbf{d}}^{(k)}$ that moves image $\mathbf{f}$ to image $\mathbf{g}(\mathbf{x}+\mathbf{u}^{(k)})$. The resolution leads exactly to the same linear system (4.33) as with the modified Gauss-Newton method of the standard DIC problem. It thus has the double advantage of leading to a constant operator while remaining within the strict framework of a Gauss-Newton. Only the update of the running approximation $\mathbf{u}^{(k)}$ changes: it requires to inverse the kinematic transformation to propagate correction $-\tilde{\mathbf{d}}^{(k)}$ from image $\mathbf{f}$ to $\mathbf{g}$. In the literature, the ICGN algorithm was mainly applied to subset DIC methods associated with affine transformations (rigid body translations, linear warping or homographies) since in this case the inversion was trivial. In [Passieux and Bouclier, 2019] we propose inverse and forward CGN algorithms for the field of FE-DIC with general kinematic discretizations. The key point is to consider a linearization of the displacement to approximate the inversion. We do not go further into the details in the present manuscript. Note that at the end, the only difference compared to the common DIC solver lies in the addition of a second correction term (obtained from two $\frac{n}{2} \times \frac{n}{2}$ vector-matrix products in 2D) to $\mathbf{u}^{(k)}$ at each iteration.

With these CGN alternatives, whatever the angle of rotation, even up to extreme rotations angles such as $\theta = 180°$, we have able to obtain accurate results within a minimal number of iterations. We also studied the extra computing cost which appears to be very modest since there are only two additional matrix-vector products of size $n/2$ to be carried out at each iteration.

Summary and discussion. To sum up, we have proposed in this first section a mathematical analysis of the most commonly used algorithm in FE (and subset) DIC. In order to do so, we simply apply the standards of gradient-based optimization to the non-linear least-squares problem encountered in DIC. It has been shown that the algorithm widely used in the experimental mechanics community consists of a modified Gauss-Newton and that it is usually convergent when applied to the measurement of solid mechanics phenomena. More precisely, a condition on the DIC operators has been established to ensure to provide a descent direction. This condition is also interpreted as a condition on the displacement field. Contrary to what is sometimes stated in the literature, this condition (positivity of the gradient of the kinematic transformation $\boldsymbol{F}^{(\infty)} = (\mathbf{I} + \nabla \mathbf{U}^{(\infty)})^T$) is much broader than the case of small deformations (or small rotations). In particular, we have been able to obtain accurate results for rigid rotations up to angles of 90° (using an appropriate choice of the step-size) and for very large strain levels.

For very specific kinematic transformations (such as when rotations exceed 90°), the classic algorithm may not converge. In such situations, it should be stressed that even if the algorithm is initialized very close to the solution (even with the exact solution if it exists) it will diverge. We show that updating the correlation operator at each iteration (like in the exact Gauss-Newton) [Neggers et al., 2016] is not the only way to reach convergence in this case. Several alternatives mainly based on the family of Compositional Gauss-Newton algorithms are proposed for the specific situation of FE-DIC. At very little extra cost and using the same operators (and the same image gradients) as with the usual solver, we have been able to obtain accurate results even in case of very large rotations. This tends to confirm that the approximation on images gradients in DIC is not the problem.

The proposed new algorithms for global (or FE) -DIC may prove useful in particular (i) for evolution problems, where one operator is assembled and factorized once for all GN iterations and for each time-step and (ii) for stereo DIC where projector gradients may evolve during iterations. Additionally, the treatment that we needed to perform to achieve the inversion in case of FE-DIC may be easily transpose to the case of subset-DIC. This would allow to enlarge the scope of the ICGN algorithm in the field of subset-DIC: we should be able to end up with an ICGN strategy adapted to higher-order subset-DIC. For better numerical efficiency, these solvers could be coupled with HPC tools [Merta et al., 2014, Passieux et al., 2015b, Ronovsky and Vasatova, 2017, Bouclier and Passieux, 2017, Wang and Kemao, 2018, Tournier et al., 2019]. A work in this direction is performed in the remainder of this chapter.

2 A domain coupling method for FE-DIC with mechanical regularization

The initial DIC problem relying on the least-square minimization of the graylevel mismatch (4.1) cannot be solved pointwise without considering some regularization (with an associated characteristic length). Indeed, merely looking for a vector-valued displacement function from a scalar-valued pixel function makes it an under-determined problem (broadly speaking, we have one scalar equation for two unknowns). In practice, this regularization length is associated to the window or element size (given by the basis functions $(N_i)_{i\in\{1,\dots,n\}}$ (4.3)) when using subset or FE-DIC, respectively. This way of regularizing DIC (*i.e.*, using formulation (4.4)) leads to a tradeoff between FE interpolation error and so-called ultimate random error (that is related to the ill-posedness of the inverse problem) [Bornert et al., 2009, Passieux et al., 2015a]. Indeed, the finer the mesh, the better the accuracy of the numerical solution but the worse the well-posedness of the inverse problem. Another great interest of using finite elements in DIC is that it is possible to regularize the DIC problem more softly, based on the knowledge of a FE mechanical model [Réthoré et al., 2009, Réthoré, 2010, Leclerc et al., 2011, Leclerc et al., 2012, Réthoré et al., 2013, Réthoré, 2015, Lehoucq et al., 2015]. From a mathematical point of view, the mechanical regularization can be viewed as a specific Tikhonov regularization [Tarantola, 2014], the Tikhonov matrix being chosen in accordance with the mechanical phenomenon to be observed. Originally introduced for fracture analysis [Réthoré et al., 2009], this mechanically regularized FE-DIC (named R-DIC in the following) is of special interest when facing some challenging situations, like, for instance, in Digital Volume Correlation (DVC) [Leclerc et al., 2012], where the speckle pattern is not rich enough [Requena et al., 2009, Morgeneyer et al., 2013], or for identification purposes [Réthoré, 2010, Réthoré et al., 2013].

In this section, we design a DD algorithm that allows for analyzing large images with R-DIC. However, the drawback of FE (or any global) -DIC over subset-DIC when high resolution images are required is the computational cost [Leclerc et al., 2011, Passieux and Périé, 2012, Gomes Perini et al., 2014]. Indeed, subset based DIC approaches lead to a set of small independent nonlinear systems of equations (formulated on each subset) that are highly parallelisable, whereas the global DIC method leads to one global non-linear system whose resolution can become prohibitive with a large number of DOF. In order to realize this, one may look at the structure of operator $\widetilde{\widetilde{\mathbf{H}}}_j$ (see Eq. (4.34)): in case of FE-DIC it is a sort of a FE "mass" matrix (thus sparse but global) while in subset DIC it simply constitutes a block diagonal operator (the basis functions gathered in $\mathbf{L_p}$ being discontinuous from a subset to another). This feature certainly explains why the subset-DIC approach is almost always encountered in the current commercial DIC software.

After reviewing the mechanical regularization scheme, we develop here a novel method to couple different domains analyzed by R-DIC. The challenge is that not only the displacement must be continuous across the interface, but also the underlying mechanical models used to regularize must be in equilibrium. If the kinematic compatibility can be classically enforced by introducing a Lagrange multiplier (as in chapters 2 and 3), the static constraint requires a specific treatment. Indeed, the mechanical regularization in R-DIC relies on the minimization of the L^2-norm of the internal forces, which is not standard in computational mechanics. To be able to split the regularization term, we propose to make use of a new interface unknown, which can be interpreted as the interface reaction force but does not constitute a Lagrange multiplier from a numerical point of view. The method is finally extended to parallel computing thanks to the use of an advanced Krylov solver and the construction of a dedicated preconditioner. This was actually the first work for me connected to DIC and, more broadly, to numerical optimization. It is the result of a collaboration with Pr. J.-C. Passieux on DIC that I started at the beginning of my assistant professor position at INSA-Toulouse. More precisely, this part is extracted from [Bouclier and Passieux, 2017].

2.1 Mechanical regularization

The mechanical regularization consists in complementing FE-DIC with an additional penalization on the distance between the estimated displacement field and its projection onto the space of FE mechan-

ical solutions. More precisely, in the context of linear elasticity, the method consists in adding to the DIC functional j (see (4.11)) the L^2-norm of the internal forces (in the spirit of the Equilibrium Gap Method [Claire et al., 2004]):

$$j_{\text{reg}}(\mathbf{u}) = \frac{1}{2}\|\overline{\mathbf{K}}\,\mathbf{u}\|_2^2 = \frac{1}{2}\mathbf{u}^T\overline{\mathbf{K}}^T\overline{\mathbf{K}}\,\mathbf{u}. \tag{4.43}$$

As in section 1, $\mathbf{u}$ denote the DOF of the FE displacement u^h. $\overline{\mathbf{K}}\,\mathbf{u}$ is the vector that collects the internal forces for each DOF except those supported by the nodes that are concerned with Dirichlet or non-zero Neumann boundary conditions (see Fig. 4.2 for an illustration in the case of a bi-axial tensile test). Such a DOF selection appears necessary here since we do not know well the boundary conditions. Operator $\overline{\mathbf{K}}$ is in practice obtained as follows:

$$\overline{\mathbf{K}} = \mathbf{S}\,\mathbf{K}, \tag{4.44}$$

where $\mathbf{K}$ is the elastic FE stiffness matrix for the considered mesh and $\mathbf{S}$ is a selection matrix that allows to select the DOF to be regularized. $\mathbf{S}$ formally reads as a diagonal matrix with one if the corresponding DOF is controlled and zero otherwise. From here on, it has to be underlined that the norm application in (4.43) is over $\mathbb{R}^n$ (*i.e.*, the space related to the DOF) while the norm for the initial DIC residual (4.11) was over $\mathbb{R}^m$ (*i.e.*, the space related to the image pixels).

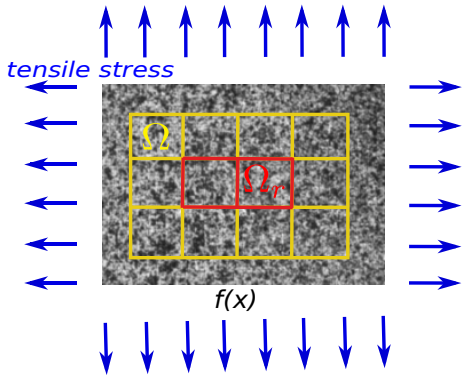

Figure 4.2 – Reference image f with its underlying mesh for FE-DIC with mechanical regularization. Note that only the DOF in subdomain Ω_r are regularized.

A weighted sum of both quadratic distances ($j(\mathbf{u})$ and $j_{\text{reg}}(\mathbf{u})$) is then considered for the minimization:

$$j_{\text{tot}}(\mathbf{u}) = j(\mathbf{u}) + \eta(l_c)\; j_{\text{reg}}(\mathbf{u}), \tag{4.45}$$

where $\eta(l_c)$ is the weighting parameter. It has been shown that such a regularization introduces a mechanical low-pass filter whose cut-off wavelength l_c can be controlled [Leclerc et al., 2012]. For the sake of readability, we omit the dependence on l_c in the following: we write $\eta(l_c) = \eta$. The study and proper choice of this parameter (see, for instance, [Leclerc et al., 2011, Réthoré et al., 2009, Claire et al., 2004]) is beyond the scope the works reported in this section, whose purpose is to develop a coupling method for FE-DIC that uses such a regularization. Replacing Eq. (4.11) by Eq. (4.45) and applying the same strategy as in section 1.3, system (4.33) becomes as follows to compute the modified Gauss-Newton update at iteration k:

$$\left(\widetilde{\widetilde{\mathbf{H}}}_j + \eta\,\overline{\mathbf{K}}^T\overline{\mathbf{K}}\right)\mathbf{d}^{(k)} = \mathbf{b}_F^{(k)} - \eta\,\overline{\mathbf{K}}^T\overline{\mathbf{K}}\,\mathbf{u}^{(k)} \qquad \text{with} \qquad \mathbf{u}^{(k+1)} = \mathbf{u}^{(k)} + \mathbf{d}^{(k)}. \tag{4.46}$$

The new correlation operator $\widetilde{\widetilde{\mathbf{H}}}_j + \eta\,\overline{\mathbf{K}}^T\overline{\mathbf{K}}$ is symmetric positive definite as its classical counterpart. In the following, this mechanically regularized FE-DIC method is denoted by R-DIC.

Remark. *Even if a strict equivalent of* (4.43) *is not available in the continuous setting, minimizing* $j_{\text{reg}}(\mathbf{u})$ *may be interpreted as minimizing* $\|\text{div}(\sigma)\|$ *over the region of interest* Ω *and* $\|\sigma n\|$ *over the traction-free*

boundaries of $\overline{\Omega}$ (σ and n being, respectively, the Cauchy stress tensor and the outward unit normal to Ω).

Remark. *Although the above introduced regularization scheme can be interpreted as a specific Tikhonov regularization, it may be noticed that a distinction is usually performed in the field of DIC between the mechanical and the Tikhonov regularization. Indeed, Tikhonov regularization often means in the DIC community that a penalization on the Laplacian of the displacement is performed [Passieux and Périé, 2012, Dufour et al., 2016, Pierré et al., 2017].*

2.2 Coupling method

We now address the coupling of multiple domains in R-DIC. Our starting point is the coupling method developed for FE-DIC without mechanical regularization in [Passieux et al., 2015b]. From this contribution, the proposed scheme simply constitutes an extension to be able to take into account an elastic regularization of the optical flow. From the point of view of domain coupling, it can be viewed as an extension of the Mortar non-overlapping coupling, typically performed in the field of domain decomposition (see chapter 3), that enables to separate term (4.45) between the subdomains. The specific nature of term (4.43) leads us to build an original mixed method. To ease the reading, the same formalism as in chapters 2 and 3 is used in what follows for the presentation of the coupling method.

2.2.1 R-DIC coupling problem

Let us consider a non-overlapping partition of the region of interest Ω into a set subdomains Ω_s. In addition, we subdivide images f and g in a set of rectangular subset images f_s and g_s surrounding subdomain Ω_s as it is usually performed in subset-based approaches [Sutton et al., 2009]. Without loss of generality, the method is first presented in the case of two subdomains: Ω_1 and Ω_2 that are connected along interface Γ. As well, we introduce for the mechanical regularization the two subdomains Ω_{r_1} and Ω_{r_2} with their common interface Γ_r (see Fig. 4.3, the corresponding initial FE-DIC problem being the one illustrated in Fig. 4.2). Regarding the discretization, we consider in this chapter the simple case of matching meshes. However, let us quote that the method could apply in the more general context of non-matching (or even non-conforming) interfaces, provided that the same precautions as in chapters 2 and 3 are taken.

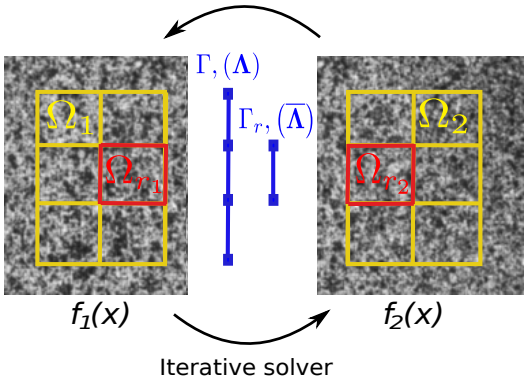

Figure 4.3 – Domain Ω decomposition in two subdomains Ω_s and two subset images f_s. Note that subdomains and submeshes are not overlapping but subset images are.

2.2.2 Formulation of the coupling method

In view of developing a DD solver for R-DIC in a second step, we frist need to write the reference problem (minimization of cost function (4.45)) as a sum of local problems over Ω_1 and Ω_2 and to restrict the exchange of data to interface Γ.

Case of FE-DIC without mechanical regularization. When restricted to FE-DIC without mechanical regularization (minimization of cost function (4.4)), it suffices to make use of the additivity of the integral with respect to domain Ω and to prescribe the displacement continuity across interface Γ to satisfy the C^0 regularity of the FE space $\mathscr{U}^h$. This strategy is performed in [Passieux et al., 2015b] by resorting to a Lagrange multiplier-type formulation. More precisely, this leads to the following Lagrangian:

$$L_{\text{DIC}}(u_1^h, u_2^h, \lambda^h) = \frac{1}{2}\int_{\Omega_1}\Big(f_1(x) - g_1 \circ \phi(x, u_1^h)\Big)^2 \mathrm{d}\Omega_1 + \frac{1}{2}\int_{\Omega_2}\Big(f_2(x) - g_2 \circ \phi(x, u_2^h)\Big)^2 \mathrm{d}\Omega_1 + b\Big(\lambda^h, u_1^h - u_2^h\Big), \quad (4.47)$$

where bilinear form b is defined as in Eq. (2.6) and $\lambda^h \in \mathscr{M}^h$ ($\mathscr{M}^h$ being spanned by the trace on Γ of the FE shape functions of $\mathscr{U}^h$). Combining then the procedure of section 1.3 and of chapters 2 or 3 (see, *e.g.*, Eq. (2.8)) to minimize L_{DIC}, system (4.33) is augmented as follows to compute the modified Gauss-Newton update at iteration k:

$$\begin{bmatrix} \widetilde{\widetilde{\mathbf{H}}}_{j_1} & 0 & \mathbf{C}_1^T \\ 0 & \widetilde{\widetilde{\mathbf{H}}}_{j_2} & -\mathbf{C}_2^T \\ \mathbf{C}_1 & -\mathbf{C}_2 & 0 \end{bmatrix} \begin{bmatrix} \mathbf{d}_1^{(k)} \\ \mathbf{d}_2^{(k)} \\ \boldsymbol{\lambda} \end{bmatrix} = \begin{bmatrix} \mathbf{b}_{F_1}^{(k)} \\ \mathbf{b}_{F_2}^{(k)} \\ -\mathbf{C}_1\mathbf{u}_1^{(k)} + \mathbf{C}_2\mathbf{u}_2^{(k)} \end{bmatrix} \quad \text{with} \quad \mathbf{u}^{(k+1)} = \mathbf{u}^{(k)} + \mathbf{d}^{(k)}. \quad (4.48)$$

$\mathbf{C}_1$ and $\mathbf{C}_2$ are the standard Mortar operators (see, *e.g.*, Eq. (2.9)).

Extension to R-DIC. For the term $j_{\text{reg}}(\mathbf{u})$ in Eq. (4.43), such a strategy to build the coupling does not directly apply since the norm over $\mathbb{R}^n$ cannot be easily split to obtain separated contributions between subdomains Ω_1 and Ω_2. Indeed, considering that the displacement is continuous across Γ, we can only make use of the additivity of vector $\overline{\mathbf{K}}\mathbf{u}$ on Ω to get:

$$\min_{\mathbf{u}} \frac{1}{2}\Big(\|\overline{\mathbf{K}}\,\mathbf{u}\|_2^2\Big) = \min_{\substack{\mathbf{u}_1,\mathbf{u}_2 \\ \mathbf{u}_1 = \mathbf{u}_2 \text{ on } \Gamma}} \frac{1}{2}\Big(\|\overline{\mathbf{K}}_1\,\mathbf{u}_1 + \overline{\mathbf{K}}_2\,\mathbf{u}_2\|_2^2\Big), \quad (4.49)$$

with:

$$\|\overline{\mathbf{K}}_1\,\mathbf{u}_1 + \overline{\mathbf{K}}_2\,\mathbf{u}_2\|_2^2 = \mathbf{u}_1^T\overline{\mathbf{K}}_1^T\overline{\mathbf{K}}_1\mathbf{u}_1 + \mathbf{u}_2^T\overline{\mathbf{K}}_2^T\overline{\mathbf{K}}_2\mathbf{u}_2 + 2\mathbf{u}_1^T\overline{\mathbf{K}}_1^T\overline{\mathbf{K}}_2\mathbf{u}_2. \quad (4.50)$$

The problem of directly using expression (4.50) is that it requires to merge the contributions of the subdomains, which is not compatible with parallel computer architectures. As a consequence, we propose instead to consider the following coupling approximation for the minimization of $j_{\text{reg}}(\mathbf{u})$:

$$\min_{\mathbf{u}_1,\mathbf{u}_2} \frac{1}{2}\Big(\|\overline{\mathbf{K}}_1\,\mathbf{u}_1 + \overline{\mathbf{K}}_2\,\mathbf{u}_2\|_2^2\Big) \approx \min_{\substack{\mathbf{u}_1,\mathbf{u}_2,\overline{\boldsymbol{\lambda}} \\ \mathbf{u}_1 = \mathbf{u}_2 \text{ on } \Gamma}} \frac{1}{2}\Big(\|\overline{\mathbf{K}}_1\,\mathbf{u}_1 + \overline{\mathbf{C}}_1^T\,\overline{\boldsymbol{\lambda}}\|_2^2 + \|\overline{\mathbf{K}}_2\,\mathbf{u}_2 + \overline{\mathbf{C}}_2^T\,\overline{\boldsymbol{\lambda}}\|_2^2\Big). \quad (4.51)$$

In this equation, a new unknown $\overline{\lambda}^h$ (with corresponding DOF vector $\overline{\boldsymbol{\lambda}}$) is introduced to control the mechanical equilibrium at the subdomains interface Γ_r. $\overline{\lambda}^h$ is searched for in space $\overline{\mathscr{M}}^h$ that is spanned by the trace on Γ_r of the shape functions of $\mathscr{U}^h$ (see, again, Fig. 4.3). $\overline{\mathbf{C}}_s$ are the associated Mortar coupling operators. It has to be noted that the hypothetical case of an exact satisfaction of the mechanical equilibrium between subdomains is recovered with the proposed coupling. In this case, the coupling cost function (4.51) reaches zero at interface Γ_r and thus, $\overline{\boldsymbol{\lambda}}$ exactly corresponds to the discrete interface reaction forces of the two subdomains. However, it has also to be underlined that the proposed coupling is suitable for the more general situation of a displacement u^h that does not exactly satisfy the discrete interface equilibrium constraint. Indeed, we emphasize that the static constraint is not enforced exactly as it is done for the displacement (see third term in Eq. (4.47)), but through a minimization using the L^2 norm. This allows to represent a little discrepancy between the two discrete interface reaction forces of the two subdomains.

This is of crucial importance here because there is no reason that the mechanical residual (4.51) reaches zero at Γ_r when combined with the correlation residual (4.47).

By performing a weighted sum of the two residuals (4.47) and (4.51), we are able to write the version of Eqs. (4.48) that involves a mechanical regularization of the optical flow. The corresponding linear system reads:

$$\begin{bmatrix} \widetilde{\widetilde{\mathbf{H}}}_{j_1}+\eta\,\overline{\mathbf{K}}_1^T\overline{\mathbf{K}}_1 & 0 & \mathbf{C}_1^T & \eta\,\overline{\mathbf{K}}_1^T\overline{\mathbf{C}}_1^T \\ 0 & \widetilde{\widetilde{\mathbf{H}}}_{j_1}+\eta\,\overline{\mathbf{K}}_2^T\overline{\mathbf{K}}_2 & -\mathbf{C}_2^T & \eta\,\overline{\mathbf{K}}_2^T\overline{\mathbf{C}}_2^T \\ \mathbf{C}_1 & -\mathbf{C}_2 & 0 & 0 \\ \eta\,\overline{\mathbf{C}}_1\overline{\mathbf{K}}_1 & \eta\,\overline{\mathbf{C}}_2\overline{\mathbf{K}}_2 & 0 & \eta\left(\overline{\mathbf{C}}_1\overline{\mathbf{C}}_1^T+\overline{\mathbf{C}}_2\overline{\mathbf{C}}_2^T\right) \end{bmatrix} \begin{bmatrix} \mathbf{d}_1^{(k)} \\ \mathbf{d}_2^{(k)} \\ \boldsymbol{\lambda} \\ \overline{\boldsymbol{\lambda}} \end{bmatrix} = \begin{bmatrix} \mathbf{b}_{F_1}^{(k)}-\eta\,\overline{\mathbf{K}}_1^T\overline{\mathbf{K}}_1\mathbf{u}_1^{(k)} \\ \mathbf{b}_{F_2}^{(k)}-\eta\,\overline{\mathbf{K}}_2^T\overline{\mathbf{K}}_2\mathbf{u}_2^{(k)} \\ -\mathbf{C}_1\mathbf{u}_1^{(k)}+\mathbf{C}_2\mathbf{u}_2^{(k)} \\ -\eta\overline{\mathbf{C}}_1\overline{\mathbf{K}}_1\mathbf{u}_1^{(k)}-\eta\overline{\mathbf{C}}_2\overline{\mathbf{K}}_2\mathbf{u}_2^{(k)} \end{bmatrix}. \tag{4.52}$$

In practice, the coupling Gauss-Newton algorithm is initialized by the solution of classical FE-DIC problems without mechanical regularization on each subdomain independently. This provides a good initial estimate since the remaining work performed by the coupling algorithm only consists in imposing the continuity of the displacement across Γ and ensuring the mechanical equilibrium of the underlying mechanical models used for regularization.

Remark. *Even if it can be interpreted as the interface reaction force, let us notice that the new unknown $\overline{\lambda}^h$ does not constitute a Lagrange multiplier from a numerical point of view. As a consequence, the situation differs from what we more usually have in computational mechanics, which explains the atypical structure of system* (4.52) *(compared,* e.g.*, to system* (3.14) *where two real Lagrange multipliers were used). The products of Mortar coupling operators and stiffness matrices appear (see cross terms) and the diagonal term associated to the second interface unknown is not zero.*

Remark. *It may be noted that there is no evidence that the constructed coupling formulation is consistent with the initial R-DIC problem. This is inherent to the fact that the mechanical equilibrium is controlled through a minimization. Except in the hypothetical case of an exact satisfaction of the interface equilibrium constraint, the equality in Eq.* (4.51) *may not be reached. Nevertheless, we were not able to observe any representative difference between the coupling solution (coming from system* (4.52)*) and the initial solution (obtained in Eq.* (4.46)*) in our numerical experiments. Whatever the level of regularization is, the method yields the solution of the standard one domain R-DIC problem, which accounts for the reliability of the proposed coupling strategy to be used in R-DIC analysis.*

2.3 Application to high performance computing

As mentionned at the begining of section 2, the drawback of FE-DIC over subset-DIC is the computational cost when high resolution measurements on large images are required. The computational burden associated to FE-DIC in such situations is mostly due to the inversion of the finite element systems (4.33) (or (4.46) in R-DIC) and to image interpolations (required to compute the right hand side $\mathbf{b}_F^{(k)}$, see Eqs. (4.34) and (4.12)). As demonstrated in [Passieux et al., 2015b], a dual DD method for FE-DIC without mechanical regularization can be implemented to combine the advantages of FE-DIC (direct bridge with simulation, continuity, etc) and subset-DIC (parallelization ability). By making use of the coupling formulation introduced in section 2.2, we now extend the strategy for the parallel computation of R-DIC. The same path as in chapter 3[section 3] , *i.e.* based on the adaptation of the initial one-level FETI algorithm [Farhat and Roux, 1991], is followed here. Compared to the work performed in chapter 3, more simplicity is expected since, as stated above, the local R-DIC operators $\widetilde{\widetilde{\mathbf{H}}}_{j_s}+\eta\,\overline{\mathbf{K}}_s^T\overline{\mathbf{K}}_s$ (see (4.52)) are invertible (in other words, the formulation and solving of a coarse problem is not required any more). However, the

important challenge here is that the coupling formulation is atypical for the field of computational mechanics (see again structure of system (4.52) compared to that of (3.14)), thus implying to resort to an advanced Krylov solver and to develop a new preconditioner.

2.3.1 Construction of the interface problem

The starting point is to write the interface problem associated to the coupling. This is simply preformed by applying procedure (3.17)-(3.22) without caring about the floating subdomains issue. System (4.52) is first split into the following coupled equations:

$$\mathbf{d}_s^{(k)} = \left(\widetilde{\widetilde{\mathbf{H}}}_{j\,s} + \eta\,\overline{\mathbf{K}}_s^T\overline{\mathbf{K}}_s\right)^{-1}\left(\mathbf{b}_{F_s}^{(k)} - \eta\,\overline{\mathbf{K}}_s^T\overline{\mathbf{K}}_s\mathbf{u}_s^{(k)} - \mathbf{C}_s^T\boldsymbol{\lambda} - \eta\,\overline{\mathbf{K}}_s^T\overline{\mathbf{C}}_s^T\overline{\boldsymbol{\lambda}}\right) \quad \forall s, \tag{4.53a}$$

$$\left.\begin{array}{l}\displaystyle\sum_s \mathbf{C}_s\left(\mathbf{d}_s^{(k)} + \mathbf{u}_s^{(k)}\right) = \mathbf{0} \\ \displaystyle\sum_s \eta\,\overline{\mathbf{C}}_s\left(\overline{\mathbf{K}}_s\left(\mathbf{d}_s^{(k)} + \mathbf{u}_s^{(k)}\right) + \overline{\mathbf{C}}_s^T\overline{\boldsymbol{\lambda}}\right) = \mathbf{0}\end{array}\right. ; \tag{4.53b}$$

assuming now an arbitrary number of subdomains. Note that sign + or - has been included in $\mathbf{C}_s$ in the above equations: $\mathbf{C}_s$ formally read as rectangular signed Boolean operators such that if a DOF belongs to Γ, its value is set to 1, and the corresponding DOF on the other side of Γ is set to -1. By substituting Eq. (4.53a) into Eq. (4.53b), the coupled problem can then be condensed onto the interface DOF, which gives:

$$\mathbf{F}_{\text{tot}}\,\boldsymbol{\lambda}_{\text{tot}} = \mathbf{t}_{\text{tot}}^{(k)}. \tag{4.54}$$

The *so-called* dual Schur complement operator $\mathbf{F}_{\text{tot}}$, the total Lagrange multiplier DOF vector $\boldsymbol{\lambda}_{\text{tot}}$, and the condensed right hand side $\mathbf{t}_{\text{tot}}^{(k)}$ read as follows:

$$\mathbf{F}_{\text{tot}} = \begin{bmatrix} \mathbf{F}^{\lambda\lambda} & \mathbf{F}^{\lambda\overline{\lambda}} \\ \left(\mathbf{F}^{\lambda\overline{\lambda}}\right)^T & \mathbf{F}^{\overline{\lambda}\overline{\lambda}} \end{bmatrix} ;\ \boldsymbol{\lambda}_{\text{tot}} = \begin{bmatrix} \boldsymbol{\lambda} \\ \overline{\boldsymbol{\lambda}} \end{bmatrix} \quad \text{and} \quad \mathbf{t}_{\text{tot}}^{(k)} = \begin{bmatrix} \mathbf{t}^k \\ \overline{\mathbf{t}}^k \end{bmatrix}, \tag{4.55}$$

where, denoting by $\mathbf{I}_s$ the local identity matrix (whose size is the number of local displacement DOF):

$$\mathbf{F}^{\lambda\lambda} = \sum_s \left(\widetilde{\widetilde{\mathbf{H}}}_{j\,s} + \eta\,\overline{\mathbf{K}}_s^T\overline{\mathbf{K}}_s\right)^{-1}\mathbf{C}_s^T \ ; \tag{4.56a}$$

$$\mathbf{F}^{\lambda\overline{\lambda}} = \sum_s \mathbf{C}_s\left(\widetilde{\widetilde{\mathbf{H}}}_{j\,s} + \eta\,\overline{\mathbf{K}}_s^T\overline{\mathbf{K}}_s\right)^{-1}\eta\,\overline{\mathbf{K}}_s^T\overline{\mathbf{C}}_s^T \ ; \tag{4.56b}$$

$$\mathbf{F}^{\overline{\lambda}\overline{\lambda}} = \sum_s \eta\,\overline{\mathbf{C}}_s\left(\overline{\mathbf{K}}_s\left(\widetilde{\widetilde{\mathbf{H}}}_{j\,s} + \eta\,\overline{\mathbf{K}}_s^T\overline{\mathbf{K}}_s\right)^{-1}\eta\,\overline{\mathbf{K}}_s^T - \mathbf{I}_s\right)\overline{\mathbf{C}}_s^T \ ; \tag{4.56c}$$

$$\mathbf{t}^k = \sum_s \mathbf{C}_s\left(\mathbf{u}_s^{(k)} + \left(\widetilde{\widetilde{\mathbf{H}}}_{j\,s} + \eta\,\overline{\mathbf{K}}_s^T\overline{\mathbf{K}}_s\right)^{-1}\left(\mathbf{b}_{F_s}^{(k)} - \eta\,\overline{\mathbf{K}}_s^T\overline{\mathbf{K}}_s\mathbf{u}_s^{(k)}\right)\right) \ ; \tag{4.56d}$$

$$\overline{\mathbf{t}}^k = \sum_s \eta\,\overline{\mathbf{C}}_s\overline{\mathbf{K}}_s\left(\mathbf{u}_s^{(k)} + \left(\widetilde{\widetilde{\mathbf{H}}}_{j\,s} + \eta\,\overline{\mathbf{K}}_s^T\overline{\mathbf{K}}_s\right)^{-1}\left(\mathbf{b}_{F_s}^{(k)} - \eta\,\overline{\mathbf{K}}_s^T\overline{\mathbf{K}}_s\mathbf{u}_s^{(k)}\right)\right). \tag{4.56e}$$

Remark. *It has to be noticed here that the dual Schur complement operator* $\mathbf{F}_{\text{tot}}$ *is symmetric but non positive-definite although the initial R-DIC operator* (4.46) *is. Once again, one must keep in mind that* $\overline{\boldsymbol{\lambda}}$ *does not constitute a Lagrange multiplier, which is responsible for these atypical developments.*

2.3.2 Parallel resolution

Iterative solution algorithm. With above developments, we now need (at each modified Gauss-Newton iteration k) to solve interface problem (4.54) and to apply Eq. (4.53a) to obtain the modified Gauss-Newton

update. Following the domain decomposition framework such as in chapter 3, interface problem (4.54) is solved using a Krylov iterative solver in order to fit parallelization criteria. The interest of such iterative algorithm is that they are only based on matrix-vector products involving $\mathbf{F}_{\text{tot}}$ which, given its structure, can be performed in parallel between the different subdomains. Indeed, denoting by $\mathbf{y}_{\text{tot}}$ any vector of the size of the interface problem such that:

$$\mathbf{y}_{\text{tot}} = \begin{bmatrix} \mathbf{y} \\ \\ \overline{\mathbf{y}} \end{bmatrix}, \tag{4.57}$$

and repeating the reasoning of Eq. (3.24), the matrix-vector product $\mathbf{F}_{\text{tot}}\mathbf{y}_{\text{tot}}$ corresponds to the following computation:

$$\mathbf{F}_{\text{tot}}\mathbf{y}_{\text{tot}} = \begin{bmatrix} \sum_s \mathbf{C}_s \left(\mathbf{v}_s^2 + \overline{\mathbf{v}}_s^2\right) \\ \\ \sum_s \eta\, \overline{\mathbf{C}}_s \overline{\mathbf{K}}_s \left(\mathbf{v}_s^2 + \overline{\mathbf{v}}_s^2\right) - \sum_s \eta\, \overline{\mathbf{C}}_s \overline{\mathbf{C}}_s^T \overline{\mathbf{y}} \end{bmatrix}, \tag{4.58}$$

where $\mathbf{v}_s^2$ and $\overline{\mathbf{v}}_s^2$ are the solutions of the set of local (*i.e.*, independent on each subdomain) systems :

$$\begin{cases} \left(\widetilde{\widetilde{\mathbf{H}}}_{j\,s} + \eta\, \overline{\mathbf{K}}_s^T \overline{\mathbf{K}}_s\right) \mathbf{v}_s^2 = \mathbf{C}_s^T \mathbf{y} \\ \left(\widetilde{\widetilde{\mathbf{H}}}_{j\,s} + \eta\, \overline{\mathbf{K}}_s^T \overline{\mathbf{K}}_s\right) \overline{\mathbf{v}}_s^2 = \eta\, \overline{\mathbf{K}}_s^T \overline{\mathbf{C}}_s^T \overline{\mathbf{y}} \end{cases}. \tag{4.59}$$

Regarding the Krylov solver, since matrix $\mathbf{F}_{\text{tot}}$ is symmetric but non positive-definite, a preconditioned GMRES algorithm [Saad and Schultz, 1986] is considered here (in comparison to the more classical Conjugate Gradient algorithm used for symmetric positive-definite systems, such as in chapter 3). We do not go more in details about this algorithm in the present manuscript; the interested reader is referred to [Bouclier and Passieux, 2017] for additional information.

We finally add some remarks highlighting the interest of integrating a dedicated DD solver into the optimization loop of DIC. A global overview of the proposed full scheme to efficiently perform R-DIC in the presence of massive data is given in Fig. 4.4. First and foremost, it has to be noted that not only the system inversions but also the image interpolations can be performed in parallel since both the mesh and the images are subdivided. Then, it has to be emphasized that the constructed mesh and images subdivisions are used to perform the initialization of the "coupling" modified Gauss-Newton (4.52) on each subdomain independently. This stage is highly parallelisable because no communications are required between subdomains. Finally, we proceed as follows for the initialization of the Krylov iterative solver: at first correlation iteration ($k = 0$), the initial $\boldsymbol{\lambda}_{\text{tot}}$ is set to zero; then, for the next correlation iterations ($k > 0$), the initial $\boldsymbol{\lambda}_{\text{tot}}$ is set to the last value of the previous GMRES resolution. This is a simple but efficient way to reduce the number of Krylov iterations.

Preconditioning. Once again following what is commonly done in the field of computational structural mechanics (see, *e.g.*, [Gosselet and Rey, 2006] for a review), we now propose a Dirichlet-like preconditioner to speed-up the GMRES resolution. We consider that we address here the coupling between subdomains of comparable stiffness so we focus on the standard Dirichlet preconditioner (see Eq. (3.28) in chapter 3). Note that the difficulty (in comparison with what was performed in chapter 3) is that we cannot exactly derive the primal counterpart of the proposed dual formulation here since this one is not based on a pure Lagrange multiplier method. From here on, we use the following notation for the local R-DIC operator:

$$\widetilde{\widetilde{\mathbf{H}}}\eta\overline{\mathbf{K}}_s = \widetilde{\widetilde{\mathbf{H}}}_{j\,s} + \eta\, \overline{\mathbf{K}}_s^T \overline{\mathbf{K}}_s. \tag{4.60}$$

We also introduce new operators $\mathbf{C}_s^{\text{loc}}$, $\overline{\mathbf{C}}_s^{\text{loc}}$, $\mathbf{A}_s$ and $\overline{\mathbf{A}}_s$ such that:

$$\mathbf{C}_s = \mathbf{A}_s \mathbf{C}_s^{\text{loc}} \;\text{ and }\; \overline{\mathbf{C}}_s = \overline{\mathbf{A}}_s \overline{\mathbf{C}}_s^{\text{loc}}. \tag{4.61}$$

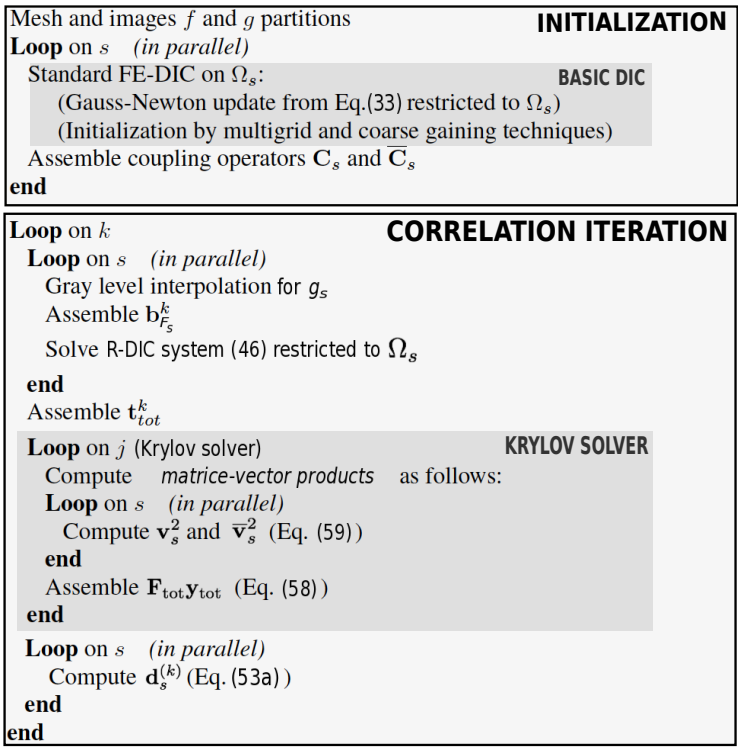

Figure 4.4 – Overview of the proposed DD R-DIC algorithm.

$\mathbf{C}_s^{\text{loc}}$ (respectively $\overline{\mathbf{C}}_s^{\text{loc}}$) is the local trace operator which projects the n_s^u local displacements of Ω_s onto the n_s^λ (resp. $n_s^{\overline{\lambda}}$) local interface displacements of Γ_s (resp. Γ_{r_s}). $\mathbf{A}_s$ and $\overline{\mathbf{A}}_s$ are the associated assembly operators that exchange data lying on one subdomain interface with its neighboring subdomains. Using above notations, operator $\mathbf{F}_{\text{tot}}$ can be rewritten as follows:

$$\mathbf{F}_{\text{tot}} = \sum_s \mathbf{AA}_s \, \mathbf{F}_s \, \mathbf{AA}_s^T, \tag{4.62}$$

with:

$$\mathbf{AA}_s = \begin{bmatrix} \mathbf{A}_s & \mathbf{0} \\ \mathbf{0} & \overline{\mathbf{A}}_s \end{bmatrix} \; ; \; \mathbf{F}_s = \begin{bmatrix} \mathbf{F}_s^{\lambda\lambda} & \mathbf{F}_s^{\lambda\overline{\lambda}} \\ \left(\mathbf{F}_s^{\lambda\overline{\lambda}}\right)^T & \mathbf{F}_s^{\overline{\lambda}\overline{\lambda}} \end{bmatrix}, \tag{4.63}$$

and where:

$$\mathbf{S}_s^{\lambda\lambda} = \mathbf{C}_s^{\text{loc}} \left(\widetilde{\overline{\mathbf{H}}}\eta\overline{\mathbf{K}}_s\right)^{-1} \mathbf{C}_s^{\text{loc}\,T} \; ; \tag{4.64a}$$

$$\mathbf{S}_s^{\lambda\overline{\lambda}} = \mathbf{C}_s^{\text{loc}} \left(\widetilde{\overline{\mathbf{H}}}\eta\overline{\mathbf{K}}_s\right)^{-1} \eta\, \overline{\mathbf{K}}_s^T \mathbf{C}_s^{\text{loc}\,T} \; ; \tag{4.64b}$$

$$\mathbf{S}_s^{\overline{\lambda}\overline{\lambda}} = \eta\, \overline{\mathbf{C}}_s^{\text{loc}} \left(\overline{\mathbf{K}}_s \left(\widetilde{\overline{\mathbf{H}}}\eta\overline{\mathbf{K}}_s\right)^{-1} \eta\, \overline{\mathbf{K}}_s^T - \mathbf{I}_s\right) \overline{\mathbf{C}}_s^{\text{loc}\,T}. \tag{4.64c}$$

The Dirichlet preconditioner (3.28) associated to the condensed dual operator $\mathbf{F}_{\text{tot}}$ in (4.62) simply reads:

$$\tilde{\mathbf{F}}_{\text{tot}}^{-1} = \sum_s \mathbf{AA}_s \, (\mathbf{F}_s)^{-1} \, \mathbf{AA}_s^T. \tag{4.65}$$

However, given the atypical structure of system (4.52) regarding $\overline{\boldsymbol{\lambda}}$, it is not possible this time to directly relate $(\mathbf{F}_s)^{-1}$ to a local primal Schur complement (as in (3.29)). As a result, we propose at this step to compute

$(\mathbf{F}_s)^{-1}$ as:

$$(\mathbf{F}_s)^{-1} = \begin{bmatrix} \left(\mathbf{F}_s^{\lambda\lambda}\right)^{-1} + \left(\mathbf{F}_s^{\lambda\lambda}\right)^{-1}\left(\mathbf{F}_s^{\lambda\overline{\lambda}}\right)\left(\mathbf{D}_s^{\overline{\lambda\lambda}}\right)^{-1}\left(\mathbf{F}_s^{\lambda\overline{\lambda}}\right)^T\left(\mathbf{F}_s^{\lambda\lambda}\right)^{-1} & -\left(\mathbf{F}_s^{\lambda\lambda}\right)^{-1}\left(\mathbf{F}_s^{\lambda\overline{\lambda}}\right)\left(\mathbf{D}_s^{\overline{\lambda\lambda}}\right)^{-1} \\ -\left(\left(\mathbf{F}_s^{\lambda\lambda}\right)^{-1}\left(\mathbf{F}_s^{\lambda\overline{\lambda}}\right)\left(\mathbf{D}_s^{\overline{\lambda\lambda}}\right)^{-1}\right)^T & \left(\mathbf{D}_s^{\overline{\lambda\lambda}}\right)^{-1} \end{bmatrix}, \tag{4.66}$$

where:

$$\mathbf{D}_s^{\overline{\lambda\lambda}} = \mathbf{F}_s^{\overline{\lambda\lambda}} - \left(\mathbf{F}_s^{\lambda\overline{\lambda}}\right)^T\left(\mathbf{F}_s^{\lambda\lambda}\right)^{-1}\left(\mathbf{F}_s^{\lambda\overline{\lambda}}\right), \tag{4.67}$$

and to make use of the available local primal Schur complement associated to unknown $\boldsymbol{\lambda}$, *i.e.*:

$$\left(\mathbf{F}_s^{\lambda\lambda}\right)^{-1} = \left(\mathbf{C}_s^{\text{loc}}\left(\widetilde{\widetilde{\mathbf{H}}}\eta\overline{\mathbf{K}}_s\right)^{-1}\mathbf{C}_s^{\text{loc}\,T}\right)^{-1} = \left[\widetilde{\widetilde{\mathbf{H}}}\eta\overline{\mathbf{K}}_s\right]_{bb} - \left[\widetilde{\widetilde{\mathbf{H}}}\eta\overline{\mathbf{K}}_s\right]_{bi}\left(\left[\widetilde{\widetilde{\mathbf{H}}}\eta\overline{\mathbf{K}}_s\right]_{ii}\right)^{-1}\left[\widetilde{\widetilde{\mathbf{H}}}\eta\overline{\mathbf{K}}_s\right]_{ib}. \tag{4.68}$$

As in (3.29), $[\square]_i$ denotes the restriction to internal DOF of local quantity $\square$ and $[\square]_b$ the restriction to interface DOF. The computational cost for evaluating $\left(\mathbf{F}_s^{\lambda\lambda}\right)^{-1}$ is therefore related to the computation of term $\left(\left[\widetilde{\widetilde{\mathbf{H}}}\eta\overline{\mathbf{K}}_s\right]_{ii}\right)^{-1}\left[\widetilde{\widetilde{\mathbf{H}}}\eta\overline{\mathbf{K}}_s\right]_{ib}$: it requires to factorize $\left[\widetilde{\widetilde{\mathbf{H}}}\eta\overline{\mathbf{K}}_s\right]_{ii}$ and to solve n_s^λ linear systems of size $n_s^{u_i} \times n_s^{u_i}$ ($n_s^{u_i}$ being the number of local internal displacements). This is affordable because (i) it has to be done once at the beginning of the modified Gauss-Newton algorithm, (ii) it is local and thus, (iii) it can be done in parallel between subdomains. In addition, we need to evaluate $\mathbf{F}_s^{\overline{\lambda\lambda}}$ and $\mathbf{F}_s^{\lambda\overline{\lambda}}$. This requires to compute $\left(\widetilde{\widetilde{\mathbf{H}}}\eta\overline{\mathbf{K}}_s\right)^{-1}\overline{\mathbf{K}_\mathbf{s}}^T\mathbf{C}_s^{\text{loc}\,T}$ which is affordable as well. The factorization of $\widetilde{\widetilde{\mathbf{H}}}\eta\overline{\mathbf{K}}_s$ (already performed to solve (4.59)) is used for that and $n_s^{\overline{\lambda}}$ linear systems of size $n_s^u \times n_s^u$ are solved. Therefore, we end up with a strategy that involves only local resolutions and that is completely parallelisable. A slight additional cost is then necessary to apply the proposed preconditioning but it leads to a drastic reduction of the number of GMRES iterations, as shown in the example below.

Remark. *Let us quote that using the developments of previous chapter, the proposed preconditioner which is built here in case of matching interfaces may be simply extended to the case of non-matching (and even non-conforming) interfaces. In such situations, one would need to compute the Mortar operators as true "mass" matrices and to add weights of form* $\left(\mathbf{C}_s\,\mathbf{C}_s^T\right)^{-1}$ *as in* (3.28).

2.3.3 Application to the analysis of real high resolution images

Experimental set-up and DD model. The developed DD R-DIC method is now applied to the analysis of high resolution images of a real experiment. It has to be said as of now that only a proof of concept is given in the following: the true implementation in parallel has not been achieved yet. A four point bending test is performed on an open hole polymethyl methacrylate specimen (see Fig. 4.5). More precisely, the pattern consists of a parallelepipedic coupon of dimension 200 × 20 × 5 mm with an 8 mm hole drilled in the center. A black and white speckle pattern is sprayed onto the surface of the specimen and a high resolution CCD camera (29 megapixels) is used to capture images (4384 × 6576 pixels). The physical size of one pixel is 19.4 μm. An unstructured finite element mesh (including both linear triangles and quadrangles of 15 pixels width in average) is adjusted on the image (see Fig. 4.6) to perform FE-DIC. An elastic regularization of the optical flow is adopted ($\eta = 10^{-3}$) for R-DIC. The mesh and images are decomposed into 180 subdomains for the DD computation. The resulting average subdomain size is 160 pixels per side. With such a discretization, the displacement field includes 62522 DOF and the interface problem (4.54) contains 21174 interface DOF (distributed as follows: 10604 DOF for $\boldsymbol{\lambda}$ and 10570 d.o.f for $\overline{\boldsymbol{\lambda}}$). The analysis is finally performed with a stopping tolerance for correlation and Krylov iterations of 10^{-3}.

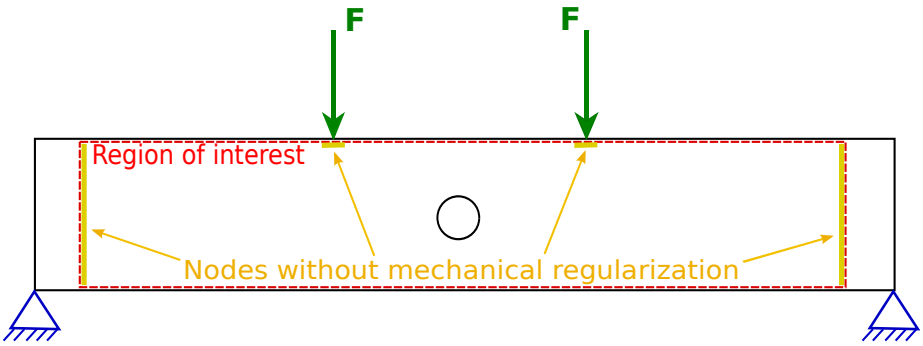

Figure 4.5 – Four point bending test: illustration of the experimental set up.

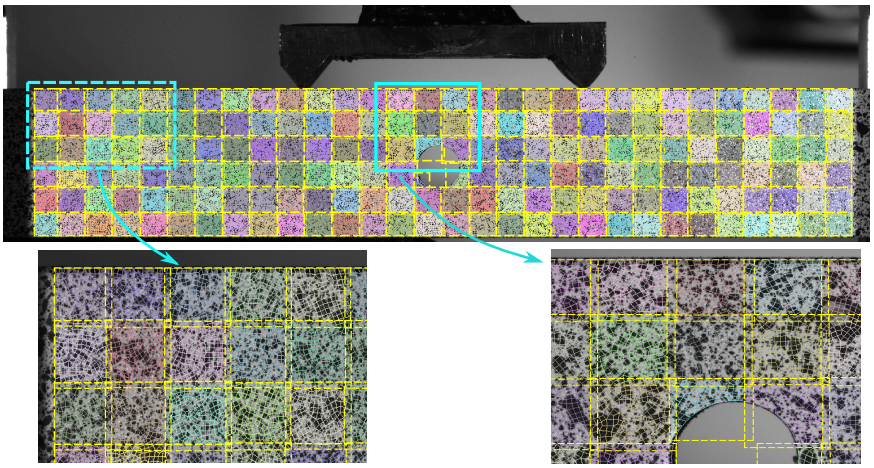

Figure 4.6 – Reference image and domain decomposition (180 subdomains) for the four point bending test. The overlapping subset images f_s are in yellow dashed line. The finite elements belonging to a same subdomain are plotted with the same color. Two zooms are provided below the image.

Domain decomposition solution. Fig. 4.7 shows the deformed configurations obtained with the considered domain decomposition (amplification factor of 50). The color scale corresponds to the horizontal component of the displacement field. More precisely, the solution associated to the parallel initialization of the coupling modified Gauss-Newton algorithm (*i.e.*, where classical FE-DIC problems without mechanical regularization are solved on each subdomain independently) is first plotted (see Fig. 4.7(a)). From this initialization, the solution obtained using the domain decompostion method of [Passieux et al., 2015b] (*i.e.* based on system (4.48)) is shown in Fig. 4.7(b) while Fig. 4.7(c) presents the solution computed with the proposed DD R-DIC algorithm.

We clearly see the improvement of the solution through the different situations. In the initial solution (Fig. 4.7(a)), the displacement continuity is not verified and sharp oscillations are present in the measured field. Nevertheless, the solution constitutes a good initialization of the proposed DD algorithm: the global displacement field at the interior of the subdomains does not seem too far from the intended solution. With the domain decomposition algorithm of [Passieux et al., 2015b], the displacement becomes continuous across the subdomains but the field measurement still suffers from some instabilities which leads to a non-smooth solution (see Fig. 4.7(b)). When performing the proposed DD R-DIC algorithm, not only the displacement becomes continuous across the subdomains but also the mechanical equilibrium of the structure is ensured which removes the oscillations of the measured field (see Fig. 4.7(c)). In [Bouclier and Passieux, 2017], we also showed that the obtained DD R-DIC solution actually appears indistinguishable from the equivalent one-domain R-DIC solution on this test case, which accounts for the consistency of the developed coupling. As a result, the proposed DD R-DIC strategy enables to compute in

parallel an accurate mechanically sound solution from high resolution images.

2.3.4 Convergence of the DD algorithm.

We finally investigate the convergence of the DD R-DIC algorithm. The variation of the norm of the Krylov residual as a function of the Krylov iteration j is plotted in Fig. 4.8 for the developed preconditioned GMRES solver (denoted by PGMRES in the figure). For comparison purpose, the solution associated to the GMRES solver without preconditioning is added to the graph. These results confirm the efficiency of the parallel initialization of the coupling modified Gauss-Newton algorithm (see block *Initialization* in Fig. 4.4). Indeed, it takes in this case only three extra correlation iterations to obtained the desired solution (of Figure 4.7(c)) from the initialization (shown in Figure 4.7(a)). It can also be noticed that the number of iterations of the Krylov solver decreases as the correlation iteration k increases, which is due to the use of previous vector $\boldsymbol{\lambda}_{\text{tot}}$ for the initialization of the Krylov solver. Finally, we observe that the constructed preconditioner allows for a drastic reduction of the number of iterations of the Krylov algorithm (reduction by a factor of ten on this example). With its efficient initialization and preconditioning, the proposed DD algorithm appears then suitable for high performance computing when high resolution images and meshes are jointly used.

Remark. *Since at this stage only a sequential implementation of the method has been performed, it is not possible to provide a relevant estimate of the speed-up of the DD R-DIC solver with respect to the standard R-DIC method. However, providing some implementation cares, it has been possible to observe that one iteration of PGMRES is about* 70 *% longer than one iteration of GMRES. From a global point of view, taking into account that the number of iterations of the Krylov algorithm is divided by ten with preconditioning, and including the times devoted to the construction and assembling of the preconditioner, we were able to observe that the method involving PGMRES is about* 4 *times faster than the method using a simple GMRES.*

Summary and discussion. In this second section, we have built a novel coupling algorithm to recover displacement continuity and mechanical equilibrium from two independent FE-DIC analysis with mechanical regularization (R-DIC). Contrary to what has been done in chapter 3, it is required to introduce an additional interface unknown that is not a Lagrange multiplier for the enforcement of the static constraint. This results in the derivation of an original mixed method that has been properly handled to accurately solve the correlation problem. The application illustrated in this section concerns the parallel computation of R-DIC to make it an HPC tool. Since the condensed operator is not positive-definite, a GMRES iterative strategy is implemented. In addition, a dedicated preconditioner combining explicit inverses and local primal Schur complements is constructed for acceleration purpose. Such an algorithm allows to benefit from all the great advantages of using FE in DIC (direct bridge with simulation, continuity, mechanical regularization, robustness to perform identification, etc) while limiting its main drawback, namely the computational cost (including the computation time and memory requirements). The method can thus be viewed as a bridge between subset and FE-DIC methods.

In the near future, it is expected that the true implementation in parallel of our solver would be of great interest to properly tackle the today massive amount of data encountered in experimental mechanics. This problematic seems to have been subjected to a growing interest in many fields of physics given the improved performance of digital imaging tools, for example in the medical area [Merta et al., 2014, Ronovsky and Vasatova, 2017, Tournier et al., 2019] or in the sector of mechanics of materials [Wang and Kemao, 2018, Liu et al., 2019]. To further improve the iterative solver, we may also draw inspiration from the field of data assimaliation in other contexts (see, *e.g.*, [Rabier, 2005] for a review in the field of weather prediction). Indeed, the DIC framework as introduced in section 1 shares many similarities with the variational data assimilation theory. We are currently working in this direction with X. Vasseur and

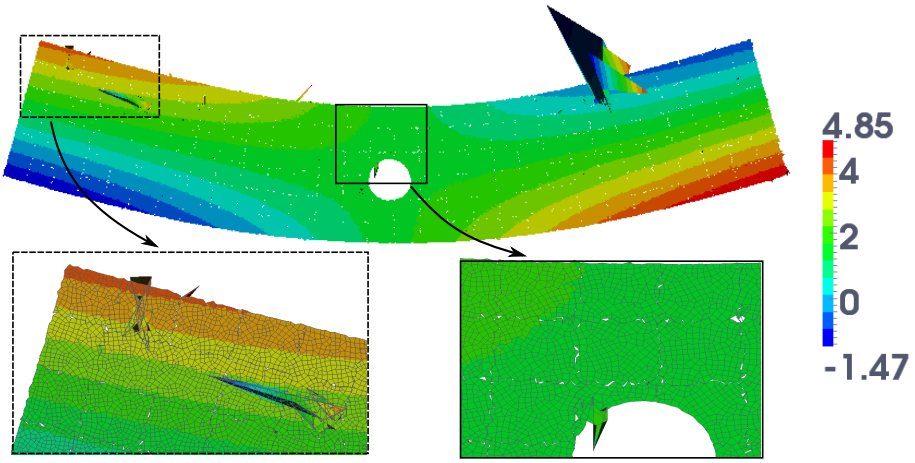

(a) FE-DIC solution (without mechanical regularization) computed independently on each subdomain (block *Initialization* in Fig. 4.4).

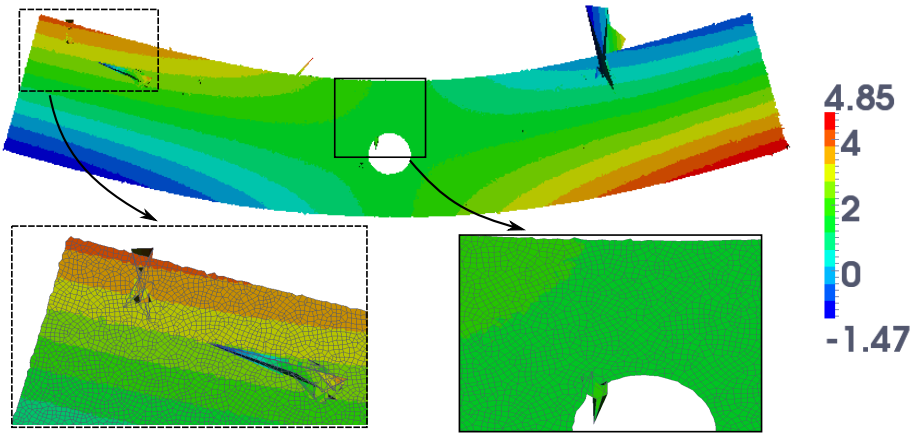

(b) Continuous solution without mechanical regularization obtained with the domain decomposition algorithm of [Passieux et al., 2015b].

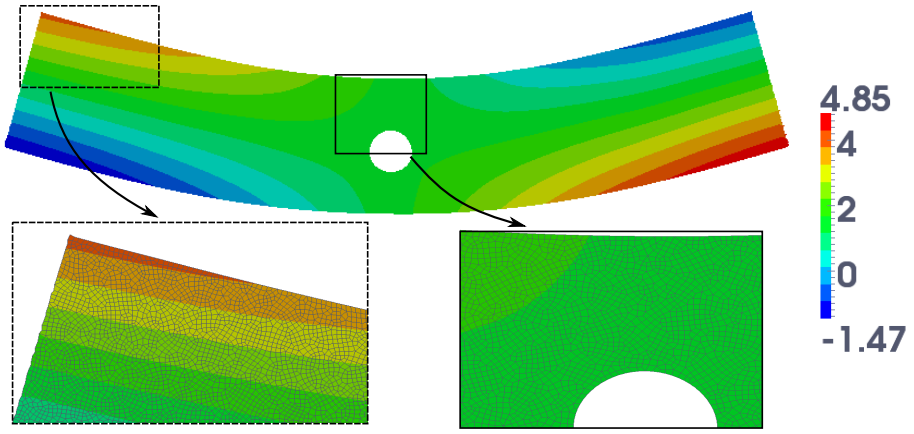

(c) Continuous solution with mechanical regularization obtained with the proposed domain decomposition algorithm (block *Correlation iterations* in Fig. 4.4).

Figure 4.7 – Displacement solution in pixels (amplification factor 50, distribution of the horizontal displacement) for the four point bending test.

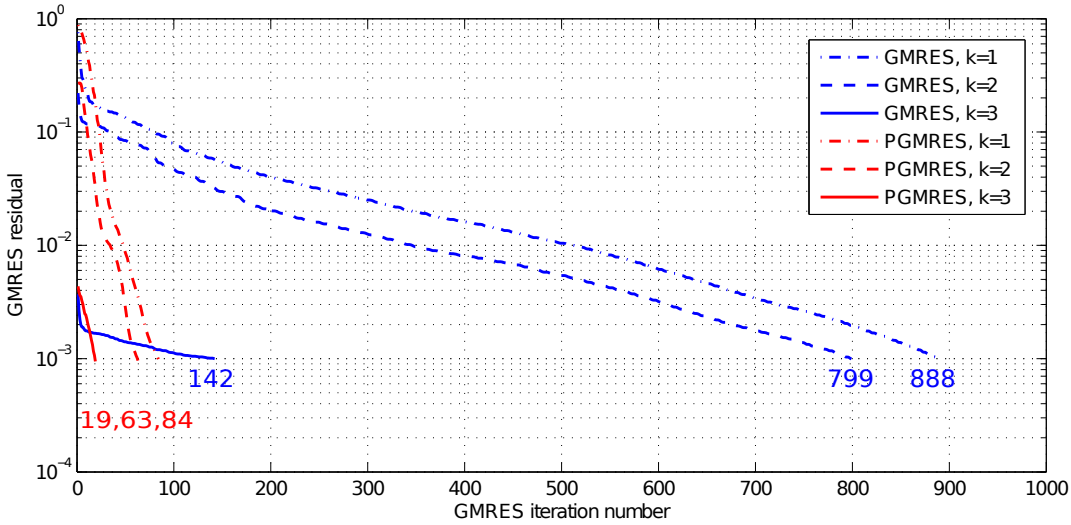

Figure 4.8 – Variation of the norm of the GMRES residual as a function of the GMRES iteration number j for each correlation iteration k (see block *Correlation iterations* in Fig. 4.4). The final number j obtained for each iteration k is reported below the curves. GMRES, GMRES without preconditioning. PGMRES, GMRES with the proposed preconditioner.

Y. Diouane from IRIT in Toulouse. In particular, we consider the class of Limited-Memory Preconditioners (LMP) that has proved to be effective to solve a sequence of linear systems whose operator does not change too much [Tshimanga et al., 2008].

The HPC application is not the only one of the proposed coupling method. For instance, it could also be useful for multiscale or multi-resolution DIC [Bornert et al., 2010, Passieux et al., 2015a] and when the regularization model needs to be multiscale too [Réthoré, 2015]. Indeed, bounding the displacements fields and enforcing the equilibrium of the mechanical models (possibly) coming from different scales seems of particular interest to measure phenomena in structural mechanics. In [Bouclier and Passieux, 2017], the coupling method has also proved to be relevant to measure of one smooth displacement field from two sets of images at nearfield and farfield resolutions, respectively. This opens to door for the design of advanced identification procedure: the farfield measurement is used to provide representative boundary conditions, while the nearfield measurement produces high spatial resolution kinematic fields in a region where the model parameters are sensitive [Passieux et al., 2015a].

Finally, it may be noted that I have been (or am currently) involved in some other works related to DIC that share the same philosophy as the one reported here. For instance, in [Passieux et al., 2018], we have developed a new regularized reduced-order/DIC method to extract useful information from a sequence of large images acquired over time. The idea was to write the minimization problem over the space-time domain and to look for the displacement field in a separated time-space form, as widely performed in computational mechanics [Ammar et al., 2006, Bouclier et al., 2013c, Zou et al., 2018a]. This enabled us to prescribe a mechanically sound time-dependency of the solution which acted as a regularization for the dynamic phenomenon to be measured. Then, we are currently working, through the PhD thesis of Ali Rouwane [Rouwane, 2021] who I co-supervise with J.-N. Périé and J.-C. Passieux, on the 3D measurement of interior strain fields from large volume images (the long-term goal being the mechanical characterization of the microstructure of materials). To this end, we first build an image-based mechanical model by means of spline functions and embedded domain approaches [Verhoosel et al., 2015], and then use it to regularize DVC. This allows use to observe local bending at the microscopic scale of cellular materials [Rouwane et al., 2020]. Lastly, we are addressing with J.-N. Périé and J.-C. Passieux, through the PhD

thesis of Raphaël Fouque [Fouque, 2021], the mechanical identification from multiscale stereoscopic images. After deriving a dedicated pattern for multiscale DIC [Fouque et al., 2020], the idea will be to capture the physical texture of the non-planar sample to ease the identification process using a large number of (assumed multiscale) cameras.

CHAPTER 5

Mesh-based 3D shape measurement with stereocorrelation

Contents

When the specimen geometry or mechanical loading is not planar, a stereo digital image correlation (SDIC) method can be implemented, as an improvement to the more standard 2D-DIC performed in chapter 4. Making use of at least two cameras and sophisticated numerical schemes, it is actually possible to access the three components of the displacement at the non-planar surface of the specimen. This method, initially developed in the context of subset-DIC [Lucas and Kanade, 1981, Garcia et al., 2002], has recently been extended to the framework of global approaches [Réthoré et al., 2013, Dufour et al., 2015a, Pierré et al., 2017]. For instance, global SDIC has been successfully used for the analysis of complex experiments such as structural tests [Dufour et al., 2016, Serra et al., 2017a, Serra et al., 2017b]. Before estimating the displacement measurement, SDIC requires a calibration phase aiming at determining the parameters of the cameras (focal length, true location in the reference frame of the experimental lab, etc) and the actual shape of the specimen. Indeed, although it may appear surprising at first glance for researchers in the field of scientific computing, it has to be underlined that the actual shape of the specimen surely does not correspond to the theory, because of surface roughness, manufacturing defects, pre-load or relaxation of residual stresses, to name a few. Given the strong dependency of the kinematic fields to the shape of the surface (especially in the normal direction), the proper estimation of the real surface is an essential prerequisite for 3D surface displacement measurements.

The shape measurement really constitutes a challenge in FE-SDIC. Indeed, if the use of a FE mesh facilitates the coupling of measurements with simulation tools, it also provides a unique, fine description of both the geometry and the displacement, which often makes the FE shape measurement problem highly ill-posed. As a remedy, we propose in this chapter a novel hybrid isogeometric-FE strategy that can measure a shape in terms of spline functions while considering as an input and output the FE mesh used for displacement measurement. From a scientific computing point of view, the idea here is to make use of the intrinsic attractive properties of splines introduced in chapter 1 (namely, their increased smoothness, their ability to be refined without altering the geometry, and their possible link with standard C^0 functions) to regularize, in a geometrical and non-invasive manner, the mesh-based shape measurement problem

occurring in FE-SDIC. This work has been performed very recently in the PhD of thesis of Morgane Chapelier [Chapelier, 2021], who I co-supervise with Pr. J.C. Passieux, following some developments on FE-SDIC achieved in the PhD thesis of Guillaume Colantonio. This work has led to [Colantonio et al., 2020]. The interested reader is advised to consult this reference for further details on that topic.

1 Mesh-based shape measurement in stereo-DIC

To start with, this section introduces the calibration phase occurring in FE-SDIC with a particular emphasis on the shape measurement problem. We recall that the difficulty when using a FE mesh is that it leads to a shape measurement problem which is highly ill-posed. The standard method for regularizing the FE shape measurement problem is also described hereafter.

1.1 Camera model

Let us assume that we have an existing CAD description of the nominal geometry of the specimen, which, in experimental mechanics, is generally the case. Let Ω be here a surface domain referred to as Region of Interest (ROI) and such that $\Omega \subset \mathbb{R}^3$ corresponds to the visible surface of the theoretical shape. The aim of the shape measurement is thus to find the geometrical transformation that updates Ω in order to fit the true experimental surface. As classically done in SDIC [Sutton et al., 1999], each camera c is equipped with a camera model P_c that maps any 3D point $X \in \Omega$ expressed in the world reference system $\mathscr{R}_w$ to the corresponding coordinates in pixels x_c in the image frame. Mathematically, it is written as:

$$P_c : \left(\Omega \subset \mathbb{R}^3\right) \times \mathbb{R}^6 \mapsto \mathbb{R}^2, \ (X, p_c) \mapsto x_c = P_c(X, p_c), \tag{5.1}$$

where p_c is a vector collecting the model's parameters. More precisely, camera models P_c can be either linear (in homogeneous coordinates) or non-linear to take into account lens distortions. It depends on two sets of parameters: the intrinsic parameters (focal length, image center, horizontal/vertical aspect ratio, skew and possible distortion parameters) and the extrinsic parameters (3 rotations and 3 translations that map the reference frame of the specimen $\mathscr{R}_w$ to that of the imaging sensor $\mathscr{R}_c$). The calibration of these parameters must be done prior to any measurement. In this study, intrinsic parameters are calibrated using calibration targets and a classic photogrammetric technique as described in [Lavest et al., 1998, Garcia, 2001]. In the following, the instrinic parameters will be assumed to be known and only the extrinsic parameters will be considered, such that for each camera c, the camera model P_c will be entirely defined by $p_c \in \mathbb{R}^6$ (in accordance with (5.1)).

Remark. *It is important to point out here that the CAD model of the nominal geometry has to be understood as the minimal, boundary-fitted spline mesh that properly capture the initial smooth geometry. In other words, we assume in this chapter that the difficult task of building a consistent spline mesh from a raw geometric model as generated by a CAD modeler (see chapter 1) has been handled in a pre-processing step.*

1.2 Coupled calibration and shape measurement problem

As depicted in Fig. 5.1, the graylevel conservation assumption [Horn and Schunck, 1981] states that the graylevel value $f_c(x_c)$ of the projections x_c in each image f_c of any 3D point X should be equal: $f_0(x_0) = f_1(x_1)$. Since both the actual shape and position of the specimen (with respect to the stereo rig) are not known exactly, the graylevel conservation is not fulfilled. The calibration of the stereo rig thus consists in a coupled problem aiming at finding the extrinsic parameters $p = \left(p_0, p_1\right)$ in addition to a shape correction field $S(X), \forall X \in \Omega$, such that the advection of the nominal surface Ω by the correction field $S(X)$ corresponds to the actual surface.

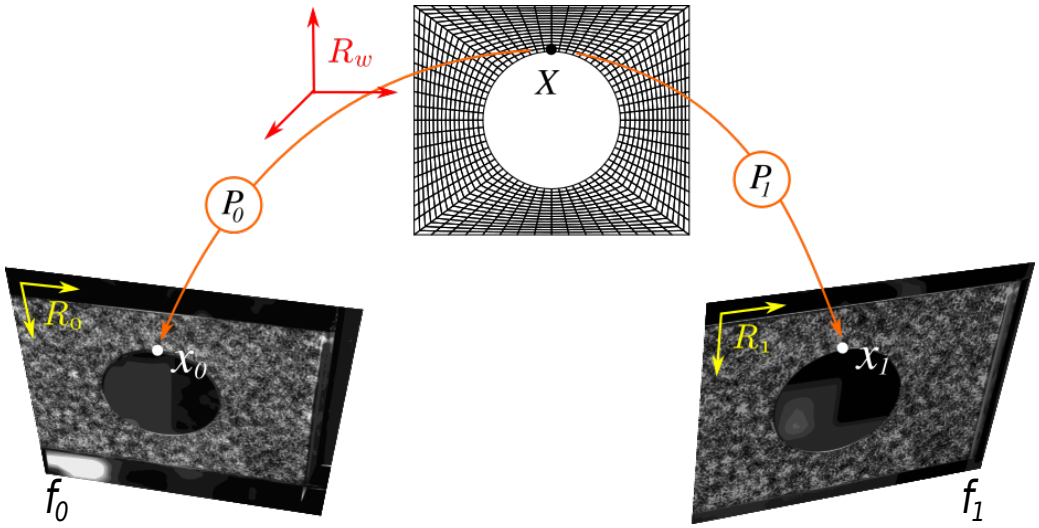

Figure 5.1 – Principle of the formulation of the calibration phase in FE-SDIC. A 3D point X and its corresponding projections x_0 and x_1 onto the image planes.

More precisely, the shape correction and the camera parameters minimize the graylevel mismatch:

$$S^\star, p^\star = \underset{S\in\mathscr{U}, p\in\mathbb{R}^{12}}{\operatorname{argmin}}\ j_{\text{cal}}(S(X), p) \qquad \text{with} \qquad j_{\text{cal}}(S(X), p) = \frac{1}{2}\int_\Omega \Big(r_{\text{cal}}\big(S(X), p\big)\Big)^2\, \mathrm{d}\Omega, \tag{5.2}$$

and where the graylevel residual $r_{\text{cal}}(S(X), p)$ is defined $\forall X \in \Omega$ as:

$$r_{\text{cal}}\big(S(X), p\big) = f_0\big(P_0(X + S(X), p_0)\big) - f_1\big(P_1(X + S(X), p_1)\big). \tag{5.3}$$

Let us highlight, at this stage, that the graylevel residual is defined in Ω, *i.e.* in the reference system of the model, which differs from subset-based SDIC, where it is written in the image frames. This the key point of global SDIC [Dufour et al., 2015a, Pierré et al., 2017]. The unknown vector p gathering the extrinsic parameters is already discrete so we can directly make it become $\mathbf{p}$ in the dicrete setting. The shape correction field S lies in an infinite space (denoted by $\mathscr{U}$ in (5.2)) so an approximation subspace for S must be defined for the numerical resolution. In FE-SDIC [Pierré et al., 2017], the core-idea is to consider here the same FE mesh as the one which enables to accurately describe the solution in FE simulations (*i.e.*, the analysis-suitable FE mesh). As for FE-DIC in chapter 4, the goal is to simplify the dialog with standard simulation software. As a result, making use of the same notations as in chapter 1 (see, *e.g.*, (1.1)), we look for the FE field S^h such that:

$$S^h(X) = \sum_{i=1}^{n_{FE}} L_i(X)\, q_i = \mathbf{L}^T(X)\, \mathbf{q}, \tag{5.4}$$

where $\mathbf{L}$ is a $(3n_{FE} \times 3)$ matrix gathering the n_{FE} standard Lagrange shape functions L_i and $\mathbf{q}$ is a vector that collects the $3n_{FE}$ corresponding DOF. In addition, note that q_i in (5.4) is the subset of $\mathbf{q}$ gathering the three components $\{q_i^1, q_i^2, q_i^3\}$ of the field $S^h(X)$ associated to shape function L_i. Problem (5.2) is an unconstrained optimization problem involving two different sets of unknowns. Its resolution is based on a fixed point algorithm which consists in alternatively minimizing the graylevel functional j_{cal} with respect to $\mathbf{p}$ (calibration) and to $\mathbf{q}$ (shape measurement). The two resulting minimization problems are detailed in the following.

Minimization with respect to the camera parameters. The shape correction field $S^h(X)$ being fixed, the set of parameters $\mathbf{p}$ is the solution of the following calibration problem:

$$\mathbf{p}^\star = \underset{\mathbf{p}\in\mathbb{R}^{12}}{\operatorname{argmin}}\ j_{\text{cal}}(\mathbf{L}^T(X)\, \mathbf{q}, \mathbf{p}). \tag{5.5}$$

Following the discussion of previous chapter, such a non-linear least-square problem is efficiently solved using a Gauss-Newton algorithm, see [Pierré et al., 2017] for details.

Minimization with respect to the shape correction field. The extrinsic camera parameters $\mathbf{p}$ being fixed, the DOF vector $\mathbf{q}$ is the solution of the following shape measurement problem:

$$\mathbf{q}^\star = \underset{\mathbf{q}\in\mathbb{R}^{3n_{FE}}}{\arg\min}\, j_{\text{cal}}(\mathbf{L}^T(X)\,\mathbf{q},\mathbf{p}) \tag{5.6}$$

This non-linear least-square problem is also solved using a Gauss-Newton algorithm. At iteration $k+1$, the solution is sought as $\mathbf{q}^{(k+1)} = \mathbf{q}^{(k)} + \mathbf{d}_q^{(k)}$, where the descent direction $\mathbf{d}_q^{(k)}$ is the solution of the following linear system [Pierré et al., 2017]:

$$\mathbf{H}_{FE}^{(k)}\mathbf{d}_q^{(k)} = \mathbf{b}_{FE}^{(k)} \qquad \text{with} \qquad \left\{\begin{array}{rcl} \mathbf{H}_{FE}^{(k)} &=& \displaystyle\int_\Omega \mathbf{L}\,(\mathbf{J}_0^{(k)\,T}\nabla f_0^{(k)} - \mathbf{J}_1^{(k)\,T}\nabla f_1^{(k)})\,(\mathbf{J}_0^{(k)\,T}\nabla f_0^{(k)} - \mathbf{J}_1^{(k)\,T}\nabla f_1^{(k)})^T\mathbf{L}^T\,\mathrm{d}\Omega \\ \mathbf{b}_{FE}^{(k)} &=& \displaystyle -\int_\Omega \mathbf{L}\,(\mathbf{J}_0^{(k)\,T}\nabla f_0^{(k)} - \mathbf{J}_1^{(k)\,T}\nabla f_1^{(k)})\; r_{\text{cal}}(\mathbf{L}^T(X)\,\mathbf{q}^{(k)},\mathbf{p})\,\mathrm{d}\Omega \end{array}\right. . \tag{5.7}$$

In the above equation, $\nabla f_c^{(k)} = \nabla f_c(P_c(X+\mathbf{L}^T(X)\mathbf{q}^{(k)}))$ where ∇f_c defines the gradient of the graylevel image f_c and $\mathbf{J}_c^{(k)} = \mathbf{J}_c(X+\mathbf{L}^T(X)\mathbf{q}^{(k)})$ where $\mathbf{J}_c$ denotes the Jacobian with respect to X of the projector P_c (5.1), *i.e.* such that $(\mathbf{J}_c)_{ij} = \partial P_{ci}/\partial X_j$, $\forall (i,j)\in\{1,2\}\times\{1,2,3\}$.

Remark. *Up to now, the shape correction field was defined as homogeneous to a displacement field, with three components corresponding to the three spatial dimensions. But, since a shape correction field tangent to the surface does not actually modify the geometry (problem* (5.6) *allows for global and local sliding of the surface [Pierré et al., 2017]), it is solved in projection onto the normal of the nominal surface. This treatment can be viewed as a firts regularization of problem* (5.6)*. More precisely, the shape correction field becomes a scalar field. The operator and right-hand side become:*

$$\mathbf{Z}^T\mathbf{H}_{FE}^{(k)}\mathbf{Z} \quad \text{and} \quad \mathbf{Z}^T\mathbf{b}_{FE}^{(k)}, \tag{5.8}$$

respectively, with $\mathbf{Z}$ being a $3n_{FE}\times n_{FE}$ operator representing the normal. In what follows, although we keep notations $\mathbf{H}_{FE}^{(k)}$ and $\mathbf{b}_{FE}^{(k)}$ of (5.7) *for simplicity, the reader must keep in mind that the projection onto the normal of the nominal surface is performed.*

Remark. *Given the discussion of chapter 4, the interested reader may think of developing a modified Gauss-Newton scheme to end up with constant operators for the iterative resolution of problems* (5.5) *and* (5.6)*. From this point of view, it may be emphasized that the operators here (such as $\mathbf{H}_{FE}^{(k)}$ and $\mathbf{b}_{FE}^{(k)}$ for shape measurement) are quite different from the FE-DIC operators (they involve the Jacobians of the camera projectors and the gradients of the two images). As a result, it seems, at least from our numerical experiments, that taking both the Hessian and gradient operators (of j_{cal}) constant severely affect the convergence. Nevertheless, although it may not appear easy at first glance to extend the ICGN approach, the very simple strategy of modifying only the right hand side might be relevant here to ensure computational time saving (similarly as in Eq.* (4.42) *in chapter 4). Corresponding investigations are in progress.*

Remark. *As any gradient-based optimization algorithm, the question of the initial guess of $\mathbf{p}$ and $\mathbf{q}$ is crucial. On the one hand, as stated above, the theoretical shape is supposed to be a good approximation of the actual shape in experimental mechanics, therefore $\mathbf{q}=\mathbf{0}$ is a good initialization. On the other hand, the extrinsic parameters are not known. It is usually initialized by picking manually some (at least 3) points on the mesh and on each image. However, even under these conditions, and particularly when the discrepancy between theoretical and real shape is significant, a pyramidal multi-scale initialization technique may be relevant to improve convergence. This last point is more deeply discussed in the next paragraph.*

1.3 Standard regularization of FE shape measurement

As stated above, in FE-SDIC as in most FE simulations, a unique interpolation subspace is used for both the approximation of the geometry and of the displacement (basic principle of isoparametric FE). The approximation subspace is therefore entirely defined by the choice of a FE mesh. However, the shape of the specimen is generally rather smooth and regular and it should require less DOF than the displacement field which may comprise important gradients. Another way of considering FE-SDIC would consist in a suitable mix of an appropriate mesh for shape measurement and a different finer FE mesh that properly compute the displacement (*i.e.*, an analysis-suitable mesh). Using standard FE, such a regularization approach would require non-trivial projection procedures between unstructured 3D surface meshes, which are often accompanied with a modification of the (generally curved) geometry.

As a result, the common practice for mesh-based shape measurement consists in using the same refined, analysis-suitable FE mesh both for shape and displacement measurement, but adding specific regularization terms when looking for the shape to avoid getting wiggly, irregular descriptions. Such a regularization is also employed in a multi-scale initialization phase similarly as for the initialization of FE-DIC (see beginning of section 1.2 in chapter 4). For FE shape measurement, the idea consists in filtering the images (once again usually by means of pixel aggregation) and regularizing the shape simultaneously. A classic way of regularizing is to resort to what is reffered to as the Tikhonov regularization technique in the DIC community, *i.e.* to complement system (5.7) as follows:

$$(\mathbf{H}_{FE}^{(k)} + \eta\,\mathbf{T})\,\mathbf{d}_q^{(k)} = \mathbf{b}_{FE}^{(k)} - \eta\,\mathbf{T}\,\mathbf{q}^{(k)}, \tag{5.9}$$

where $\mathbf{T}$ is a linear operator such that $\mathbf{T}\,\mathbf{q}$ expresses the gradient of $S^h(X)$ and η is a penalization parameter whose value can be interpreted as the filter cut-off frequency (see, *e.g.*, [Dufour et al., 2016, Pierré et al., 2017] for more details). The larger η, the higher the regularization level. In practice, choosing the correct regularization length may be tricky. More importantly, a satisfying value may not exist in some challenging situations where the real and theoretical shapes are far from each other, as will be seen in section 3. That is why we propose, in the following, a novel regularization scheme for FE shape measurement that has a strong geometrical meaning.

2 Non-invasive multilevel geometric regularization

Our regularization strategy is based on the projection of the FE mesh-based shape measurement problem (5.6) onto more regular spline-based subspaces. As stated in chapter 4, spline-based functions have already been successfully used in DIC given their high degree of regularity (see, *e.g.*, [Cheng et al., 2002, Xie and Farin, 2004, Réthoré et al., 2010a, Elguedj et al., 2010, Kleinendorst et al., 2015]). In the context of shape measurement, their interest is expected to be even more important since these functions are particularly adapted to optimize free-form surfaces [Kiendl et al., 2014, Hirschler et al., 2019c].

2.1 Inspiration: structural shape optimization

From a mathematical and a numerical point of view, we notice that the mesh-based shape measurement problem (5.6) coming from the experimental mechanics community shares many similarities with the shape optimization problem encountered in structural design. Indeed, structural shape optimization also aims at finding the optimal geometry of a structure and involves a FE mesh in the process [Haftka and Grandhi, 1986, Haftka and Gürdal, 1993]. The difference only lies in the desired objective which is related to the fulfillment of a certain structural behavior in shape optimization (see chapter 6 for more information) while it concerns the fitting with the real surface in shape measurement. Therefore, the purpose here is to draw inspiration from the techniques developed in the area of shape optimization to improve the field of mesh-based shape measurement.

Initial FE and CAD based shape optimization. One approach in shape optimization is actually very close to what is performed for shape measurement (with respect to (5.9)): it consists in using the spatial location of the FE nodes as the design variables (*i.e.*, the variables that update the geometrical shape) in combination with delicate mesh regularization techniques to prevent the appearance of irregular, "unrealistic" shapes [Firl et al., 2013, Bletzinger, 2014]. This strategy is classified as the FE-based approach in the shape optimzation framework. Meanwhile, another class of techniques, denoted by the computer-aided-design (CAD)-based approach, has also emerged for shape optimization: the idea is to resort to the same spline-based functions as in CAD software to describe the geometry, namely the B-Spline and NURBS functions [Cohen et al., 1980, Piegl and Tiller, 1997] (see chapter 1 as a reminder). The design variables are this time the spatial location of the control points of the spline entities, which, given the high degree of regularity of spline functions, enables to get a light and smooth parametrization of the geometry and of its update [Braibant and Fleury, 1984, Olhoff et al., 1991]. Figs. 5.2 and 5.3 illustrate the situation for a B-Spline curve and a NURBS surface, respectively (note that the initial spline entities have already been introduced in chapter 1, see Fig. 1.2). The difficulty with this second family of methods is then transferred to the connection of the design model (*i.e.*, the geometrical model where the design variables are defned) and the analysis model (*i.e.*, the fine numerical model that provides simulations of good quality) [Hasan Imam, 1982, Bletzinger et al., 1992]. Indeed, in CAD-based approach the design model is based on splines while the analysis model is based on standard FE.

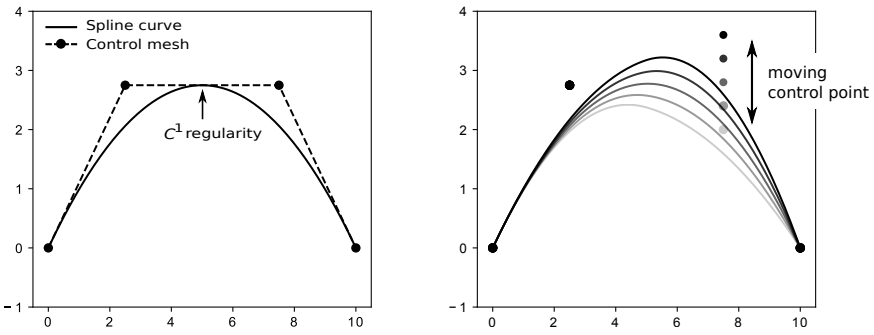

(a) Initial B-spline model along with its control mesh (degree $p = 2$ and knot-vector $\Xi_1 = \{0,0,0,0.5,1,1,1\}$).

(b) Modification of the shape by moving vertically the third control point.

Figure 5.2 – Shape modification of a two-element quadratic C^1 B-spline curve.

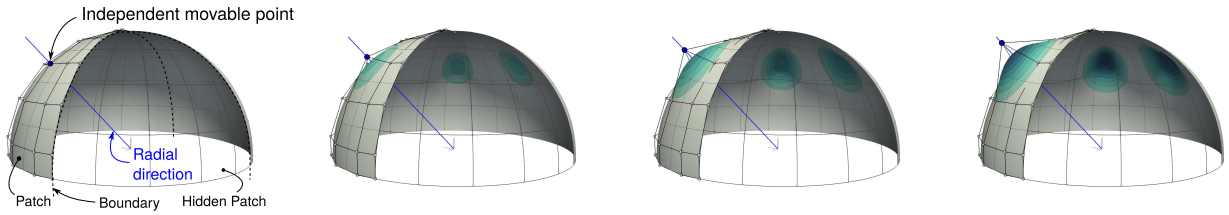

Figure 5.3 – Shape modification of a hemisphere (made of 4 quadratic C^1 NURBS patches). The control point moves radially.

Multilevel isogeometric shape optimization. Benefiting from the discussion of chapter 1, it appears obvious that one way to naturally communicate between the design and anaysis models is to use the IGA framework [Hughes et al., 2005, Cottrell et al., 2009] since it enables to get an analysis model also made of splines functions. That is why isogeometric (IG) shape optimization has been successfully applied to a wide range of applications since the advent of IGA (see [Wall et al., 2008, Nagy et al., 2011, Nagy et al., 2013,

Kiendl et al., 2014, Hirschler et al., 2019c, Wang et al., 2018] among others). More precisely, it is based on a multilevel design concept offered by the spline technology in which one can refine the geometry without altering its initial shape and regularity [Cottrell et al., 2007] (see again chapter 1). As a consequence, different refinement levels of the same spline-based geometry are considered to define both design and analysis spaces (see Figs 5.4(a)-5.4(b) (already present in chapter 1) and 5.5 for illustration in case of a B-Spline curve and a NURBS surface, respectively). The coarser level is dedicated to the parametrization of the shape to get "realistic" structures while the finer level defines the analysis model and is set to ensure accurate mechanical solutions.

Remark. *NURBS also offer the opportunity to apply shape variation by modifying the control point weights. Nevertheless, unless a very coarse NURBS model is considered [Qian, 2010, Nagy et al., 2013], it appears from the IG shape optimization community that it is generally sufficient for free-form surfaces to only use the control point coordinates (see,* e.g., *[Kiendl et al., 2014]). We will perform similarly in this work.*

Remark. *In a general context, additional attention may be required when updating the shape for a rather fine spline geometric model. Indeed, if the control points are allowed to independently move in every spatial direction, fold-overs may appear. However, as noted through Eq.* (5.8)*, only the normal component of the displacement will be considered for the update of the geometry in our shape measurement, which naturally circumvents the problem.*

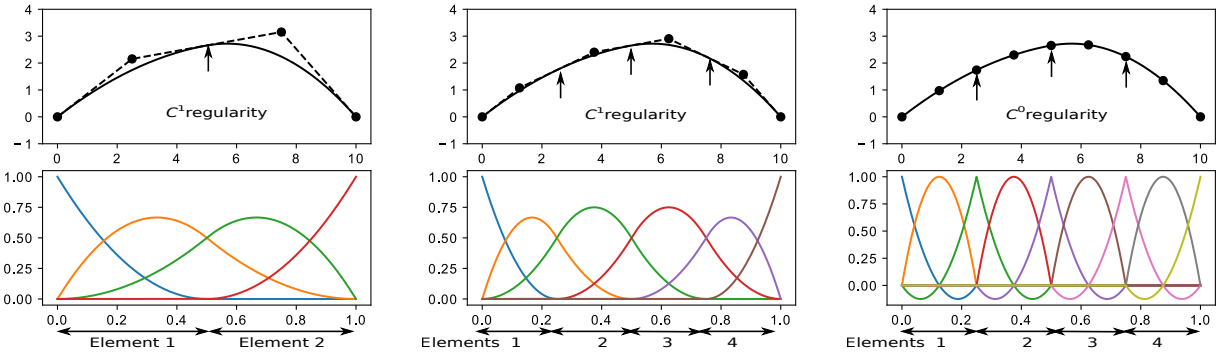

(a) Example of a design B-Spline model composed of two quadratic C^1 elements.

(b) Example of an analysis B-Spline model composed of four quadratic C^1 elements.

(c) Resulting fine FE model using the IGA-FEM bridge of chapter 1 (the final mesh is made of 4 standard C^0 – C^0 elements).

Figure 5.4 – Going from a coarse spline representation to a fine FE mesh without modifying the initial geometry: (top) geometries; (bottom) shape functions.

IGA in mesh-based shape measurement. A first attempt in applying IGA to shape measurement has been recently performed in [Beaubier et al., 2014, Dufour et al., 2015a, Dufour et al., 2016]. In these pioneering works, the authors considered a higher-order B-spline (monolevel) parametrization of the surface (thereby acting on a geometrical object which is consistent with CAD) both for shape and displacement measurements. The authors also went towards the identification of mechanical models by comparing the measured isogeometric displacement field with a computed one using a dedicated isogeometric code [Dufour et al., 2015b]. However, besides the effort to implement spline functions in the SDIC framework, the problem is that the user ends up with an experimental displacement field that is expressed on a spline basis, whereas most simulation tools are based on standard FE. Splines clearly provide flexibility for shape and displacement measurements but make connection with most of today's numerical models more complex and so, are opposed to the core idea of global approaches to DIC.

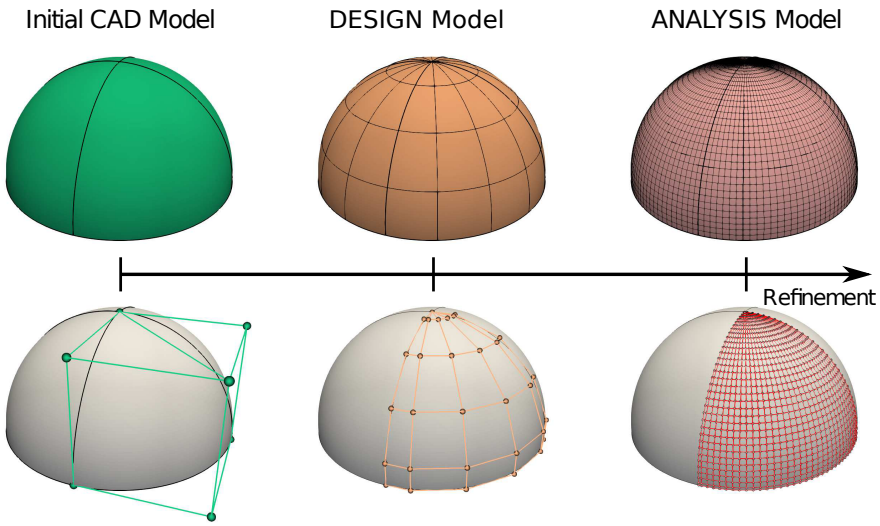

Figure 5.5 – Multilevel design approach: design and analysis spaces describe the exact same geometry and are initially obtained through different refinement levels of the initial CAD model: (top) NURBS elements; (bottom) Control points).

2.2 The proposed geometric regularization scheme

Herein, we build a hybrid IGA/FEM methodology for mesh-based shape measurement that draws up the best of each technology. On the one hand, we consider as an input and output the FE mesh that is fine enough to properly describe the underlying mechanics. In a second step, the FE mesh will thus be suitable for displacement measurement using stereo-DIC and this resulting kinematic field will be easily compared to a computed one obtained from existing, standard FE codes. On the other hand, we undertake to use the splines along with an extension of the isogeometric multilevel design concept (see again Figs 5.4(a)-5.4(b) and 5.5) for the description of the geometry and of its update in the shape measurement process. The additional ingredient of our approach is to make use the previously developed IGA-FEM bridge (see chapter 1 and [Tirvaudey et al., 2019a]) to be able to communicate between the different approximation subspaces for the geometry (multilevel B-Spline or NURBS parametrizations) and for the displacement (analysis-suitable FE mesh).

Principle. Let us start by noticing that the multilevel isogeometric concept performed in shape optimization can be easily extended to carry out a sort of multilevel design: one may begin with a coarse design model to represent the major tendencies of the surface and then refine the spline model to get the sharper variations. A similar idea has recently emerged in [Bandara and Cirak, 2017]. Based on that observation, the key point of our regularization strategy is to build a set of multilevel spline parametrizations of the geometry and to relate them to the multi-scale images used for the initialization of the shape measurement (see Eq. (5.9)). More precisely, the principle is illustrated in Fig. 5.6. The different approximation subspaces that describe the geometry are chosen in accordance with the resolution of the images so that the shape measurement problem is naturally regularized at each scale (number of DOF versus number of pixels, no need for additional regularizing terms). Moving from scale s to finer scale $s-1$, the spline design space is enhanced while keeping the same geometry, and the initial solution for the shape measurement problem of scale $s-1$ is taken as the final solution of scale s. Since it is based on functions coming from the geometric design community, the proposed regularization scheme has a strong geometrical meaning, that is why we refer to geometric regularization to characterize our technique.

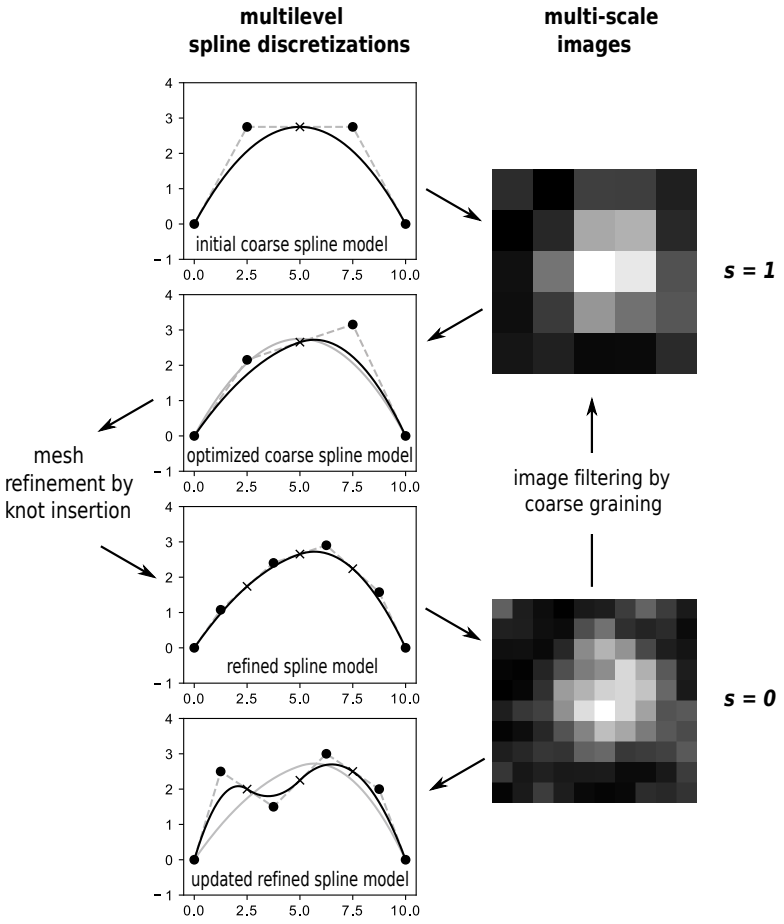

Figure 5.6 – Principle of the proposed geometric regularization: a multilevel spline design process is coupled with the multi-scale initialization of shape measurement.

Formulation. To mathematically formulate the different operations, let us now recycle some of the notations introduced in chapter 1. We denote by $\mathbf{D}^{c,f}$ the spline refinement operator that relate the coarse spline matrix functions $\mathbf{R}^c$ to the fine one $\mathbf{R}^f$ and, conversely, the fine control points' locations $\mathbf{x}^f$ to the coarse control points' ones $\mathbf{x}^c$:

$$\mathbf{R}^c = \mathbf{D}^{c,f}\mathbf{R}^f \quad \text{and} \quad \mathbf{x}^f = \left(\mathbf{D}^{c,f}\right)^T \mathbf{x}^c. \tag{5.10}$$

Such transformations enable to communicate between the different multilevel spline discretizations of Fig. 5.6. Recalling that the desired input and output in our methodology is the fine (analysis-suitable) FE mesh, it is now required to establish a link between this FE mesh and these different (multilevel) spline-based descriptions. This is where the IGA-FEM bridge developed in chapter 1 comes into play. As a remainder it enables to map a n-element p-degree C^0 basis onto a smooth (possibly rational) n-element p-degree spline basis. This transformation leads to the building of the Bézier-based operator $\mathbf{D}_{FE}$ that will relate the fine standard nodal Lagrange discretization (same description as in Eq. (5.4)) to the finest smooth spline discretization:

$$\mathbf{R}^f = \mathbf{D}_{FE}\mathbf{L} \quad \text{and} \quad \mathbf{x}^{FE} = \mathbf{D}_{FE}^T \mathbf{x}^f. \tag{5.11}$$

As an example, this treatment has been performed to obtain the FE model of Fig. 5.4(c) starting with the spline model of Fig. 5.4(b). From the resulting FE mesh, we then have the opportunity to recover the refined spline Hessian and gradient operators without implementing IGA but simply by projecting the related FE operators onto the reduced, spline basis (see again chapter 1). More specifically, from Eq. (5.7) we can

compute the associated spline operator $\mathbf{H}_{IG}^{f}$ such that (superscript k omitted):

$$\begin{aligned}\mathbf{H}_{IG}^{f} &= \int_{\Omega} \mathbf{R}^{f}\,(\mathbf{J}_0{}^{T}\nabla f_0 - \mathbf{J}_1{}^{T}\nabla f_1)\,(\mathbf{J}_0{}^{T}\nabla f_0 - \mathbf{J}_1{}^{T}\nabla f_1)^{T}\mathbf{R}^{f\,T}\,\mathrm{d}\Omega \\ &= \int_{\Omega} \mathbf{D}_{FE}\mathbf{L}\,(\mathbf{J}_0{}^{T}\nabla f_0 - \mathbf{J}_1{}^{T}\nabla f_1)\,(\mathbf{J}_0{}^{T}\nabla f_0 - \mathbf{J}_1{}^{T}\nabla f_1)^{T}\mathbf{L}^{T}\mathbf{D}_{FE}^{T}\,\mathrm{d}\Omega \\ &= \mathbf{D}_{FE}\,\mathbf{H}_{FE}\,\mathbf{D}_{FE}^{T}.\end{aligned} \tag{5.12}$$

As well, the spline gradient operator $\mathbf{b}_{IG}^{f}$ can be obtained from its FE counterpart $\mathbf{b}_{FE}$ (see Eq. (5.7)) as follows:

$$\mathbf{b}_{IG}^{f} = \mathbf{D}_{FE}\,\mathbf{b}_{FE}. \tag{5.13}$$

Furthermore, the same procedure can be applied to recover the coarse spline operators from the fine FE ones:

$$\begin{cases}\mathbf{H}_{IG}^{c} = \mathbf{D}^{c,f}\,\mathbf{H}_{IG}^{f}\left(\mathbf{D}^{c,f}\right)^{T} = \mathbf{D}^{c,f}\,\mathbf{D}_{FE}\,\mathbf{H}_{FE}\,\mathbf{D}_{FE}^{T}\left(\mathbf{D}^{c,f}\right)^{T} \\ \mathbf{b}_{IG}^{c} = \mathbf{D}^{c,f}\,\mathbf{b}_{IG}^{f} = \mathbf{D}^{c,f}\,\mathbf{D}_{FE}\,\mathbf{b}_{FE}\end{cases}. \tag{5.14}$$

Consequently, the isogeometric regularized shape measurement systems of form $\mathbf{H}_{IG}^{c}\mathbf{d}_{q^c} = \mathbf{b}_{IG}^{c}$ and $\mathbf{H}_{IG}^{f}\mathbf{d}_{q^f} = \mathbf{b}_{IG}^{f}$ can be solved instead of the ill-posed fine FE shape measurement systems (5.7). Finally, let us remember that the resulting isogeometric DOF vectors, denoted by $\mathbf{q}^{c}$ or $\mathbf{q}^{f}$, can be back-converted in terms of nodal FE shape update $\mathbf{q}$:

$$\mathbf{q} = \mathbf{D}_{FE}^{T}\left(\mathbf{D}^{c,f}\right)^{T}\mathbf{q}^{c} \quad \text{or} \quad \mathbf{q} = \mathbf{D}_{FE}^{T}\mathbf{q}^{f}, \tag{5.15}$$

so that a unique basis is used for the representation of the surface at each multilevel step. For more clarity, an overview of the different transformations is given in Figure 5.7.

Remark. *As in chapter 1, we clearly observe through Eqs.* (5.13) *and* (5.14) *that our method can be interpreted as a reduced-order method: the initial FE-based system is projected onto the reduced smoother isogeometric basis. Note, however, that specifically choosing the isogeometric basis as the reduced basis here seems to be highly relevant since (i) it is geometrically sound and (ii) operator* $\mathbf{D}^{c,f}\,\mathbf{D}_{FE}$ *is sparse which enables good computational time saving.*

Remark. *It may also be noticed here that, as for the non-invasive implementation of IGA in chapter 1, the proposed scheme is essentially applied to quadratic functions since almost all standard FE codes do not go beyond second-order Lagrange finite elements. In other terms, the idea is to start with a quadratic B-Spline or NURBS description of the nominal shape (which is sufficient to represent most of engineering surfaces) and then build upon it a fine quadratic FE mesh (of identical geometry) that could be used for 3D displacement measurement. Nevertheless, let us emphasize again that the proposed methodology could be directly applied to higher-order spline-based discretization, provided that the corresponding higher-order FE are available in a FE-SDIC environment.*

Global scheme. Finally, an overview of the proposed regularization scheme included in the full calibration of the whole stereo rig is given in Fig. 5.8. For simplicity, we denote by $\mathbf{D}_s$ the extraction operator that maps the fine FE space onto the spline discretization of scale s, *i.e.* $\mathbf{D}_s$ is defined such that:

$$\mathbf{D}_0 = \mathbf{D}_{FE} \quad \text{and} \quad \mathbf{D}_s = \left(\prod_{i=0}^{s-1}\mathbf{D}^{(s-i),(s-i-1)}\right)\mathbf{D}_{FE},\ \forall s \in \{1,..,n_s\}, \tag{5.16}$$

where n_s is the number of scales and $s = 0$ corresponds to the finest scale while $s = n_s$ refers to the coarsest scale. As can be observed, making use of the IGA-FEM bridge, the implementation is performed from

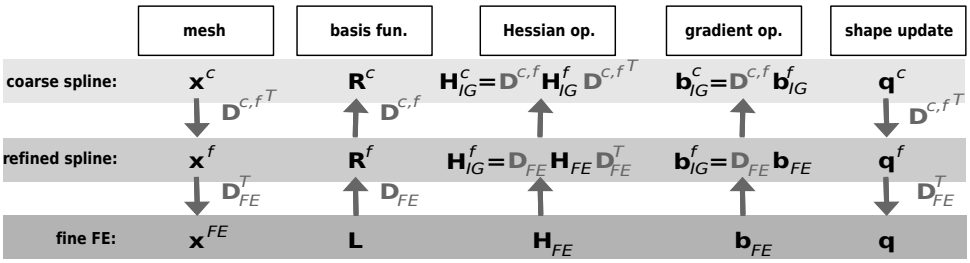

Figure 5.7 – Overview of the different transformations enabling to communicate between the fine (analysis-suitable) FE mesh and the different (multilevel) spline-based discretizations.

standard FE-SDIC routines with minimal effort, that is why we refer to as non-invasive to characterize our strategy (see also chapters 1 and 2 where the concept of non-invasiveness in the field of computational mechanics is further discussed). Summarizing, we proceed as follows for the regularization. From the initial CAD representation of the theoretical surface, we build in the pre-processing step a fine analysis-suitable FE mesh and the different multilevel spline discretizations through their corresponding extraction operators $\mathbf{C}_s$. Then, entering into the shape measurement loop and beginning with the coarsest scale, we project, at each iteration of the Gauss-Newton solver, the FE hessian and gradient onto the first-level spline space and solve the associated regularized spline system. We thus end up with the spline shape update that can be converted in terms of nodal FE shape update so that the FE hessian and gradient can be updated for the next iteration. Going to the finest scale, we finally repeat the previous procedure with the different refined spline spaces to regularize at each scale. The final shape can be given either in terms of splines (thereby directly compatible with CAD environments) or in terms of finite elements (thus facilitating the communication with numerical simulations).

From initial CAD $\mathbf{x}^c$ *and fine images, build:* **PRE-PROCESS**
- FE mesh: $\mathbf{x}^{FE}$
- multilevel extraction operators: $\mathbf{D}_s, \forall s$
- multi-scale images: $f_0^s,\ f_1^s\ \forall s$

Decreasing loop on s *(multi-scale loop)* **STEREO CALIBRATION**
Loop on i *(fixed point loop)*
Calibration of cameras' parameters
(Gauss-Newton to solve problems of form (5.5))
Loop on k **REGULARIZED SHAPE MEASUREMENT**
Compute $\mathbf{H}_{FE}^k$ and $\mathbf{b}_{FE}^k$ from $\mathbf{q}^k$, f_0^s and f_1^s
(Classic FE shape measurement routine)
Solve IG regularized system: $\mathbf{D}_s\mathbf{H}_{FE}^k\mathbf{D}_s^T\mathbf{d}_{q_s}^k = \mathbf{D}_s\mathbf{b}_{FE}^k$
Update IG shape: $\mathbf{q}^{s^{k+1}} = \mathbf{q}^{s^k} + \mathbf{d}_{q^s}^k$
Update FE shape: $\mathbf{q}^{k+1} = \mathbf{D}_s^T\mathbf{q}^{s^{k+1}}$
end
end
end

Build final optimal shape: **POST-PROCESS**
- IG description: $\mathbf{x}^f = \mathbf{x}^f + \mathbf{q}^f$
- FE description: $\mathbf{x}^{FE} = \mathbf{x}^{FE} + \mathbf{q}$

Figure 5.8 – Overview of the proposed regularization scheme included in the full calibration of a stereo rig.

3 Assessment of the proposed regularization through a real example

The proposed regularization technique for FE mesh-based shape measurement is now assessed through the analysis of a real experiment. A steel open-hole tensile specimen of size 180 × 50 × 2 mm and hole diameter 28 mm is considered. A dedicated speckle pattern is laser printed over a layer of uniform white paint. A pair of 5 Mpx CCD cameras and 50 mm lenses is used to capture the 8bit 2452x2052 digital images presented in Fig. 5.1. The stereo-angle is set around 25° which represents a good compromise between in-plane and out-of-plane uncertainties [Balcaen et al., 2017]. The intrinsic parameters of the non-linear camera models (first order radial distortions) are calibrated prior to the experiment using a series of digital images of a calibration target made of a grid of 12x9 dots with a step size of 3 mm. As stated previously, the obtained intrinsic parameters are considered fixed in the remainder of the study.

More precisely, the configuration for shape measurement is as follows. The specimen is clamped at the top and bottom jaws of an electro-mechanical tensile testing machine. Since the jaws are slightly misaligned, the hyper-static clamping generated a torsional moment and the specimen twisted. The misalignment was around 2 or 3° which should generate significant waviness. With this test case, it is possible to analyze the method in a configuration where the difference between the theoretical (considered flat) and real (twisted) shapes is significantly greater than in standard mechanical experiments.

3.1 Pre-processing: construction of the multilevel spline design spaces and FE mesh

The nominal geometry of the sample consists in a plate with a circular hole. We proceed as classically in IGA for the building of the first spline model: 4 quadratic C^0-C^0 elements compose the coarse spline mesh, as depicted in Fig. 5.9(a). Note that this geometry is similar to the one in chapter 1, see Fig. 1.4. Once again, the interested reader is referred to, *e.g.*, [Piegl and Tiller, 1997, Cottrell et al., 2009] for more details regarding NURBS constructions. Along the radial direction, even if degree 1 would be sufficient, we also take degree 2 so as to be consistent with the final FE-mesh that is made of standard 9-node (*i.e.* bi-quadratic) elements. Starting with the NURBS model of Fig. 5.9(a), we then only perform knot-insertion (inserting one knot at a time) to get the different (multilevel) NURBS parametrizations (see Figs. 5.9(b) and (c)). We finally further carry out knot-insertion and apply the IGA-FEM mapping of Eq. (5.11) to obtain the analysis-suitable FE-mesh (see Fig. 5.9(d)).

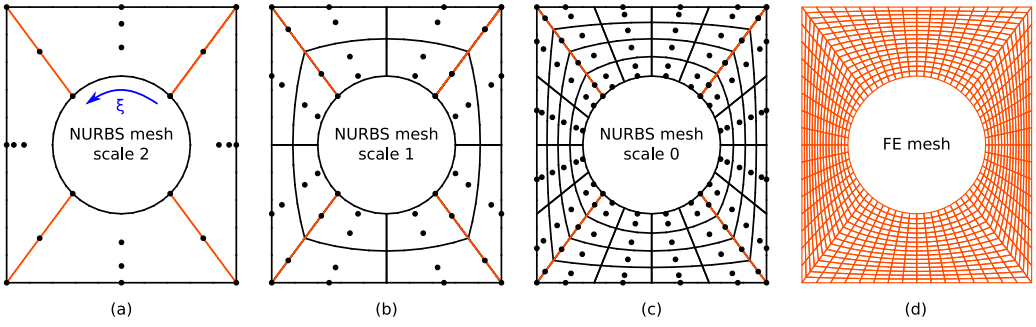

Figure 5.9 – Initial CAD parametrization, multilevel NURBS meshes and final fine FE mesh. The C^0 lines are in orange. The final FE mesh is composed of 1000 elements.

3.2 Shape measurement results

Classic FE-based shape measurement without any regularization. A first classic FE shape measurement is performed using the FE mesh given in Fig. 5.9(d) without any regularization. The obtained shape is represented in Fig. 5.10. In order to compare the shape measurements obtained with the different techniques,

and in particular with the standard subset-based approach, we choose the color data to represent the distance to the best fitting plane (BFP) instead of directly plotting the shape correction field $S^h(X)$. Indeed, $S^h(X)$ is not available with the subset approach [Garcia, 2001, Garcia et al., 2002]. The obtained shape is typical of a twist test. The waviness is around one millimeter, which, at the scale of this specimen, is large. In addition, the resulting shape is relatively noisy. Even though the noise is one order of magnitude smaller than the artificially large shape correction field, it still seems large and unphysical.

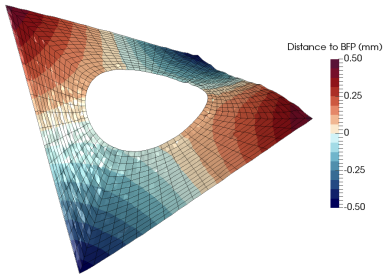

Figure 5.10 – Twisted specimen: shape obtained with classic FE-SDIC without regularization (def. scale fact. x30).

Use of standard Tikhonov regularization. In order to regularize this noise, a classic Tikhonov regularization technique is considered here. The shape obtained for three different regularization weights is given in Fig. 5.11. As expected, using Tikhonov regularization, the shape measurements appear clearly smoother, especially for large values of the regularization weight (see Figs. 5.11(a) and (b)). For a lower value, the solution looks more like the shape obtained without regularization which means that the regularization is not sufficient (see Fig. 5.11(c) with respect to Fig. 5.10). Now, the interested point to observe here is that high levels of regularization may also affect the shape. Indeed, on Fig. 5.11(d), the influence of the regularization weight on the shape is depicted, with the subset approach as the reference. Using a too large regularization weight reduces the displacement magnitudes and underestimates the shape waviness. This is due to the differential nature of the Tikhonov regularization (5.9): we recall that it relies on the gradient of the shape, thereby eliminating, *e.g.*, the rotations. Asymptotically, using very large values of regularization would lead to an almost constant correction field, which would correspond to a rigid body translation of the observed surface with respect to the theoretical CAD. In other words, a satisfying value of the regularization weight may not exist, as it seems to be the case here.

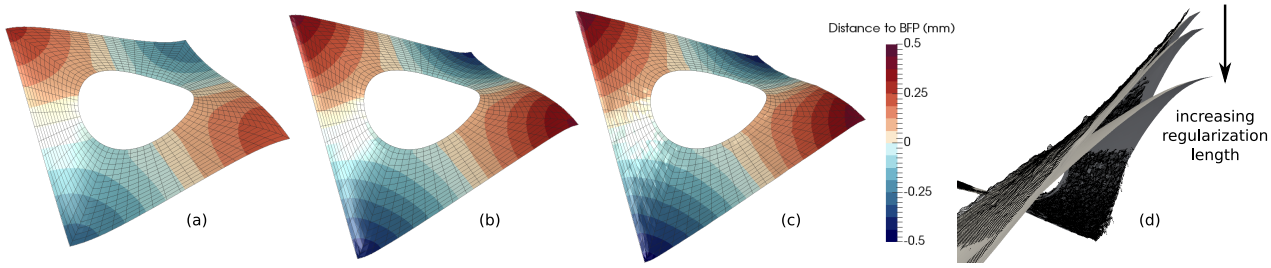

Figure 5.11 – Twisted specimen: shape obtained using a classic FE-SDIC with Tikhonov regularization for different values of the regularization length: decreasing values of the regularization length from (a) to (c) respectively (def. scale fact. x30).

Use of the proposed geometric regularization. Next, the proposed geometric regularization scheme is considered with the same image set. The multi-scale initialization technique described in Fig. 5.6 is applied with three scales using the three NURBS meshes of Fig. 5.9. The corresponding shapes obtained at

each scale are given in Fig. 5.12. First, it can be observed that the shapes obtained at the three scales are very smooth. Indeed, the very low-dimensional spline approximation subspace acts as a very strong regularization technique. Each of the three shapes are very similar to each other and also in good agreement with the shape provided by the subset DIC method. In addition, the reduction in the correction field's magnitude observed when using the Tikhonov regularization does not occur here. Even at the highest scale, where the spline representation is particularly coarse, a very good approximation of the shape is already obtained. This property of the geometric regularization is particularly interesting for the highest scales of the multi-scale approach, since they are associated to high regularization levels.

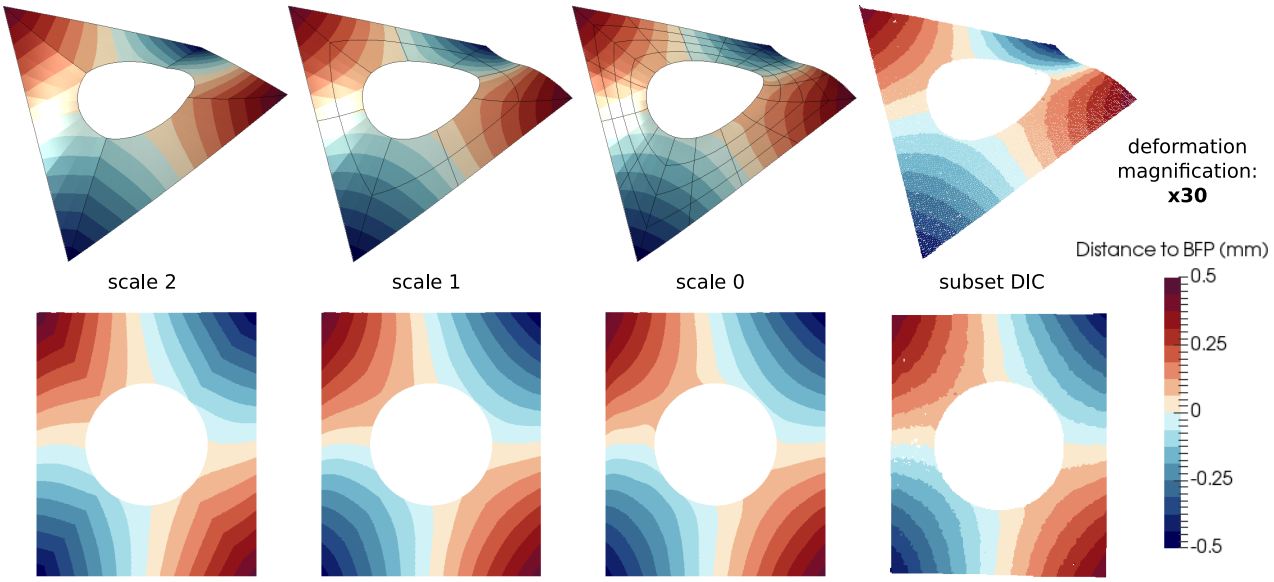

Figure 5.12 – Twisted specimen with the proposed geometric regularization (def. scale fact. x30).

Finally, Fig. 5.13(left) presents the evolution of the standard deviation of the graylevel residual field in percent of the reference image dynamics (later denoted *relative residual*) as a function of the iteration number. It compares the convergence of the problem with and without iterating between calibration of extrinsic parameters (• symbols) and shape correction problems (× symbols). It can be seen that, at least on this case, converging the fixed point algorithm (by alternating between calibration and shape problems) is mandatory to converge towards an accurate solution. It is the case here because the actual shape is significantly different from the initial CAD. On the (right) side of the same figure, the relative residual is plotted as a function of the CPU time normalized by the CPU time taken by one iteration at scale 0, for the monoscale (only scale 0) and multi-scale approaches. It can be seen that, although the number of iterations may increase, the computational time is clearly reduced (divided by 2 in this case), since the higher scales are associated to low definition images whose interpolation is far cheaper. Note also, that when using the multi-scale approach, the value of the relative residual was lower than that of the monoscale alternative. Lower relative residual emerges from the fact that the multi-scale initialisation, in addition to convergence acceleration, was designed to avoid local minima.

Summary and discussion. Recapitulating, we have developed in this chapter a hybrid IGA-FEM strategy for the regularization of the FE mesh-based shape measurement. From a regularization point of view, the proposed strategy draws inspiration from the techniques developed recently in the isogeometric shape optimization community, especially with the multilevel design concept [Kiendl et al., 2014, Hirschler et al., 2019c, Wang et al., 2018]. By making use of the advanced spline refinement procedures and of the IGA-FEM bridge developed in chapter 1, the key idea here is to extract, from the initial FE subspace,

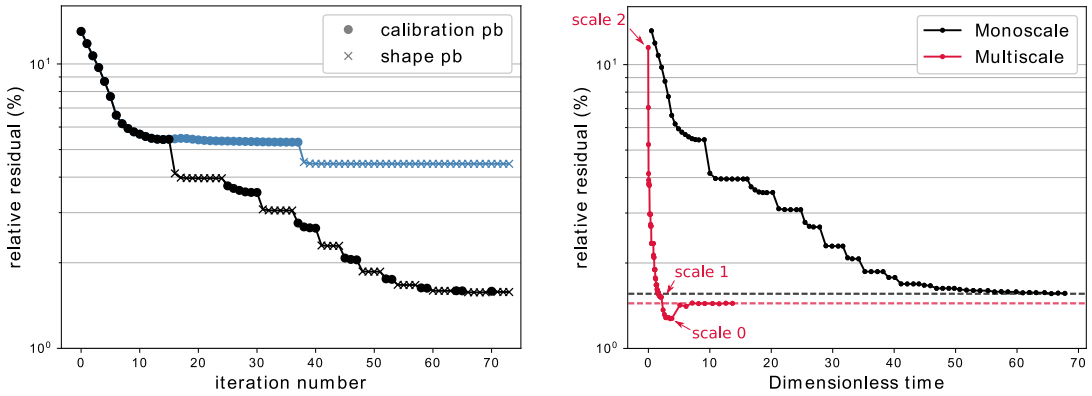

Figure 5.13 – Convergence of the algorithm on the twisted use case: (left) convergence (VS iterations) of the relative residual with (black) and without (blue) the fixed point iterations and (right) convergence speed (VS dimensionless time) for the monoscale and multi-scale approaches.

smoother multilevel spline parametrizations of the geometry and to relate them with the multi-scale images used for the initialization of shape measurement. This treatment enables to efficiently regularize the problem at each scale. Our results clearly indicate the superiority of the approach, especially as the real and the theoretical shapes are far from each other. We always manage to obtain a consistent smooth final shape within a limited number of iterations (see also [Colantonio et al., 2020] where additional tests are carried out), while the standard Tikhonov regularization appears to fail in presence of rotations. From a practical point of view, the proposed approach consists of nothing more than projecting the ill-posed FE shape measurement problem onto more regular spline subspaces by using appropriate operators. But among the possible reduced bases which may regularize the FE shape problem, the one presented here yields the isogeometric system that has the great advantages to be geometrically sound and sparse. As a result, we end up with a technique that draws up the best of IGA and FEM technologies. On the one hand, we benefit from the increased smoothness of spline functions for the description of the geometry and of its update. On the other hand, we can perform the resolution in a non-invasive manner from an existing FE-SDIC code and, we are able to describe the final shape using the same fine FE mesh as the one which could be used for displacement measurement and identification of mechanical models.

The interested reader may notice that the proposed methodology is inspired from the current practice in isogeometric shape optimization except for the last ingredient that consists of complementing the multilevel isogeometric concept with the IGA-FEM bridge [Tirvaudey et al., 2019a]. Conversey, this last component could be interesting for the field of shape optimization and particularly within the original CAD-based approach [Hasan Imam, 1982, Braibant and Fleury, 1984], since it would enable to naturally relate the (spline-based) design and (FE-based) analysis spaces. We actually did some work in this direction, see [Bouclier et al., 2019]. More precisely, by means of the same kind of transformations as the ones here, we have been able to build an analysis 8-node FE shell mesh sufficiently close (in terms of geometry) to an initial design NURBS shell mesh. The interest is that this FE mesh can be computed using an existing FE industrial software, taken as a black-box. In other words, we are able to perform isogeometric shape optimization without implementing IGA practically. Some results of isogeometric shape optimization of shells have been obtained using the well-known industrial software Abaqus.

Returning to the case of FE shape measurement, the limit of our method is that it involves an input FE mesh that is (at least) quadratic (and even made of elements exhibiting a tensor product strucutre, *i.e* the 9-node element) so that we are able to extract from the corresponding FE analysis space different smooth quadratic spline design spaces. To generalize the method to any arbitrary FE mesh, we are currently working on an extension using the concept of Free-Form Deformation (FFD) originating from the graphic design

area [Sederberg and Parry, 1986], and also applied in engineering fields as, for example, aerostructural optimization [Duvigneau, 2006, Lassila and Rozza, 2010, Kenway and Martins, 2014]. It enables to decouple the design space from the geometry to be updated. We further discuss the idea of FFD in the next chapter where we extend it for the isogeometric structural shape optimization of stiffened panels.

CHAPTER 6

Isogeometric shape optimization of complex shell structures

Contents

Designing structural parts against the material limits, the impact of loads, and many other constraints, is a standard interest in engineering. However, finding the best possible design, namely the optimal design, is a complex discipline that combines mathematics and mechanics. More importantly than for shape measurement in previous chapter, a close link between the geometric and analysis model is essential in structural shape optimization since both models constantly communicate inside the optimization loop. As a result, shape optimization is a great application of IGA since the latter integrates CAD and analysis. Let us point out here that, once again as in previous chapter, the initial CAD model has to be understood as the minimal boundary-fitted spline mesh that properly capture the initial smooth geometry. Since the advent of IGA, isogeometric structural shape optimization has been the object of intensive studies; see, *e.g.* [Wall et al., 2008, Qian, 2010, Nagy et al., 2010, Nagy et al., 2011, Nagy et al., 2013, Kiendl et al., 2014, Taheri and Hassani, 2014, Wang and Turteltaub, 2015, Fußeder et al., 2015, Kang and Youn, 2016, Lian et al., 2017, Wang et al., 2017, Choi and Cho, 2018, Lei et al., 2018, Wang et al., 2018, Hirschler et al., 2019c, Weeger et al., 2019]. A general procedure, which has been improved over the years [Daxini and Prajapati, 2017, Wang et al., 2018], is commonly adopted. Roughly speaking, it is based on (i) a multilevel spline concept between the design and analysis models [Nagy et al., 2013, Kiendl et al., 2014, Wang and Turteltaub, 2015, Hirschler et al., 2019c] and (ii) updating the shape by altering the spatial location of the control points.

From this overview, it appears that isogeometric shape optimization has not yet been truly applied to real-world structures. More precisely, mainly simple geometries modeled as single patch structures have been considered. However, as underlined in chapter 3 (see especially Fig. 3.1), it is well-known that a single spline patch cannot represent large and complex geometries. We are interested here in stiffened structures which are omnipresent in aeronautics (see chapter 3 again). The final goal is to be able to properly optimize the shape and position of the stiffeners, and also if desired, the global shape of the panel. Such an issue has been faced in the standard FEM community: see, *e.g.*, [Mulani et al., 2013, Locatelli et al., 2014,

Singh et al., 2017]. It can be noted that these frameworks lack of compactness in the sense that several softwares are used during the different steps of optimization (geometry parametrization, meshing, analysis), which necessarily involves some approximations, thereby severely affecting the robustness and flexibility of the shape design process.

Based on what has been yet successfully developed in chapter 3 for computing stiffened panels, this chapter aims at applying isogeometric shape optimization for designing representative aerostructures. The key point concerns the "geometrical" handling of non-conforming multipatch discretizations for shape optimization. We present a methodology inspired from Free-Form Deformation techniques [Sederberg and Parry, 1986] and we introduce an embedded shell formulation. It enables to impose complex geometric constraints between non-conforming patches in a simple and suitable manner. This work has been performed in the PhD thesis of Thibaut Hirschler [Hirschler, 2019] and has mainly been published in [Hirschler et al., 2019b]. The interested reader is advised to consult these references for completeness. Finally, we open the door for the efficient design of structural details within such complex macrostructures by running a shape optimization process that calls upon the non-conforming non-invasive algorithm of chapter 2(section 3.2). This last work shares the same philosophy as in [Hirschler et al., 2019b] and has been actually achieved before in [Bouclier and Passieux, 2018].

1 Isogeometric shape optimization

To start with, we outline here the basics of isogeometric shape optimization. The main ingredients regarding the design aspect have already been given in chapter 5(section 2.1) given the proximity of the shape measurement and shape optimization problem. As a result, we only formalize here the isogeometric shape optimization approach and sometimes refer to the illustrations of previous chapter. Since the intended application concerns aerostructures in this chapter, an emphasis on shells is made regarding the illustrations. For further details on isogeometric structural shape optimization, the interested reader is advised to consult [Hirschler, 2019](chapter 3) and [Hirschler et al., 2019c], from which this part was extracted.

1.1 Optimization flowchart

Fig. 6.1 describes the main steps of the shape optimization process. It gets an initial CAD model as a main input. As an output the optimal shape is provided and, an interesting point to notice is that this shape is a spline geometry too. Therefore, the result is directly usable by designers and, thus, for production. There is no need to re-design the final geometry in a CAD environment as it would be the case with FE-based optimization. From a global point of view,the optimal spline geometry is obtained from an iterative process with three steps. Each iteration consists in:

1. updating the current shape in a hopefully better one,
2. running the analysis for this new geometry and then inferring mechanical and/or geometrical properties of interest,
3. computing new design variations to further improve the structure.

A more detailed description of each step of the process is given in the following paragraphs.

1.2 Multilevel design

As highlighted in previous chapter (see especially Fig. 5.5), the main ingredient is the multilevel approach which allows to define the design and analysis models in a versatile manner. Indeed, both design and analysis models are initially obtained through spline refinement of the initial geometry of the structure and

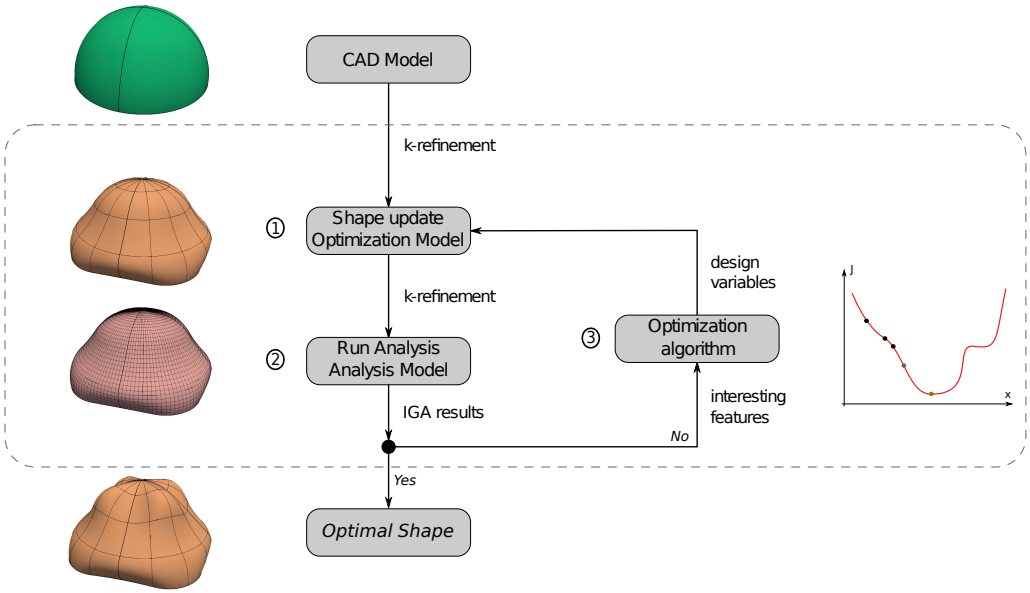

Figure 6.1 – Isogeometric shape optimization flowchart: overview of the main steps of the process.

thus represent the exact same geometry during the optimization process. The shape variations are imposed on the design model. Therefore, depending on the complexity of the admitted shape variations, one can choose an appropriate discretization level. Then, the level of refinement for the analysis model is defined so as to ensure good quality of the computation. Obviously, the analysis model is finer than the optimization model. Finally, thanks to the refinement procedure of spline functions, the link between both models is kept (see Eq. (5.10) as a reminder). Once again, we refer the interested reader to, *e.g.*, [Piegl and Tiller, 1997, Lee and Park, 2002] for more details on refinement strategies of splines and their matrix representation.

1.3 Design variables

The isogeometric framework provides a proper and accurate way to vary the geometry. It has long been established that shape control of splines is very comfortable and leads to smooth optimal design [Hasan Imam, 1982, Braibant and Fleury, 1984]. Indeed, a straightforward and natural way of modifying the shape of the structure is to move the control points (see again Figs. 5.2 and 5.3). As in previous chapter, even in case of NURBS we only use the control point coordinates as design variables, the influence of the weights being minimal in case of general free-form surfaces [Qian, 2010, Kiendl et al., 2014]. Eventually, as quickly mentioned in previous chapter, taking the control point coordinates as design variables requires attention to avoid local non-injectivities due to fold-overs. In the context of isogeometric shape optimization, links between design variables and move directions are usually set up to avoid these challenges [Wall et al., 2008, Kiendl et al., 2014, Taheri and Hassani, 2014, Wang et al., 2017]. Fig. 5.3 showed this idea in the case of a hemisphere. By letting only each design control point moving in the radial direction, we avoid mesh distortion problems.

1.4 Formulation and resolution

A constrained optimization problem. A typical shape optimization problem can be formulated as the minimization of a given objective function carried out over a set of admissible domains. In this work, we focus on the common shape optimization problem that consists of minimizing the compliance (in other words, maximizing the rigidity of the structure) under a given volume constraint (otherwise the solution would be an infinite volume). Other objective or constraint functions could have been considered as the

mass, the displacement of a given point of the structure, the maximal stress, or in the non-linear regime, the critical buckling load for instance. The design space is limited by lower bound $\mathbf{s}_l$ and upper bound $\mathbf{s}_u$ which surround the n_s design variables collected in vector $\mathbf{s} = (s_1, s_2, \dots, s_{n_s})$. The volume of the structure (or, equivalently the surface area in case of shape optimization of shells) is denoted by V which has to be lower than a prescribed volume V_0. In the discrete setting, the shape optimization problem formally consists of looking for the design variables $\mathbf{s}$ such that:

$$\min f(\mathbf{s}, \mathbf{u}(\mathbf{s})) \quad \text{where} \quad f(\mathbf{s}, \mathbf{u}(\mathbf{s})) = \frac{1}{2}\mathbf{f}(\mathbf{s})^T\mathbf{u}(\mathbf{s}) \quad \text{subject to} \quad \begin{aligned} &\mathbf{s}_l \leq \mathbf{s} \leq \mathbf{s}_u, \\ &V(\mathbf{s}) \leq V_0. \end{aligned} \tag{6.1}$$

$\mathbf{f}$ and $\mathbf{u}$ are quantities coming from the discrete governing equations of the direct problem, *i.e.* in our case, the isogeometric distretized mechanical problem. $\mathbf{u}$ is interpreted as the state variable of the problem here. It is obviously the displacement DOF vector that comes from the resolution of the mechanical problem corresponding to a given set of design variables $\mathbf{s}$: $\mathbf{K}(\mathbf{s})\mathbf{u}(\mathbf{s}) = \mathbf{f}(\mathbf{s})$.

This work is not focused on the development of a new, specific optmization algorithm. There are actually plenty of efficient numerical methods to solve such an optimization problem (see, *e.g.*, [Nocedal and Wright, 2006]). We use here the gradient-based algorithm `SLSQP` [Kraft, 1988] available in many scientific packages, as for instance `SciPy` [Jones et al., 01]. From the simple algorithms presented in chapter 4 in case of unconstrained optimization, the algorithm used here is based on the SQP method [Fletcher, 1987] that can be viewed as an extension of the Newton method for constrained optimization. At each major iteration, an approximation is made of the Hessian of the Lagrangian function associated to (6.1) using a quasi-Newton updating method. These methods are appealing because the Hessian is not directly computed but approximated through the gradient variations during the resolution, thereby offering simplicity, minimal computational cost and good convergence properties. A popular method for this approximation is the BFGS Hessian update strategy [Broyden, 1970].

Sensitivity analysis. The crucial issue when using such algorithms is the computation of the sensitivities, *i.e.* the gradient of the objective function (and constraint function) with respect to the design variables. For a proper and fast computation of the sensitivities, global finite difference, which consists in perturbing each design variables with a small variation and evaluate the response of the structure for each of these perturbations, is often proscribed in favor of semi or even full analytical derivation. In our case of the compliance as objective function, a simple chain rule to derive the composition $f(\mathbf{s}, \mathbf{u}(\mathbf{s}))$ leads to the following result for the i^{th} component of the gradient [Nagy et al., 2013, Kiendl et al., 2014]:

$$\left(\nabla f\right)_i = \mathbf{u}^T\left(\frac{\partial \mathbf{f}}{\partial s_i} - \frac{1}{2}\frac{\partial \mathbf{K}}{\partial s_i}\mathbf{u}\right), \tag{6.2}$$

where $\frac{\partial \mathbf{f}}{\partial s_i}$ (respectively, $\frac{\partial \mathbf{K}}{\partial s_i}$) denote the vector (resp. matrix) gathering the derivative with respect to s_i of the components of $\mathbf{f}$ (resp. $\mathbf{K}$). In the present situation, the problem is self-adjoint so the adjoint sensitivities performed above do not involve any equations to be solved, while global finite difference sensitivities would have required n_s additional problem resolutions. In the semi-analytical framework, the derivatives of the force vector and stiffness matrix with respect to the design variables in (6.2) are approximated by first-order finite differences. As a result, one has to build as many stiffness matrices and force vectors as the number of design variables, but there is no need to solve the state governing equations for each design variable. The interest of semi-analytical sensitivities, besides the appearing simplicity, is the independence to the element formulation. This is very convenient from an implementation point of view. However, it may be less robust because of the parameter to choose in the finite difference.

To overcome this issue it is possible by uing IGA to evaluate the sensitivities in a fully analytical fashion [Qian, 2010, Nagy et al., 2013, Taheri and Hassani, 2014, Lei et al., 2018]. Basically, the procedure follows three steps; first, one expresses the link between the design variables and the control points of the

design model; then, one makes use of the isogeometric bridge to transfer the sensitivities to the control points of the analysis model; and finally, one explicitly differentiates the IGA operators with respect to the control points which is easier when resorting to a finite element formulation based on curvilinear coordinates (as it is the case for shells, see chapter 3(section 2.2)). In this work, we compute the sensitivities analytically for better robustness and minimal computational cost. We do not go further into the details here, the interested reader is advised to consult [Hirschler, 2019](chapter 3) and [Hirschler et al., 2020] for further insights regarding this point.

Remark. *To conclude this first section, it may be noticed that, in case of shape optimization, the initial guess for the gradient-based algorithm is straightforward: this is the first shape provided by the designers according to their experiences. Thus, the process of Fig. 6.1 modifies the shape of the structure in the neighborhood of the initial geometry, which most of times results in a mechanical response significantly improved from that of the initial configuration. The main problematic rather conerns the choice of an appropriate design space. Note finally that a similar procedure as the one for initializing the shape measurement problem of previous chapter can be applied here: starting with a very coarse discretization, the design model is refined successively each time a minimum is reached, which results in an efficient filtering strategy as shown by [Bandara and Cirak, 2017].*

2 Design of innovative stiffened structures

Applying the isogeometric shape optimization strategy introduced above for designing large stiffened aerostructures is a challenging task from both geometric and analysis sides. From the analysis point of view, we have built in chapter 3 an efficient strategy to couple non-conforming discretizations. After reminding the interest of such a DD solver to be integrated into the shape optimization loop, we focus in this section on the geometrical aspect. Indeed, an adequate methodology needs to be developed in order to impose the shape modification of complex isogeometric structures with multiple parts.

2.1 Interest of a DD solver for the shape optimization of complex structures

Structural optimization is computationally expensive because it requires a large successive number of structural (and sensitivity) analysis (see again Fig. 6.1). If the goal is to design complex, real-world structures, then it is crucial that these computations are efficiently performed. In this context, the non-conforming DD solver developed in chapter 3 provides some benefits. First, the use of non-conforming discretizations is convenient during the shape update since (i) it avoids to call on cumbersome meshing procedures to impose matching meshes between the stiffeners and the panel (see Fig. 3.1 as a reminder). Then, the proposed DD algorithm enables (ii) not to recompute the parts of the structure in non-design areas at each optimization iteration. As an example, this means that we do not need to re-assemble and re-factorize the stiffness operator of the panel if only the position and shape of the stiffeners are to be optimized. Finally, similarly as in chapter 4, the choice of the starting point of the iterative DD solver may be improved during the optimization iterations by (iii) taking the solution of the previous design. We recall that we have not implemented the method in parallel within the scope of this work. We only discussed the issue here in order to motivate future researches in this direction.

Remark. *As stated previously, Problem (6.1) involving the compliance is self-adjoint so no additional direct resolution is required for the evaluation of the sensitivities. However, the computation of the sensitivities for general objective functions are often performed with the adjoint method which requires the computation of an adjoint problem (same operator* $\mathbf{K}$ *but different right-hand side). Consequently, the benefits highlighted above for the computation of* $\mathbf{u}$ *also applies in the general context for the computation of the sensitivities.*

2.2 Geometric modeling: embedded surfaces

From the geometrical point of view, we first build a modeling based on the use of embedded (or immersed) surfaces to handle the geometric constraint of keeping the different parts of the structures connected during shape modification.

2.2.1 Geometric challenges

The simple case of a portion of a cylinder with one stiffener helps to highlight the geometric challenges to be faced. A first (design) configuration can be defined as depicted in Fig. 6.2(left). Two classical spline surfaces describe the portion of cylinder and the stiffener. During the design, or more specifically, the optimization process, the designer may want to modify the shape of the different parts by moving the control points of the design spline model (following the procedure outlined in section 1 and Fig. 6.1). The first difficulty occurs when trying to modify the shape of the stiffener (see Fig. 6.2(top)). We want the bottom of the stiffener to perfectly lie on the cylinder. This geometric constraint is not easily fulfilled: sliding the control points along the edge of the cylinder disconnects the surfaces. The second difficulty is to modify the global shape (here the portion of cylinder) while keeping the substructure connected (see Fig. 6.2(bottom)). More precisely, the question here is: how to transfer the shape update from the global part to its substructure? If we move one control point of the main surface, the stiffener does not lie anymore on it. In this simple case, one could formulate an appropriate condition in order to glue the stiffener but, in general, it is not a trivial task. In case of curvilinear stiffeners lying on a curved surface, re-parametrizations and approximations appear inevitable if the standard isogeometric strategy for shape optimization is adopted. Instead, we are looking here for a compact approach that does not require cumbersome re-parametrization procedures. This is particularly crucial to get a robust shape optimization strategy.

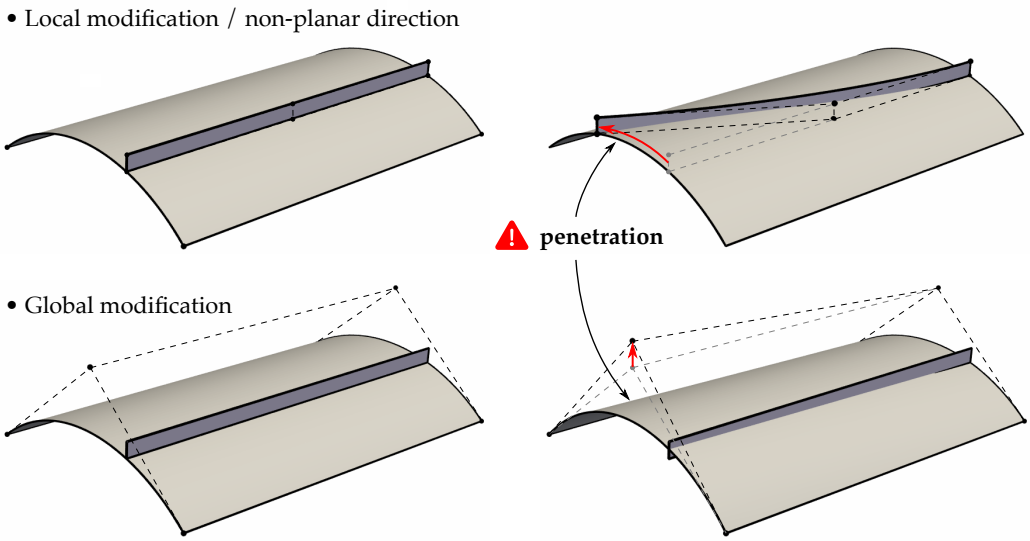

Figure 6.2 – Geometric difficulties to impose design modifications to a stiffened cylinder: (top) while moving, the stiffener disconnects with the cylinder, and (bottom) the stiffener does not follow the shape variation of the cylinder.

2.2.2 Using spline compositions for shape updating

Embedded surface. We introduce the concept of embedded surface in order to overcome the geometric challenges highlighted in Fig. 6.2. The idea comes from [Bauer et al., 2017] who considered univariate embedded entities. More precisely, in [Bauer et al., 2017], they embed curves into a surface to model cables in

membrane structures or to apply line boundary conditions to a shell structure without being limited to the edges of the surface. A similar procedure is undertaken to define the stiffener (see Fig 6.3 for illustration). We do not use classical spline surfaces to describe the stiffeners. Instead of a simple surface, we introduce the composition of a spline volume and a spline surface. In other words, we immerse a surface into the parametric space of a volume. The volume can be seen as a mapping that smartly transforms the embedded surface in order to create a final surface with the desired properties. This idea offers a novel strategy to generate geometric models of stiffened structures. This new approach is formalized in Fig. 6.4.

As stated at the begining of the chapter, the proposed strategy can be related to FFD techniques which are commonly used in graphic design to deform objects and are also applied, *e.g.*, for aerostructural optimization [Duvigneau, 2006, Lassila and Rozza, 2010, Kenway and Martins, 2014]. In that sense, the design approach presented here is not entirely disconnected from the current industrial methods. However, the interested reader could notice in the following that the transformation of the full embedded entity will be performed whereas only the FE-node locations are altered by the volume mapping in the standard FE-based FFD approach. From here on, we will interpret the embedded entities (*i.e.*, the stiffeners) as *slave parts* since their shapes are driven by external geometric properties. Conversely, the *master parts* (*i.e.*, the panels) are those which dictate specific constraints during the shape update.

Mathematical description. Let us now mathematically formulate the geometric modeling. We define the mapping V^h as a spline volume, *i.e.*, following notations introduced in chapter 1:

$$V^h(\xi_1,\xi_2,\xi_3) = \sum_i^{n_{IG}^{3D}} R_i(\xi_1,\xi_2,\xi_3)x_i, \tag{6.3}$$

where R_i are trivariate spline basis functions and x_i are the related control point locations. The parametric coordinates ξ_1, ξ_2 and ξ_3 are defined over the parametric domain denoted by $\bar{\Omega}$ (see Fig. 6.3 again, left). The embedded surface $\bar{A}^h$ is a spline surface defined as:

$$\bar{A}^h(\theta_1,\theta_2) = \sum_j^{n_{IG}^{2D}} \bar{R}_j(\theta_1,\theta_2)\bar{x}_j, \tag{6.4}$$

with $\bar{R}_j$ some bivariate spline basis functions and $\bar{x}_j$ the location of the associated control points living in the parametric space of the volume. As in chapter 3, θ_1 and θ_2 are the parametric coordinates associated to the immersed surface. Under the consideration that the codomain of $\bar{A}^h$ is included in domain $\bar{\Omega}$, we finally compose the two previous mapping (6.3) and (6.4) to get the physical surface:

$$A^h(\theta_1,\theta_2) = V^h \circ \bar{A}^h(\theta_1,\theta_2) = V^h\big(\,\bar{A}^h(\theta_1,\theta_2)\,\big). \tag{6.5}$$

The final surface A^h is parametrized by the same set of variables (θ_1,θ_2) as the embedded surface $\bar{A}^h$ and it returns value in the physical space $\mathbb{R}^3$.

Potential for shape optimization. If the approach eases the construction of complex stiffened structures, it also offers interesting features related to shape optimization in a general context. Indeed, using spline compositions offers two possibilities for imposing shape deformations. By modifying the volume (through the location of control points x_i), one can act on the global shape. By acting on the embedded entities (*i.e.*, moving control points $\bar{x}_j$), one can modify specific parts, as for instance the stiffeners. The bonding conditions at the interfaces are automatically satisfied (from a geometrical point of view). This point will be further accounted for in section 2.4 where results of shape optimization of stiffened structures will be presented. Finally, it is worth noting at this stage that the proposed embedded strategy is adapted to the analytical derivation of the sensitivities since there exists an exact link between the shape parameters and the resulting analysis models (in other words, no approximations are involved during the shape update and transformation into the analysis model). Details regarding the computation of the analytical sensitivities associated to the embedded approach can be found in [Hirschler, 2019](chapter 5).

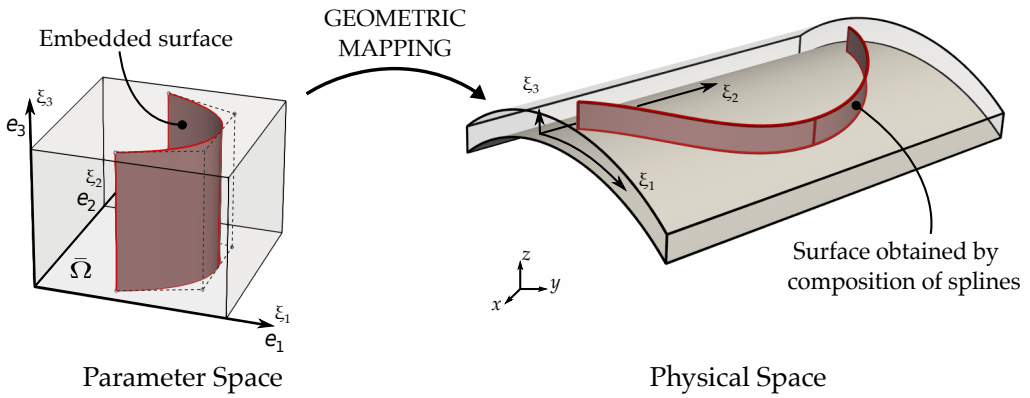

Figure 6.3 – Construction of a stiffened structure using embedded surfaces. The final surface describing the stiffener is obtained by the composition of a spline surface and a spline volume.

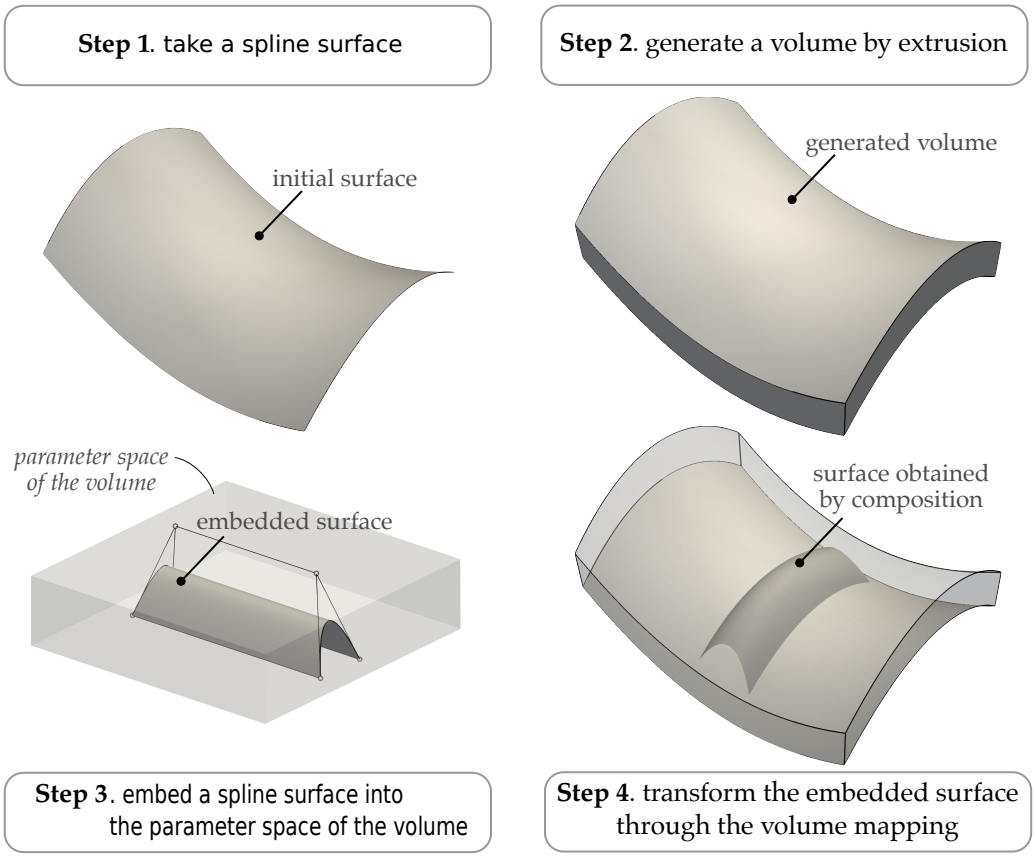

Figure 6.4 – Generating a geometric model of a stiffened structure by using the embedded strategy.

2.3 Analysis: an embedded Kirchhoff-Love shell element

We have introduced the use of spline compositions for geometric requirements in section 2.2. In order to carry out the shape optimization process of Fig. 6.1, we also need to perform the structural analysis. To this end, we now build an embedded Kirchhoff-Love shell element that takes into account the geometrical spline composition. The basic components presented in chapter 3(section 2.2) for the standard isogeometric Kirchhoff-Love shell serve as prerequisites here.

Mid-surface defined by spline composition. The continuum formulation of the embedded Kirchhoff-Love is formally identical to the standard Kirchhoff-Love formulation. The same kinematic assumptions are postulated. It means that all the equations from (3.3) to (3.8) remain true. Things become different at the discretization step since the spline composition comes into play. The starting point of the Kirchhoff-Love element formulation is the definition of the covariant base vectors (see Eqs. (3.1) and (3.2)). Taking Eq. (6.5), we observe that the surface is parametrized and, therefore, it has curvilinear coordinates which are θ_1 and θ_2. As a consequence, the definition of the covariant base vectors is straightforward and is given by the chain rule (same treatment as in (4.36) for instance):

$$a_\alpha^h = \frac{\partial A^h}{\partial \theta_\alpha} = \sum_{k=1,3} \left[\bar{A}^h_{,\theta_\alpha} \cdot e_k\right] V^h_{,\xi_k}\left(\bar{A}^h\right) \quad \alpha = 1,2\,, \tag{6.6}$$

where the subscript $(\cdot)_{,\xi} = \partial(\cdot)/\partial\xi$ indicates the partial derivative with respect to variable ξ and e_k are the unit basis vectors associated to the volume coordinate system in the parameter space (*i.e.* corresponding to direction ξ_k, see Fig. 6.3(left)). Then, given Eq. (3.8), the derivatives of the covariant base vectors versus the curvilinear coordinates are also required. Starting from Eq. (6.6), we thus need to apply one more time the chain rule, which yields:

$$a^h_{\alpha,\theta_\beta} = \sum_{k=1,3} \left[\bar{A}^h_{,\theta_\alpha\theta_\beta} \cdot e_k\right] V^h_{,\xi_k}\left(\bar{A}^h\right) + \sum_{k=1,3}\sum_{l=1,3} \left[\bar{A}^h_{,\theta_\alpha} \cdot e_k\right]\left[\bar{A}^h_{,\theta_\beta} \cdot e_l\right] V^h_{,\xi_k\xi_l}\left(\bar{A}^h\right). \tag{6.7}$$

Remark. *It may be noticed from Eq. (6.7) that we recover the need for a smooth C^1 surface for the Kirchhoff-Love shell formulation (since second-order derivatives of the surface are involved). This requirement can be satisfied here with two spline mapping of higher regularity. Indeed, if both the embedded surface $\bar{A}^h$ and the volume mapping V^h are C^1, then the spline composition A^h is* de facto *C^1.*

Approximation space for the displacement field. Applying Galerkin's method raises the question of the choice of the approximation space for the displacement field. In fact, the isoparametric concept may not be applicable in case of a spline composition. We basically have two choices in the present situation (once again, we make sure that the displacement field is at least C^1 to be consistent with the Kirchhoff-Love formulation, see again (3.8)):

1. based on the trivariate spline discretization of the mapping (6.3):

$$u^h(\theta_1,\theta_2) = \sum_i R_i\left(\bar{A}^h(\theta_1,\theta_2)\right) u_i, \tag{6.8}$$

2. based on the bivariate spline discretization of the embedded surface (6.4):

$$u^h(\theta_1,\theta_2) = \sum_i \bar{R}_j(\theta_1,\theta_2)\, \bar{u}_j. \tag{6.9}$$

The first choice provides an immersed-like approach where the deformation of the shell is prescribed by the surrounding volume (see, *e.g.*, [Burman et al., 2015, Schillinger and Ruess, 2015] and chapter 2). The second choice is close to the standard Kirchhoff-Love isogeometric shell. The mapping only plays a role

from the geometric point of view since it modifies the shape of the embedded surface but it is not involved in the solution space. We consider for the intended applications in this work the second approach given its numerical and implementation simplicity (no need for specific quadrature rules, for specific treatments to counterbalance the ill-conditioning of the system, etc). Consequently, the difference with respect to the standard shell formulation essentially lies in the additional trivariate mapping step that modifies the shape of the undeformed configuration. Finally, introducing approximation u^h from (6.9) into (3.7) and (3.8) and applying the equilibrium of the shell leads to the typical system (3.9) where the trivariate spline mapping is introduced into (3.10).

Remark. *We emphasize again at this stage that the other crucial ingredient from the analysis point of view of our methodology is the use of the DD solver of chapter 3 which is adapted to the coupling of non-conforming isogeometric shell patches. In the present situation of the embedded Kirchhoff-Love shell formulation, only some precautions regarding the implementation (to take into account the additional trivariate mapping to define the interface) are required. The particular point that has made possible such a straightforward extension is the pure algebraic approach followed to define the local null-spaces and pseudo-inverses in the DD solver (see chapter 3(section 3.3)). Indeed, the embedded shell formulation being non-isoparametric, it is impossible to build, in general, the kernel of the stiffness operators of the embedded shells* a priori. *We refer the interested reader to [Hirschler et al., 2019a] and [Hirschler, 2019](chapter 4) for more information regarding this point.*

2.4 Optimal design of multipatch shell structures

We now show that introducing embedded surfaces into the IGA-based shape optimization framework offers new possibilities. It enables to tackle challenging optimization problems in a proper and accurate manner. More precisely, we apply here the developed approach to three problems. First, the stiffened roof illustrates that relating the design variables to the control points of the volume mapping (6.3) help to optimize the global shape of structures composed of multiple parts. We will see that the global shape modifications of the roof are automatically transferred to the stiffeners. Then, the curved wall problem shows how the design modifications of the embedded surfaces allow to optimize the shape and the position of stiffeners along curved and complex geometries. In other words, we will demonstrate with this second test case that relating the design variables to the control points of the surface mapping (6.4) offers a smooth way to optimize local parts of a global structure. Finally, the aircraft wing-box problem proves the applicability of our approach to design innovative real aeronautical structures. The examples are provided below with minimal explanation to simplify the presentation. If one is interested in repeating the numerical experiments, all necessary data and details can be found in [Hirschler et al., 2019b] and [Hirschler, 2019](chapter 6). It is also worth noting that additional test cases were investigated in these two references, including a few where analytical solutions were available: it was observed that our shape optimization approach enabled to recover these reference solutions.

2.4.1 Global optimization: stiffened roof

The problem of the stiffened roof is derived from the initial shape optimization problem of a roof under vertical uniform load [Bletzinger et al., 2005, Kegl and Brank, 2006]. Two stiffeners are added to the initial square plate. We introduce two embedded surfaces to define these stiffeners. The model generation is described in Fig. 6.5. The 4 corners of the plate are fixed.

In this problem, only global optimization is performed; that is, the embedded surfaces remain unchanged during the optimization. Therefore, the shape modifications of the stiffeners are only imposed by the design updates of the surface representing the roof. To this purpose, the design variables are associated to the control points of the volume mapping. The volume mapping is discretized in 4-by-4-by-1 elements. Degree 3 is taken in directions ξ_1 and ξ_2 while degree 1 is kept in direction ξ_3 (see red points in Fig. 6.5).

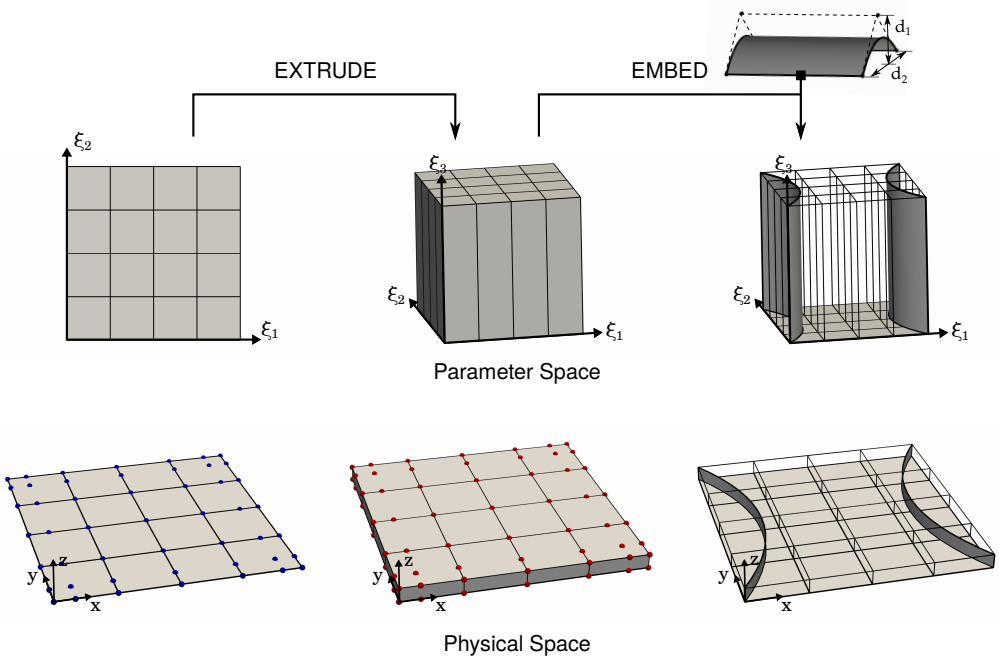

Figure 6.5 – Construction of the geometry of the stiffened roof: starting from the square plate, the first step consists in generating a volume by extrusion. Degree one is set in the direction of the extrusion. Once the volume is obtained, B-Spline surfaces (each made of a single element of degree 2-by-1) are embedded into the parametric space of the volume. Finally, the compositions of these embedded surfaces with the volume give the final surfaces that describe the stiffeners.

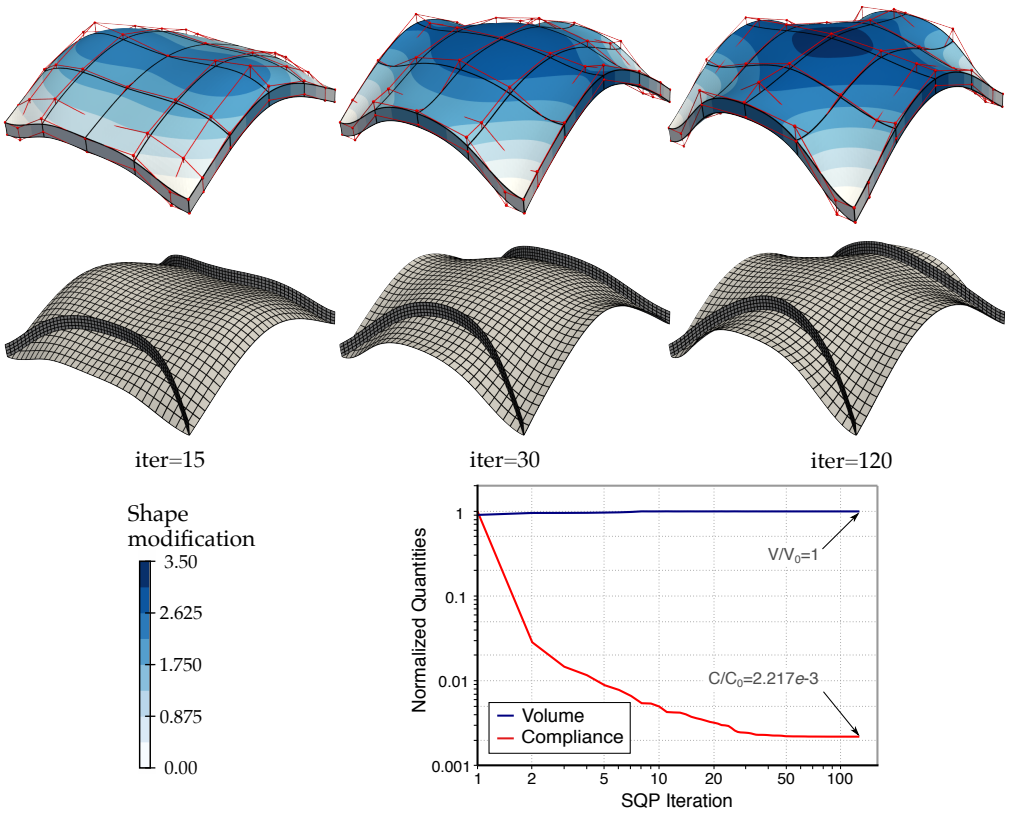

Figure 6.6 – Evolution of the shape and of the relative compliance and relative volume during optimization. The associated analysis model is depicted below the design model. The stiffeners are perfectly lying on the roof during the whole process.

In the end, the optimization model has 45 design variables that move the control points of the mapping in the vertical direction z. The analysis model is defined such that the roof and both stiffeners are discretized into 1024 and 256 bi-cubic elements, respectively. The area of the roof without the stiffeners is constrained to be lower than 110% of the initial area of the square plate. The shape evolution of the design and analysis models is presented in Fig. 6.6(top). In addition, the evolution of the relative compliance during the resolution of the optimization problem is shown in Fig. 6.6(bottom). The final shape is obtained after 120 iterations of the optimization algorithm. The compliance is drastically reduced: final relative compliance is equal to $C_{\text{opt}}/C_0 = 2.217 \cdot 10^{-3}$. It is interesting to notice that the final shape has two planes of symmetry. This was expected since the problem presents these symmetries. Therefore, some design variables have identical optimal values. The fact that we obtain the symmetries without setting groups of design variables is a meaningful indication to validate the result.

From an engineering point of view, this problem of the stiffened roof highlights an interesting issue. We manage to solve the optimization problem with the substructure. One could also simplify the problem by ignoring in the optimization process the stiffeners, assuming that they only have small influence on the behavior of the global structure. We actually tried to solve in a first step the optimization problem without the stiffeners, and we built the substructure afterwards. We computed the compliance on this new global structure and we got a compliance approximately 15% higher than the one obtained when optimizing the structure with the stiffeners. Given the simplicity of this structure, it highlights that tacking into account, during the optimization, sub-parts as stiffeners, holes, and other geometric details can be essential to design more complex structures of better quality.

2.4.2 Local optimization: curved wall

The second problem addresses the optimization of the shape and the position of a quite complex "cylindrical" stiffener lying on a curved surface that represents a wall. Contrary to the stiffened roof problem, we do not modify the geometry of the wall which is here the master part. For this problem, we focus on the substructure only. In order to optimally design this substructure, we move the control points of the embedded surface (*i.e.*, the control points defined in the parametric space of the volume).

The geometric construction of the stiffened curved wall by means of the proposed embedded approach is described in Fig. 6.7. The wall originally represents a quarter cylinder. We move some control points of this initial NURBS surface to generate the final curved wall and build the volume by extrusion in the radial direction (see Fig. 6.7(top-right)). The initial shape of the embedded surface is described in Fig. 6.7(bottom). A set of design variables is defined so as to be able to modify the cross-section and the position of the stiffener. With the chosen discretization, six groups of four control points are spread out along the main direction of the stiffener. For each group of control points, we define four design variables as explained in Fig. 6.7(bottom-right). Therefore, a total of $6 \times 4 = 24$ design variables is used for this example. The area of the stiffener is constrained to be lower than the initial one V_0. Additional inequality constraints between the design variables are included into the optimization problem in order to prevent the occurrence of undesired shapes during the resolution. Then, the analysis model is defined through k-refinement of the optimization model: the wall is discretized with 32-by-32 bi-cubic NURBS elements and the embedded surface is composed of 16-by-64 cubic B-Spline elements. Finally, the bottom of both the wall and the stiffener are considered fixed and a pressure is applied over the wall (see Fig. 6.7(top-left)).

The optimization results are given in Fig. 6.8. During the resolution, the stiffener moves along the wall until it is located at the middle. As for the previous example, this result was predictable given the symmetry of the problem. In addition, it may be observed that the cross-section of the stiffener is larger at the bottom than at the top of the wall. This makes sense here since a large cross-section at the bottom improves the fixation of the overall structure. The cross-section also becomes larger where the deformations are critical. The compliance of the final multipatch shape is equal to $C_{\text{opt}} = 2.416 \cdot 10^{-3}$, which is 39% lower that for the initial configuration. Recalling that only local shape variations are performed here, the gain is significant

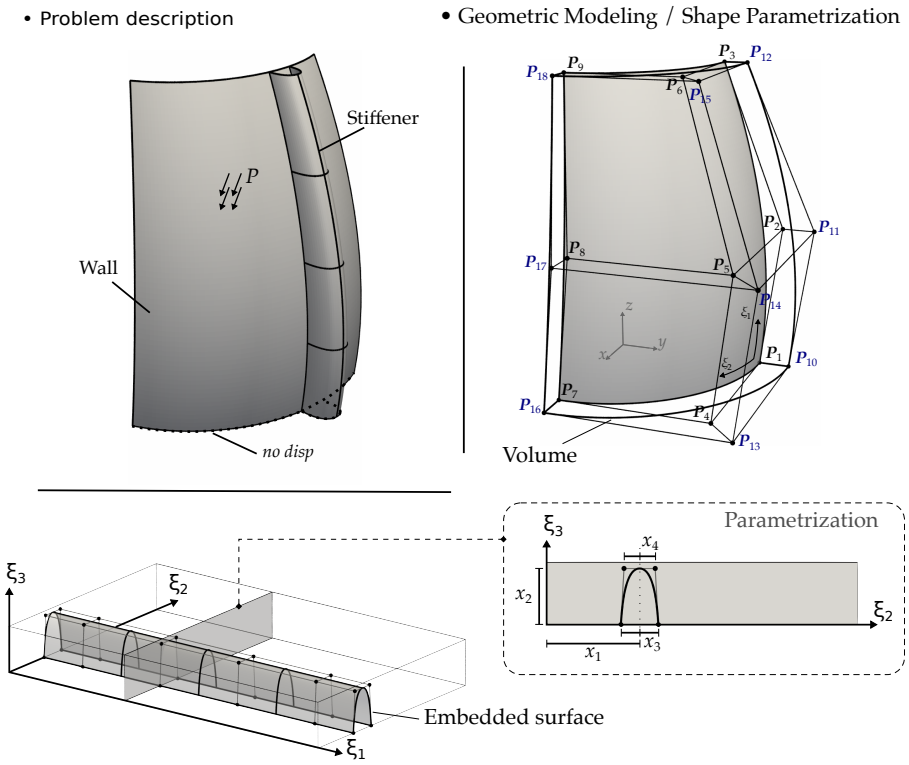

Figure 6.7 – Problem description and geometric construction of the curved wall. The panel is generated using a quadratic NURBS element. The stiffener is elaborated using a B-Spline embedded surface made of 2-by-4 quadratic elements. The design variables are associated to the control points of the embedded surface (4 variables for each arches).

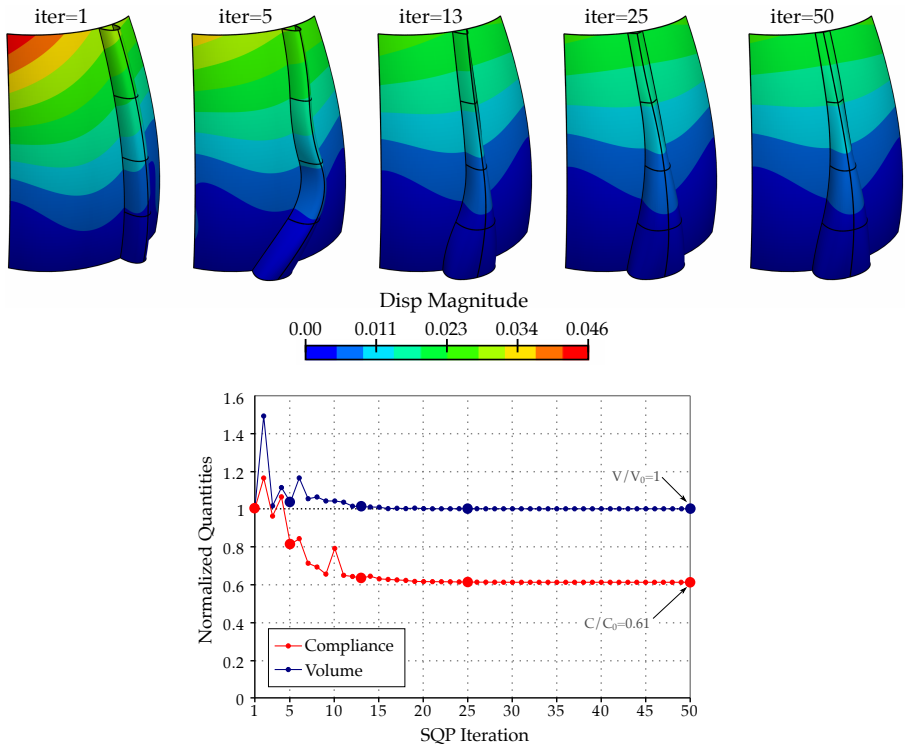

Figure 6.8 – Optimization histories for the resolution of the curved wall problem: (top) evolution of the geometry and the displacement field, and (bottom) evolution of the compliance and the volume. While sliding, the stiffener remains perfectly coincident with the wall.

and highlights the potential of our methodology to handle local optimization of complex structures.

2.4.3 Designing an aircraft wing-box

We have mainly shown so far how the embedded approach enables to add stiffeners to curved panels. However, the method should not be limited to this purpose. To demonstrate the flexibility of the developed approach and its potential to handle more sophisticated models, we finally apply it to design the internal substructure of a real wing. Several parametrization-based methods have been recently suggested in order to obtain alternative designs to classical wing box designs characterized by straight and parallel ribs and spars [Jutte et al., 2014, Locatelli et al., 2014, Dubois et al., 2018]. The inspiration for curved structural components comes from dragonfly wings [Jongerius and Lentink, 2010]. The main issue in these (FE-based) approaches comes from the numerous intermediary (approximation) steps that separate the definition of the design and analysis models. This prevents from a proper sensitivity analysis and thus makes the use of gradient-based optimization algorithm almost impossible. Furthermore, the geometrical description is limited (most authors start from a planar geometry and then extrude it in the normal direction). Our approach appears more generic and full analytical sensitivities can be computed thanks to the isogeometric link between design and analysis (see again [Hirschler, 2019](chapters 3 and 5) and [Hirschler et al., 2020] for details regarding sensitivity analysis).

Versatile construction of an aircraft wing. We consider the case of a subsonic aircraft wing adapted from [Vassberg et al., 2008]. We build the wing with its internal substructure made of ribs and spars. To this purpose, we adopt the strategy depicted in Fig. 6.9. The starting point is to describe the outer geometry which defines the skin. In our case, we use four B-Spline surfaces, two for the top and two others for the bottom (see Fig. 6.9(a)). Once it has been done, we define two B-Spline volumes that fill the domain delimited by the skin (see Fig. 6.9(b)). For each volume, we now have the possibility to embed spline surfaces in its parameter space, as shown in Fig. 6.9(c). The spline composition of the embedded surfaces with the volume mapping leads to surfaces that are perfectly lying inside the domain delimited by the skin and no geometric approximation at the interfaces are introduced (see Figs. 6.9(c) and (d)). At the end, it leads to a model with 16 patches (4 quadratic standard shell patches for the skin, 8 and 4 quadratic embedded shell patches for the ribs and the spars, respectively). In addition to being tedious to generate, an analysis-suitable model of the wing (*i.e.*, with only matching interfaces as discussed in Fig. 3.1) would lead to a much larger number of patches. It could not be achieved without calling upon specific geometric modelers. Here, the modeling task is thus simplified and offers more flexibility.

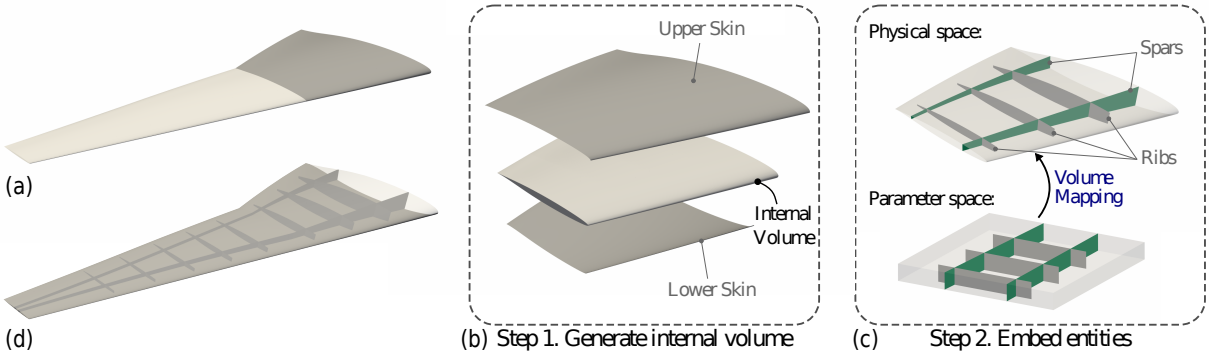

Figure 6.9 – Construction of the model of the wing by means of the proposed embedded approach.

Design capabilities and shape optimization. As in the previous example, we perform here local optimization; that is, we move the control points associated to the embedded surfaces to impose shape modifications to the internal substructure of the wing. More precisely, the geometric model and the definition of

the design variables are depicted in Fig. 6.10. Each rib is described with a B-Spline of one single element with degree two in the main direction, and degree one in the vertical direction. The same applies for the spars except that they are discretized with two elements which allows to set more design parameters. The control points of the spars are movable in the ξ_1-direction of the volume parameter space (see Fig. 6.10(bottom)). The same motion is prescribed to the edges joining the upper and the lower skin. Thus, four design variables per spar are set. One common design variable is defined at the junction between the spars embedded in the volume 1 and 2 in order to maintain there connection. Additionally, three design variables per rib are defined, and move the control points in the ξ_2-direction of the volume parameter space (see Fig. 6.10(bottom)). We end up with a total of 38 design variables. We also add geometric constraints into the formulation of the optimization problem that guarantee a minimal distance between the ribs. The wing is finally considered fixed on its right end and a pressure is applied to its top skin.

- Geometric Modeling

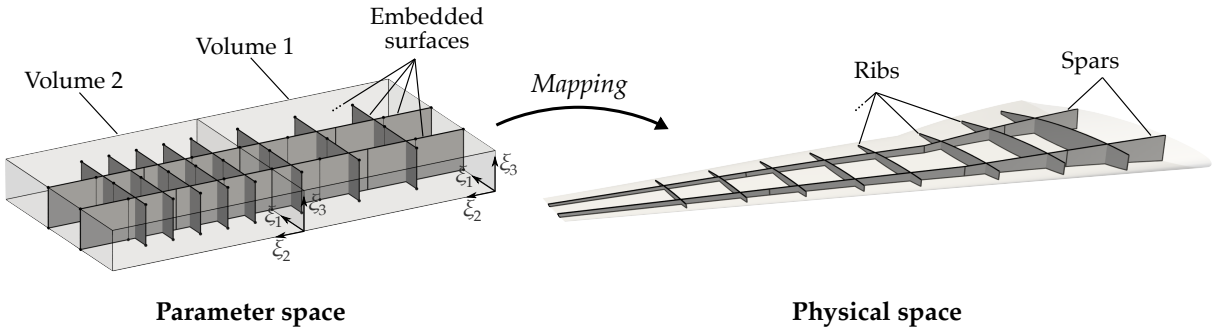

- Shape parametrization

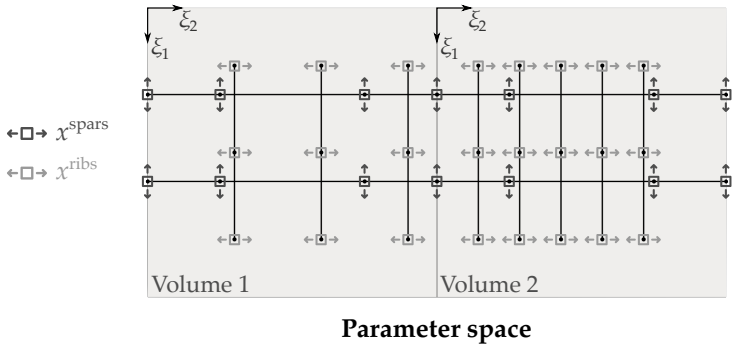

Figure 6.10 – Construction of the geometric model of the representative wing (top) and definition of the design variables for the shape optimization of its internal substructure (bottom).

The optimization results are given in Fig. 6.11. Thanks to the construction, the curvature and the cross-section variations of the wing are automatically taken into account during the optimization process. The volume mapping can be interpreted as a function that enables to keep the structural components inside the volume delimited by the skins. No additional procedures are required that could have broken the link between the shape parameters and the final geometric model of the wing, as in alternative FE-based approaches [Jutte et al., 2014, Locatelli et al., 2014, Dubois et al., 2018]. One can observe the evolution of the deformation of the wing during the optimization. The overall displacement of the wing is drastically reduced. The maximal displacement of the final design is about 10 times lower than the one of the initial design. The compliance is therefore reduced to a great extent, $C^{opt}/C_0 = 0.213$, whereas the overall area is kept constant. The final design has ribs and spars with curved shapes. It proves that curved structural components can largely improve the mechanical behavior of the wing. It coincides with the observations

from other recent works [Mulani et al., 2013, Jutte et al., 2014, Locatelli et al., 2014, Zhao and Kapania, 2016, Dubois et al., 2018, Wang et al., 2019]. Such innovative designs can surely improve further aircraft structures, and more generally, stiffened structures. It also motivates the construction of a robust and efficient framework that enables to design these new future designs. We believe that such numerical experiments account for the potential of our method to meet this challenge.

3 Towards the optimal design of structural details within macro-structures

The combination of the DD solver developed in chapter 3 with the immersed modeling approach introduced in previous section allows for proper and effective design of complex multipatch isogeometric structures. To go even further regarding the complexity of the envisaged structures, we now open the door, through a simple numerical experiment, for the efficient design of structural details within such large macro-structures. To this end, the idea here is to make use of the modeling and analysis strategies built in chapter 2. Indeed, as highlighted throughout chapter 3, the DD solver and the non-invasive algorithms of chapter 2 are both appropriate in a multiresolution context. Only the application differs: the DD solver is suitable for multipatch isogeometric structures while the non-invasive algorithms are adapted for integrating local details into global isogeometric structures. More precisely, we make use here of the non-invasive algorithm (2.36)-(2.37) to adapt to any non-conforming configuration encountered through a shape optimization process. For the presentation, we recycle the notations of chapter 2; in particular, subscripts 1 and 2 are related to quantities of the global and local models, respectively. We also recall that domain $\Omega_1 = \Omega_{11} \cup \Omega_{12} \cup \Gamma$ characterizes the global isogeometric model, and the local model of domain Ω_2 is expected to replace the global model in subdomain Ω_{12} through data exchanges across Γ.

A simple test case. As a preliminary example, we consider here the simple shape optimization problem illustrated in Fig. 6.12(a). The detailed setup for this problem can be found in [Bouclier and Passieux, 2018]. The position of an inclusion within a global plate is optimized so as to provide, as in previous sections, maximal rigidity for the structure. The design variables are the horizontal and vertical coordinate of the center of the inclusion, denoted by x_c and y_c, respectively (see Fig. 6.12(a) again). Standard 2D elasticity is used here for the mechanical modeling. The Young's modulus of the inclusion is chosen to be a hundred times smaller than that of the plate ($E_1 = 10^3$ and $E_2 = 10$). As an optimization algorithm, we make use, this time, of the black box `fminsearch` available in `matlab`. This routine uses a gradient-free algorithm: it is the Nelder-Mead simplex algorithm as described in [Lagarias et al., 1998]. For sure, more sophisticated iterative schemes, as based on the gradient as in previous sections, could be used to improve the optimization performance. Nevertheless, our goal here being to prove the interest of making use of the non-invasive solver developed in chapter 2(section 3.2) for the analysis step (see Fig. 6.1 again, step 2) rather than building an advanced optimization tool, we choose to initiate the study with this simple algorithm. (Once again, let us quote here that this last experiment has actually been carried out before the works achieved regarding the shape optimization of stiffened structures [Hirschler et al., 2019b].) Starting with an inclusion located at position $x_c^0 = 2$ and $y_c^0 = 2$, the optimization process is expected to lead to the configuration of a central inclusion, *i.e.* such that $x_c^{ref} = 3.5$ and $y_c^{ref} = 5$. Indeed, the further the inclusion is from all plate boundaries, the less stress concentration is encountered around the inclusion. For illustration purpose, the solution in terms of Von Mises stress is plotted for the initial configuration and the expected optimized one (see Figs. 6.12(b) and 6.12(c), respectively).

Interest of a global/local non-invasive solver for the shape optimization of local details. The optimization algorithm here calls upon the non-conforming, non-invasive algorithm (2.36)-(2.37) to get the displacement solution at each configuration encountered through the optimization process. A maximum number of iterations of 20 is prescribed for the non-invasive iterative algorithm. From a general point of view, we

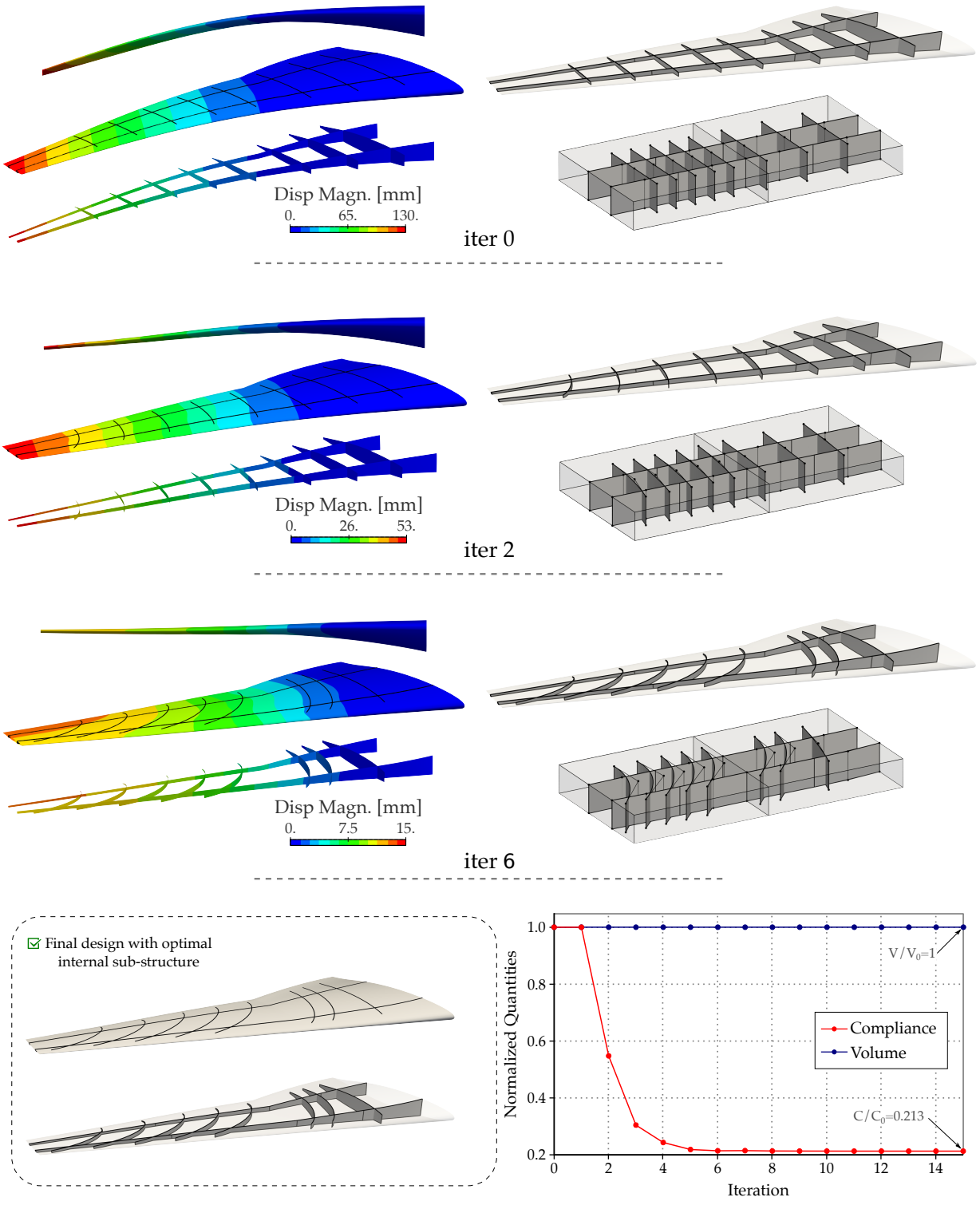

Figure 6.11 – Optimization histories for the resolution of the wing problem, and final design of the ribs and spars.

recover the same benefits as when we make use of the DD solver of chapter 3 for the shape optimization of multipatch structures (see section 2.1): (i) no need for cumbersome meshing procedures to impose matching meshes between the plate and the inclusion, (ii) no need to fully rebuild and recompute the global/local structure at each optimization iteration, and (iii) possibility to take the solution of the design n as an initial guess to speed up the non-invasive solver running at optimization step $n+1$.

More precisely, focusing on point (ii) in the situation described in Fig. 6.12(a), the stiffness operators $\mathbf{K}_1$ and $\left[\mathbf{K}_2+\left(\overline{\mathbf{K}}_{22}^{N\,T}-\overline{\mathbf{K}}_{22}^{N}\right)\right]$ in (2.36)-(2.37) are assembled and factorized once for all in a pre-processing step. Then, the only things to do to compute the successive coupled solutions encountered at each iteration of the optimization process are:

1. build the integration rule for the small immersed region Ω_{12};

2. assemble $\mathbf{r}_{12}$, $\overline{\mathbf{K}}_{11}^{N}$, $\overline{\mathbf{K}}_{12}^{N}$ and $\overline{\mathbf{K}}_{21}^{N}$;

3. perform few lower and upper triangular resolutions to solve alternatively problems (2.36) and (2.37).

Conversely, a direct solver would require to fully rebuild and recompute the resulting global/local problem (2.32) (that may also appear ill-conditioned) at each of these steps.

Remark. *It may be noticed that in the more general situation where the shape of the local detail is modified (along with its position), the local operator* $\left[\mathbf{K}_2+\left(\overline{\mathbf{K}}_{22}^{N\,T}-\overline{\mathbf{K}}_{22}^{N}\right)\right]$ *needs to be updated at each optimization iteration as well. However, we still save the assembling and resolution of the global model (over* Ω_1*), which is expected to be significantly larger (and thus requiring more computational resources) than the local model over* Ω_2*.*

Results. Figs. 6.12(d) and 6.12(e) show the convergence of the objective function and of the design variables, respectively. The convergence criterion for the optimization algorithm relies on the stagnation of the objective function as well as of the design variables: it stops when it gets below 10^{-4}. It can be observed that we are able to recover the expected optimized configuration through the optimization process, which accounts for the ability of the non-invasive solver to adapt to any arbitrary non-conforming situations, in particular when the edge of an element of the local model approaches that of an element of the global model.

Even if further studies have not been carried out yet, we believe that the use of a dedicated global/local non-invasive algorithm should definitely facilitate the process and ensure computational time saving in the context of shape optimization of structural details. In addition, let us point out that the strategy may be easily applied to complex shell structures as the ones of previous section. In this case, an analog treatment as in Fig. 6.12(a) for the design modification could be performed in the parameter space of the shell. More precisely, considering a shell surface obtained by the composition (6.5), the idea would be to define the design variables of the local details in the parameter space of the embedded surface. The spline surface mapping (6.4) would, in some sense, act as the volume mapping (6.3) to transfer the shape of the local details into the parameter space of the volume (before the volume mapping put everything in the physical space). From this point of view, the success of the study shown in Fig. 6.12 and the combination of this result with the ones of previous section open the door for the development of effective optimization tools, based on some non-invasive and DD numerical algorithms, to handle realistic applications. This motivates future research in this direction and, more generally, encourages to make use of such algorithms when performing multiresolution processes.

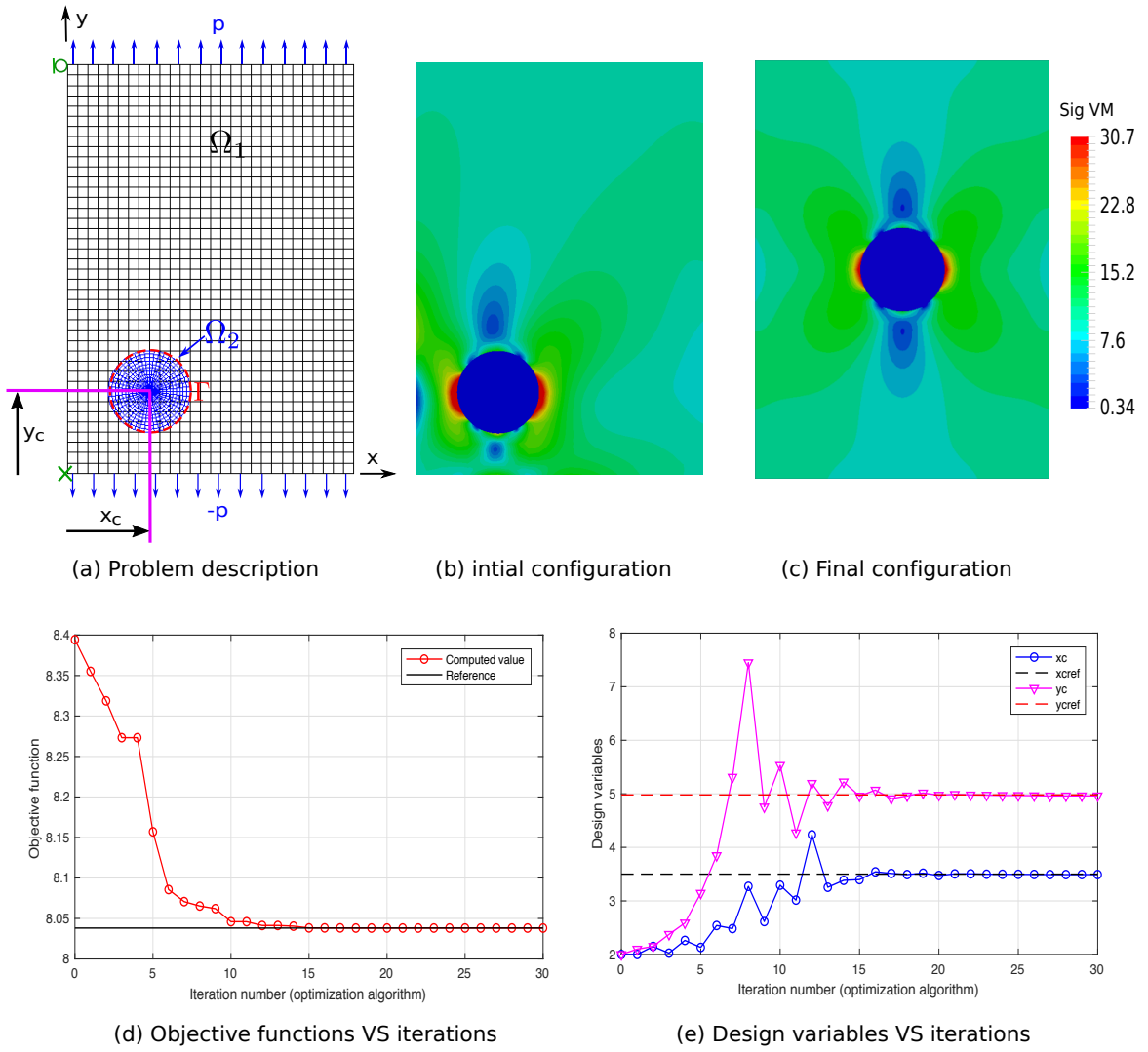

(a) Problem description (b) intial configuration (c) Final configuration

(d) Objective functions VS iterations (e) Design variables VS iterations

Figure 6.12 – Simple optimization problem: the position of the inclusion (x_c, y_c) in the plate is optimized so as to provide minimal compliance for the structure. The optimization algorithm calls upon the non-conforming non-invasive Nitsche solver of chapter 2(section 3.2) each time the objective function needs to be evaluated.

Summary and discussion. This final chapter addresses the optimal design of representative aerostructures in the context of IGA. We recall that the cornerstone of the problem concerns the handling of multipatch shell models with non-conforming parametrizations. After answering the issue from an analysis point of view with the construction of a dedicated DD solver in chapter 3, and formalizing its interest to be integrated in a shape optimization loop, we develop in this chapter a full geometrical framework that enables to perform the isogeometric shape optimization of any complex stiffened structure found in aeronautics. More precisely, drawing inspiration from the Free-Form Deformation (FFD) concept [Sederberg and Parry, 1986, Kenway and Martins, 2014], we introduce an embedded geometrical modeling that enables to properly impose shape changes to stiffened structures. It simply consists in defining the stiffener mid-surface by a spline composition of an embedded surface with a volume mapping related to the panel. Using this embedded (or immersed) approach, one can either modify the embedded surface for local optimization or the volume mapping for global optimization of complex shell structures. The final geometric model obtained by spline composition is also directly used in the analysis step by formulating a

new isogeometric, embedded Kirchhoff-Love shell element. This means that the original idea behind IGA is maintained since both the design and the analysis are performed on a common geometrical model. It is particularly attractive in the context of structural optimization since it provides an exact link between the shape parameters and the resulting analysis model, thus allowing to derive full analytical sensitivities for accurate and effective gradient-based optimization. Our approach thus appears very robust and generic in contrast with the current FE-based framework [Jutte et al., 2014, Locatelli et al., 2014, Dubois et al., 2018], where several intermediary approximation steps separate the design and analysis models. We have been able, in particular, to create a versatile model of a wing with its internal substructure. Due to the use of embedded entities, the internal substructure automatically follows the outer geometry of the wing during shape update. This brings the possibility to explore new types of design while in usual aero-structural optimization, mainly sizing variables such as the thicknesses of the shell components are introduced into the design process [Kenway and Martins, 2014, Keye et al., 2017].

To go even further regarding the complexity of the envisaged structures, we additionally open the door, by carrying out a simple numerical experiment, for the efficient design of structural details within large macro-structures. The idea is to make use, this time, of the global/local non-invasive strategies of chapter 2 for the analysis step within the optimization process. We recover the same benefits as when using the DD solver of chapter 3 for the shape optimization of multipatch structures, namely it avoids calling upon cumbersome meshing procedures and rebuilding and recomputing the whole coupled problem at each optimization iteration. This should, *e.g.*, foster the handling of trimmed isogeometric entities, thus offering a simple process to conduct the shape optimization of geometrical details (such as holes [Wall et al., 2008, Fußeder et al., 2015] or inclusions) or even to perform local topology optimization [Seo et al., 2010, Parvizian et al., 2012, Groen et al., 2017].

Given its robustness and versatility, the developed framework appears promising for addressing the complex field of Multidisciplinary Design Optimization (MDO) [Balesdent et al., 2012, Martins and Lambe, 2013]: for instance, one can simultaneously optimize the outer geometry of the aerostructure regarding some aerodynamic criteria and the shape of the internal substructure (possibly including even more local details) regarding the structural behavior. Other prospects of our methodology concern the extension to more sophisticated structural behaviors, such as involving vibration or buckling which is crucial for slender structures [Lund and Stegmann, 2006, Nagy, 2011, Stanford et al., 2014]. If the derivation of analytical sensitivities in the situation of eigenfrequency optimization seems staightforward, it might be easier to resort to some solid-shell formulations [Bouclier et al., 2015b, Caseiro et al., 2015] in case of buckling optimization. Perhaps the design of dedicated optimization algorithms would be necessary as well here. Note finally that the proposed approach is surely not limited to aerostructures, but could basically be applied to any other models composed of global and local parts (on can think, *e.g.*, of designing optimal micro-structured geometries using a similar procedure [Massarwi et al., 2018, Antolin et al., 2019]). According to us, the use of the FFD concept to perform shape optimization is a relevant idea and should be widely considered when the objective is to address complex situations. It can actually be viewed as the counterpart of the immersed (or embedded) approach for numerical simulation: FFD-based shape optimization offers the opportunity to decouple the design space from the actual geometry while immersed methods allow for distinguishing the approximation of the displacement from the discretization of the geometry. The same attractiveness as the one attributed to immersed methods in the context of scientific computing is thus expected when using the FFD concept into the field of shape optimization.

CHAPTER 7

General conclusion and prospect

The present document addresses **computational structural mechanics** in general, starting by the development of simulation tools both advanced and efficient, but also pragmatic, and going up to the resolution of optimization problems allowing to improve the design of structures and to better understand the underlying mechanical phenomena. To this end, the proposed numerical strategies are based on **IsoGeometric Analysis** (IGA) that possesses certain benefits over standard Finite Element Methods (FEM), given the direct use for the analysis of the smoother functions of geometric modeling in Computer-Aided-Design (CAD) and computer graphics. In particular, IGA provides an increased per-degree-of-freedom accuracy for the analysis of regular mechanical phenomena and offers a natural regularization scheme for general optimization problems. In addition, various original **domain coupling** algorithms are built in order to enhance the numerical efficiency of the methods (domain decomposition type solvers for high-performance computing on parallel computer architectures) and to make them non-invasive (*i.e.*, to simplify their implementation) with regard to available computational packages. In this context, a particular care is taken to handle any non-conforming coupling situations that could be met during a multiresolution process, such as during structural optimization. These algorithms also allow not to recompute the full coupled problem when some regions do not need to be modified. Finally, in terms of optimization properly speaking, two main research fields are investigated: the **shape optimization** of aeronautic-type structures and the **Digital Image Correlation** (DIC) in a broad sense (thus also including the calibration phase in stereocorrelation). For even more effectiveness, the above computational tools are complemented by further developments, such as the formulation of a specific geometric modeling enabling to properly update the shape of any arbitrary stiffened structures, or the careful analysis of the optimization algorithm of DIC.

Given the range of developed algorithms and of treated topics, the works reported here offer **multiple prospects** that have been mentioned all over the document and, in particular, in the paragraphs entitled "Summary and discussion". Among the potential perspectives and as an example, the one that I would especially like to focus on in the future concerns the field of **data assimilation for experimental solid mechanics**. Data assimilation in this context can be viewed as the higher-level optimization problem of DIC: it consists of optimizing the parameters of the numerical model (material parameters, boundary conditions, etc.) so that its numerical response matches with the measurements obtained by DIC. This research field is also commonly referred to as **mechanical characterization** or **model identification** [Molimard et al., 2005, Avril et al., 2008, Périé et al., 2009, Roux and Hild, 2018]. Such a subject seems crucial nowadays given the genuine digital revolution initiated in the area of experimental mechanics. Indeed, the improved performance of digital imaging tools offer access to rich experimental observations that may change fundamentally our vision on mechanical models [Leygue et al., 2018, Chinesta et al., 2018, Dalémat et al., 2019]. Meanwhile, as the volume of the measured informations is increasing, the classic data mining techniques used to quantitatively exploit these large data-sets are no longer sufficient [Gomes Perini et al., 2014, Bouclier and Passieux, 2017, Passieux et al., 2018, Neggers et al., 2018b]. For instance, with the advent of volume imaging techniques (MRI, ultrasound, optical coherence tomography, etc.), it now becomes possible to obtain accurate 3D images of a sample at its microstructure scale (see, *e.g.*, Fig. 1(b)). This massive amount of data opens the door for identifying numerous mechanical parameters using a limited number but more complex mechanical tests [Réthoré et al., 2013, Passieux et al., 2015a, Neggers et al., 2019]. To this end, it appears necessary, in particular, **(i) to optimize the experimental setup parametrization** (*e.g.*, sam-

ple shape, loading conditions) in view of providing a vast amount of useful data, and **(ii) to develop and implement sophisticated computational methods to treat the resulting large data-sets** through the resolution of the optimization problem of identification. I have very recently started to care about these two issues, especially in the PhD Theses of Morgane Chapelier [Chapelier, 2021] and Ali Rouwane [Rouwane, 2021] who I co-supervise with J.-C. Passieux and J.-N. Périé, respectively. Since the works reported in this manuscript concern the computation of structures (and/or materials) with high-performance in an optimization context, they should provide a good basis for addressing the general field of data assimilation in experimental solid mechanics. More generally, such a research topic is at the **interface between structural mechanics, applied mathematics and computer science**. As a result, I intend to treat the subject by pursuing and enhancing my current collaborations with the computational and experimental mechanics researchers of ICA, with the optimizers of IMT, and with the computer scientists of IRIT ("Institut de Recherche en Informatique de Toulouse").

More precisely, **research focus (i)** indicated above concerns the development of a **numerical methodology** in order **to design innovative experimental tests** that allow to **identify**, at best, **multiple mechanical properties**. At this time, it seems that very little work has been achieved in this direction and therefore the corresponding research field appears to be relatively open. We may essentially note the contribution of [Bertin et al., 2016] that establishes the framework on the topic but remains quite limited both from a numerical and application point of view. The key idea is to study **the spectral properties of the covariance operator** of the identified parameters due to measurement noise in order to **maximize the sensitivity of the measured displacement** fields to those parameters. Only one geometrical design variable for the sample was considered (*e.g.*, a fillet radius) and no advanced computational methods for the direct resolution as well as for the optimization loop were called upon. We are also aware of the work in progress by [Chamoin et al., 2020] that seeks to use a topology optimization process based on the SIMP (Solid Isotropic Material with Penalization) technique [Bendsøe, 1989, Sigmund, 2001], so that the optimization problem formulated in [Bertin et al., 2016] can be solved without any *a priori* knowledge on the specimen shape. The drawback with such an approach is that the optimization problem may not be constraint enough and therefore the algorithm may require additional tedious procedures to avoid leading to strange configurations with respect to the involved mechanics. As a consequence, it seems that **extending the isogeometric shape optimization framework** outlined in chapter 6 to regularize and solve this **new optimization problem** might constitute an interesting option. Furthermore, the **non-conforming, non-invasive coupling algorithm** of chapter 2 would certainly be well appropriate to solve the involved direct problem in a **multiresolution context corresponding to slight geometrical variations** (positioning of holes, inclusions, see also last test case of chapter 6), or even corresponding to small modifications of the boundary conditions.

Challenge (ii) raised above is general in the field and it appears obvious that the use of **HPC techniques** such as the ones built in chapter 4(section 2) for DIC constitutes a good starting point for answering such an issue. Now, we require to more closely look at the type of obtained measurements (stereo, volume, confocal, hyperspectral imaging, etc.) to ensure an efficient treatment of the whole experiment/measurement/identification process. In particular, the tools developed in this manuscript appear promising for the **mechanical characterization from volume image data**, thus offering the opportunity in the long term to calibrate a model at the scale of its microstructure [Chelaghma, 2018, Naylor, 2019]. In addition to the massive amount of data [Liu et al., 2019] (the current tomographic images can easily reach $2000 \times 2000 \times 2000$ voxels), the Digital Volume Correlation (DVC) problem [Bay et al., 1999, Leclerc et al., 2012, Buljac et al., 2018b] is in general extremely ill-posed since a dedicated speckle pattern cannot be applied, which makes the **regularization a central issue** [Gomes Perini et al., 2014]. As a solution, we propose to build in [Rouwane, 2021] a dedicated **image-based model** and to use it as a regularization vector of the correlation problem following an similar approach as the one of chapter 4(section 2), which also proved to be efficient for the mechanical characterization itself [Réthoré, 2010, Réthoré et al., 2013]. We could

then directly implement the HPC techniques of chapter 4. However, it seems that the construction of an image-based model suitable for predictive simulation requires to resort to complex modeling procedures, such as grouping together **immersed boundary approaches (thus non-conforming)** with higher-order and **smoother functions** [Lian et al., 2013, Schillinger and Ruess, 2015, Verhoosel et al., 2015]. This often leads to large-scale and ill-posed stiffness operators, which make the resolution a tricky task. A few very recent works addressed the problematic in the context of linear monophasic materials [de Prenter et al., 2017, Badia and Verdugo, 2018, Jomo et al., 2019], and nothing seems to have been achieved yet in a more general framework, such as to handle non-linear heterogeneous materials (*e.g.*,). Here, the **strategies of chapter 4 could be combined with the non-conforming, non-invasive algorithm of chapter 2** to efficiently solve the DVC problem (and then the related identification problem) while using immersed-type approaches. Finally, the resulting procedure could be complemented by other recent developments regarding non-invasive coupling, such as those of [Duval et al., 2016] et [Oumaziz et al., 2018] in view of **handling possible non-linearities** within the constituents as well as within the interface, respectively. From a conceptual point of view, **resorting to the global/local non-invasive method appears original** not only for image correlation but also for image-based simulation where more classic Schwartz/domain decomposition or even multigrid -type strategies are rather considered [de Prenter et al., 2017, Badia and Verdugo, 2018, Jomo et al., 2019, Liu et al., 2019]. Such a research project should lead to the construction of a **pathbreaking platform** enabling the **proper and fine identification of mechanical properties** from different sets of images taken both using **tomographic or classical imaging**, which, to the best of our knowledge, has not yet been achieved.

Bibliography

[Abaqus, 614] Abaqus (6.14). Abaqus 6.14 documentation, keywords reference guide. (Cité en page 40.)

[Akhras et al., 2016] Akhras, H.-A., Elguedj, T., Gravouil, A., and Rochette, M. (2016). Isogeometric analysis-suitable trivariate NURBS models from standard B-Rep models. *Computer Methods in Applied Mechanics and Engineering*, 307:256–274. (Cité en pages 16 et 43.)

[Akkerman et al., 2011] Akkerman, I., Bazilevs, Y., Kees, C. E., and Farthing, M. W. (2011). Isogeometric analysis of free-surface flow. *Journal of Computational Physics*, 230(11):4137–4152. (Cité en page 9.)

[Ambati et al., 2018] Ambati, M., Kiendl, J., and De Lorenzis, L. (2018). Isogeometric Kirchhoff–Love shell formulation for elasto-plasticity. *Computer Methods in Applied Mechanics and Engineering*, 340:320–339. (Cité en page 9.)

[Amini et al., 2009] Amini, A. M., Dureisseix, D., Cartraud, P., and Buannic, N. (2009). A domain decomposition method for problems with structural heterogeneities on the interface: Application to a passenger ship. *Computer Methods in Applied Mechanics and Engineering*, 198(41):3452 – 3463. (Cité en pages 63, 68 et 72.)

[Ammar et al., 2006] Ammar, A., Mokdad, B., Chinesta, F., and Keunings, R. (2006). A new family of solvers for some classes of multidimensional partial differential equations encountered in kinetic theory modeling of complex fluids. *Journal of Non-Newtonian Fluid Mechanics*, 139(3):153–176. (Cité en page 104.)

[Annavarapu et al., 2012] Annavarapu, C., Hautefeuille, M., and Dolbow, J. (2012). A robust Nitsche's formulation for interface problems. *Computer Methods in Applied Mechanics and Engineering*, 225:44–54. (Cité en pages 44 et 51.)

[Antolin et al., 2019] Antolin, P., Buffa, A., Cohen, E., Dannenhoffer, J. F., Elber, G., Elgeti, S., Haimes, R., and Riesenfeld, R. (2019). Optimizing micro-tiles in micro-structures as a design paradigm. *Computer-Aided Design*, 115:23–33. (Cité en page 142.)

[Antolin et al., 2018] Antolin, P., Buffa, A., and Fabre, M. (2018). A priori error for unilateral contact problems with Lagrange multipliers and isogeometric analysis. *IMA Journal of Numerical Analysis*, 39(4):1627–1651. (Cité en page 9.)

[Apostolatos et al., 2014a] Apostolatos, A., Breitenberger, M., Wüchner, R., and Bletzinger, K.-U. (2014a). Domain decomposition methods and kirchhoff-love shell multipatch coupling in isogeometric analysis. In *B. Jüttler, B. Simeon (Eds.), Isogeometric Analysis and Applications 2014, Springer International Publishing*. (Cité en pages 44, 62 et 65.)

[Apostolatos et al., 2019] Apostolatos, A., De Nayer, G., Bletzinger, K.-U., Breuer, M., and Wüchner, R. (2019). Systematic evaluation of the interface description for fluid–structure interaction simulations using the isogeometric mortar-based mapping. *Journal of Fluids and Structures*, 86:368–399. (Cité en page 9.)

[Apostolatos et al., 2014b] Apostolatos, A., Schmidt, R., Wüchner, R., and Bletzinger, K.-U. (2014b). A Nitsche-type formulation and comparison of the most common domain decomposition methods in isogeometric analysis. *International Journal for Numerical Methods in Engineering*, 97:473–504. (Cité en page 44.)

[Arnold et al., 2002] Arnold, D., Brezzi, F., Cockburn, B., and Marini, D. (2002). Unified analysis of discontinuous Galerkin methods for elliptic problems. *SIAM J. Numerical Analysis*, 39:1749–1779. (Cité en page 51.)

[Auricchio et al., 2012a] Auricchio, F., Calabro, F., Hughes, T. J., Reali, A., and Sangalli, G. (2012a). A simple algorithm for obtaining nearly optimal quadrature rules for NURBS-based isogeometric analysis. *Computer Methods in Applied Mechanics and Engineering*, 249:15–27. (Cité en page 23.)

[Auricchio et al., 2010] Auricchio, F., Da Veiga, L. B., Hughes, T., Reali, A., and Sangalli, G. (2010). Isogeometric collocation methods. *Mathematical Models and Methods in Applied Sciences*, 20(11):2075–2107. (Cité en page 23.)

[Auricchio et al., 2012b] Auricchio, F., Da Veiga, L. B., Hughes, T. J., Reali, A., and Sangalli, G. (2012b). Isogeometric collocation for elastostatics and explicit dynamics. *Computer methods in applied mechanics and engineering*, 249:2–14. (Cité en page 23.)

[Avril et al., 2008] Avril, S., Bonnet, M., Bretelle, A.-S., Grédiac, M., Hild, F., Ienny, P., Latourte, F., Lemosse, D., Pagano, S., Pagnacco, E., and Pierron, F. (2008). Overview of identification methods of mechanical parameters based on full-field measurements. *Experimental Mechanics*, 48(4):381–402. (Cité en page 143.)

[Badia and Verdugo, 2018] Badia, S. and Verdugo, F. (2018). Robust and scalable domain decomposition solvers for unfitted finite element methods. *Journal of Computational and Applied Mathematics*, 344:740–759. (Cité en pages 58 et 145.)

[Baiges et al., 2012] Baiges, J., Codina, R., Henke, F., Shahmiri, S., and Wall, W. (2012). A symmetric method for weakly imposing Dirichlet boundary conditions in embedded finite element meshes. *International Journal for Numerical Methods in Engineering*, 90:636–658. (Cité en page 51.)

[Baker and Matthews, 2001] Baker, S. and Matthews, I. (2001). Equivalence and efficiency of image alignment algorithms. In *Proceedings of the 2001 IEEE Computer Society Conference on Computer Vision and Pattern Recognition*, volume 1, pages 1090–1097. (Cité en page 90.)

[Baker and Matthews, 2004] Baker, S. and Matthews, I. (2004). Lucas-kanade 20 years on: A unifying framework. *International Journal of Computer Vision*, 56(3):221–255. (Cité en page 90.)

[Balcaen et al., 2017] Balcaen, R., Reu, P.-L., Lava, P., and Debruyne, D. (2017). Stereo-DIC uncertainty quantification based on simulated images. *Experimental Mechanics*, 57(6):939–951. (Cité en page 118.)

[Balesdent et al., 2012] Balesdent, M., Bérend, N., Dépincé, P., and Chriette, A. (2012). A survey of multidisciplinary design optimization methods in launch vehicle design. *Structural and Multidisciplinary optimization*, 45(5):619–642. (Cité en page 142.)

[Bandara and Cirak, 2017] Bandara, K. and Cirak, F. (2017). Isogeometric shape optimisation of shell structures using multiresolution subdivision surfaces. *Computer-Aided Design*, 95:62–71. (Cité en pages 59, 114 et 127.)

[Bauer et al., 2017] Bauer, A., Breitenberger, M., Philipp, B., Wüchner, R., and Bletzinger, K.-U. (2017). Embedded structural entities in NURBS-based isogeometric analysis. *Computer Methods in Applied Mechanics and Engineering*, 325:198–218. (Cité en page 128.)

[Bay et al., 1999] Bay, B., Smith, T., Fyhrie, D., and Saad, M. (1999). Digital volume correlation: three-dimensional strain mapping using x-ray tomography. *Experimental Mechanics*, 39(3):217–226. (Cité en page 144.)

[Bazilevs et al., 2007] Bazilevs, Y., Calo, V., Cottrell, J., Hughes, T., Reali, A., and Scovazzi, G. (2007). Variational multiscale residual-based turbulence modeling for large eddy simulation of incompressible flows. *Computer methods in applied mechanics and engineering*, 197(1-4):173–201. (Cité en page 9.)

[Bazilevs et al., 2010] Bazilevs, Y., Calo, V., Cottrell, J.-A., Evans, J.-A., Hughes, T.-J.-R., Lipton, S., Scott, M., and Sederberg, T. (2010). Isogeometric analysis using T-splines. *Computer Methods in Applied Mechanics and Engineering*, 199:229–263. (Cité en pages 9 et 15.)

[Bazilevs et al., 2012] Bazilevs, Y., Hsu, M.-C., and Scott, M. (2012). Isogeometric fluid–structure interaction analysis with emphasis on non-matching discretizations, and with application to wind turbines. *Computer Methods in Applied Mechanics and Engineering*, 249:28–41. (Cité en pages 52 et 77.)

[Beaubier et al., 2014] Beaubier, B., Dufour, J., Hild, F., Roux, S., Lavernhe, S., and Lavernhe-Taillard, K. (2014). CAD-based calibration and shape measurement with StereoDIC - Principle and application on test and industrial parts. *Experimental Mechanics*, 54(3):329–341. (Cité en page 113.)

[Belytschko et al., 1985] Belytschko, T., Stolarski, H., Liu, W. K., Carpenter, N., and Ong, J. S. (1985). Stress projection for membrane and shear locking in shell finite elements. *Computer Methods in Applied Mechanics and Engineering*, 51(1-3):221–258. (Cité en page 74.)

[Bendsøe, 1989] Bendsøe, M. P. (1989). Optimal shape design as a material distribution problem. *Structural optimization*, 1:193–202. (Cité en page 144.)

[Benson et al., 2010] Benson, D., Bazilevs, Y., Hsu, M., and Hughes, T. (2010). Isogeometric shell analysis: The Reissner–Mindlin shell. *Computer Methods in Applied Mechanics and Engineering*, 199(5):276 – 289. Computational Geometry and Analysis. (Cité en page 59.)

[Bernadou and Cubier, 1998] Bernadou, M. and Cubier, A. (1998). Numerical analysis of junctions between thin shells part 1: Continuous problems. *Computer Methods in Applied Mechanics and Engineering*, 161:349 – 363. (Cité en page 65.)

[Bernadou et al., 1989] Bernadou, M., Fayolle, S., and Léné, F. (1989). Numerical analysis of junctions between plates. *Computer Methods in Applied Mechanics and Engineering*, 74:307 – 326. (Cité en page 65.)

[Bertin et al., 2016] Bertin, M.-B.-R., Hild, F., and Roux, S. (2016). Optimization of a cruciform specimen geometry for the identification of constitutive parameters based upon full-field measurements. *Strain*, 52:307–323. (Cité en page 144.)

[Besnard et al., 2006] Besnard, G., Hild, F., and Roux, S. (2006). "finite-element" displacement fields analysis from digital images: Application to Portevin-le Châtelier bands. *Experimental Mechanics*, 46(6):789–803. (Cité en page 81.)

[Bettinotti et al., 2014] Bettinotti, O., Allix, O., Perego, U., Oancea, V., and Malherbe, B. (2014). A fast weakly intrusive multiscale method in explicit dynamics. *International Journal for Numerical Methods in Engineering*, 100(8):577–595. (Cité en page 31.)

[Bhardwaj et al., 2002] Bhardwaj, M., Pierson, K., Reese, G., Walsh, T., Day, D., Alvin, K., Peery, J., Farhat, C., and Lesoinne, M. (2002). Salinas: a scalable software for high-performance structural and solid mechanics simulations. In *Proceedings of SC02*. (Cité en page 30.)

[Black and Jepson, 1998] Black, M. J. and Jepson, A. D. (1998). EigenTracking: Robust matching and tracking of articulated objects using a view-based representation. *International Journal of Computer Vision*, 26(1):63–84. (Cité en page 85.)

[Blanchard et al., 2019] Blanchard, M., Allix, O., Gosselet, P., and Desmeure, G. (2019). Space/time global/local noninvasive coupling strategy: Application to viscoplastic structures. *Finite Elements in Analysis and Design*, 156:1–12. (Cité en page 31.)

[Bletzinger, 2014] Bletzinger, K.-U. (2014). A consistent frame for sensitivity filtering and the vertex assigned morphing of optimal shape. *Structural and Multidisciplinary Optimization*, 49(6):873–895. (Cité en page 112.)

[Bletzinger et al., 1992] Bletzinger, K.-U., Kimmich, S., and Ramm, E. (1992). Efficient modeling in shape optimal design. *Computing Systems in Engineering*, 2:483–495. (Cité en page 112.)

[Bletzinger et al., 2005] Bletzinger, K.-U., Wüchner, R., Daoud, F., and Camprubí, N. (2005). Computational methods for form finding and optimization of shells and membranes. *Computer Methods in Applied Mechanics and Engineering*, 194(30-33):3438–3452. (Cité en page 132.)

[Borden et al., 2011] Borden, M. J., Scott, M. A., Evans, J. A., and Hughes, T. J. (2011). Isogeometric finite element data structures based on Bézier extraction of NURBS. *International Journal for Numerical Methods in Engineering*, 87(1-5):15–47. (Cité en pages 10, 16, 26 et 27.)

[Bornert et al., 2009] Bornert, M., Brémand, F., Doumalin, P., Dupré, J.-C., Fazzini, M., Grédiac, M., Hild, F., Mistou, S., Molimard, J., Orteu, J.-J., Robert, L., Surrel, Y., Vacher, P., and Wattrisse, B. (2009). Assessment of digital image correlation measurement errors: methodology and results. *Experimental Mechanics*, 49(3):353–370. (Cité en page 92.)

[Bornert et al., 2010] Bornert, M., Vales, F., Gharbi, H., and Nguyen Minh, D. (2010). Multiscale full-field strain measurements for micromechanical investigations of the hydromechanical behaviour of clayey rocks. *Strain*, 46(1):33–46. (Cité en page 104.)

[Bouclier et al., 2013a] Bouclier, R., Elguedj, T., and Combescure, A. (2013a). Efficient isogeometric NURBS-based solid-shell elements: Mixed formulation and Bbar-Method. *Computer Methods in Applied Mechanics and Engineering*, 267:86–110. (Cité en page 74.)

[Bouclier et al., 2013b] Bouclier, R., Elguedj, T., and Combescure, A. (2013b). On the development of NURBS-based isogeometric solid shell elements: 2D problems and preliminary extension to 3D. *Computational Mechanics*, 52(5):1085–1112. (Cité en page 59.)

[Bouclier et al., 2015a] Bouclier, R., Elguedj, T., and Combescure, A. (2015a). Development of a mixed displacement-stress formulation for the analysis of elastoplastic structures under small strains: Application to a locking-free, NURBS-based solid-shell element. *Computer Methods in Applied Mechanics and Engineering*, 295:543 – 561. (Cité en pages 9 et 59.)

[Bouclier et al., 2015b] Bouclier, R., Elguedj, T., and Combescure, A. (2015b). An isogeometric locking-free NURBS-based solid-shell element for geometrically nonlinear analysis. *International Journal for Numerical Methods in Engineering*, 101:774–808. (Cité en pages 9, 59 et 142.)

[Bouclier et al., 2013c] Bouclier, R., Louf, F., and Chamoin, L. (2013c). Real-time validation of mechanical models coupling PGD and constitutive relation error. *Computational Mechanics*, 52(4):861–883. (Cité en page 104.)

[Bouclier and Passieux, 2017] Bouclier, R. and Passieux, J.-C. (2017). A domain coupling method for finite element digital image correlation with mechanical regularization: Application to multiscale measurements and parallel computing. *International Journal for Numerical Methods in Engineering*, 111(2):123–143. (Cité en pages 4, 89, 91, 92, 98, 101, 104 et 143.)

[Bouclier and Passieux, 2018] Bouclier, R. and Passieux, J.-C. (2018). A Nitsche-based non-intrusive coupling strategy for global/local isogeometric structural analysis. *Computer Methods in Applied Mechanics and Engineering*, 340:253–277. (Cité en pages 3, 4, 5, 42, 43, 44, 50, 52, 53, 54, 57, 124 et 138.)

[Bouclier et al., 2016] Bouclier, R., Passieux, J.-C., and Salaün, M. (2016). Local enrichment of nurbs patches using a non-intrusive coupling strategy: geometric details, local refinement, inclusion, fracture. *Computer Methods in Applied Mechanics and Engineering*, 300:1–26. (Cité en pages 3, 4, 37, 42, 43, 44 et 45.)

[Bouclier et al., 2017] Bouclier, R., Passieux, J.-C., and Salaün, M. (2017). Development of a new, more regular, mortar method for the coupling of nurbs subdomains within a nurbs patch: Application to a non-intrusive local enrichment of nurbs patches. *Computer Methods in Applied Mechanics and Engineering*, 316(1):123–150. (Cité en pages 3, 38, 42 et 44.)

[Bouclier et al., 2019] Bouclier, R., Passieux, J.-C., Tirvaudey, M., Chamoin, L., and Chapelier, M. (2019). Un pont global entre IGA et FEM: Calcul et optimisation de forme, isogéométrique, non-intrusif à partir d'un code EF industriel. In *14e Colloque National en Calcul des Structures, CSMA (Giens, Fr)*. (Cité en page 121.)

[Bovet et al., 2017] Bovet, C., Parret-Fréaud, A., Spillane, N., and Gosselet, P. (2017). Adaptive multipreconditioned FETI: Scalability results and robustness assessment. *Computers and Structures*, 193:1 – 20. (Cité en pages 63 et 78.)

[Braibant and Fleury, 1984] Braibant, V. and Fleury, C. (1984). Shape optimal design using B-spline. *Computer Methods in Applied Mechanics and Engineering*, 44:247–267. (Cité en pages 112, 121 et 125.)

[Breitenberger et al., 2015] Breitenberger, M., Apostolatos, A., Philipp, B., Wüchner, R., and Bletzinger, K.-U. (2015). Analysis in computer aided design: Nonlinear isogeometric B-Rep analysis of shell structures. *Computer Methods in Applied Mechanics and Engineering*, 284:401–457. (Cité en page 62.)

[Brivadis et al., 2015] Brivadis, E., Buffa, A., Wohlmuth, B., and L., W. (2015). Isogeometric mortar methods. *Computer Methods in Applied Mechanics and Engineering*, 284:292–319. (Cité en pages 33, 44 et 50.)

[Broyden, 1970] Broyden, C. G. (1970). The convergence of a class of double-rank minimization algorithms. *IMA Journal of Applied Mathematics*, 6:76–90. (Cité en page 126.)

[Bruck et al., 1989] Bruck, H., McNeill, S., Sutton, M., and Peters, W. (1989). Digital image correlation using Newton-Raphson method of partial differential correction. *Experimental Mechanics*, 29:261–267. (Cité en page 85.)

[Buffa et al., 2019] Buffa, A., Puppi, R., and Vázquez, R. (2019). A minimal stabilization procedure for isogeometric methods on trimmed geometries. *arXiv:1902.04937v3 [math]*. (Cité en pages 44 et 51.)

[Buljac et al., 2018a] Buljac, A., Jailin, C., Mendoza, A., Neggers, J., Taillandier-Thomas, T., Bouterf, A., Smaniotto, B., Hild, F., and Roux, S. (2018a). Digital volume correlation: Review of progress and challenges. *Experimental Mechanics*, 58(5):661–708. (Cité en page 89.)

[Buljac et al., 2018b] Buljac, A., Jailin, C., Mendoza, A., Neggers, J., Taillandier-Thomas, T., Bouterf, A., Smaniotto, B., Hild, F., and Roux, S. (2018b). Digital volume correlation: review of progress and challenges. *Experimental Mechanics*, 58:661–708. (Cité en page 144.)

[Burman, 2011] Burman, E. (2011). A penalty-free nonsymmetric Nitsche-type method for the weak imposition of boundary conditions. *SIAM J. Numerical Analysis*, 50:1959–1981. (Cité en page 51.)

[Burman et al., 2015] Burman, E., Claus, S., Hansbo, P., Larson, M.-G., and Massing, A. (2015). CutFEM: Discretizing geometry and partial differential equations. *International Journal for Numerical Methods in Engineering*, 104:472–501. (Cité en pages 43, 44, 53 et 131.)

[Calabro et al., 2017] Calabro, F., Sangalli, G., and Tani, M. (2017). Fast formation of isogeometric Galerkin matrices by weighted quadrature. *Computer Methods in Applied Mechanics and Engineering*, 316:606–622. (Cité en pages 23 et 27.)

[Cardoso and Cesar de Sa, 2014] Cardoso, R. P. R. and Cesar de Sa, J. M. A. (2014). Blending moving least squares techniques with nurbs basis functions for nonlinear isogeometric analysis. *Computational Mechanics*, 53(6):1327–1340. (Cité en page 59.)

[Caseiro et al., 2015] Caseiro, J., Valente, R., Reali, A., Kiendl, J., Auricchio, F., and de Sousa, R. A. (2015). Assumed natural strain NURBS-based solid-shell element for the analysis of large deformation elasto-plastic thin-shell structures. *Computer Methods in Applied Mechanics and Engineering*, 284:861 – 880. (Cité en pages 59 et 142.)

[Chamoin et al., 2020] Chamoin, L., Jailin, C., Diaz, M., and Quesada, L. (2020). Coupling between topology optimization and digital image correlation for the design of specimen dedicated to selected material parameters identification. *International Journal of Solids and Structures*, submitted. (Cité en page 144.)

[Chantrait et al., 2014] Chantrait, T., Rannou, J., and Gravouil, A. (2014). Low intrusive coupling of implicit and explicit time integration schemes for structural dynamics: Application to low energy impacts on composite structures. *Finite Elements in Analysis and Design*, 86:23–33. (Cité en page 31.)

[Chapelier, 2021] Chapelier, M. (2018-2021). *Développement de stratégies d'optimisation de forme isogéométriques pour la mécanique expérimentale*. PhD thesis, Université de Toulouse. (Cité en pages 5, 108 et 144.)

[Chelaghma, 2018] Chelaghma, S. (2015-2018). *Functionalization of Carbon/PEKK composites for aerospace applications: characterization, modeling and influence on the composite properties*. PhD thesis, Université de Toulouse. (Cité en pages 3 et 144.)

[Chen and Borst, 2018] Chen, L. and Borst, R. (2018). Adaptive refinement of hierarchical T-splines. *Computer Methods in Applied Mechanics and Engineering*, 337:220–245. (Cité en pages 15 et 16.)

[Cheng et al., 2002] Cheng, P., Sutton, M., Schreier, H., and McNeill, S. R. (2002). Full-field speckle pattern image correlation with B-spline deformation function. *Experimental mechanics*, 42(3):344–352. (Cité en pages 84, 85 et 111.)

[Chevreuil et al., 2013] Chevreuil, M., Nouy, A., and Safatly, E. (2013). A multiscale method with patch for the solution of stochastic partial differential equations with localized uncertainties. *Computer Methods in Applied Mechanics and Engineering*, 255:255–274. (Cité en pages 31 et 37.)

[Chinesta et al., 2018] Chinesta, F., Cueto, E., Abisset-Chavanne, E., Duval, J. L., and El Khaldi, F. (2018). Virtual, digital and hybrid twins: a new paradigm in data-based engineering and engineered data. *Archives of Computational Methods in Engineering*, 27:105–134. (Cité en page 143.)

[Chinesta et al., 2011] Chinesta, F., Ladevèze, P., and Cueto, E. (2011). A short review on model order reduction based on proper generalized decomposition. *Arch Comput Methods Eng*, 18:395–404. (Cité en page 20.)

[Choi and Cho, 2018] Choi, M.-J. and Cho, S. (2018). Constrained isogeometric design optimization of lattice structures on curved surfaces: computation of design velocity field. *Structural and Multidisciplinary Optimization*, 58:17–34. (Cité en page 123.)

[Cirak et al., 2000] Cirak, F., Ortiz, M., and Schröder, P. (2000). Subdivision surfaces: a new paradigm for thin-shell finite-element analysis. *International Journal for Numerical Methods in Engineering*, 47(12):2039–2072. (Cité en page 64.)

[Cirak et al., 2002] Cirak, F., Scott, M. J., Antonsson, E. K., Ortiz, M., and Schröder, P. (2002). Integrated modeling, finite-element analysis, and engineering design for thin-shell structures using subdivision. *Computer-Aided Design*, 34(2):137–148. (Cité en page 9.)

[Claire et al., 2004] Claire, D., Hild, F., and Roux, S. (2004). A finite element formulation to identify damage fields: the equilibrium gap method. *Int J. Numer Methods Eng*, 61(2):189–208. (Cité en page 93.)

[CodeAster, 2014] CodeAster (2014). *Electricite de France*. http://www.code-aster.org. (Cité en pages 10, 22 et 27.)

[Cohen et al., 1980] Cohen, E., Lyche, T., and Riesenfeld, R. (1980). Discrete B-spline and subdivision techniques in computer aided geometric design and computer graphics. *Computer Graphics and Image Processing*, 14:87–111. (Cité en pages 9, 11, 12 et 112.)

[Colantonio et al., 2020] Colantonio, G., Chapelier, M., Bouclier, R., Passieux, J.-C., and Marenic, E. (2020). Non-invasive multilevel geometric regularization of mesh-based 3D shape measurement. *International Journal for Numerical Methods in Engineering*, Online first. (Cité en pages 5, 108 et 121.)

[Cormier et al., 1999] Cormier, N., Smallwood, B., Sinclair, G., and Meda, G. (1999). Aggressive submodelling of stress concentrations. *International Journal for Numerical Methods in Engineering*, 46(6):889–909. (Cité en page 30.)

[Cottrell et al., 2009] Cottrell, J., Hughes, T.-J.-R., and Bazilevs, Y. (2009). *Isogeometric Analysis: Toward Integration of CAD and FEA*. Wiley. (Cité en pages 9, 11, 12, 13, 55, 112 et 118.)

[Cottrell et al., 2007] Cottrell, J.-A., Hughes, T.-J.-R., and Reali, A. (2007). Studies of refinement and continuity in isogeometric structural analysis. *Computer Methods in Applied Mechanics and Engineering*, 196:4160–4183. (Cité en pages 9, 12, 14, 16 et 113.)

[Cottrell et al., 2006] Cottrell, J. A., Reali, A., Bazilevs, Y., and Hughes, T. J. (2006). Isogeometric analysis of structural vibrations. *Computer methods in applied mechanics and engineering*, 195(41-43):5257–5296. (Cité en page 9.)

[Cresta et al., 2007] Cresta, P., Allix, O., Rey, C., and Guinard, S. (2007). Nonlinear localization strategies for domain decomposition methods in structural mechanics. *Computer Methods in Applied Mechanics and Engineering*, 196:1436–1446. (Cité en page 30.)

[Dalcin et al., 2016] Dalcin, L., Collier, N., Vignal, P., Côrtes, A., and Calo, V. M. (2016). PetIGA: A framework for high-performance isogeometric analysis. *Computer Methods in Applied Mechanics and Engineering*, 308:151–181. (Cité en page 23.)

[Dalémat et al., 2019] Dalémat, M., Coret, M., Leygue, A., and Verron, E. (2019). Measuring stress field without constitutive equation. *Mechanics of Materials*, 136:103087. (Cité en page 143.)

[Dauge et al., 2015] Dauge, M., Düster, A., and Rank, E. (2015). Theoretical and numerical investigation of the finite cell method. *Journal of Scientific Computing*, 65:1039–1064. (Cité en pages 43 et 53.)

[Daxini and Prajapati, 2017] Daxini, S. D. and Prajapati, J. M. (2017). Parametric shape optimization techniques based on Meshless methods: A review. *Structural and Multidisciplinary Optimization*, 56(5):1197–1214. (Cité en page 123.)

[de Prenter et al., 2017] de Prenter, F., Verhoosel, C.-V., van Zwieten, G.-J., and van Brummelen, V.-H. (2017). Condition number analysis and preconditioning of the finite cell method. *Computer Methods in Applied Mechanics and Engineering*, 316:297–327. (Cité en pages 43, 53, 58 et 145.)

[Dittmann et al., 2019] Dittmann, M., Schuß, S., Wohlmuth, B., and Hesch, C. (2019). Weak Cn coupling for multi-patch isogeometric analysis in solid mechanics. *International Journal for Numerical Methods in Engineering*, 118(11):678–699. (Cité en pages 45 et 50.)

[Dokken et al., 2013] Dokken, T., Lyche, T., and Pettersen, K. (2013). Polynomial splines over locally refined box-partitions. *Computer Aided Geometric Design*, 30:331–356. (Cité en page 15.)

[Dolean et al., 2015] Dolean, V., Jolivet, P., and Nataf, F. (2015). *An introduction to domain decomposition methods: algorithms, theory, and parallel implementation*, volume 144. SIAM. (Cité en page 71.)

[Dornisch et al., 2013] Dornisch, W., Klinkel, S., and Simeon, B. (2013). Isogeometric Reissner–Mindlin shell analysis with exactly calculated director vectors. *Computer Methods in Applied Mechanics and Engineering*, 253:491 – 504. (Cité en page 59.)

[Dornisch et al., 2017] Dornisch, W., Stoeckler, J., and Müller, R. (2017). Dual and approximate dual basis functions for B-splines and NURBS – Comparison and application for an efficient coupling of patches with the isogeometric mortar method. *Computer Methods in Applied Mechanics and Engineering*, 316:449–496. (Cité en page 62.)

[Dornisch et al., 2015] Dornisch, W., Vitucci, G., and Klinkel, S. O. (2015). The weak substitution method: an application of the mortar method for patch coupling in NURBS-based isogeometric analysis. *International Journal for Numerical Methods in Engineering*, 103:205–234. (Cité en pages 33 et 44.)

[Doumalin, 2000] Doumalin, P. (1997-2000). *Microextensometrie locale par correlation d'images numériques : application aux études micromécaniques par microscopie électronique à balayage*. PhD thesis, École polytechnique, Palaiseau. (Cité en page 85.)

[Dubois et al., 2018] Dubois, A., Farhat, C., Abukhwejah, A. H., and Shageer, H. M. (2018). Parameterization Framework for the MDAO of Wing Structural Layouts. *AIAA Journal*, 56:1627–1638. (Cité en pages 136, 137, 138 et 142.)

[Dufour et al., 2015a] Dufour, J.-E., Beaubier, B., Hild, F., and Roux, S. (2015a). CAD-based displacement measurements with Stereo-DIC. *Experimental Mechanics*, 55(9):1657–1668. (Cité en pages 9, 107, 109 et 113.)

[Dufour et al., 2015b] Dufour, J.-E., Hild, F., and Roux, S. (2015b). Shape, displacement and mechanical properties from isogeometric multiview stereocorrelation. *The Journal of Strain Analysis for Engineering Design*, 50(7):470–487. (Cité en page 113.)

[Dufour et al., 2016] Dufour, J.-E., Leclercq, S., Schneider, J., Roux, S., and Hild, F. (2016). 3D surface measurements with isogeometric stereocorrelation–Application to complex shapes. *Optics and Lasers in Engineering*, 87:146 – 155. (Cité en pages 85, 94, 107, 111 et 113.)

[Duong et al., 2017] Duong, T. X., Roohbakhshan, F., and Sauer, R. A. (2017). A new rotation-free isogeometric thin shell formulation and a corresponding continuity constraint for patch boundaries. *Computer Methods in Applied Mechanics and Engineering*, 316:43 – 83. (Cité en pages 62 et 65.)

[Dureisseix and Farhat, 2001] Dureisseix, D. and Farhat, C. (2001). A numerically scalable domain decomposition method for the solution of frictionless contact problems. *International Journal for Numerical Methods in Engineering*, 50:2643–2666. (Cité en page 63.)

[Duval et al., 2015] Duval, A., Elguedj, T., Al-Akhras, H., and Maurin, F. (2015). abqNURBS: implémentation d'éléments isogéométriques dans Abaqus et outils de pré-et post-traitement dédiés. In *12e Colloque national en calcul des structures*. (Cité en page 19.)

[Duval et al., 2018] Duval, M., Losinski, A., Passieux, J.-C., and Salaün, M. (2018). Residual error based adaptive mesh refinement with the non-intrusive patch algorithm. *Computer Methods in Applied Mechanics and Engineering*, 329:118–143. (Cité en page 32.)

[Duval et al., 2016] Duval, M., Passieux, J.-C., Salaün, M., and Guinard, S. (2016). Non-intrusive coupling: recent advances and scalable nonlinear domain decomposition. *Archives of Computational Methods in Engineering*, 23(1):17–38. (Cité en pages 31, 33, 37, 38, 47, 54, 58 et 145.)

[Duvigneau, 2006] Duvigneau, R. (2006). Adaptive parameterization using free-form deformation for aerodynamic shape optimization. *Research Report INRIA*. (Cité en pages 122 et 129.)

[Düster et al., 2007] Düster, A., Niggl, A., and Rank, E. (2007). Applying the hp–d version of the fem to locally enhance dimensionally reduced models. *Applied Mechanical Engineering*, 196:3524–3533. (Cité en page 38.)

[D'Angella et al., 2018] D'Angella, D., Kollmannsberger, S., Rank, E., and Reali, A. (2018). Multi-level Bézier extraction for hierarchical local refinement of isogeometric analysis. *Computer Methods in Applied Mechanics and Engineering*, 328:147–174. (Cité en pages 15 et 16.)

[Echter et al., 2013] Echter, R., Oesterle, B., and Bischoff, M. (2013). A hierarchic family of isogeometric shell finite elements. *Computer Methods in Applied Mechanics and Engineering*, 254:170 – 180. (Cité en pages 9, 59, 62 et 64.)

[Elfverson et al., 2019] Elfverson, D., Larson, M., and Larsson, K. (2019). A new least squares stabilized Nitsche method for cut isogeometric analysis. *arXiv:1804.05654v3 [math]*. (Cité en pages 44 et 51.)

[Elguedj et al., 2008] Elguedj, T., Bazilevs, Y., Calo, V. M., and Hughes, T. J. (2008). Bbar and Fbar projection methods for nearly incompressible linear and non-linear elasticity and plasticity using higher-order NURBS elements. *Computer methods in applied mechanics and engineering*, 197(33-40):2732–2762. (Cité en page 9.)

[Elguedj et al., 2010] Elguedj, T., Réthoré, J., and Buteri, A. (2010). Isogeometric analysis for strain field measurements. *Computer Methods in Applied Mechanics and Engineering*, 200(1-4):40–56. (Cité en pages 84 et 111.)

[Evans et al., 2015] Evans, E.-J., Scott, M., Li, X., and Thomas, D. (2015). Hierarchical T-splines: Analysis-suitability, Bézier extraction, and application as an adaptive basis for isogeometric analysis. *Computer Methods in Applied Mechanics and Engineering*, 284:284. (Cité en pages 15 et 16.)

[Evans et al., 2009] Evans, J. A., Bazilevs, Y., Babuška, I., and Hughes, T. J. (2009). n-Widths, sup-infs, and optimality ratios for the k-version of the isogeometric finite element method. *Computer Methods in Applied Mechanics and Engineering*, 198(21-26):1726–1741. (Cité en page 9.)

[Farhat et al., 1998] Farhat, C., Chen, P.-S., Mandel, J., and Roux, F. X. (1998). The two-level FETI method Part II: Extension to shell problems, parallel implementation and performance results. *Computer Methods in Applied Mechanics and Engineering*, 155(1):153 – 179. (Cité en pages 63, 68, 71, 74 et 78.)

[Farhat et al., 2001] Farhat, C., Lesoinne, M., Le Tallec, P., Pierson, K., and Rixen, D. (2001). FETI-DP: A dual-primal unified FETI method–part I: A faster alternative to the two-level FETI method. *International Journal for Numerical Methods in Engineering*, 50:1523–1544. (Cité en pages 63, 68, 74 et 78.)

[Farhat and Roux, 1991] Farhat, C. and Roux, F. (1991). A method of finite element tearing and interconnecting and its parallel solution algorithm. *International Journal for Numerical Methods in Engineering*, 32:1205–1227. (Cité en pages 62, 69, 71 et 96.)

[Farin, 2002] Farin, G. (2002). *Curves and surfaces for CAGD: a practical guide*. Morgan Kaufmann Publishers Inc., San Francisco. (Cité en pages 9 et 11.)

[Fedele et al., 2013] Fedele, R., Galantucci, L., and Ciani, A. (2013). Global 2D digital image correlation for motion estimation in a finite element framework: a variational formulation and a regularized, pyramidal, multi-grid implementation. *International Journal for Numerical Methods in Engineering*, 96(12):739–762. (Cité en pages 81 et 88.)

[Fehrenbach and Masmoudi, 2008] Fehrenbach, J. and Masmoudi, M. (2008). A fast algorithm for image registration. *Comptes Rendus Mathématique*, 346(9-10):593–598. (Cité en pages 81 et 85.)

[Firl et al., 2013] Firl, M., Wüchner, R., and Bletzinger, K.-U. (2013). Regularization of shape optimization problems using FE-based parametrization. *Structural and Multidisciplinary Optimization*, 47:507–521. (Cité en page 112.)

[Fletcher, 1987] Fletcher, R. (1987). *Practical methods of optimization*. John Wiley & Sons. (Cité en page 126.)

[Fouque, 2021] Fouque, R. (2018-2021). *Identification de propriétés mécaniques par corrélation d'images stéréoscopiques multi-échelles*. PhD thesis, Universié de Toulouse. (Cité en pages 5 et 105.)

[Fouque et al., 2020] Fouque, R., Bouclier, R., Passieux, J.-C., and Périé, J.-N. (2020). Fractal pattern generation for multiscale Digital Image Correlation. *Experimental Mechanics*, submitted. (Cité en pages 5, 85 et 105.)

[Fries and Omerovic, 2016] Fries, T.-P. and Omerovic, S. (2016). Higher-order accurate integration of implicit geometries. *Computer Methods in Applied Mechanics and Engineering*, 106:323–371. (Cité en pages 43 et 53.)

[Fries et al., 2017] Fries, T.-P., Omerovic, S., Schöllhammer, D., and Steidl, J. (2017). Higher-order meshing of implicit geometries - part i: Integration and interpolation in cut elements. *Computer Methods in Applied Mechanics and Engineering*, 313:759–784. (Cité en pages 43 et 53.)

[Fritz et al., 2004] Fritz, A., Hüeber, S., and Wohlmuth, B. I. (2004). A comparison of mortar and Nitsche techniques for linear elasticity. *Calcolo*, 41(3):115–137. (Cité en page 77.)

[Fußeder et al., 2015] Fußeder, D., Simeon, B., and Vuong, A.-V. (2015). Fundamental aspects of shape optimization in the context of isogeometric analysis. *Computer Methods in Applied Mechanics and Engineering*, 286:313–331. (Cité en pages 57, 59, 123 et 142.)

[Gander and Japhet, 2013] Gander, M. and Japhet, C. (2013). Algorithm 932: Pang: Software for non-matching grid projections in 2d and 3d with linear complexity. *ACM Transactions on Mathematical Software, Association for Computing Machinery*, 40(1):6–1625. (Cité en page 40.)

[Garcia, 2001] Garcia, D. (2001). *Mesure de formes et de champs de déplacements tridimensionnels par stéréo-corrélation d'images*. PhD thesis, Institut National Polytechnique de Toulouse. (Cité en pages 108 et 119.)

[Garcia et al., 2002] Garcia, D., Orteu, J.-J., and Penazzi, L. (2002). A combined temporal tracking and stereo-correlation technique for accurate measurement of 3d displacements: Application to sheet metal forming. *Journal of Materials Processing Technology*, 125-126:736–742. (Cité en pages 107 et 119.)

[Gendre et al., 2009] Gendre, L., Allix, O., and Gosselet, P. (2009). Non-intrusive and exact global/local techniques for structural problems with local plasticity. *Computational Mechanics*, 44:233–245. (Cité en pages 30, 31, 37, 38, 54 et 58.)

[Geuzaine and Remacle, 2009] Geuzaine, C. and Remacle, J.-F. (2009). Gmsh: a three-dimensional finite element mesh generator with built-in pre- and post-processing facilities. *International Journal for Numerical Methods in Engineering*, 79(11):1309–1331. (Cité en page 47.)

[Glowinski et al., 2005] Glowinski, R., He, J., Lozinski, A., Rappaz, J., and Wagner, J. (2005). Finite element approximation of multi-scale elliptic problems using patches of elements. *Numer. Math.*, 101(4):663–687. (Cité en page 38.)

[Gomes Perini et al., 2014] Gomes Perini, L., Passieux, J.-C., and Périé, J.-N. (2014). A multigrid PGD-based algorithm for volumetric displacement fields measurements. *Strain*, 50(4):355–367. (Cité en pages 85, 92, 143 et 144.)

[Gosselet et al., 2018] Gosselet, P., Blanchard, M., Allix, O., and Guguin, G. (2018). Non-invasive global-local coupling as a Schwarz domain decomposition method: acceleration and generalization. *Advanced Modeling and Simulation in Engineering Sciences*, 5(4). (Cité en pages 31 et 39.)

[Gosselet and Rey, 2006] Gosselet, P. and Rey, C. (2006). Non-overlapping domain decomposition methods in structural mechanics. *Archives of Computational Methods in Engineering*, 13:515–572. (Cité en pages 62, 70, 77 et 98.)

[Gosselet et al., 2013] Gosselet, P., Rey, C., and Pebrel, J. (2013). Total and selective reuse of krylov subspaces for the solution to a sequence of nonlinear structural problems. *International Journal for Numerical Methods in Engineering*, 94:60–83. (Cité en page 43.)

[Gosselet et al., 2015] Gosselet, P., Rixen, D., Roux, F.-X., and Spillane, N. (2015). Simultaneous-FETI and Block-FETI: robust domain decomposition with multiple search directions. *International Journal for Numerical Methods in Engineering*, 104:905–927. (Cité en page 63.)

[Gras et al., 2013] Gras, R., Leclerc, H., Roux, S., Otin, S., Schneider, J., and Périé, J.-N. (2013). Identification of the out-of-plane shear modulus of a 3d woven composite. *Experimental Mechanics*, 53(5):719–730. (Cité en page 89.)

[Groen et al., 2017] Groen, J. P., Langelaar, M., Sigmund, O., and Ruess, M. (2017). Higher-order multi-resolution topology optimization using the finite cell method. *International Journal for Numerical Methods in Engineering*, 110(10):903–920. (Cité en page 142.)

[Guguin et al., 2014] Guguin, G., Allix, O., Gosselet, P., and Guinard, S. (2014). Nonintrusive coupling of 3D and 2D laminated composite models based on finite element 3D recovery. *International Journal for Numerical Methods in Engineering*, 98(5):324–343. (Cité en pages 31, 33 et 39.)

[Guguin et al., 2016] Guguin, G., Allix, O., Gosselet, P., and Guinard, S. (2016). On the computation of plate assemblies using realistic 3d joint model: a non-intrusive approach. *Advanced Modeling and Simulation in Engineering Sciences*, 3(1):1–18. (Cité en pages 31 et 39.)

[Guinard et al., 2018] Guinard, S., Bouclier, R., Toniolli, M., and Passieux, J.-C. (2018). Multiscale analysis of complex aeronautical structures using robust non-intrusive coupling. *Advanced Modeling and Simulation in Engineering Sciences*, 5(1). (Cité en pages 3, 4, 29, 31, 38, 39, 41, 58 et 59.)

[Guo, 2017] Guo, Y. (2017). Global-local model coupling for composite shell structures in the framework of isogeometric analysis. *Composite Structures*, 176:617–629. (Cité en page 42.)

[Guo et al., 2018] Guo, Y., Heller, J., Hughes, T. J., Ruess, M., and Schillinger, D. (2018). Variationally consistent isogeometric analysis of trimmed thin shells at finite deformations, based on the step exchange format. *Computer Methods in Applied Mechanics and Engineering*, 336:39 – 79. (Cité en pages 62 et 77.)

[Guo and Ruess, 2015] Guo, Y. and Ruess, M. (2015). Nitsche's method for a coupling of isogeometric thin shells and blended shell structures. *Computer Methods in Applied Mechanics and Engineering*, 284:881 – 905. (Cité en pages 62 et 77.)

[Guo et al., 2017] Guo, Y., Ruess, M., and Schillinger, D. (2017). A parameter-free variational coupling approach for trimmed isogeometric thin shells. *Computational Mechanics*, 59(4):693–715. (Cité en page 62.)

[Gupta et al., 2012] Gupta, P., Pereira, J., Kim, D.-J., Duarte, C., and Eason, T. (2012). Analysis of three-dimensional fracture mechanics problems: A non-intrusive approach using a generalized finite element method. *Engineering Fracture Mechanics*, 90:41–64. (Cité en page 31.)

[Haftka and Grandhi, 1986] Haftka, R. and Grandhi, R. (1986). Structural shape optimization – a survey. *Computer Methods in Applied Mechanics and Engineering*, 57(1):91–106. (Cité en page 111.)

[Haftka and Gürdal, 1993] Haftka, R. and Gürdal, Z. (1993). *Elements of Structural Optimization*. Third revised and expanded ed., Kluwer Academic Publishers. (Cité en page 111.)

[Hansbo, 2005] Hansbo, P. (2005). Nitsche's method for interface problems in computational mechanics. *GAMM-Mitteilungen*, 28:183–206. (Cité en page 52.)

[Hartmann et al., 2016] Hartmann, S., Benson, D., and Nagy, A. (2016). Isogeometric analysis with LS-DYNA. In *Journal of Physics: Conference Series*, volume 734, page 032125. IOP Publishing. (Cité en page 19.)

[Hartmann et al., 2011] Hartmann, S., Benson, D. J., and Lorenz, D. (2011). About isogeometric analysis and the new NURBS-based finite elements in LS-DYNA. In *S. Hartmann, DJ Benson, D. Lorenz//8th European LSDYNA Users Conference, Strasbourg*, volume 10. (Cité en page 19.)

[Hasan Imam, 1982] Hasan Imam, M. (1982). Three-dimensional shape optimization. *International Journal for Numerical Methods in Engineering*, 18:661 – 673. (Cité en pages 112, 121 et 125.)

[Hennig et al., 2016] Hennig, P., Müller, S., and Kästner, M. (2016). Bézier extraction and adaptive refinement of truncated hierarchical NURBS. *Computer Methods in Applied Mechanics and Engineering*, 305:316–339. (Cité en pages 15 et 16.)

[Herrema et al., 2019] Herrema, A. J., Johnson, E. L., Proserpio, D. M., Wu, M. C. H., Kiendl, J., and Hsu, M.-C. (2019). Penalty coupling of non-matching isogeometric Kirchhoff-Love shell patches with application to composite wind turbine blades. *Computer Methods in Applied Mechanics and Engineering*, 346:810–840. (Cité en pages 62, 67 et 68.)

[Hesch and Betsch, 2012] Hesch, C. and Betsch, P. (2012). Isogeometric analysis and domain decomposition methods. *Computer Methods in Applied Mechanics and Engineering*, 213:104–112. (Cité en page 44.)

[Hild and Roux, 2006] Hild, F. and Roux, S. (2006). Measuring stress intensity factors with a camera: Integrated digital image correlation (I-DIC). *Comptes Rendus Mécanique*, 334(1):8–12. (Cité en page 85.)

[Hild and Roux, 2012] Hild, F. and Roux, S. (2012). Comparison of local and global approaches to digital image correlation. *Experimental Mechanics*, 52(9):1503–1519. (Cité en page 89.)

[Hirai et al., 1984] Hirai, I., Wang, B.-P., and Pilkey, W.-D. (1984). An efficient zooming method for finite element analysis. *International Journal for Numerical Methods in Engineering*, 20(9):1671–1683. (Cité en page 30.)

[Hirschler, 2019] Hirschler, T. (2016-2019). *IsoGeometric Modeling for the Optimal Design of Aerostructures*. PhD thesis, Université de Lyon. (Cité en pages 4, 5, 60, 67, 70, 72, 124, 127, 129, 132 et 136.)

[Hirschler et al., 2019a] Hirschler, T., Bouclier, R., Dureisseix, D., Duval, A., Elguedj, T., and Morlier, J. (2019a). A dual domain decomposition algorithm for the analysis of non-conforming isogeometric Kirchhoff-Love shells. *Computer Methods in Applied Mechanics and Engineering*, 357:112578. (Cité en pages 4, 44, 60, 62, 66, 70 et 132.)

[Hirschler et al., 2019b] Hirschler, T., Bouclier, R., Duval, A., Elguedj, T., and Morlier, J. (2019b). The embedded isogeometric Kirchhoff-Love shell: from design to shape optimization of non-conforming stiffened multipatch structures. *Computer Methods in Applied Mechanics and Engineering*, 349:774–797. (Cité en pages 4, 5, 44, 57, 60, 62, 124, 132 et 138.)

[Hirschler et al., 2019c] Hirschler, T., Bouclier, R., Duval, A., Elguedj, T., and Morlier, J. (2019c). Isogeometric sizing and shape optimization of thin structures with a solid-shell approach. *Structural and Multidisciplinary Optimization*, 59(3):767–785. (Cité en pages 5, 59, 64, 111, 113, 120, 123 et 124.)

[Hirschler et al., 2020] Hirschler, T., Bouclier, R., Duval, A., Elguedj, T., and Morlier, J. (2020). A new framework for analytical discrete sensitivity in the context of isogeometric shape optimization. *Structural and Multidisciplinary Optimization*, submitted. (Cité en pages 5, 127 et 136.)

[Hofer and Langer, 2017] Hofer, C. and Langer, U. (2017). Dual-primal isogeometric tearing and interconnecting solvers for multipatch dg-iga equations. *Computer Methods in Applied Mechanics and Engineering*, 316:2–21. (Cité en page 63.)

[Horn and Schunck, 1981] Horn, B. and Schunck, G. (1981). Determining optical flow. *Artificial Intelligence*, 17:185–203. (Cité en pages 83 et 108.)

[Hosseini et al., 2013] Hosseini, S., Remmers, J., Verhoosel, C., and Borst, R. (2013). An isogeometric solid-like shell element for nonlinear analysis. *International Journal for Numerical Methods in Engineering*, 95:238–256. (Cité en page 59.)

[Hubrich et al., 2017] Hubrich, S., Di Stolfo, P., Kudela, L., Kollmannsberger, S., Rank, E., Schröder, A., and Düster, A. (2017). Numerical integration of discontinuous functions: moment fitting and smart octree. *Computational Mechanics*, 60(5):863–881. (Cité en page 53.)

[Hubrich and Düster, 2019] Hubrich, S. and Düster, A. (2019). Numerical integration for nonlinear problems of the finite cell method using an adaptive scheme based on moment fitting. *Computers and Mathematics with Applications*, 77(7):1983–1997. (Cité en page 53.)

[Hughes et al., 2010] Hughes, T. J., Reali, A., and Sangalli, G. (2010). Efficient quadrature for NURBS-based isogeometric analysis. *Computer methods in applied mechanics and engineering*, 199(5-8):301–313. (Cité en page 23.)

[Hughes et al., 2005] Hughes, T. J. R., Cottrell, J., and Bazilevs, Y. (2005). Isogeometric analysis: CAD, finite elements, NURBS, exact geometry and mesh refinement. *Computer Methods in Applied Mechanics and Engineering*, 194:4135–4195. (Cité en pages 9, 11, 55 et 112.)

[Jara-Almonte and Knight, 1988] Jara-Almonte, C.-C. and Knight, C.-E. (1988). The specified boundary stiffness/force sbsf method for finite element subregion analysis. *International Journal for Numerical Methods in Engineering*, 26(7):1567–1578. (Cité en page 30.)

[Jiang et al., 2015] Jiang, W., Annavarapu, C., Dolbow, J., and Harari, I. (2015). A robust Nitsche's formulation for interface problems with spline-based finite elements. *International Journal for Numerical Methods in Engineering*, 104:676–696. (Cité en pages 44 et 51.)

[Jolivet et al., 2014] Jolivet, P., Hecht, F., Nataf, F., and Prud'Homme, C. (2014). Scalable domain decomposition preconditioners for heterogeneous elliptic problems. *Scientific Programming*, 22:157–171. (Cité en pages 63 et 78.)

[Jomo et al., 2019] Jomo, J., de Prenter, F., Elhaddad, M., d'angella, D., Verhoosel, C., Kollmannsberger, S., Kirschke, J., Nübel, V., Van Brummelen, H., and Rank, E. (2019). Robust and parallel scalable iterative solutions for large-scale finite cell analyses. *Finite Elements in Analysis and Design*, 163:14–30. (Cité en pages 58 et 145.)

[Jones et al., 01] Jones, E., Oliphant, T., Peterson, P., et al. (2001–). SciPy: Open source scientific tools for Python. (Cité en pages 83 et 126.)

[Jongerius and Lentink, 2010] Jongerius, S. R. and Lentink, D. (2010). Structural Analysis of a Dragonfly Wing. *Experimental Mechanics*, 50:1323–1334. (Cité en page 136.)

[Joulaian et al., 2016] Joulaian, M., Hubrich, S., and Düster, A. (2016). Numerical integration of discontinuities on arbitrary domains based on moment fitting. *Computational Mechanics*, 57(6):979–999. (Cité en page 53.)

[Jutte et al., 2014] Jutte, C. V., Stanford, B., Wieseman, C. D., and Moore, J. B. (2014). Aeroelastic Tailoring of the NASA Common Research Model via Novel Material and Structural Configurations. In *52nd Aerospace Sciences Meeting*, pages 1–20. (Cité en pages 136, 137, 138 et 142.)

[Kamensky and Bazilevs, 2019] Kamensky, D. and Bazilevs, Y. (2019). tIGAr: automating isogeometric analysis with FEniCS. *Computer Methods in Applied Mechanics and Engineering*, 344:477–498. (Cité en page 27.)

[Kamensky et al., 2017] Kamensky, D., Hsu, M.-C., Yu, Y., Evans, J. A., Sacks, M. S., and Hughes, T. J. (2017). Immersogeometric cardiovascular fluid–structure interaction analysis with divergence-conforming B-splines. *Computer methods in applied mechanics and engineering*, 314:408–472. (Cité en page 9.)

[Kamga and Pironneau, 2007] Kamga, J.-B.-A. and Pironneau, O. (2007). Numerical zoom for multiscale problems with an application to nuclear waste disposal. *Journal of Computational Physics*, 224:403–413. (Cité en page 38.)

[Kang and Youn, 2016] Kang, P. and Youn, S.-K. (2016). Isogeometric shape optimization of trimmed shell structures. *Structural and Multidisciplinary Optimization*, 53:825–845. (Cité en page 123.)

[Kegl and Brank, 2006] Kegl, M. and Brank, B. (2006). Shape optimization of truss-stiffened shell structures with variable thickness. *Computer Methods in Applied Mechanics and Engineering*, 195(19-22):2611–2634. (Cité en page 132.)

[Kelley, 1982] Kelley, F.-S. (1982). Mesh requirements for the analysis of a stress concentration by the specified boundary displacement method. In *Proceedings of the Second International Computers in Engineering Conference, ASME.* (Cité en page 30.)

[Kenway and Martins, 2014] Kenway, G. K. and Martins, J. R. (2014). Multipoint high-fidelity aerostructural optimization of a transport aircraft configuration. *Journal of Aircraft*, 51(1):144–160. (Cité en pages 122, 129, 141 et 142.)

[Kerfriden et al., 2012] Kerfriden, P., Passieux, J., and Bordas, S. (2012). Local/global model order reduction strategy for the simulation of quasi-brittle fracture. *International Journal for Numerical Methods in Engineering*, 89(2):154–179. (Cité en page 20.)

[Keye et al., 2017] Keye, S., Klimmek, T., Abu-Zurayk, M., Schulze, M., and Ilic, C. (2017). Aero-structural optimization of the NASA common research model. In *18th AIAA/ISSMO Multidisciplinary Analysis and Optimization Conference*, page 4145. (Cité en page 142.)

[Kiendl, 2011] Kiendl, J. (2011). *Isogeometric Analysis and Shape Optimal Design of Shell Structures*. PhD thesis, Technische Universitat Munchen, Lehrstuhl fur Statik. (Cité en page 64.)

[Kiendl et al., 2009] Kiendl, J., Bletzinger, K.-U., Linhard, J., and Wüchner, R. (2009). Isogeometric shell analysis with Kirchhoff–Love elements. *Computer Methods in Applied Mechanics and Engineering*, 198(49):3902 – 3914. (Cité en pages 9, 59, 62, 63 et 74.)

[Kiendl et al., 2015] Kiendl, J., Hsu, M.-C., Wu, M. C., and Reali, A. (2015). Isogeometric Kirchhoff–Love shell formulations for general hyperelastic materials. *Computer Methods in Applied Mechanics and Engineering*, 291:280 – 303. (Cité en pages 59 et 64.)

[Kiendl et al., 2014] Kiendl, J., Schmidt, R., Wüchner, R., and Bletzinger, K.-U. (2014). Isogeometric shape optimization of shells using semi-analytical sensitivity analysis and sensitivity weighting. *Computer Methods in Applied Mechanics and Engineering*, 274:148 – 167. (Cité en pages 9, 59, 111, 113, 120, 123, 125 et 126.)

[Kikis et al., 2019] Kikis, G., Dornisch, W., and Klinkel, S. (2019). Adjusted approximation spaces for the treatment of transverse shear locking in isogeometric reissner–mindlin shell analysis. *Computer Methods in Applied Mechanics and Engineering*, 354:850 – 870. (Cité en page 59.)

[Kirchner and Niemann, 1992] Kirchner, H. and Niemann, H. (1992). Finite element method for determination of optical flow. *Pattern Recognition Letters*, 13(2):131 – 141. (Cité en page 81.)

[Klawonn and Widlund, 2001] Klawonn, A. and Widlund, O. (2001). FETI and Neumann-Neumann iterative substructuring methods: Connections and new results. *Communications on Pure and Applied Mathematics*, 54(1):57–90. (Cité en page 72.)

[Kleinendorst et al., 2015] Kleinendorst, S., Hoefnagels, J., Verhoosel, V., and Ruybalid, A. (2015). On the use of adaptive refinement in isogeometric digital image correlation. *International Journal for Numerical Methods in Engineering*, page Online First. (Cité en pages 84 et 111.)

[Kleiss et al., 2012] Kleiss, S. K., Pechstein, C., Jüttler, B., and Tomar, S. (2012). IETI – isogeometric tearing and interconnecting. *Computer Methods in Applied Mechanics and Engineering*, 247-248:201 – 215. (Cité en page 63.)

[Kollmannsberger et al., 2015] Kollmannsberger, S., Özcan, A., Baiges, J., Ruess, M., Rank, E., and Reali, A. (2015). Parameter-free, weak imposition of Dirichlet boundary conditions and coupling of trimmed and non-conforming patches. *International Journal for Numerical Methods in Engineering*, 101:670–699. (Cité en page 51.)

[Kozubek et al., 2013] Kozubek, T., Vondrák, V., Menšík, M., Horák, D., Dostál, Z., Hapla, V., Kabelíková, P., and Čermák, M. (2013). Total FETI domain decomposition method and its massively parallel implementation. *Advances in Engineering Software*, 60-61:14–22. (Cité en page 71.)

[Kraft, 1988] Kraft, D. (1988). *A Software Package for Sequential Quadratic Programming*. Deutsche Forschungs- und Versuchsanstalt für Luft- und Raumfahrt Köln: Forschungsbericht. (Cité en page 126.)

[Kudela et al., 2015] Kudela, L., Zander, N., Bog, T., Kollmannsberger, S., and Rank, E. (2015). Efficient and accurate numerical quadrature for immersed boundary method. *Advanced Modeling and Simulation in Engineering Sciences*, 2:110. (Cité en pages 43 et 53.)

[Lacour, 1997] Lacour, C. (1994-1997). *Analyse et résolution numérique de méthodes de sous-domaines non conformes pour des problèmes de plaques.* PhD thesis, Université Pierre et Marie Curie - Paris VI. (Cité en page 72.)

[Ladeveze et al., 2001] Ladeveze, P., Arnaud, L., Rouch, P., and Blanzé, C. (2001). The variational theory of complex rays for the calculation of medium-frequency vibrations. *Engineering Computations*, 18:193–214. (Cité en page 51.)

[Lagarias et al., 1998] Lagarias, J. C., Reeds, J. A., Wright, M. H., and Wright, P. E. (1998). Convergence properties of the Nelder–Mead simplex method in low dimensions. *SIAM Journal on optimization*, 9(1):112–147. (Cité en page 138.)

[Lai et al., 2017] Lai, Y., Zhang, Y. J., Liu, L., Wei, X., Fang, E., and Lua, J. (2017). Integrating CAD with Abaqus: a practical isogeometric analysis software platform for industrial applications. *Computers & Mathematics with Applications*, 74(7):1648–1660. (Cité en page 19.)

[Lassila and Rozza, 2010] Lassila, T. and Rozza, G. (2010). Parametric free-form shape design with PDE models and reduced basis method. *Computer Methods in Applied Mechanics and Engineering*, 199(23-24):1583–1592. (Cité en pages 122 et 129.)

[Lavest et al., 1998] Lavest, J.-M., Viala, M., and Dhome, M. (1998). Do we really need an accurate calibration pattern to achieve a reliable camera calibration? In Burkhardt, H. and Neumann, B., editors, *Computer Vision — ECCV'98*, pages 158–174, Berlin, Heidelberg. Springer Berlin Heidelberg. (Cité en page 108.)

[Le Tallec et al., 1991] Le Tallec, P., De Roeck, Y.-H., and Vidrascu, M. (1991). Domain-decomposition methods for large linearly elliptic three dimensional problems. *Journal of Computational and Applied Mathematics*, 34:93–117. (Cité en page 62.)

[Leclerc et al., 2012] Leclerc, H., Périé, J.-N., Hild, F., and Roux, S. (2012). Digital volume correlation: What are the limits to the spatial resolution? *Mechanics & Industry*, 13(6):361–371. (Cité en pages 89, 92, 93 et 144.)

[Leclerc et al., 2009] Leclerc, H., Périé, J.-N., Roux, S., and Hild, F. (2009). Integrated digital image correlation for the identification of mechanical properties. *Lectures Notes in Computer Sciences*, 5496:161–171. (Cité en page 81.)

[Leclerc et al., 2011] Leclerc, H., Périé, J.-N., Roux, S., and Hild, F. (2011). Voxel-scale digital volume correlation. *Experimental Mechanics*, 51(4):479–490. (Cité en pages 89, 92 et 93.)

[Lee and Park, 2002] Lee, B.-G. and Park, Y. (2002). Degree elevation of nurbs curves by weighted blossom. *Korean Journal of Computational & Applied Mathematics*, 9(1):151–165. (Cité en pages 14 et 125.)

[Legrain, 2013] Legrain, G. (2013). A NURBS enhanced extended finite element approach for unfitted CAD analysis. *Computational Mechanics*, 52:913–929. (Cité en pages 43 et 53.)

[Lehoucq et al., 2015] Lehoucq, R. B., Turner, D. Z., and Garavito-Garz, C. A. (2015). PDE constrained optimization for Digital Image Correlation. *Sandia Report*, Sand2015-8515. (Cité en page 92.)

[Lei et al., 2018] Lei, Z., Gillot, F., and Jezequel, L. (2018). Shape Optimization for Natural Frequency with Isogeometric Kirchhoff-Love Shell and Sensitivity Mapping. *Mathematical Problems in Engineering*, 2018:1–11. (Cité en pages 123 et 126.)

[Leygue et al., 2018] Leygue, A., Coret, M., Réthoré, J., Stainier, L., and Verron, E. (2018). Data-based derivation of material response. *Computer Methods in Applied Mechanics and Engineering*, 331:184–196. (Cité en page 143.)

[Lian et al., 2017] Lian, H., Kerfriden, P., and Bordas, S. (2017). Shape optimization directly from CAD: An isogeometric boundary element approach using T-splines. *Computer Methods in Applied Mechanics and Engineering*, 317:1–41. (Cité en page 123.)

[Lian et al., 2013] Lian, W.-D., Legrain, G., and Cartraud, P. (2013). Image-based computational homogenization and localization: comparison between X-FEM/levelset and voxel-based approaches. *Computational Mechanics*, 51:279–293. (Cité en page 145.)

[Lipton et al., 2010] Lipton, S., Evans, J. A., Bazilevs, Y., Elguedj, T., and Hughes, T. J. (2010). Robustness of isogeometric structural discretizations under severe mesh distortion. *Computer Methods in Applied Mechanics and Engineering*, 199(5-8):357–373. (Cité en page 9.)

[Liu et al., 2019] Liu, X., Réthoré, J., Baietto, M.-C., Sainsot, P., and Lubrecht, A. A. (2019). An efficient strategy for large scale 3d simulation of heterogeneous materials to predict effective thermal conductivity. *Computational Materials Science*, 166:265 – 275. (Cité en pages 102, 144 et 145.)

[Liu et al., 2014] Liu, Y. J., Sun, Q., and Fan, X. L. (2014). A non-intrusive global/local algorithm with non-matching interface: Derivation and numerical validation. *Computer Methods in Applied Mechanics and Engineering*, 277:81–103. (Cité en pages 37 et 38.)

[Locatelli et al., 2014] Locatelli, D., Mulani, S. B., and Kapania, R. K. (2014). Parameterization of Curvilinear Spars and Ribs for Optimum Wing Structural Design. *Journal of Aircraft*, 51(2):532–546. (Cité en pages 124, 136, 137, 138 et 142.)

[Lucas and Kanade, 1981] Lucas, B. and Kanade, T. (1981). An iterative image registration technique with an application to stereo vision. In *Proceedings of Imaging Understanding Workshop*, pages 121–130. (Cité en pages 81 et 107.)

[Lund and Stegmann, 2006] Lund, E. and Stegmann, J. (2006). Eigenfrequency and buckling optimization of laminated composite shell structures using discrete material optimization. In *IUTAM Symposium on Topological Design Optimization of Structures, Machines and Materials*, pages 147–156. Springer. (Cité en page 142.)

[Mandel, 1993] Mandel, J. (1993). Balancing domain decomposition. *Communications in Numerical Methods in Engineering*, 9:233–241. (Cité en page 62.)

[Maquart, 2019] Maquart, T. (2016-2019). *Trivariate Models Generation From Unstructured Surface Manifolds For Isogeometric Analysis - Application To Reduced Order Modeling With Geometric Parameters*. PhD thesis, Université de Lyon. (Cité en page 61.)

[Martins and Lambe, 2013] Martins, J. R. and Lambe, A. B. (2013). Multidisciplinary design optimization: a survey of architectures. *AIAA journal*, 51(9):2049–2075. (Cité en page 142.)

[Marussig and Hughes, 2018] Marussig, B. and Hughes, T.-J.-R. (2018). A review of trimming in isogeometric analysis: Challenges, data exchange and simulation aspects. *Archives of Computational Methods in Engineering*, 25:1059–1127. (Cité en page 16.)

[Massarwi et al., 2019] Massarwi, F., Antolin, P., and Elber, G. (2019). Volumetric untrimming: Precise decomposition of trimmed trivariates into tensor products. *Computer Aided Geometric Design*, 71:1–15. (Cité en pages 16 et 43.)

[Massarwi et al., 2018] Massarwi, F., Machchhar, J., Antolin, P., and Elber, G. (2018). Hierarchical, random and bifurcation tiling with heterogeneity in micro-structures construction via functional composition. *Computer-Aided Design*, 102:148–159. (Cité en page 142.)

[Mathieu et al., 2015] Mathieu, F., Leclerc, H., Hild, H., and Roux, S. (2015). Estimation of elastoplastic parameters via weighted FEMU and intergrated DIC. *Experimental Mechanics*, 55(1):105–119. (Cité en pages 25 et 81.)

[Maurin et al., 2018] Maurin, F., Greco, F., Coox, L., Vandepitte, D., and Desmet, W. (2018). Isogeometric collocation for Kirchhoff–Love plates and shells. *Computer Methods in Applied Mechanics and Engineering*, 329:396 – 420. (Cité en page 59.)

[Merta et al., 2014] Merta, M., Vašatová, A., Hapla, V., and Horák, D. (2014). Parallel implementation of total-FETI DDM with application to medical image registration. In Erhel, J., Gander, M. J., Halpern, L., Pichot, G., Sassi, T., and Widlund, O., editors, *Domain Decomposition Methods in Science and Engineering XXI*, pages 917–925. Springer International Publishing. (Cité en pages 91 et 102.)

[Molimard et al., 2005] Molimard, J., Riche, R., Vautrin, A., and Lee, J. (2005). Identification of the four orthotropic plate stiffnesses using a single open-hole tensile test. *Experimental Mechanics*, 45(5):404–411. (Cité en pages 81 et 143.)

[Morganti et al., 2015] Morganti, S., Auricchio, F., Benson, D., Gambarin, F., Hartmann, S., Hughes, T., and Reali, A. (2015). Patient-specific isogeometric structural analysis of aortic valve closure. *Computer Methods in Applied Mechanics and Engineering*, 284:508–520. (Cité en page 9.)

[Morgeneyer et al., 2013] Morgeneyer, T., Helfen, L., Mubarak, H., and Hild, F. (2013). 3D digital volume correlation of synchrotron radiation laminography images of ductile crack initiation: An initial feasibility study. *Experimental Mechanics*, 53(4):543–556. (Cité en page 92.)

[Moës et al., 1999] Moës, N., Dolbow, J., and Belytschko, T. (1999). A finite element method for crack growth without remeshing. *International Journal for Numerical Methods in Engineering*, 46:131–150. (Cité en page 53.)

[Mulani et al., 2013] Mulani, S., Slemp, W., and Kapania, R. (2013). Ebf3panelopt: An optimization framework for curvilinear blade-stiffened panels. *Thin-Walled Structures*, 63:13–26. (Cité en pages 57, 124 et 138.)

[Müller et al., 2013] Müller, B., Kummer, F., and Oberlack, M. (2013). Highly accurate surface and volume integration on implicit domains by means of moment-fitting. *International Journal for Numerical Methods in Engineering*, 96:512–528. (Cité en page 53.)

[Nagy, 2011] Nagy, A.-P. (2011). *Isogeometric design optimisation*. PhD thesis, Aerospace Engineering, Delft University of Technology. (Cité en page 142.)

[Nagy et al., 2010] Nagy, A. P., Abdalla, M. M., and Gürdal, Z. (2010). Isogeometric sizing and shape optimisation of beam structures. *Computer Methods in Applied Mechanics and Engineering*, 199(17-20):1216–1230. (Cité en page 123.)

[Nagy et al., 2011] Nagy, A. P., Abdalla, M. M., and Gürdal, Z. (2011). Isogeometric design of elastic arches for maximum fundamental frequency. *Structural and Multidisciplinary Optimization*, 43(1):135–149. (Cité en pages 113 et 123.)

[Nagy and Benson, 2015] Nagy, A.-P. and Benson, D.-J. (2015). On the numerical integration of trimmed isogeometric elements. *Computer Methods in Applied Mechanics and Engineering*, 284:165–185. (Cité en pages 43 et 53.)

[Nagy et al., 2013] Nagy, A. P., IJsselmuiden, S. T., and Abdalla, M. M. (2013). Isogeometric design of anisotropic shells: Optimal form and material distribution. *Computer Methods in Applied Mechanics and Engineering*, 264:145 – 162. (Cité en pages 9, 59, 113, 123 et 126.)

[Naylor, 2019] Naylor, R. (2016-2019). *Prédiction des premiers endommagements des composites tissés par modélisation à l'échelle microscopique et validation multi-échelle*. PhD thesis, Université Paris–Saclay. (Cité en page 144.)

[Neggers et al., 2018a] Neggers, J., Allix, O., Hild, F., and Roux, S. (2018a). Big data in experimental mechanics and model order reduction: Today's challenges and tomorrow's opportunities. *Archives of Computational Methods in Engineering*, 25(1):143–164. (Cité en page 89.)

[Neggers et al., 2018b] Neggers, J., Allix, O., Hild, F., and Roux, S. (2018b). Big data in experimental mechanics and model order reduction: today's challenges and tomorrow's opportunities. *Archives of Computational Methods in Engineering*, 25:143–164. (Cité en page 143.)

[Neggers et al., 2016] Neggers, J., Blaysat, B., Hoefnagels, J. P. M., and Geers, M. G. D. (2016). On image gradients in digital image correlation. *International Journal for Numerical Methods in Engineering*, 105:243–260. (Cité en pages 89, 90 et 91.)

[Neggers et al., 2019] Neggers, J., Mathieu, F., Hild, F., and Roux, S. (2019). Simultaneous full-field multi-experiment identification. *Mechanics of Materials*, 133:71–84. (Cité en page 143.)

[Neggers et al., 2017] Neggers, J., Mathieu, F., Hild, F., Roux, S., and Swiergiel, N. (2017). Improving full-field identification using progressive model enrichments. *International Journal of Solids and Structures*, 118-119:213 – 223. (Cité en page 83.)

[Nguyen et al., 2015] Nguyen, V. P., Anitescu, C., Bordas, S. P., and Rabczuk, T. (2015). Isogeometric analysis: an overview and computer implementation aspects. *Mathematics and Computers in Simulation*, 117:89–116. (Cité en page 23.)

[Nguyen et al., 2014] Nguyen, V.-P., Kerfriden, P., Brino, M., Bordas, S.-P.-A., and Bonisoli, E. (2014). Nitsche's method for two and three dimensional nurbs patch coupling. *Computational Mechanics*, 53:1163–1182. (Cité en pages 42, 44, 51 et 53.)

[Nguyen-Thanh et al., 2017] Nguyen-Thanh, N., Zhou, K., Zhuang, X., Areias, P., Nguyen-Xuan, H., Bazilevs, Y., and Rabczuk, T. (2017). Isogeometric analysis of large-deformation thin shells using RHT-splines for multiple-patch coupling. *Computer Methods in Applied Mechanics and Engineering*, 316:1157 – 1178. (Cité en page 62.)

[Nocedal and Wright, 2006] Nocedal, J. and Wright, S. J. (2006). *Numerical Optimization*. Springer, New York, NY, USA, second edition. (Cité en pages 82, 85 et 126.)

[Nouy and Pled, 2018] Nouy, A. and Pled, F. (2018). A multiscale method for semi-linear elliptic equations with localized uncertainties and non-linearities. *ESAIM: Mathematical Modelling and Numerical Analysis*, 52(5):1763–1802. (Cité en pages 31 et 37.)

[Néron et al., 2015] Néron, D., Boucard, P., and Relun, N. (2015). Time-space PGD for the rapid solution of 3D nonlinear parametrized problems in the many-query context. *International Journal for Numerical Methods in Engineering*, 103:275–292. (Cité en page 43.)

[Occelli et al., 2019] Occelli, M., Elguedj, T., Bouabdallah, S., and Morançay, L. (2019). LR B-splines implementation in the Altair RadiossTM solver for explicit dynamics isogeometric analysis. *Advances in Engineering Software*, 131:166–185. (Cité en pages 15 et 19.)

[Oden et al., 1998] Oden, J. T., Babuska, I., and Baumann, C. E. (1998). A discontinuous hp finite element method for diffusion problems. *Journal of Computational Physics*, 146:491–519. (Cité en page 51.)

[Oden and Zohdi, 1997] Oden, J.-T. and Zohdi, T.-I. (1997). Analysis and adaptive modeling of highly heterogeneous elastic structures. *Computer Methods in Applied Mechanics and Engineering*, 148(3):367–391. (Cité en page 32.)

[Olhoff et al., 1991] Olhoff, N., Bendsøe, M., and Rasmussen, J. (1991). On CAD-integrated structural topology and design optimization. *Computer Methods in Applied Mechanics and Engineering*, 89:259–279. (Cité en page 112.)

[Oumaziz et al., 2018] Oumaziz, P., Gosselet, P., Boucard, P.-A., and Abbas, M. (2018). A parallel non-invasive multiscale strategy for a mixed domain decomposition method with frictional contact. *International Journal for Numerical Methods in Engineering*, 115(8):893–912. (Cité en pages 31, 58 et 145.)

[Pan et al., 2013] Pan, B., Li, K., and Tong, W. (2013). Fast, robust and accurate digital image correlation calculation without redundant computations. *Experimental Mechanics*, 53(7):1277–1289. (Cité en page 90.)

[Pan et al., 2014] Pan, B., Wang, B., Wu, D., and Lubineau, G. (2014). An efficient and accurate 3d displacements tracking strategy for digital volume correlation. *Optics and Lasers in Engineering*, 58:126 – 135. (Cité en page 90.)

[Parvizian et al., 2012] Parvizian, J., Düster, A., and Rank, E. (2012). Topology optimization using the finite cell method. *Optimization and Engineering*, 13(1):57–78. (Cité en page 142.)

[Passieux and Bouclier, 2019] Passieux, J.-C. and Bouclier, R. (2019). Classic and Inverse Compositional Gauss-Newton in Global DIC. *International Journal for Numerical Methods in Engineering*, 119:453–468. (Cité en pages 4, 82, 89, 90 et 91.)

[Passieux et al., 2018] Passieux, J.-C., Bouclier, R., and Périé, J.-N. (2018). A space-time PGD-DIC algorithm: Application to 3D mode shapes measurements. *Experimental Mechanics*, 58(7):1195–1206. (Cité en pages 4, 89, 104 et 143.)

[Passieux et al., 2015a] Passieux, J.-C., Bugarin, F., David, C., Périé, J.-N., and Robert, L. (2015a). Multiscale displacement field measurement using digital image correlation: Application to the identification of elastic properties. *Experimental Mechanics*, 55(1):121–137. (Cité en pages 58, 81, 92, 104 et 143.)

[Passieux and Périé, 2012] Passieux, J.-C. and Périé, J.-N. (2012). High resolution digital image correlation using Proper Generalized Decomposition: PGD-DIC. *International Journal for Numerical Methods in Engineering*, 92(6):531–550. (Cité en pages 89, 92 et 94.)

[Passieux et al., 2015b] Passieux, J.-C., Périé, J.-N., and Salaün, M. (2015b). A dual domain decomposition method for finite element digital image correlation. *International Journal for Numerical Methods in Engineering*, 102(10):1670–1682. (Cité en pages 89, 91, 94, 95, 96, 101 et 103.)

[Passieux et al., 2013] Passieux, J.-C., Réthoré, J., Gravouil, A., and Baietto, M.-C. (2013). Local/global non-intrusive crack propagation simulation using a multigrid X-FEM solver. *Computational Mechanics*, 56(2):1381–1393. (Cité en pages 31, 33, 38, 48, 49 et 58.)

[Périé et al., 2009] Périé, J.-N., Leclerc, H., Roux, S., and Hild, F. (2009). Digital image correlation and biaxial test on composite material for anisotropic damage law identification. *International Journal of Solids and Structures*, 46(11–12):2388–2396. (Cité en pages 81 et 143.)

[Piegl and Tiller, 1997] Piegl, L. and Tiller, W. (1997). *The NURBS book*. 2Nd. Springer, New york. (Cité en pages 9, 11, 14, 112, 118 et 125.)

[Pierré et al., 2017] Pierré, J.-E., Passieux, J.-C., and Périé, J.-N. (2017). Finite element stereo digital image correlation: framework and mechanical regularization. *Experimental Mechanics*, 53(7):443–456. (Cité en pages 84, 85, 94, 107, 109, 110 et 111.)

[Pierré et al., 2016] Pierré, J.-E., Passieux, J.-C., Périé, J.-N., Bugarin, F., and Robert, L. (2016). Unstructured finite element-based digital image correlation with enhanced management of quadrature and lens distortions. *Optics and Lasers in Engineering*, 77:44–53. (Cité en page 84.)

[Qian, 2010] Qian, X. (2010). Full analytical sensitivities in NURBS based isogeometric shape optimization. *Computer Methods in Applied Mechanics and Engineering*, 199:2059–2071. (Cité en pages 113, 123, 125 et 126.)

[Quarteroni et al., 2015] Quarteroni, A., Manzoni, A., and Negri, F. (2015). *Reduced basis methods for partial differential equations: an introduction*, volume 92. Springer. (Cité en page 20.)

[Rabier, 2005] Rabier, F. (2005). Overview of global data assimilation developments in numerical weather-prediction centres. *Quarterly Journal of the Royal Meteorological Society*, 131:3215 – 3233. (Cité en page 102.)

[Rank, 1992] Rank, E. (1992). Adaptive remeshing and h–p domain decomposition. *Computer Methods in Applied Mechanics and Engineering*, 101:299–313. (Cité en page 38.)

[Rannou et al., 2010] Rannou, J., Limodin, N., Réthoré, J., Gravouil, A., Ludwig, W., Baietto-Dubourg, M.-C., Buffiére, J.-Y., Combescure, A., Hild, F., and Roux, S. (2010). Three dimensional experimental and numerical multiscale analysis of a fatigue crack. *Computer Methods in Applied Mechanics and Engineering*, 199:1307–1325. (Cité en page 81.)

[Renard, 2018] Renard, M. (2018). STELIA Aerospace imprime en 3D un panneau de fuselage. (Cité en page 3.)

[Requena et al., 2009] Requena, G., Fiedler, G., Seiser, B., Degischer, P., Michiel, M. D., and Buslaps, T. (2009). 3D-quantification of the distribution of continuous fibres in unidirectionally reinforced composites. *Composites Part A: Applied Science and Manufacturing*, 40(2):152–163. (Cité en page 92.)

[Réthoré, 2010] Réthoré, J. (2010). A fully integrated noise robust strategy for the identification of constitutive laws from digital images. *Int. J. Numer. Meth. Eng.*, 84(6):631–660. (Cité en pages 81, 89, 92 et 144.)

[Réthoré et al., 2010a] Réthoré, J., Elguedj, T., Simon, P., and Coret, M. (2010a). On the use of NURBS functions for displacement derivatives measurement by digital image correlation. *Experimental Mechanics*, 50:1099–1116. (Cité en pages 9, 84 et 111.)

[Réthoré et al., 2008] Réthoré, J., Hild, F., and Roux, S. (2008). Extended digital image correlation with crack shape optimization. *Int. J. Num. Meth. Eng.*, 73(2):248–272. (Cité en page 83.)

[Réthoré et al., 2013] Réthoré, J., Muhibullah, Elguedj, T., Coret, M., Chaudet, P., and Combescure, A. (2013). Robust identification of elasto-plastic constitutive law parameters from digital image using 3D kinematics. *Int. J. Solids and Structures*, 50:73–85. (Cité en pages 81, 89, 92, 107, 143 et 144.)

[Réthoré et al., 2009] Réthoré, J., Roux, S., and Hild, F. (2009). An extended and integrated digital image correlation technique applied to the analysis of fractured samples. *Eur J. Comput Mech*, 18:285–306. (Cité en pages 92 et 93.)

[Réthoré et al., 2010b] Réthoré, J., Roux, S., and Hild, F. (2010b). Hybrid analytical and extended finite element method (HAX-FEM): A new enrichment procedure for cracked solids. *International Journal for Numerical Methods in Engineering*, 81(3):269–285. (Cité en page 48.)

[Riviere, 2008] Riviere, B. (2008). *Discontinuous Galerkin Methods For Solving Elliptic And Parabolic Equations: Theory and Implementation*. Society for Industrial and Applied Mathematics, Philadelphia, PA, USA. (Cité en page 51.)

[Rivière et al., 2001] Rivière, B., Wheeler, M. F., and Girault, V. (2001). A priori error estimates for finite element methods based on discontinuous approximation spaces for elliptic problems. *SIAM J. Numerical Analysis*, 39:902–931. (Cité en page 51.)

[Rixen, 2002] Rixen, D. J. (2002). Extended preconditioners for the FETI method applied to constrained problems. *International Journal for Numerical Methods in Engineering*, 54(1):1–26. (Cité en page 72.)

[Rixen and Farhat, 1999] Rixen, D. J. and Farhat, C. (1999). A simple and efficient extension of a class of substructure based preconditioners to heterogeneous structural mechanics problems. *International Journal for Numerical Methods in Engineering*, 44(4):489–516. (Cité en page 72.)

[Rixen et al., 1999] Rixen, D. J., Farhat, C., Tezaur, R., and Mandel, J. (1999). Theoretical comparison of the FETI and algebraically partitioned FETI methods, and performance comparisons with a direct sparse solver. *International Journal for Numerical Methods in Engineering*, 46(4):501–533. (Cité en pages 70 et 78.)

[Rogers, 2000] Rogers, D. F. (2000). *An introduction to NURBS: with historical perspective*. Elsevier. (Cité en pages 9 et 11.)

[Ronovsky and Vasatova, 2017] Ronovsky, A. and Vasatova, A. (2017). Elastic image registration based on domain decomposition with mesh adaptation. *Mathematical Analysis and Numerical Mathematics*, 15(2):322–330. (Cité en pages 91 et 102.)

[Rouwane, 2021] Rouwane, A. (2018-2021). *Propriétés mécaniques à partir de corrélation d'images volumiques éléments finis*. PhD thesis, Université de Toulouse. (Cité en pages 4, 104 et 144.)

[Rouwane et al., 2020] Rouwane, A., Bouclier, R., Passieux, J.-C., and Périé, J.-N. (2020). Microstructure-Driven DIC: A fairly-priced image-based mechanical model for the regularization of digitial image correlation. *In preparation*. (Cité en pages 4 et 104.)

[Roux and Hild, 2018] Roux, S. and Hild, F. (2018). Optimal procedure for the identification of constitutive parameters from experimentally measured displacement fields. *International Journal of Solids and Structures*, 184:14–23. (Cité en page 143.)

[Ruess et al., 2014] Ruess, M., Schillinger, D., Özcan, A.-I., and Rank, E. (2014). Weak coupling for isogeometric analysis of non-matching and trimmed multi-patch geometries. *Computer Methods in Applied Mechanics and Engineering*, 169:46–71. (Cité en pages 43, 44, 51 et 53.)

[Réthoré, 2015] Réthoré, J. (2015). Automatic crack tip detection and stress intensity factors estimation of curved cracks from digital images. *International Journal for Numerical Methods in Engineering*. (Cité en pages 58, 92 et 104.)

[Saad, 2009] Saad, M.-H. (2009). *Elasticity, Theory, Applications, and Numerics*. Academic Press, Oxford. (Cité en page 55.)

[Saad and Schultz, 1986] Saad, Y. and Schultz, M. H. (1986). GMRES: A generalized minimal residual algorithm for solving nonsymmetric linear systems. *SIAM Journal on Scientific and Statistical Computing*, 7(3):856–869. (Cité en page 98.)

[Sanders et al., 2012] Sanders, J., Laursen, T., and Puso, M. (2012). A nitsche embedded mesh method. *Computational Mechanics*, 49:243–257. (Cité en page 52.)

[Schillinger et al., 2016a] Schillinger, D., Harari, I., Hsu, M.-C., Kamensky, D., Stoter, K.-F.-S., Yu, Y., and Ying, Z. (2016a). The non-symmetric Nitsche method for the parameter-free imposition of weak boundary and coupling conditions in immersed finite elements. *Computer Methods in Applied Mechanics and Engineering*, 309:625–652. (Cité en pages 44, 51 et 53.)

[Schillinger et al., 2014] Schillinger, D., Hossain, S. J., and Hughes, T. J. (2014). Reduced Bézier element quadrature rules for quadratic and cubic splines in isogeometric analysis. *Computer Methods in Applied Mechanics and Engineering*, 277:1–45. (Cité en page 23.)

[Schillinger and Ruess, 2015] Schillinger, D. and Ruess, M. (2015). The finite cell method: A review in the context of higher-order structural analysis of CAD and image-based geometric models. *Archives of Computational Methods in Engineering*, 22(3):391–455. (Cité en pages 43, 44, 53, 55, 56, 131 et 145.)

[Schillinger et al., 2016b] Schillinger, D., Ruthala, P. K., and Nguyen, L. H. (2016b). Lagrange extraction and projection for NURBS basis functions: A direct link between isogeometric and standard nodal finite element formulations. *International Journal for Numerical Methods in Engineering*, 108(6):515–534. (Cité en pages 10, 17, 18, 19 et 26.)

[Schöllhammer and Fries, 2019] Schöllhammer, D. and Fries, T. P. (2019). Kirchhoff–Love shell theory based on tangential differential calculus. *Computational Mechanics*, 64(1):113–131. (Cité en page 77.)

[Schuß et al., 2019] Schuß, S., Dittmann, M., Wohlmuth, B., Klinkel, S., and Hesch, C. (2019). Multi-patch isogeometric analysis for Kirchhoff-Love shell elements. *Computer Methods in Applied Mechanics and Engineering*, 349:91–116. (Cité en pages 45, 62 et 65.)

[Scott et al., 2012] Scott, M., Li, X., Sederberg, T., and Hughes, T.-J.-R. (2012). Local refinement of analysis-suitable T-splines. *Computer Methods in Applied Mechanics and Engineering*, s 213–216:206–222. (Cité en page 15.)

[Scott et al., 2014] Scott, M., Thomas, D., and Evans, E.-J. (2014). Isogeometric spline forests. *Computer Methods in Applied Mechanics and Engineering*, 269:222–264. (Cité en page 15.)

[Scott et al., 2011] Scott, M. A., Borden, M. J., Verhoosel, C. V., Sederberg, T. W., and Hughes, T. J. (2011). Isogeometric finite element data structures based on Bézier extraction of T-splines. *International Journal for Numerical Methods in Engineering*, 88(2):126–156. (Cité en pages 16 et 27.)

[Sederberg and Parry, 1986] Sederberg, T. W. and Parry, S. R. (1986). Free-form deformation of solid geometric models. *ACM SIGGRAPH computer graphics*, 20(4):151–160. (Cité en pages 122, 124 et 141.)

[Seitz et al., 2016] Seitz, A., Farah, P., Kremheller, J., Wohlmuth, B. I., Wall, W. A., and Popp, A. (2016). Isogeometric dual mortar methods for computational contact mechanics. *Computer Methods in Applied Mechanics and Engineering*, 301:259–280. (Cité en page 9.)

[Seo et al., 2010] Seo, Y.-D., Kim, H.-J., and Youn, S.-K. (2010). Isogeometric topology optimization using trimmed spline surfaces. *Computer Methods in Applied Mechanics and Engineering*, 199(49-52):3270–3296. (Cité en page 142.)

[Serra et al., 2017a] Serra, J., Pierré, J.-E., Passieux, J.-C., Périé, J.-N., Bouvet, C., and Castanié, B. (2017a). Validation and modeling of aeronautical composite structures subjected to combined loadings: the VERTEX project. Part 1: Experimental setup, FE-DIC instrumentation and procedures. *Composite Structures*, 179:224–244. (Cité en pages 84 et 107.)

[Serra et al., 2017b] Serra, J., Pierré, J.-E., Passieux, J.-C., Périé, J.-N., Bouvet, C., Castanié, B., and Petiot, C. (2017b). Validation and modeling of aeronautical composite structures subjected to combined loadings: the VERTEX project. Part 2: Load envelopes for the assessment of panels with large notches. *Composite Structures*, 180:550–567. (Cité en page 107.)

[Sevilla et al., 2008] Sevilla, R., Fernandez Mendez, S., and Huerta, A. (2008). NURBS enhanced finite element method (NEFEM). *International Journal for Numerical Methods in Engineering*, 76:56–83. (Cité en page 53.)

[Shojaee et al., 2012] Shojaee, S., Izadpanah, E., Valizadeh, N., and Kiendl, J. (2012). Free vibration analysis of thin plates by using a nurbs-based isogeometric approach. *Finite Elements in Analysis and Design*, 61:23–34. (Cité en page 9.)

[Shroff et al., 2017] Shroff, S., Acar, E., and Kassapoglou, C. (2017). Design, analysis, fabrication, and testing of composite grid-stiffened panels for aircraft structures. *Thin-Walled Structures*, 119:235 – 246. (Cité en page 59.)

[Sigmund, 2001] Sigmund, O. (2001). A 99 line topology optimization code written in Matlab. *Structural and multidisciplinary optimization*, 21:120–127. (Cité en page 144.)

[Singh et al., 2017] Singh, K., Zhao, W., and Kapania, R. K. (2017). An Optimization Framework for Curvilinearly Stiffened Composite Pressure Vessels and Pipes. In *Volume 3A: Design and Analysis*, volume 3A-2017, page V03AT03A066. ASME. (Cité en page 124.)

[Sommerwerk et al., 2017] Sommerwerk, K., Woidt, M., Haupt, M.-C., and Horst, P. (2017). Reissner–Mindlin shell implementation and energy conserving isogeometric multi-patch coupling. *International Journal for Numerical Methods in Engineering*, 109:982–1012. (Cité en page 62.)

[Spillane et al., 2013] Spillane, N., Dolean, V., Hauret, P., Nataf, F., and Rixen, D. J. (2013). Solving generalized eigenvalue problems on the interfaces to build a robust two-level FETI method. *Comptes Rendus Mathematique*, 351(5-6):197–201. (Cité en page 78.)

[Spillane and Rixen, 2013] Spillane, N. and Rixen, D. (2013). Automatic spectral coarse spaces for robust finite element tearing and interconnecting and balanced domain decomposition algorithms. *International Journal for Numerical Methods in Engineering*, 95(11):953–990. (Cité en page 78.)

[Srinivasan et al., 1996] Srinivasan, S., Biggers, S.-B., and Latour, R.-A. (1996). Identifying global/local interface boundaries using an objective search method. *International Journal for Numerical Methods in Engineering*, 39:805–828. (Cité en page 30.)

[Stanford et al., 2014] Stanford, B., Beran, P., and Bhatia, M. (2014). Aeroelastic topology optimization of blade-stiffened panels. *Journal of Aircraft*, 51(3):938–944. (Cité en page 142.)

[Stanier et al., 2016] Stanier, S., Blaber, J., Take, W., and White, D. (2016). Improved image-based deformation measurement for geotechnical applications. *Canadian Geotechnical Journal*, 53(5):727–739. (Cité en page 90.)

[Stavrev et al., 2016] Stavrev, A., Nguyen, L.-H., Shen, R., Varduhn, V., Behr, M., Elgeti, S., and Schillinger, D. (2016). Geometrically accurate, efficient, and flexible quadrature techniques for the tetrahedral finite cell method. *Computer Methods in Applied Mechanics and Engineering*, 310:646–673. (Cité en pages 43 et 53.)

[Stavroulakis et al., 2018] Stavroulakis, G., Tsapetis, D., and Papadrakakis, M. (2018). Non-overlapping domain decomposition solution schemes for structural mechanics isogeometric analysis. *Computer Methods in Applied Mechanics and Engineering*, 341:695 – 717. (Cité en page 63.)

[Stefanica, 2001] Stefanica, D. (2001). A numerical study of FETI algorithms for mortar finite element methods. *SIAM Journal on Scientific Computing*, 23(4):1135–1160. (Cité en pages 62 et 72.)

[Stefanica, 2005] Stefanica, D. (2005). Parallel FETI algorithms for mortars. *Applied Numerical Mathematics*, 54(2):266 – 279. (Cité en pages 62, 70 et 72.)

[Steger, 1991] Steger, J. (1991). The chimera method of flow simulation. In *Workshop on applied CFD, Univ of Tennessee Space Institute*. (Cité en page 38.)

[Steger et al., 1983] Steger, J., Dougherty, F., and J.A., B. (1983). A chimera grid scheme, advances in grid generation. In *ASME FED 5*. (Cité en page 38.)

[Sun et al., 2005] Sun, Y., Pang, J., Wong, C. K., and Su, F. (2005). Finite element formulation for a digital image correlation method. *Applied Optics*, 44(34):7357–7363. (Cité en page 81.)

[Sutton et al., 2009] Sutton, M., Orteu, J.-J., and Schreier, H. (2009). *Image correlation for shape, motion and deformation measurements: Basic Concepts, Theory and Applications*. Springer, New York, NY (USA). (Cité en pages 81 et 94.)

[Sutton et al., 1983] Sutton, M., Wolters, W., Peters, W., Ranson, W., and McNeill, S. (1983). Determination of displacements using an improved digital correlation method. *Image and Vision Computing*, 1(3):133–139. (Cité en page 81.)

[Sutton et al., 1999] Sutton, M. A., Zhao, W., McNeill, S. R., Helm, J. D., Piascik, R. S., and Riddel, W. T. (1999). Local crack closure measurements: Development of a measurement system using computer vision and a far-field microscope. In *Advances in fatigue crack closure measurement and analysis: second volume, STP 1343 , R. C. McClung and J. C. Newman Jr., eds.*, pages 145–156. (Cité en page 108.)

[Sánchez, 2016] Sánchez, J. (2016). The Inverse Compositional Algorithm for Parametric Registration. *Image Processing On Line*, 6:212–232. (Cité en page 90.)

[Taheri and Hassani, 2014] Taheri, A. and Hassani, B. (2014). Simultaneous isogeometrical shape and material design of functionally graded structures for optimal eigenfrequencies. *Computer Methods in Applied Mechanics and Engineering*, 277:46 – 80. (Cité en pages 123, 125 et 126.)

[Tarantola, 2014] Tarantola, A. (2014). *Inverse Problem Theory and Methods for Model Parameter Estimation*. SIAM. (Cité en page 92.)

[Teschemacher et al., 2018] Teschemacher, T., Bauer, A. M., Oberbichler, T., Breitenberger, M., Rossi, R., Wüchner, R., and Bletzinger, K.-U. (2018). Realization of cad-integrated shell simulation based on isogeometric b-rep analysis. *Advanced Modeling and Simulation in Engineering Sciences*, 5(1):19. (Cité en page 16.)

[Thomas et al., 2018] Thomas, D., Engvall, L., Schmidt, S., Tew, K., and Scott, M. (2018). U-splines: Splines over unstructured meshes. *Preprint, https://coreform.com/usplines*. (Cité en page 15.)

[Tirvaudey, 2019] Tirvaudey, M. (2016-2019). *Couplage AIG/MEF pour l'analyse de détails structuraux par une approche non-intrusive et certifiée*. PhD thesis, Université de Toulouse. (Cité en pages 3, 4, 10, 32, 42, 43, 44 et 45.)

[Tirvaudey et al., 2019a] Tirvaudey, M., Bouclier, R., Passieux, J.-C., and Chamoin, L. (2019a). Non-invasive implementation of nonlinear Isogeometric Analysis in an industrial FE software. *Engineering Computations*, 37(6):237–261. (Cité en pages 3, 10, 20, 21, 22, 25, 45, 50, 114 et 121.)

[Tirvaudey et al., 2019b] Tirvaudey, M., Chamoin, L., Bouclier, R., and Passieux, J.-C. (2019b). A posteriori error estimation and adaptivity in non-intrusive couplings between concurrent models. *Computer Methods in Applied Mechanics and Engineering*, submitted. (Cité en pages 3 et 32.)

[Tong, 2013] Tong, W. (2013). Formulation of Lucas–Kanade digital image correlation algorithms for non-contact deformation measurements: A review. *strain*, 49:313–334. (Cité en page 90.)

[Toselli and Widlund, 2006] Toselli, A. and Widlund, O. (2006). *Domain decomposition methods-algorithms and theory*, volume 34. Springer Science & Business Media. (Cité en page 71.)

[Totaro and Nicola, 2012] Totaro, G. and Nicola, F. D. (2012). Recent advance on design and manufacturing of composite anisogrid structures for space launchers. *Acta Astronautica*, 81(2):570 – 577. (Cité en page 59.)

[Tournier et al., 2019] Tournier, P.-H., Aliferis, I., Bonazzoli, M., De Buhan, M., Darbas, M., Dolean, V., Hecht, F., Jolivet, P., El Kanfoud, I., Migliaccio, C., et al. (2019). Microwave tomographic imaging of cerebrovascular accidents by using high-performance computing. *Parallel Computing*, 85:88–97. (Cité en pages 91 et 102.)

[Touzeau et al., 2011] Touzeau, J., Chiaruttini, V., Feyel, F., and Dhia, H.-B. (2011). Approche multiéchelle arlequin pour l'étude des structures composites stratifiées. In *10e Colloque National en Calcul des Structures, Giens, France*. (Cité en page 30.)

[Tshimanga et al., 2008] Tshimanga, J., Gratton, S., Weaver, A., and Sartenaer, A. (2008). Limited-memory preconditioners, with application to incremental four-dimensional variational data assimilation. *Quarterly Journal of the Royal Meteorological Society*, 134:751 – 769. (Cité en page 104.)

[Van Beeck et al., 2014] Van Beeck, J., Neggers, J., Schreurs, P., Hoefnagels, J., and Geers, M. (2014). Quantification of three-dimensional surface deformation using global digital image correlation. *Experimental Mechanics*, 54(4):557–570. (Cité en pages 81 et 89.)

[Vassberg et al., 2008] Vassberg, J., Dehaan, M., Rivers, M., and Wahls, R. (2008). Development of a Common Research Model for Applied CFD Validation Studies. In *26th AIAA Applied Aerodynamics Conference*, pages 1–22, Reston, Virigina. (Cité en page 136.)

[Veiga et al., 2012] Veiga, L., Buffa, A., Cho, D., and Sangalli, G. (2012). Analysis-suitable T-splines are dual-compatible. *Computer Methods in Applied Mechanics and Engineering*, 249:42–51. (Cité en page 15.)

[Verhoosel et al., 2015] Verhoosel, C.-V., van Zwieten, G.-J., van Rietbergen, B., and de Borst, R. (2015). Image-based goal-oriented adaptive isogeometric analysis with application to the micro-mechanical modeling of trabecular bone. *Computer Methods in Applied Mechanics and Engineering*, 284:138–164. (Cité en pages 43, 53, 104 et 145.)

[Vuong et al., 2011] Vuong, A.-V., Giannelli, C., Jüttler, B., and Simeon, B. (2011). A hierarchical approach to adaptive local refinement in isogeometric analysis. *Computer Methods in Applied Mechanics and Engineering*, 200:3554–3567. (Cité en page 15.)

[Wall et al., 2008] Wall, W. A., Frenzel, M. A., and Cyron, C. (2008). Isogeometric structural shape optimization. *Computer Methods in Applied Mechanics and Engineering*, 197(33):2976 – 2988. (Cité en pages 9, 59, 113, 123, 125 et 142.)

[Wang et al., 2019] Wang, D., Abdalla, M. M., Wang, Z.-P., and Su, Z. (2019). Streamline stiffener path optimization (SSPO) for embedded stiffener layout design of non-uniform curved grid-stiffened composite (NCGC) structures. *Computer Methods in Applied Mechanics and Engineering*, 344:1021–1050. (Cité en page 138.)

[Wang and Kemao, 2018] Wang, T. and Kemao, Q. (2018). Parallel computing in experimental mechanics and optical measurement: A review (ii). *Optics and Lasers in Engineering*, 104:181 – 191. Optical Tools for Metrology, Imaging and Diagnostics. (Cité en pages 91 et 102.)

[Wang et al., 2018] Wang, Y., Wang, Z., Xia, Z., and Poh, L. H. (2018). Structural design optimization using isogeometric analysis: A comprehensive review. *Computer Modeling in Engineering and Sciences*, 117:455–507. (Cité en pages 113, 120 et 123.)

[Wang et al., 2017] Wang, Z. P., Poh, L. H., Dirrenberger, J., Zhu, Y., and Forest, S. (2017). Isogeometric shape optimization of smoothed petal auxetic structures via computational periodic homogenization. *Computer Methods in Applied Mechanics and Engineering*, 323:250–271. (Cité en pages 123 et 125.)

[Wang and Turteltaub, 2015] Wang, Z.-P. and Turteltaub, S. (2015). Isogeometric shape optimization for quasi-static processes. *International Journal for Numerical Methods in Engineering*, 104:347–371. (Cité en page 123.)

[Weeger et al., 2019] Weeger, O., Narayanan, B., and Dunn, M. L. (2019). Isogeometric shape optimization of nonlinear, curved 3d beams and beam structures. *Computer Methods in Applied Mechanics and Engineering*, 345:26–51. (Cité en page 123.)

[Whitcomb, 1991] Whitcomb, J. (1991). Iterative global/local finite element analysis. *Computers and Structures*, 40(4):1027–1031. (Cité en page 31.)

[Wittevrongel et al., 2015] Wittevrongel, L., Lava, P., Lomov, S., and Debruyne, D. (2015). A self adaptive global digital image correlation algorithm. *Experimental Mechanics*, 55(2):361–378. (Cité en pages 81 et 89.)

[Wohlmuth, 2000] Wohlmuth, B. (2000). A Mortar finite element method using dual spaces for the Lagrange multiplier. *SIAM Journal on Numerical Analysis*, 38(3):989–1012. (Cité en pages 33 et 34.)

[Wunderlich et al., 2019] Wunderlich, L., Seitz, A., Alaydın, M., Wohlmuth, B., and Popp, A. (2019). Biorthogonal splines for optimal weak patch-coupling in isogeometric analysis with applications to finite deformation elasticity. *Computer Methods in Applied Mechanics and Engineering*, 346:197–215. (Cité en pages 33, 44, 68, 72 et 77.)

[Wyart et al., 2008] Wyart, E., Duflot, M., Coulon, D., Martiny, P., Pardoen, T., Remacle, J., and Lani, F. (2008). Substructuring fe–xfe approaches applied to three-dimensional crack propagation. *Journal of Computational and Applied Mathematics*, 215(2):626–638. (Cité en page 30.)

[Xie and Farin, 2004] Xie, Z. and Farin, G. E. (2004). Image registration using hierarchical B-splines. *IEEE Transactions on Visualization and Computer Graphics*, 10(1):85–94. (Cité en pages 84 et 111.)

[Xu et al., 2013] Xu, G., Mourrain, B., Duvigneau, R., and Galligo, A. (2013). Analysis-suitable volume parameterization of multi-block computational domain in isogeometric applications. *Computer-Aided Design*, 45:395–404. (Cité en pages 16 et 43.)

[Zhao and Kapania, 2016] Zhao, W. and Kapania, R. K. (2016). Buckling analysis of unitized curvilinearly stiffened composite panels. *Composite Structures*, 135:365–382. (Cité en page 138.)

[Zienkiewicz et al., 2005] Zienkiewicz, O. C., Taylor, R. L., and Zhu, J. Z. (2005). *The finite element method: its basis and fundamentals*. Elsevier. (Cité en page 24.)

[Zou et al., 2018a] Zou, X., Conti, M., Díez, P., and Auricchio, F. (2018a). A nonintrusive proper generalized decomposition scheme with application in biomechanics. *International Journal for Numerical Methods in Engineering*, 113(2):230–251. (Cité en page 104.)

[Zou et al., 2018b] Zou, Z., Scott, M., Borden, M. J., Thomas, D. C., Dornisch, W., and Brivadis, E. (2018b). Isogeometric Bézier dual mortaring: Refineable higher-order spline dual bases and weakly continuous geometry. *Computer Methods in Applied Mechanics and Engineering*, 333:497–534. (Cité en pages 33 et 44.)